Determination of $|V_{cb}|$ and form factors of $\bar{B}^0 \to D^{*+}\ell^-\bar{\nu}_\ell$ decays with Belle II data

Dissertation
zur
Erlangung des Doktorgrades (Dr. rer. nat.)
der
Mathematisch-Naturwissenschaftlichen Fakultät
der
Rheinischen Friedrich-Wilhelms-Universität Bonn

von
Chaoyi Lyu
aus
Henan, China

Bonn, 10.2023

Angefertigt mit Genehmigung der Mathematisch-Naturwissenschaftlichen Fakultät der
Rheinischen Friedrich-Wilhelms-Universität Bonn

1. Gutachter:	Prof. Dr. Florian Bernlochner
2. Gutachter:	Prof. Dr. Jochen Dingfelder
Tag der Promotion:	20.12.2023
Erscheinungsjahr:	2024

Abstract

This thesis presents a determination of the Cabibbo-Kobayashi-Maskawa (CKM) matrix element magnitude $|V_{cb}|$ and form-factor parameters of $\bar{B}^0 \to D^{*+}\ell^-\bar{\nu}_\ell$ decays, where $\ell = e, \mu$. We conduct our analysis using Belle II data collected from 2019 to 2021, corresponding to an integrated luminosity of $\int \mathcal{L}dt$ =189 fb^{-1}. In the Belle II experiment, electrons and positrons collide with a center of mass energy $\sqrt{s}$ = 10.58 GeV, which corresponds to the $\Upsilon(4S)$ mass. Subsequently, more than 96% of $\Upsilon(4S)$ mesons decay to $B\bar{B}$ [1]. We reconstruct signal $\bar{B}^0 \to D^{*+}\ell^-\bar{\nu}_\ell$ decays, followed by $D^{*+} \to D^0\pi^+$ and $D^0 \to K^-\pi^+$ decays, without the explicit reconstructing the accompanying B meson produced in the $\Upsilon(4S)$ decay.

The theoretical description of the differential decay rate of the $\bar{B}^0 \to D^{*+}\ell^-\bar{\nu}_\ell$ channel relies on kinematic variables that are intimately related to the momentum of the B meson. However, due to the escape of final-state neutrinos from the Belle II detectors, it is challenging to precisely measure the momentum of the B meson. To address this problem, we have developed a novel approach for inferring the kinematic variables. This approach leverages the angular distribution of the signal B meson as well as particles produced by the accompanying B meson. Compared to previous methods, our novel approach significantly enhances the resolution of the reconstruction, achieving improvements ranging from 7% to 12%.

The determination of the signal yield in each bin of the kinematic variables includes a two-dimensional binned fit to the distributions of $\cos\theta_{BY}$ and ΔM. Here, $\cos\theta_{BY}$ represents the cosine of the angle between the B candidate and the $D^*\ell$ system (denoted as Y), while ΔM is the mass difference between the D^{*+} and D^0 candidates. Because of the finite detector resolution, the observed signal yields may deviate from the underlying true yields. To correct for this distortion, we employ the singular-value-decomposition unfolding method. Subsequently, partial decay rates in bins of kinematic variables are derived from the unfolded yields and reconstruction efficiencies, which are estimated using simulated samples.

By summing the partial decay rates of all kinematic variables we obtain the total rate. The average of the total rates over $\bar{B}^0 \to D^{*+}e^-\bar{\nu}_e$ and $\bar{B}^0 \to D^{*+}\mu^-\bar{\nu}_\mu$ decays is converted to branching fractions using the B^0 lifetime. We find $\mathcal{B}(\bar{B}^0 \to D^{*+}\ell^-\bar{\nu}_\ell) = (4.922 \pm 0.023 \pm 0.220)\%$, which is compatible with the world average [1]. We fit to the partial decay rates on four projections simultaneously to determine the values of $|V_{cb}|$ and form factor parameters in the Boyd-Grinstein-Lebed and Caprini-Lellouch-Neubert parameterizations, respectively, and find $|V_{cb}|_{\mathrm{BGL}} = (40.57 \pm 0.31 \pm 0.95 \pm 0.58) \times 10^{-3}$ and $|V_{cb}|_{\mathrm{CLN}} = (40.13 \pm 0.27 \pm 0.93 \pm 0.58) \times 10^{-3}$, where the uncertainties are statistical, systematic, and the component due to lattice QCD inputs, respectively. The leading and subleading systematic uncertainties arise from the slow pion

tracking efficiency and the ratio of B^+B^- pairs and $B^0\bar{B}^0$ pairs in the $\Upsilon(4S)$ decay, respectively.

In addition, we assess lepton flavor universality by examining three important variables, including the ratio of branching fractions and differences in lepton angular asymmetry $\mathcal{A}_{FB}$ as well as the longitudinal D^{*+} polarization fraction F_L between $\bar{B}^0 \to D^{*+}e^-\bar{\nu}_e$ and $\bar{B}^0 \to D^{*+}\mu^-\bar{\nu}_\mu$ decays. We find the ratio $R_{e/\mu} = 0.998 \pm 0.009 \pm 0.020$ and differences $\Delta\mathcal{A}_{\text{FB}} = (-17 \pm 16 \pm 16) \times 10^{-3}$ and $\Delta F_L = 0.006 \pm 0.007 \pm 0.005$, where the first and second uncertainties are statistical and systematic, respectively. All results align with the expectations of lepton flavor universality within the Standard Model.

This thesis presents the first published determination of $|V_{cb}|$ through exclusive semileptonic B decays at Belle II, and also sheds light on lepton flavor universality. Furthermore, it provides essential procedures for future measurements.

Acknowledgements

First of all, I would like to thank my supervisor, Prof. Dr. Florian Bernlochner. When I write these words, it takes me back to 2019 when he gave me the opportunity to conduct experimental research in particle physics after an interview. That was one of the most excellent moments of my life. Time has passed so quickly. I can't count how many challenges we've faced together before conferences, but I do remember that he has always been the strongest support behind me, rescuing me from those stressful days. He has been not only the leader of my scientific career in the past four years but also a remarkable example, showing me how to be a wonderful person. Unfortunately, I can't document all the stories that have touched me here because it would probably take more than 100 pages. All in all, it is a great honor to be his student. In addition, I would like to thank his wife, Julie. Due to the home office during the Covid-19 pandemic, I had fewer opportunities to speak English. I truly benefited a lot from our tandem meetings every weekend.

I would also like to express my gratitude to Prof. Dr. Jochen Dingfelder for his guidance and insightful discussions during our group meetings. I extend my heartfelt thanks to Dr. Lu Cao, who was the first colleague I met in Bonn. When I began my PhD journey from scratch, she played an important role in helping develop data analysis and practical programming skills.

Let me also take this opportunity to thank the members of my review committee in the collaboration, namely Frank Meier, Thomas Lück, and Dmitri Liventsev. Their invaluable comments and suggestions greatly enriched the physics analysis and played a crucial role in refining the paper. Without their contributions, the analysis would not have reached its current level of excellence. Additionally, I want to acknowledge the insightful perspectives shared by Christoph Schwanda and Daniel Dorner. Their contributions are highly appreciated.

Besides, I am immensely grateful for Ms. Andrea Fürstenberg, the stuff of personnel office at the institute. Her assistance has consistently made my life easier every time I needed to apply for travel approvals and university reimbursements.

Our group is like one big family. The members aren't just colleagues; they're more like my brothers and sisters. We've had meetings together, enjoyed drinks, played basketball, shared laughter, and, most importantly, supported each other during difficult times. I feel incredibly fortunate to have had these wonderful friends by my side over the past four years. Their presence ensured that I never felt lonely, and they played a crucial role in shaping me into a better person. I really love them. They are Dr. Markus Prim, Dr. William Sutcliffe, Dr. Peter Lewis, Dr. Maximilian Welsch, Dr. Raynette van Tonder, Dr. Christian Wessel, Ralf Farkas, Ilias Tsaklidis, Daniel Jacobi, Tobias Böckh, Martin Angelsmark, Michael Eliachevitch, Munira Khan, Svenja

Granderath, Alina Manthei, Henrik Junkerkalefeld, Stephan Duell, and Lucas Stötzer.

Lastly, but of utmost importance, I would like to extend my heartfelt gratitude to my parents and to everyone who has been a source of encouragement throughout my journey.

Contents

CHAPTER 1

Introduction

Particle physics is a subject that explores the fundamental building blocks of matter and their interactions. It is also known as high energy physics because experiments related to particle physics involve accelerating particles to velocities close to the speed of light. These particles then collide at the interaction point, leading to annihilation and the creation of other types of particles. The term "high energy" in this context refers to the significant kinetic energy carried by these particles.

Physics at subatomic distance scales is governed by the laws of quantum mechanics. Even though we collide the same particles every time, the outcome of a collision event is not deterministic. Experimentally, we reconstruct final-state particles in each event and, furthermore, identify the mother particle that produced them. We analyze their kinematic information and extract observables of interest for specific decay modes. These observables typically encode information about the properties of interactions and can be sensitive to various theoretical frameworks. Thus far, the Standard Model (SM) of particle physics has proven to be the most successful theoretical framework in describing the majority of discovered elementary particles and their interactions.

There are four fundamental interactions in nature: the electromagnetic interaction, weak interaction, strong interaction, and gravitational interaction. They are compared in Table 1.1 in terms of the coupling constant and mediator. The gravitational interaction between particles is negligible due to the extremely small masses and is outside the scope of collider physics.

Table 1.1: Comparison of four interactions.

Interactions	Coupling constant	Mediator
Electromagnetic interaction	$\alpha \simeq 1/137$ [1]	Photon
Weak interaction	$\alpha_W \simeq 10^{-6}$ [2]	$W^{\pm}$ and Z^0 bosons
Strong interaction	$\alpha_s(m_Z) \simeq 10^{-1}$ [1]	Gluon
Gravitational interaction	$G_N \simeq 6.7 \times 10^{-39}$ GeV^{-2} [1]	Graviton (undiscovered) [3]

1.1 Elementary particles in the Standard Model

The SM is a theoretical framework that successfully describes the elementary particles discovered to date, as depicted in Fig. 1.1, and their interactions. Although numerous extensions to the SM predict the existence of new particles, such as leptoquarks and charged Higgs bosons, as of today, no additional fundamental particles have been unquestionably discovered and confirmed through experiments. Each type of particle has an associated antiparticle with the same mass but opposite electric charge. Some neutral particles, such as photons, are their own antiparticles.

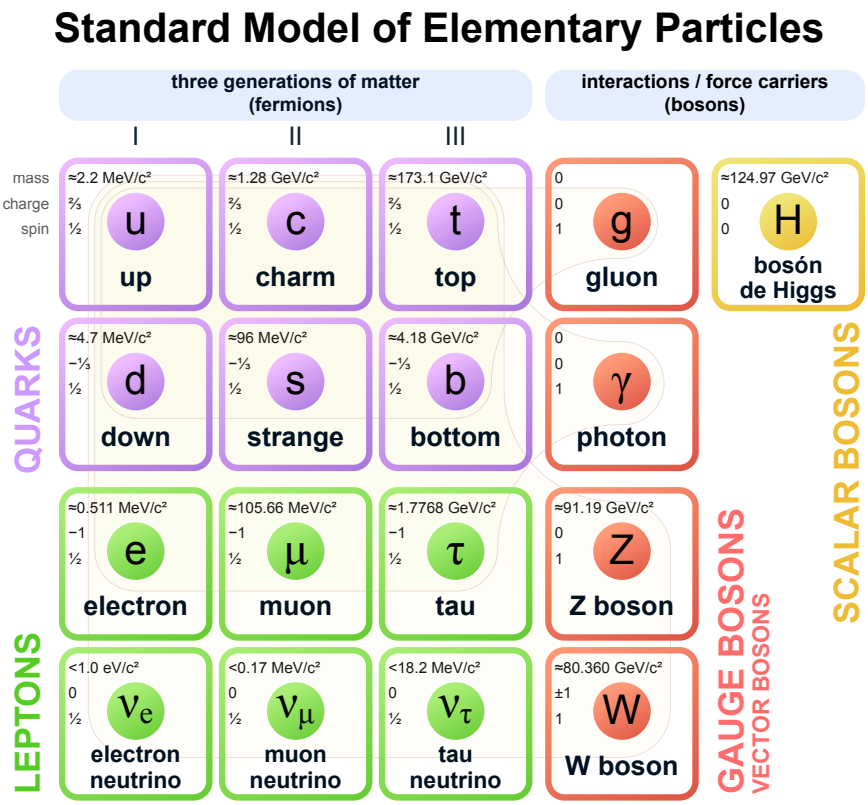

Figure 1.1: Elementary particles in the SM with information about their masses, charges, and spins [4].

In the SM, there are three generations of quarks and leptons, each with a spin of $1/2$, as depicted in the first three columns of Fig. 1.1. Leptons encompass charge-neutral neutrinos and charged leptons, which carry one unit of electric charge. In contrast, the electric charges of quarks are not integers. The up-type quarks have a charge of $2/3$ and consist of three flavors: up, charm, and top. The remaining three flavors constitute the down-type quarks, encompassing down, strange, and bottom, each with a charge of $-1/3$.

The existence of quarks was discovered through deep inelastic scattering, an extension of Rutherford scattering to much higher energies, resulting in a much finer resolution of the components of nuclei. Unlike Rutherford scattering, deep inelastic scattering shows the absorption

of kinetic energy by target nuclei, the generation of new hadrons, and even the complete fragmentation of the target nuclei. These observations provide clear evidence of the internal point-like constituents, namely quarks, of protons and neutrons.

In contrast to leptons, quarks engage in the strong interaction and are characterized by unique color charges—specifically, red, green, and blue. Similarly, an antiquark can carry one of three anticolors. However, due to color confinement, color-charged particles cannot be isolated and therefore cannot be directly observed. In the quark model, there are two primary ways to form colorless particles. One involves combining a quark and an antiquark with opposite color charges, resulting in a particle known as a meson. For example, B^0 mesons consist of a d-quark and a $\bar{b}$-quark. Additionally, three quarks or antiquarks with entirely different colors can combine to form a stable particle called a baryon. For instance, the proton is a baryon composed of two u-quarks and one d-quark.

Beyond the conventional quark model, the SM allows for the existence of many exotic states, such as the $qq\bar{q}\bar{q}$ (tetraquark) and $qqqq\bar{q}$ (pentaquark) systems. The experimental discovery of these states validates the theory of fundamental particles and enhances physicists' understanding of how quarks bind together to form composite particles [5, 6].

Charged leptons consist of the electron, muon, and tau, each with distinct properties primarily driven by their mass difference. The electron, with a mass of 0.511 MeV/c^2, stands out as the lightest and the only stable charged elementary particle in the SM. Additionally, it is the first discovered elementary particle. In 1897, J. J. Thomson observed the deflection of cathode rays in magnetic and electric fields. By analyzing the magnitude of the electrical and magnetic deflection, the ratio of mass to charge was calculated. This calculation provided clear evidence for the discovery of the electron, marking a significant milestone in the history of particle physics.

Compared to electrons, muons are approximately 200 times more massive [7]. Their relatively long lifetime of 2.2×10^{-6} seconds allows them to be observed by particle detectors in collision experiments. However, measurements of the muon's magnetic moment at the Brookhaven laboratory have revealed a puzzling 3.7σ deviation from SM predictions, suggesting gaps in our understanding of muons' behavior [8, 9].

The tau lepton, the heaviest among the charged leptons with a mass of 1.777 GeV, plays a crucial role in conducting precise tests of the flavor sector of the SM and determining its parameters. Leptonic tau decays shed light on the structure of weak currents and the universality of the couplings between tau leptons and W bosons, i.e., all leptons in the SM have identical interactions with W bosons. Meanwhile, hadronic tau decays provide opportunities to study low-energy effects of the strong interaction under exceptionally clean conditions. For a more comprehensive examination of tau-related physics, one can refer to Ref. [10].

In each generation, there is also a charge-neutral lepton known as a neutrino. Many aspects of neutrinos are still unknown to date because they travel at speeds close to that of light and rarely interact with other particles. However, this elusive nature makes them valuable tools for investigating phenomena that cannot be directly observed, such as probing the interior of the Sun or studying the early universe. Neutrinos are also considered as one of the messengers from distant astrophysical sources, offering insights into various astrophysical processes [11, 12].

All the particles discussed so far belong to the category of fermions, characterized by their half-integer spins in quantum physics. In contrast, particles with integer spins are classified as

bosons. Within the SM, the gauge bosons encompass gluons, photons, Z bosons, and W bosons. These bosons, all with a spin of 1, serve as force carriers responsible for the strong interaction, electromagnetic interaction, and weak interaction (both Z and W bosons), respectively.

The Higgs boson is the only scalar boson in the SM. Its existence was confirmed in 2012 through experiments conducted by ATLAS and CMS experiments at CERN's Large Hadron Collider (LHC). This landmark discovery led to the awarding of the 2013 Nobel Prize in Physics to François Englert and Peter W. Higgs for their theoretical predictions of the Higgs mechanism. This mechanism fundamentally explains the origin of mass for elementary particles.

1.2 Interactions in the Standard Model

The physical properties of the microscopic world, including atoms and subatomic particles, differ significantly from the everyday macroscopic world. Quantum mechanics is developed as a framework to describe these microscopic phenomena, including solutions to challenges like the black-body radiation problem and the photoelectric effect. A fundamental concept in quantum mechanics is the wave function, which associates a probability amplitude with each point in spacetime to describe particles, such as electrons.

However, quantum mechanics alone falls short in describing certain phenomena, particularly particle annihilation and production, which are commonly observed in experiments of electron-positron and proton-proton collisions, where particles are accelerated to speeds approaching that of light. To explain these phenomena, quantum field theory was established based on the principles of quantum mechanics, classical field theory, and special relativity [13, 14].

In quantum field theory, particles are represented as excited states of their respective underlying quantum fields. The interactions between particles are described using a mathematical framework known as the Lagrangian, which is also used by classical field theory, or are illustrated through Feynman diagrams, which are derived using the principles of perturbation theory in quantum mechanics.

1.2.1 Electromagnetic interaction

The theory that describes the electromagnetic force at the microscopic scale is known as quantum electrodynamics (QED). The Lagrangian density for QED is expressed as

$$\mathcal{L} = -\frac{1}{4}F_{\mu\nu}F^{\mu\nu} + i\bar{\psi}\gamma^{\mu}D_{\mu}\psi - m\bar{\psi}\psi, \tag{1.1}$$

where $F_{\mu\nu} = \partial_{\mu}A_{\nu} - \partial_{\nu}A_{\mu}$ represents the field strength tensor for the massless spin-1 field A_{μ}, and $D_{\mu}\psi = \partial_{\mu}\psi + ieA_{\mu}\psi$ describes the covariant derivative for a particle with electric charge e in the presence of the field A_{μ}. Here, ψ and $\bar{\psi} = \psi^{\dagger}\gamma^{0}$ denote the Dirac fields associated with spin-half particles, γ^{μ} are Dirac matrices, and m is the mass of the spin-half particle. The

Lagrangian is invariant under local gauge transformations

$$A_\mu \rightarrow A'_\mu = A_\mu + \partial_\mu \theta(x), \tag{1.2}$$

$$\psi \rightarrow \psi' = e^{-ie\theta(x)}\psi. \tag{1.3}$$

Expanding the Lagrangian density as

$$\mathcal{L} = -\frac{1}{4}F_{\mu\nu}F^{\mu\nu} + \bar{\psi}\left(i\gamma^\mu\partial_\mu - m\right)\psi - e\bar{\psi}\gamma^\mu\psi A_\mu, \tag{1.4}$$

we identify the interaction term $-e\bar{\psi}\gamma^\mu\psi A_\mu$ for the Dirac and massless spin-1 fields.

1.2.2 Electroweak unification

The transformation described in Eq. (1.3) corresponds to the U(1) group in mathematics. The invariance of the Lagrangian in Eq. (1.1) under U(1) transformations ensures that when charged fermions, such as electrons, undergo these gauge transformations, their interaction with the electromagnetic field remains unaltered. The modification of electromagnetic field effectively compensates for any changes in their local transformations, resulting in no observable difference in physical outcomes. This fundamental property of U(1) gauge symmetry underlies the conservation of electric charge.

Symmetry also plays a fundamental role in understanding the weak interaction. The SU(2) group is a fundamental element in the description of the weak interaction, as it allows the mixing of different particle flavors within the same multiplet. This property of SU(2) provides a natural framework for explaining flavor-changing processes.

We observe that weak gauge bosons, quarks, and charged leptons have mass. However, directly introducing a mass term into the Lagrangian would result in the breaking of the local SU(2) symmetry. To overcome this issue, the concept of spontaneous symmetry breaking (SSB) was introduced. In SSB, the global SU(2)×U(1) symmetry spontaneously breaks down, while the local SU(2)×U(1) symmetry remains preserved via the Higgs mechanism, which serves as the foundation of electroweak unification.

The Lagrangian density for the interactions between gauge bosons and the Higgs boson H in electroweak unification is expressed as

$$\mathcal{L} = -\frac{1}{4}F^a_{\mu\nu}F^{a,\mu\nu} - \frac{1}{4}J_{\mu\nu}J^{\mu\nu} + (D_\mu H)^\dagger(D_\mu H) + m^2H^\dagger H - \lambda(H^\dagger H)^2. \tag{1.5}$$

Here, the covariant derivative is defined as

$$D_\mu = \partial_\mu - igA^a_\mu\tau^a - \frac{1}{2}ig'B_\mu, \tag{1.6}$$

where g and g' are coupling constants associated with the SU(2) and U(1) gauge symmetries, respectively, and τ^a denotes the three generators of the SU(2) group, which are proportional to the 2×2 Pauli matrices. In addition, $F^a_{\mu\nu}$ and $J_{\mu\nu}$ are the SU(2) and U(1) gauge field tensors,

respectively, defined as

$$F^a_{\mu\nu} = \partial_\mu A^a_\nu - \partial_\nu A^a_\mu + g\varepsilon^{abc} A^b_\mu A^c_\nu, \tag{1.7}$$

$$J_{\mu\nu} = \partial_\mu B_\nu - \partial_\nu B_\mu, \tag{1.8}$$

where ε^{abc} represents the Levi-Civita tensor, and A^a_μ and B_μ are gauge boson fields, which we will discuss in more details later.

In Eq. (1.5), the last two terms correspond to the Higgs potential

$$V(H) = -m^2|H|^2 + \lambda|H|^4, \tag{1.9}$$

which induces a non-zero vacuum expectation value at

$$H|_{\text{min}} = \frac{1}{\sqrt{2}}\begin{pmatrix}0\\ \upsilon\end{pmatrix}, \quad \text{with } \upsilon = \frac{m}{\sqrt{\lambda}}. \tag{1.10}$$

The non-zero vacuum expectation of the Higgs field is responsible for the masses of the gauge bosons. This becomes evident when we expand the covariant derivative acting on the Higgs field

$$\begin{aligned}\left|D_\mu H\right|^2 &= \left|\left[\partial_\mu - \frac{i}{2}\begin{pmatrix} gA^3_\mu + g'B_\mu & \sqrt{2}gW^+_\mu \\ \sqrt{2}gW^-_\mu & -gA^3_\mu + g'B_\mu\end{pmatrix}\frac{1}{\sqrt{2}}\begin{pmatrix}0 & \upsilon\end{pmatrix}\right]\right|^2 \\ &= \frac{1}{4}g^2\upsilon^2 W^+_\mu W^{-\mu} + \frac{1}{8}\upsilon^2\begin{pmatrix}A^3_\mu & B_\mu\end{pmatrix}\begin{pmatrix} g^2 & -gg' \\ -gg' & g'^2\end{pmatrix}\begin{pmatrix}A^3_\mu \\ B_\mu\end{pmatrix},\end{aligned} \tag{1.11}$$

where we have defined

$$W^\pm = \frac{A^1_\mu \mp iA^2_\mu}{\sqrt{2}}. \tag{1.12}$$

In Eq. (1.11), the masses of $W^\pm$ bosons are explicit. To diagonalize the masses for the B_μ and A^3_μ fields, we rotate them as

$$\begin{cases} B_\mu = \cos\theta_w A_\mu - \sin\theta_w Z_\mu, \\ A^3_\mu = \sin\theta_w A_\mu + \cos\theta_w Z_\mu. \end{cases} \tag{1.13}$$

This rotation defines the electroweak mixing angle θ_w (also known as Weinberg angle), with its trigonometric components

$$\sin\theta_w = \frac{g'}{\sqrt{g^2 + g'^2}}, \quad \cos\theta_w = \frac{g}{\sqrt{g^2 + g'^2}}. \tag{1.14}$$

With these definitions, Eq. (1.11) can be elegantly expressed as

$$\mathcal{L} = \frac{1}{4}g^2\upsilon^2 W^+_\mu W^{-\mu} + \frac{1}{8}\upsilon^2(g^2 + g'^2)Z_\mu Z^\mu. \tag{1.15}$$

This succinctly captures the essence of the Higgs mechanism, providing a clear explanation for why the $W^{\pm}$ and Z bosons acquire mass, while the photon A_μ field remains massless.

In the fermion sector, we have three generations of SU(2) doublet pairs consisting of left-handed leptons and quarks:

$$L^i = \begin{pmatrix} \nu_{eL} \\ e_L \end{pmatrix}, \begin{pmatrix} \nu_{\mu L} \\ \mu_L \end{pmatrix}, \begin{pmatrix} \nu_{\tau L} \\ \tau_L \end{pmatrix}, \qquad Q^i = \begin{pmatrix} u_L \\ d_L \end{pmatrix}, \begin{pmatrix} c_L \\ s_L \end{pmatrix}, \begin{pmatrix} t_L \\ b_L \end{pmatrix}. \tag{1.16}$$

The right-handed fermions are singlets, and they are denoted as follows

$$u_R^i = u_R, c_R, t_R, \tag{1.17}$$

$$d_R^i = d_R, s_R, b_R, \tag{1.18}$$

$$l_R^i = e_R, \mu_R, \tau_R. \tag{1.19}$$

The Yukawa coupling describes the interaction between a (pseudo)scalar field and a Dirac field. It was initially introduced by Hideki Yukawa to explain the nuclear force between nucleons mediated by pions. Later, it found broader applications in elucidating the origin of fermion masses within the SM.

The Yukawa Lagrangian density is expressed as

$$\mathcal{L}_{\text{Yukawa}} = -g_i^L \bar{L}^i H e_R^i - g_{ij}^d \bar{Q}^i H d_R^j - g_{ij}^u \bar{Q}^i \tilde{H} u_R^j + h.c., \tag{1.20}$$

where

$$\tilde{H} = i\sigma_2 H^*, \tag{1.21}$$

and $h.c.$ stands for the Hermitian conjugate terms.

After electroweak symmetry breaking, the complex Higgs field can be expressed, without loss of generality, as

$$H(x) = \frac{1}{\sqrt{2}} \begin{pmatrix} 0 \\ \upsilon + h(x) \end{pmatrix}, \tag{1.22}$$

where $h(x)$ is a real scalar filed.

By substituting this expression into Eq. (1.20), the Lagrangian density is expanded as follows

$$\begin{aligned} \mathcal{L}_{\text{Yukawa}} = &- \frac{g_i^L}{\sqrt{2}} \begin{pmatrix} \bar{\nu}_{iL} & \bar{l}_{iL} \end{pmatrix} \begin{pmatrix} 0 \\ \upsilon + h \end{pmatrix} l_R^i - \frac{g_{ij}^d}{\sqrt{2}} \begin{pmatrix} \bar{u}_{iL} & \bar{d}_{iL} \end{pmatrix} \begin{pmatrix} 0 \\ \upsilon + h \end{pmatrix} d_R^j \\ &- \frac{g_{ij}^u}{\sqrt{2}} \begin{pmatrix} \bar{u}_{iL} & \bar{d}_{iL} \end{pmatrix} \begin{pmatrix} \upsilon + h \\ 0 \end{pmatrix} u_R^j + h.c. \\ = &- \frac{g_i^L}{\sqrt{2}} \bar{l}_{iL} l_R^i (\upsilon + h) - \frac{g_{ij}^d}{\sqrt{2}} \bar{d}_{iL} d_R^j (\upsilon + h) - \frac{g_{ij}^u}{\sqrt{2}} \bar{u}_{iL} u_R^j (\upsilon + h) + h.c.. \end{aligned} \tag{1.23}$$

Expanding it further, we obtain additional terms that involve the h field, which represent the couplings of fermions to the Higgs boson. Additionally, we find terms that include the non-zero

vacuum expectation value of the Higgs field, which are the origins of quark masses,

$$\mathcal{L}_{\text{mass}} = -\upsilon \frac{g^d_{ij}}{\sqrt{2}} \bar{d}_{iL} d^j_R - \upsilon \frac{g^u_{ij}}{\sqrt{2}} \bar{u}_{iL} u^j_R + h.c.\,. \tag{1.24}$$

Two diagonal matrices M_d and M_u play a crucial role in diagonalizing the quark mass matrices. They are related to the Yukawa coupling matrices, g_d and g_u, through the following relations

$$g_d = U_d M_d K_d^\dagger, \qquad g_u = U_u M_u K_u^\dagger, \tag{1.25}$$

with the unitary matrices U_d, U_u, K_d and K_u.

This implies that by performing a change of basis for the right-handed quarks represented by $d_R \to K_d d_R$ and $u_R \to K_u u_R$, as well as for the left-handed quarks represented by $u_L \to U_u u_L$ and $d_L \to U_d d_L$, we can observe a simplification in the mass terms, which become

$$\mathcal{L}_{\text{mass}} = -m^d_j \bar{d}^j_L d^j_R - m^u_j \bar{u}^j_L u^j_R + h.c.\,, \tag{1.26}$$

where m^d_j and m^u_j are the diagonal elements of $\frac{\upsilon}{\sqrt{2}} M_d$ and $\frac{\upsilon}{\sqrt{2}} M_u$, respectively.

Next, let us delve into the interactions between fermions and gauge bosons, which play an important role in semileptonic B decays. At the leading order, the $b \to c$ transition is primarily governed by the coupling of $W^\pm$ bosons, which subsequently decay into charged leptons and neutrinos. These gauge interactions are expressed as

$$\begin{aligned}\mathcal{L} = {} & i\bar{L}_i(\partial\!\!\!/ - ig A\!\!\!/^a \tau^a - ig' Y_L B\!\!\!/) L_i + i\bar{Q}_i(\partial\!\!\!/ - ig A\!\!\!/^a \tau^a - ig' Y_Q B\!\!\!/) Q_i \\ & + i\bar{u}^i_R(\partial\!\!\!/ - ig' Y_u B\!\!\!/) u^i_R + i\bar{d}^i_R(\partial\!\!\!/ - ig' Y_d B\!\!\!/) d^i_R \\ & + i\bar{l}^i_R(\partial\!\!\!/ - ig' Y_e B\!\!\!/) l^i_R\end{aligned} \tag{1.27}$$

where $\partial\!\!\!/ = \gamma^\mu \partial_\mu$, and the same notation applies to $A\!\!\!/$ and $B\!\!\!/$. The symbols Y_L and Y_Q represent the hypercharges for the left-handed fields, while Y_u, Y_d, and Y_e denote the right-handed fields.

These hypercharges are determined based on the observed electric charges of leptons and quarks. For instance, one can isolate the coupling of the neutral gauge bosons A^3_μ and B_μ to leptons in Eq. (1.27), and then transform to the physical A_μ - Z_μ basis. In this basis, the interaction of photons with leptons is described as

$$\mathcal{L} = \left(-\frac{1}{2} + Y_L\right) \bar{e}^i_L A\!\!\!/ e^i_L + \left(\frac{1}{2} + Y_L\right) \bar{\nu}^i_L A\!\!\!/ \nu^i_L + Y_e \bar{l}^i_R A\!\!\!/ l^i_R. \tag{1.28}$$

Given the conventional definition of electrons having a charge of -1, we determine that $Y_L = -\frac{1}{2}$ and $Y_e = -1$. The former requirement results in neutral neutrinos, which is consistent with observed phenomena in nature. Similar considerations are applied to quarks, taking into account that the up quark has a charge of $\frac{2}{3}$ and the down quark has a charge of $-\frac{1}{3}$. This leads us to the values $Y_Q = \frac{1}{6}$, $Y_u = \frac{2}{3}$, and $Y_d = -\frac{1}{3}$.

Note that the gauge bosons originally interact with quarks in the flavor basis. In this basis,

quarks from different generations are not mixed

$$\mathcal{L}_{\text{flavor-basis}} = \begin{pmatrix}\bar{u}_L & \bar{d}_L\end{pmatrix}^i \left[i\partial\!\!\!/ + \gamma_\mu \begin{pmatrix} \frac{g'}{6}B_\mu + \frac{g}{2}A^3 & \frac{g}{\sqrt{2}}W_\mu^+ \\ \frac{g}{\sqrt{2}}W_\mu^- & \frac{g'}{6}B_\mu - \frac{g}{2}A_\mu^3 \end{pmatrix} \right] \begin{pmatrix} u_L \\ d_L \end{pmatrix}^i \tag{1.29}$$
$$+ \bar{u}_R^i (i\partial\!\!\!/ + g'\frac{2}{3}B\!\!\!/) u_R^i + \bar{d}_R^i (i\partial\!\!\!/ - g'\frac{1}{3}B\!\!\!/) d_R^i.$$

When we rotate the quark fields to the mass basis, we observe that the couplings of the right-handed quarks to the B_μ field remain unaffected. The same applies to the interactions between left-handed quarks and both neutral gauge fields B_μ and A_μ^3, as they do not mix up- and down-type flavors. It becomes evident that only the coupling to $W_\mu^\pm$ is sensitive to this rotation. In the mass basis, the interaction of the $W^\pm$ bosons with quarks reads

$$\mathcal{L} = \frac{e}{\sqrt{2}\sin\theta_w}\left[W_\mu^+ \bar{u}_L^i \gamma^\mu V^{ij} d_L^j + W_\mu^- \bar{d}_L^i \gamma^\mu (V^\dagger)^{ij} u_L^j \right], \tag{1.30}$$

where we have defined the Cabibbo-Kobayashi-Maskawa (CKM) matrix

$$V = U_u^\dagger U_d = \begin{pmatrix} V_{ud} & V_{us} & V_{ub} \\ V_{cd} & V_{cs} & V_{cb} \\ V_{td} & V_{ts} & V_{tb} \end{pmatrix}. \tag{1.31}$$

These matrix elements are complex numbers, representing mixing angles and phases in the quark sector.

Moreover, the CKM matrix is unitary, and is typically parameterized using three Euler angles θ_{12}, θ_{23}, and θ_{13}, along with one CP-violating phase δ_{13} as follows

$$\begin{aligned} V = &\begin{pmatrix} 1 & 0 & 0 \\ 0 & \cos\theta_{23} & \sin\theta_{23} \\ 0 & -\sin\theta_{23} & \cos\theta_{23} \end{pmatrix} \begin{pmatrix} \cos\theta_{13} & 0 & \sin\theta_{13}e^{i\delta} \\ 0 & 1 & 0 \\ -\sin\theta_{13} & 0 & \cos\theta_{13} \end{pmatrix} \\ &\times \begin{pmatrix} \cos\theta_{12} & \sin\theta_{12} & 0 \\ -\sin\theta_{12} & \cos\theta_{12} & 0 \\ 0 & 0 & 1 \end{pmatrix} \\ = &\begin{pmatrix} c_{12}c_{13} & s_{12}c_{13} & s_{13}e^{-i\delta} \\ -s_{12}c_{23} - c_{12}s_{23}s_{13}e^{i\delta} & c_{12}c_{23} - s_{12}s_{23}s_{13}e^{i\delta} & s_{23}c_{13} \\ s_{12}s_{23} - c_{12}c_{23}s_{13}e^{i\delta} & -c_{12}s_{23} - s_{12}c_{23}s_{13}e^{i\delta} & c_{23}c_{13} \end{pmatrix}, \end{aligned} \tag{1.32}$$

where $c_{ij} = \cos\theta_{ij}$ and $s_{ij} = \sin\theta_{ij}$.

The SM does not predict the numerical values of the matrix elements. Experimental measurements reveal that the values of the mixing angles are relatively small, satisfying $s_{13} \ll s_{23} \ll s_{12} \ll 1$. To approximate these small values, the Wolfenstein parametrization is commonly employed. In this parametrization, the CKM matrix can be expressed in terms

of $\lambda = \sin\theta_{12}$ as follows

$$|V| \approx \begin{pmatrix} 1-\frac{\lambda^2}{2} & \lambda & \lambda^3 \\ -\lambda & 1-\frac{\lambda^2}{2} & \lambda^2 \\ \lambda^3 & \lambda^2 & 1 \end{pmatrix} + \mathcal{O}(\lambda^4). \tag{1.33}$$

The unitarity of the CKM matrix is an essential requirement in the SM due to its construction for three generations of flavors. The presence of non-SM physics could break the unitarity. For example, if a fourth generation of quarks were to exist in nature, the CKM matrix is not necessarily be unitary. Therefore, examining the unitarity of this matrix is a valuable tool in the search for physics beyond the SM.

Unitarity imposes the requirement that both the rows and columns of the CKM matrix must be orthonormal. This condition gives rise to a set of equations, including $V_{ud}V_{ub}^* + V_{cd}V_{cb}^* + V_{td}V_{tb}^* = 0$, which corresponds to the unitarity triangle illustrated in Fig. 1.2. There are five additional similar equations, expressed in a general form as $\sum_i V_{ij}V_{ik}^* = \delta_{jk}$.

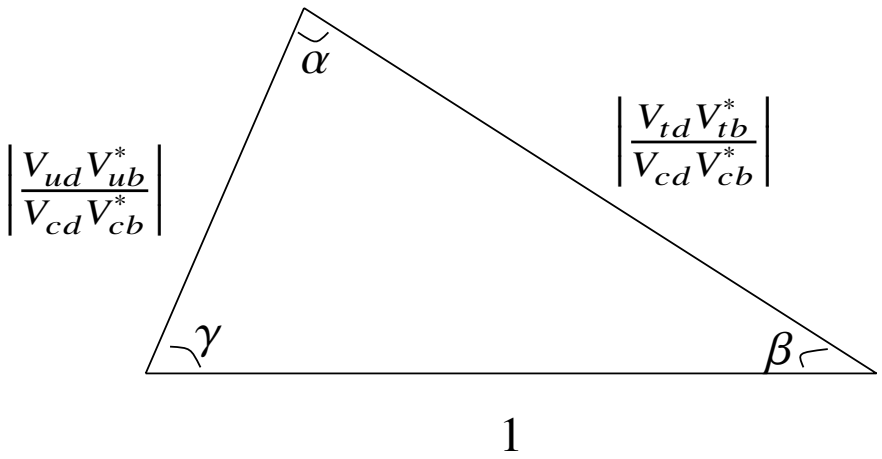

Figure 1.2: Illustration of the unitarity triangle in the complex plane, where the angles α, β, and γ are opposite to the sides 1, $\left|\frac{V_{ud}V_{ub}^*}{V_{cd}V_{cb}^*}\right|$ and $\left|\frac{V_{td}V_{tb}^*}{V_{cd}V_{cb}^*}\right|$, respectively.

With the Lagrangian density described in Eq. (1.29) and Eq. (1.30), we find the Feynman rules governing the interactions between fermions and gauge bosons. These rules are presented in Fig. 1.3 and Fig. 1.4 along with their corresponding Feynman diagrams.

1.2.3 Strong interaction

Quantum Chromodynamics (QCD) is a SU(3) gauge field theory for describing the strong interactions among quarks and gluons. The Lagrangian governing QCD is

$$\mathcal{L}_{\text{QCD}} = \sum_q \bar{\psi}_{q,a}(i\not{\partial}\delta_{ab} - g_s\gamma^\mu t^C_{ab}\mathcal{A}^C_\mu - m_q\delta_{ab})\psi_{q,b} - \frac{1}{4}F^A_{\mu\nu}F^{A\mu\nu}, \tag{1.34}$$

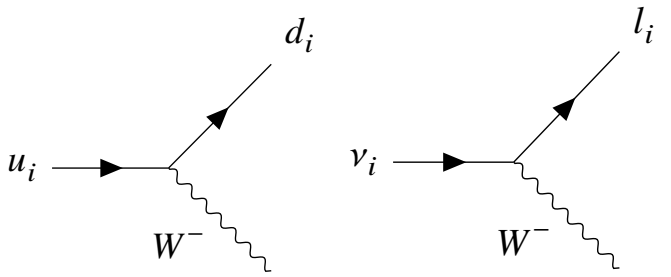

$i\frac{g}{2\sqrt{2}}V_{ij}^{*}\gamma^{\mu}(1-\gamma_5)$ $\quad$ $i\frac{g}{2\sqrt{2}}\gamma^{\mu}(1-\gamma_5)$

Figure 1.3: Feynman diagram and Feynman rules for the interactions between fermions and $W^{\pm}$ bosons, where u_i, d_i, and l_i represent up-type quarks, down-type quarks, and charged leptons, respectively.

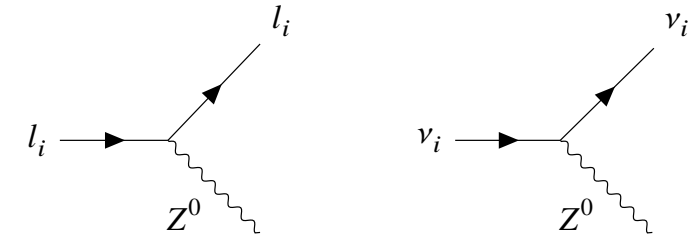

$i\frac{g}{4\cos\theta}\gamma^{\mu}[-(1-4\sin^2\theta)+\gamma_5]$ $\quad$ $i\frac{g}{4\cos\theta}\gamma^{\mu}(1-\gamma_5)$

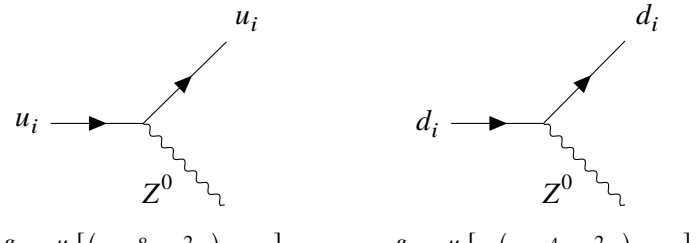

$i\frac{g}{4\cos\theta}\gamma^{\mu}\left[\left(1-\frac{8}{3}\sin^2\theta\right)-\gamma_5\right]$ $\quad$ $i\frac{g}{4\cos\theta}\gamma^{\mu}\left[-\left(1-\frac{4}{3}\sin^2\theta\right)+\gamma_5\right]$

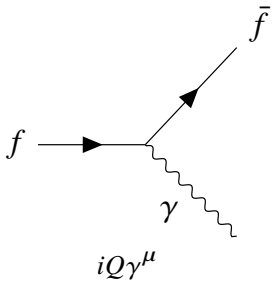

$iQ\gamma^{\mu}$

Figure 1.4: Feynman diagram and Feynman rules for the interactions betwwen fermions and charge-neutral bosons, where u_i, d_i, and l_i represent up-type quarks, down-type quarks, and charged leptons, respectively, and f denotes charged fermions.

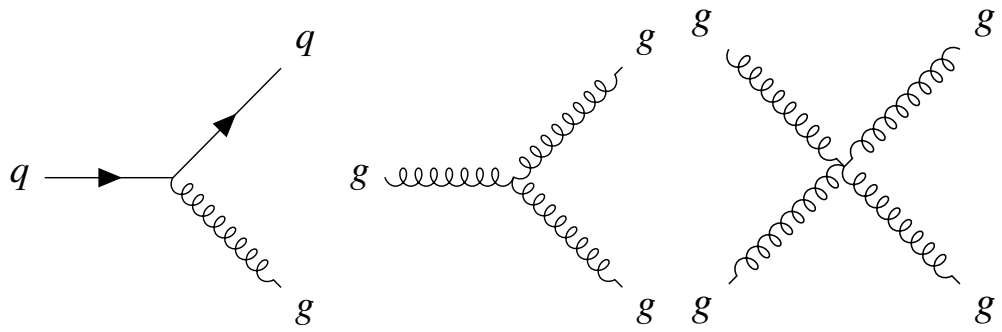

Figure 1.5: Feynman diagram representing the interaction in QCD.

where δ_{ab}, t^C_{ab}, and g_s correspond to the Kronecker delta symbol, Gell-Mann matrices, and strong coupling constant, respectively. The quark field spinors are represented by $\psi_{q,a}$ with the flavor index denoted as q and the color index as a, ranging from one to three. The gluon fields, $\mathcal{A}^C$, are associated with eight possible colors, labeled by C, ranging from one to eight. The gluon-gluon interactions are encoded in the field tensor $F^A_{\mu\nu}$, defined as

$$F^A_{\mu\nu} = \partial_\mu \mathcal{A}^A_\nu - \partial_\nu \mathcal{A}^A_\mu - g_s f_{ABC} \mathcal{A}^B_\mu \mathcal{A}^C_\nu . \tag{1.35}$$

Additionally, the Gell-Mann matrices, t^A, obey the commutation relations

$$[t^A, t^B] = i f_{ABC} t^C . \tag{1.36}$$

Here, the f_{ABC} represents the structure constants of the SU(3) group, characterizing the algebraic properties of the color charge.

This comprehensive framework serves as the foundation for our understanding of the strong force within the domain of QCD. The interaction vertices in QCD are visually represented by Feynman diagrams, as depicted in Fig. 1.5.

1.3 Open questions in particle physics

Undoubtedly, the SM is a powerful framework that successfully explains the majority of phenomena observed in collision experiments. However, it is not omnipotent, because there are still several questions related to experimental observations unaddressed. In this section, we will highlight some of the lingering questions in the field of particle physics.

- In the SM, there are a total of 19 parameters, such as the masses of fermions and the Higgs boson, the strengths of fundamental forces, and several mixing angles that govern interactions between different types of particles. However, the SM does not provide any predictions or explanations regarding the specific values of these parameters; they can only be determined through experimental observations.

- Neutrinos present a famous phenomenon known as neutrino oscillation, where a neutrino initially generated in a specific flavor state can later be observed in a different flavor state. This phenomenon provides compelling evidence that neutrinos are not massless particles, which further raises a fundamental question: what mechanism is responsible for neutrino masses?

  Another compelling question concerning neutrinos is whether they are Majorana fermions, particles that are their own antiparticles, or Dirac fermions, which are distinct from their antiparticles. This question probes the fundamental nature of neutrinos and has significant implications for our understanding of particle physics.

- The prevailing understanding of the early universe, particularly the Big Bang theory, suggests that matter and antimatter should have been produced in equal quantities during the initial stages. However, a puzzling mystery arises when we observe the present-day universe: from tiny life forms on Earth to vast celestial bodies, nearly all what we observe are made up of ordinary matter, and there is a conspicuous absence of antimatter.

  Although the CKM mechanism introduces a source of charge-parity (*CP*) violation, it is unable to account for the magnitude of the matter-antimatter asymmetry observed in the universe. The primary reason for this significant asymmetry, known as the "baryon asymmetry problem", still remains an open question in particle physics and cosmology.

- The measured motions of stars in galaxies suggest the presence of additional matter, known as dark matter, which exerts gravitational forces. Dark matter does not interact with electromagnetic radiation, making it challenging to detect. Weakly interacting massive particles (WIMPs) are hypothetical particles that are one of the proposed candidates for dark matter [15, 16]. Experimental efforts to detect WIMPs include the search for products resulting from WIMPs annihilation, such as gamma rays, neutrinos, and cosmic rays in nearby galaxies and galaxy clusters. Direct detection experiments designed to measure the collision of WIMPs with nuclei in the laboratory, as well as attempts to directly produce WIMPs in colliders, such as the LHC.

- In the 1990s, astronomers observed that distant galaxies were moving away from Earth at an accelerating rate, indicating an expansion of the universe. Initially, due to the gravitational pull of matter, this expansion was expected to slow down. To account for the observed acceleration, scientists proposed a mysterious energy known as dark energy, which permeates all of space. However, our understanding of this energy remains limited.

These pieces of evidence strongly suggest that the SM is not the ultimate explanation for all phenomena in the universe. Consequently, it is crucial to thoroughly investigate any anomalies observed in experiments, rule out the possibility of experimental errors, and validate signals pointing towards physics beyond the SM. This approach forms the cornerstone of further advancements in theoretical frameworks.

1.4 Anomalies related to $\bar{B}^0 \to D^{*+}\ell^-\bar{\nu}_\ell$ decays

There exist two important anomalies related to $\bar{B}^0 \to D^{*+}\ell^-\bar{\nu}_\ell$ decays that we will investigate in this thesis. One is the discrepancy in the measured $|V_{cb}|$ value using inclusive and exclusive semileptonic B decays. The other concerns a potential violation of lepton flavor universality. These anomalies will be discussed further in the remaining section.

1.4.1 Tension of $|V_{cb}|$ value between exclusive and inclusive determinations

The $|V_{cb}|$ value can be determined through two distinct approaches. Exclusive determinations involve extracting $|V_{cb}|$ from specific decay channels, such as $\bar{B}^0 \to D^{*+}\ell^-\bar{\nu}_\ell$, $\bar{B}^0 \to D^{+}\ell^-\bar{\nu}_\ell$, and $B_s \to D_s^{(*)}\mu\nu$ decays. In contrast, inclusive determinations are based on all relevant decay modes. For example, the determination of $|V_{cb}|$ inclusively using $B \to X_c\ell\bar{\nu}_\ell$ processes, where X_c represents a hadronic system containing a charm quark.

It is important to note that inclusive measurements cover a wide range of decay channels, including decays like the $B \to D^{**}\ell\bar{\nu}_\ell$ process that are not used in exclusive $|V_{cb}|$ determinations. As such, the inclusive determination cannot be considered as a combination of all exclusively measured channels.

The tension between the obtained values of $|V_{cb}|$ and $|V_{ub}|$ (collectively referred to as $|V_{xb}|$) from exclusive and inclusive determinations has been a long-standing puzzle. As shown in Fig. 1.6, Ref. [17] averages exclusive $|V_{xb}|$ measurements, including the result of $|V_{ub}/V_{cb}|$ provided by the LHCb collaboration, and compare the averages with the values obtained from inclusive modes. A significant discrepancy at the 3σ level is evident.

The observed tension between exclusive and inclusive determinations of $|V_{cb|}$ can be attributed to several factors. Firstly, it is worth noting that both methods rely on theoretical inputs. Exclusive determinations are based on theoretical models, and different model choices can yield different values for $|V_{cb}|$. Moreover, in exclusive determinations, theoretical inputs are required to disentangle the form factors normalization from $|V_{cb}|$. In contrast, inclusive decays involve the operator product expansion, heavy quark expansion, and the expansion of the strong coupling constant α_s, which can introduce their own theoretical uncertainties.

Secondly, statistical fluctuations and systematic uncertainties, including factors like detector calibration, acceptance, and background modeling, can impact the precision of experimental measurements and contribute to the observed tension.

To address this tension, a collaborative effort from both the theoretical and experimental communities is crucial. Researchers need to work together to refine theoretical models, reduce uncertainties, and improve the precision of experimental measurements. This collaborative approach is essential for resolving the tension and obtaining more accurate values for $|V_{cb}|$.

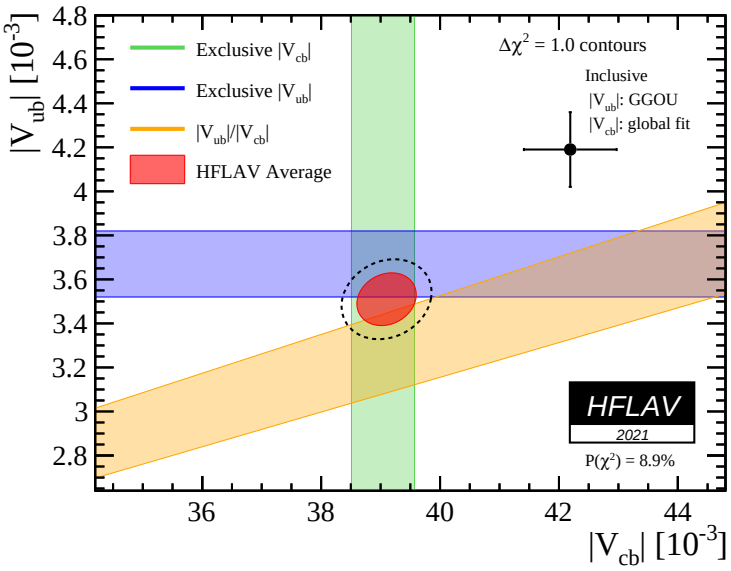

Figure 1.6: Comparison of the resulting $|V_{xb}|$ values from exclusive and inclusive determinations (taken from Ref. [17]). The data point with an error bar represents the value extracted from the inclusive modes, exhibiting a significant deviation from the averages of the exclusive determinations, as indicated by the red shaded area.

1.4.2 Possible violation of lepton flavor universality

In the SM, the electroweak coupling of the gauge bosons Z and W to leptons e, μ, and τ is expected to be independent of the lepton flavor, a principle known as lepton flavor universality. To search for possible violations of this universality, experiments often measure ratios or differences of observables involving different lepton flavors. For instance, the ratio

$$R(D^{(*)}) = \frac{\mathcal{B}(B \to D^{(*)}\tau\nu)}{\mathcal{B}(B \to D^{(*)}\ell\nu)}, \quad \text{with } \ell = e, \mu, \tag{1.37}$$

provides a sensitive probe for physics beyond the SM in the context of $b \to c\ell\nu$ and $b \to c\tau\nu$ transitions. When these experimental measurements are averaged, they show a discrepancy of around 3σ from the SM predictions, as illustrated in Fig. 1.7. The deviations of $R(D^{(*)})$ from unity are mainly attributed to the fact that the tau lepton mass is significantly greater than the masses of electrons and muons.

In response to the observed tension in $R(D^{(*)})$, various extensions to the SM have been proposed. These extensions include supersymmetry (SUSY) [18, 19], two-Higgs-doublet models (2HDM) [20, 21], and the proposal of leptoquarks [22]. These theoretical frameworks introduce new particles, interactions, and parameters that can potentially explain the deviations from SM predictions in lepton flavor universality observables.

In addition, uncertainties in the form factors that describe the hadronic structure of particles involved in these decays, as well as statistical fluctuations and experimental systematics, can

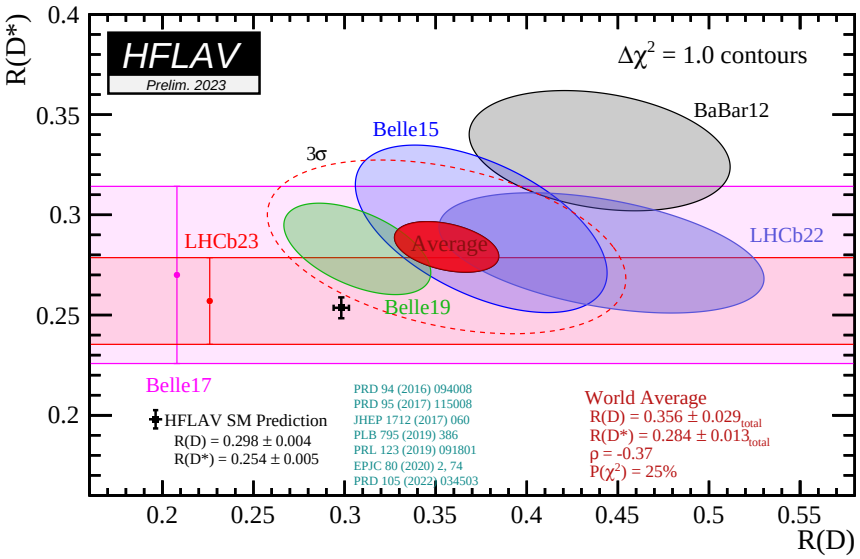

Figure 1.7: Comparison of the experimentally measured $R(D^{(*)})$ with the SM prediction (represented by the black data point with an error bar). The plot is sourced from Ref. [17].

contribute to the $R(D^{(*)})$ puzzle.

Anomalies are not limited to the comparison between the τ lepton and lighter leptons. A recent investigation of lepton flavor universality within the light lepton flavors e and μ has been conducted in the context of semileptonic $\bar{B}^0 \to D^{*+}\ell^-\bar{\nu}_\ell$ decays. This analysis re-examines the published Belle experimental data [23], where the lepton angular asymmetry $\mathcal{A}_{\mathrm{FB}}$ is computed (see Sec. 2.4 and Sec. 9.2), along with the difference between the e and μ channels: $\Delta\mathcal{A}_{\mathrm{FB}} = \mathcal{A}^{\mu}_{\mathrm{FB}} - \mathcal{A}^{e}_{\mathrm{FB}}$. Strikingly, the result reveals a 4σ deviation of $\Delta\mathcal{A}_{\mathrm{FB}}$ from the SM prediction [24], as depicted in Fig. 1.8.

These observations pose a significant challenge to the SM, potentially signifying the presence of new physics. It is of utmost importance to rigorously scrutinize the experimental setup and investigate whether non-SM contributions might be influencing the outcomes of semileptonic B decays.

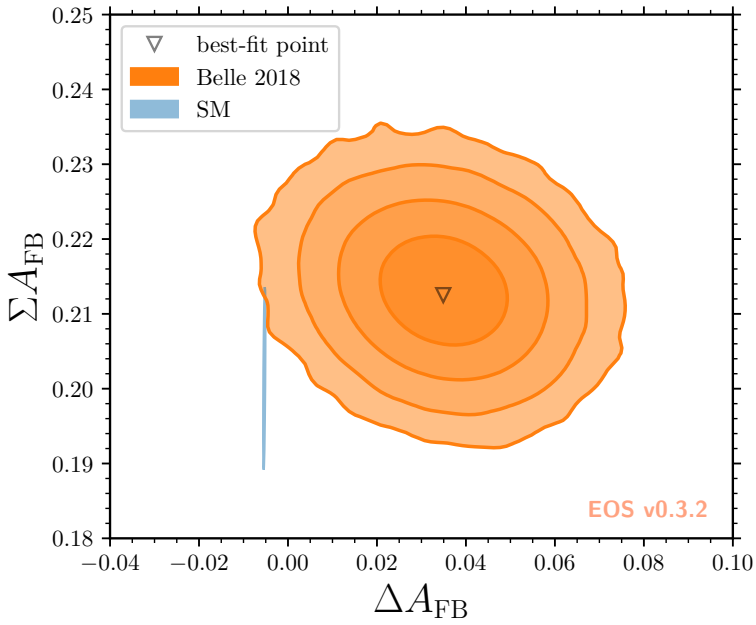

Figure 1.8: Illustration of $\sim 4\sigma$ deviations observed in the re-interpretation of the Belle data compared to the SM prediction for the $\Delta\mathcal{A}_{\rm FB}$ observable. Data source: Ref. [24].

CHAPTER 2

Theory of $\bar{B}^0 \to D^{*+}\ell^-\bar{\nu}_\ell$ decays

2.1 Form factors in $\bar{B}^0 \to D^{*+}\ell^-\bar{\nu}_\ell$ decays

The semileptonic B meson decay amplitude is described by the matrix element of the weak interaction,

$$\mathcal{M} = \frac{G_F}{\sqrt{2}} V_{cb} \langle D^*(p_{D^*})|\bar{c}\gamma_\mu(1-\gamma_5)b|\bar{B}(p_B)\rangle \left[\bar{u}(p_\ell)\gamma^\mu(1-\gamma_5)\nu(p_{\nu_\ell})\right], \tag{2.1}$$

where $\bar{u}(p_\ell)$ and $\nu(p_{\nu_\ell})$ are Dirac spinors related to the charged lepton and neutrino, respectively, $\gamma_5 = i\gamma_0\gamma_1\gamma_2\gamma_3$, and $G_F = 1.1663787 \times 10^{-5}$ GeV$^{-2}(\hbar c)^3$ is the Fermi constant.

While the leptonic matrix element is straightforward to calculate, the hadronic matrix element includes nonperturbative QCD effects and cannot be computed from first principles. However, it is possible to express the matrix element most generally in terms of tensor products of external momenta, polarizations, and spins, multiplied by a set of Lorentz invariant amplitudes known as form factors. These form factors effectively account for the nonperturbative QCD processes.

The hadronic matrix element of $\bar{B}^0 \to D^{*+}\ell^-\bar{\nu}_\ell$ decays includes the vector and axial vector

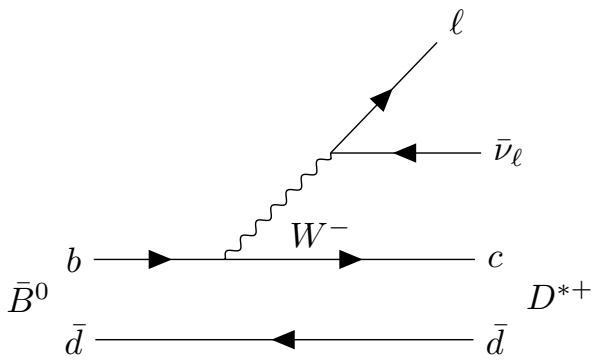

Figure 2.1: The tree-level Feynman diagram for the $\bar{B}^0 \to D^{*+}\ell^-\bar{\nu}_\ell$ decay.

currents between the B and D^* states,

$$\frac{\langle D^*(p_{D^*})|\bar{c}\gamma_\mu b|\bar{B}(p_B)\rangle}{\sqrt{m_B m_{D^*}}} = h_V\, \varepsilon^{\mu\nu\alpha\beta}\, \epsilon^*_\nu\, v'_\alpha\, v_\beta, \tag{2.2}$$

$$\begin{aligned}\frac{\langle D^*(p_{D^*})|\bar{c}\gamma_\mu\gamma_5 b|\bar{B}(p_B)\rangle}{\sqrt{m_B m_{D^*}}} = &- i\, h_{A_1}(w+1)\epsilon^{*\mu} + i\, h_{A_2}(\epsilon^*\cdot v)v^\mu \\ &+ i\, h_{A_3}(\epsilon^*\cdot v)v'^\mu,\end{aligned} \tag{2.3}$$

where $v = p_B/m_B$ and $v' = p_{D^*}/m_{D^*}$ are the four-velocities of B and D^* mesons, respectively, with p_B and p_{D^*} denoting momenta of B and D^* mesons, and $m_B = 5.279\ \text{GeV}/c^2$ and $m_{D^*} = 2.010\ \text{GeV}/c^2$ denoting masses of B and D^* mesons, respectively. Further, ϵ^* and $\varepsilon^{\mu\nu\alpha\beta}$ represent the polarization of the D^* meson and the Levi-Civita tensor, respectively.

The four form factors h_{A_1}, h_{A_2}, h_{A_3} and h_V are functions of the squared four-momentum transfer from the B meson to the D^* meson, written as $q^2 = (p_B - p_{D^*})^2$. Alternatively, they can also be expressed in terms of the variable w, which is the dot product of the four-velocities of B and D^* mesons and is related to q^2 by the equation

$$w = v\cdot v' = \frac{m_B^2 + m_{D^*}^2 - q^2}{2m_B m_{D^*}}. \tag{2.4}$$

At $w_{\min} = 1$, which corresponds to $q^2_{\max} = (m_B^2 - m_{D^*}^2)^2$, we reach the zero recoil point, where the produced D^* meson is at rest in the B meson frame. In contrast, when $q^2 = m_\ell^2$, it maximizes the value of w:

$$w_{\max} = \frac{m_B^2 + m_{D^*}^2}{2m_B m_{D^*}} \approx 1.504. \tag{2.5}$$

In the case of light leptons $\ell = e, \mu$, the hadronic matrix element can be simplified to include only the h_{A_1} form factor along with two ratios,

$$R_1 = \frac{h_V}{h_{A_1}}, \qquad R_2 = \frac{h_{A_3} + r^*\, h_{A_2}}{h_{A_1}}. \tag{2.6}$$

The differential decay rates $\mathrm{d}\Gamma(\bar{B}^0 \to D^{*+}\ell^-\bar{\nu}_\ell)/\mathrm{d}w$ in terms of these form factors are

$$\begin{aligned}\frac{\mathrm{d}\Gamma(\bar{B}^0 \to D^{*+}\ell^-\bar{\nu}_\ell)}{\mathrm{d}w} = &\frac{G_F^2 |V_{cb}|^2\, \eta_{\text{EW}}^2\, m_B^5}{48\pi^3}\, (w^2-1)^{1/2}\, (w+1)^2\, r^{*3}(1-r^*)^2 \\ &\times \left[1 + \frac{4w}{w+1}\,\frac{1 - 2wr^* + r^{*2}}{(1-r^*)^2}\right]\mathcal{F}(w)^2,\end{aligned} \tag{2.7}$$

with $r^* = m_{D^*}/m_B$, $\eta_{\mathrm{EW}} \simeq 1.0066$ [25], denoting a small electroweak correction, and

$$\begin{aligned}\mathcal{F}(w)^2 = h_{A_1}^2 \Bigg\{ & 2(1 - 2wr^* + r^{*2}) \left(1 + R_1^2 \frac{w-1}{w+1}\right) \\ & + \left[(1 - r^*) + (w-1)\left(1 - R_2\right)\right]^2 \Bigg\} \\ & \times \left[(1 - r^*)^2 + \frac{4w}{w+1}\left(1 - 2wr^* + r^{*2}\right)\right]^{-1} . \end{aligned} \tag{2.8}$$

The form factor h_{A_1} holds particular importance because, unlike R_1 or R_2, it plays a dual role in Eq. (2.8). Not only does it influence the shape of the differential decay rates $\mathrm{d}\Gamma(\bar{B}^0 \to D^{*+}\ell^-\bar{\nu}_\ell)/\mathrm{d}w$, but it also contributes to the overall normalization of the decay process, including at $w = 1$.

2.2 Heavy quark effective theory

The properties of hadrons composed of light u, d, and s quarks can be predicted using chiral effective theory [26, 27], which is developed based on the $m_q \to 0$ ($q = u, d, s$) limit of QCD. However, for hadrons containing a c-quark or b-quark, it is a suitable approximation to consider the $m_Q \to \infty$ ($Q = c, b$) limit of QCD, as the heavy quark masses m_Q are significantly larger compared to the scale of nonperturbative strong dynamics $\Lambda_{\mathrm{QCD}} \approx 200$ MeV. This concept leads to the development of heavy quark effective theory (HQET), which holds particular significance for $\bar{B}^0 \to D^{*+}\ell^-\bar{\nu}_\ell$ decays, given that both B and D^* mesons are heavy-light quark systems. In this section, we will briefly introduce heavy quark effective theory.

The most important deduction of the $m_Q \to \infty$ limit is the spin-flavor heavy quark symmetry, which is helpful for understanding properties of hadrons containing a single heavy quark. In such a system, the typical momentum transfer due to nonperturbative QCD between heavy and light quarks is of the order of Λ_{QCD}. Consequently, the velocity v of the heavy quark remains unchanged ($\Delta v = \Delta p/m_Q \approx 0$) in the $m_Q \to \infty$ limit. In this physical picture, the heavy quark behaves like a static external source, transforming as a color triplet. This color source is independent of the masses of the c- and b-quarks. This concept leads us to heavy quark flavor symmetry: the dynamics remain the same under the interchange of heavy quark flavors. Consideration of finite and distinct m_Q values for c- and b-quarks introduces leading-order flavor symmetry-breaking effects proportional to $(1/m_{Q_i} - 1/m_{Q_j})$, where Q_i and Q_j represent any two heavy quark flavors.

The strong interaction of a heavy quark exclusively occurs with gluons, given that there is no direct quark-quark interaction in the QCD Lagrangian. In the $m_Q \to \infty$ limit, this interaction becomes spin-independent, as the static heavy quarks interact solely with gluons through their chromoelectric charges. This phenomenon gives rise to heavy quark spin symmetry: the dynamics remain unchanged regardless of any spin transformations of heavy quarks. However, this spin symmetry is broken when considering finite masses for heavy quarks, as they are no longer static. The spin-dependent interactions are induced by the chromomagnetic moment and are proportional to $1/m_Q$.

The spin-flavor symmetry within the framework of heavy quark effective theory provides valuable insights into the relationships between the form factors h_V and $h_{A_{1-3}}$ in $\bar{B}^0 \to D^{*+}\ell^-\bar{\nu}_\ell$ decays. To confirm this, we can examine the typical momentum transfer between the light degrees of freedom (referred to as brown muck in Ref. [28]). The momenta of the light systems in the initial and final state mesons are on the order of $\Lambda_{\rm QCD}v$ and $\Lambda_{\rm QCD}v'$, respectively, considering their velocities are the same as the heavy quark velocity in the initial and final states. Consequently, the momentum transfer can be approximated as

$$q^2_{\rm light} \sim (\Lambda_{\rm QCD}v - \Lambda_{\rm QCD}v')^2 = 2\Lambda^2_{\rm QCD}(1-w). \tag{2.9}$$

Given that $w \sim 1$, we find

$$2\Lambda^2_{\rm QCD}(1-w) \ll m^2_{b,c}. \tag{2.10}$$

Hence, heavy quark symmetry is applicable for investigating the form factors of $\bar{B}^0 \to D^{*+}\ell^-\bar{\nu}_\ell$ decays.

The currents in HQET at the leading order that match Eq. (2.2) and Eq. (2.3) are expressed as follows:

$$\bar{c}\gamma_\mu b = \bar{c}_{v'}\gamma_\mu b_v, \tag{2.11}$$

$$\bar{c}\gamma_\mu\gamma_5 b = \bar{c}_{v'}\gamma_\mu\gamma_5 b_v, \tag{2.12}$$

where $\bar{c}_{v'}$ and b_v represent the c- and b-quark fields in HQET, respectively. Operators $\bar{c}_{v'}\Gamma b_v$ remain invariant under heavy quark spin transformations if $\Gamma \to D_c(R)\Gamma D_b^{-1}(R)$, where $D(R)_Q$ is the usual Dirac four-component spinor representation of rotations. For $B \to D^*$ matrix elements, we need to represent the currents $\bar{c}_{v'}\Gamma b_v$ in terms of B and D^* fields, which are constructed to transform similarly to the quark operator. This leads to

$$\bar{c}_{v'}\Gamma b_v = {\rm Tr}\left(\bar{H}^{(c)}_{v'}\Gamma H^{(b)}_v X\right), \tag{2.13}$$

where the field $H^{(Q)}_v$ represents a meson containing a heavy Q-quark, and transforms under heavy quark spin rotation as

$$H^{(Q)}_v \to D(R)_Q H^{(Q)}_v. \tag{2.14}$$

Additionally, X is a general matrix expressed in terms of v, v', the gamma matrices, and the identity matrix:

$$X = X_0 + X_1 \not{v} + X_2 \not{v}' + X_3 \not{v}\not{v}'. \tag{2.15}$$

Considering the properties of heavy-light meson fields, where $\not{v}H^{(b)}_v = H^{(b)}_v$ and $H^{(c)}_{v'}\not{v}' = -H^{(c)}_{v'}$, we can equivalently write

$$X = -\zeta(w), \tag{2.16}$$

where $\zeta(w)$ is known as the Isgur-Wise function. Comparing this to Eq. (2.2) and Eq. (2.3),

relationships between the form factors can be established [29]:

$$h_V(w) = h_{A_1}(w) = h_{A_3}(w) = \zeta(w), \tag{2.17}$$

$$h_{A_2}(w) = 0. \tag{2.18}$$

It is essential to emphasize that this relationship only holds in the heavy quark limit, where the quark mass approaches infinity ($m_Q \to \infty$).

2.3 Parameterization of the form factors and their ratios

Note that the form factor $h_{A_1}(w)$ and two ratios $R_1(w)$ and $R_2(w)$ depend only on the recoil parameter w, and they can be expanded in various ways. In Sec. 2.3.1, we will introduce the CLN parameterization, which was commonly employed in earlier measurements. Furthermore, in Sec. 2.3.2, we will discuss a more model-independent expansion known as the BGL parameterization.

2.3.1 CLN parameterization

Reference [30] uses dispersive bounds and quark-model input to reduce the number of parameters required to describe the form factors. The form-factor h_{A_1} is expanded with a conformal parameter,

$$z = \frac{\sqrt{w+1} - \sqrt{2}}{\sqrt{w+1} + \sqrt{2}}, \tag{2.19}$$

and a slope parameter ρ^2, as

$$h_{A_1}(z) = h_{A_1}(w=1)\left(1 - 8\rho^2 z + (53\rho^2 - 15)z^2 - (231\rho^2 - 91)z^3\right). \tag{2.20}$$

The ratios R_1 and R_2 are parametrized as follows

$$R_1(w) = R_1(1) - 0.12(w-1) + 0.05(w-1)^2, \tag{2.21}$$

$$R_2(w) = R_2(1) + 0.11(w-1) - 0.06(w-1)^2. \tag{2.22}$$

Hence, the form factors are fully characterized by four key parameters $h_{A_1}(1)$, ρ^2, $R_1(1)$, and $R_2(1)$. Among these, $h_{A_1}(1)$ plays an important role in determining the normalization of the differential decay rate, requiring constraint through theoretical inputs.

2.3.2 BGL parameterization

The BGL parameterization is associated with the form factors in the helicity basis, represented as g, f, and $\mathcal{F}_1$. They are linked to the form factors in the heavy quark basis, namely h_{A_1}, R_1, and

R_2, through the following expressions

$$f = m_B\sqrt{r^*}(w+1)\,h_{A_1}\,, \qquad g = \frac{1}{m_B\sqrt{r^*}}\,R_1\,h_{A_1}\,, \tag{2.23}$$

$$\mathcal{F}_1 = m_B^2\,\sqrt{r^*}(w+1)\left(w - r^* - (w-1)R_2\right)\,h_{A_1} \tag{2.24}$$

References [31, 32] (BGL) utilize dispersive bounds and expand the helicity-basis form factors with the conformal parameter z defined in Eq. (2.19),

$$\begin{aligned} g(z) &= \frac{1}{P_g(z)\phi_g(z)}\sum_{n=0}^{N} a_n z^n, \\ f(z) &= \frac{1}{P_f(z)\phi_f(z)}\sum_{n=0}^{N} b_n z^n, \\ \mathcal{F}_1(z) &= \frac{1}{P_{\mathcal{F}_1}(z)\phi_{\mathcal{F}_1}(z)}\sum_{n=0}^{N} c_n z^n, \end{aligned} \tag{2.25}$$

Here, b_0 and c_0 are not independent parameters; they are related by the equation

$$c_0 = \frac{(m_B - m_{D^*})\phi_{\mathcal{F}_1}(0)}{\phi_f(0)}b_0. \tag{2.26}$$

The Blaschke factors $P(z)$ serve to eliminate poles associated with on-shell production of B_c^* bound states for $q^2 < (m_B + m_{D^*})^2$

$$p_g(z) = \prod_i^4 \frac{z - z_{P_i}}{1 - z z_{P_i}}, \qquad P_f(z) = P_{\mathcal{F}_1(z)} = \prod_i^4 \frac{z - z_{P_i}}{1 - z z_{P_i}}, \tag{2.27}$$

where

$$z_P = \frac{\sqrt{(m_B + m_{D^*})^2 - m_P^2} - \sqrt{(m_B + m_{D^*})^2 - (m_B - m_{D^*})^2}}{\sqrt{(m_B + m_{D^*})^2 - m_P^2} + \sqrt{(m_B + m_{D^*})^2 - (m_B - m_{D^*})^2}}, \tag{2.28}$$

with m_P denoting the masses of the B_c^* mesons. For the form factor g, the index i ranges over the 4 vector B_c^* mesons, while for the f and $\mathcal{F}_1$ form factors, it ranges over the 4 axial-vector states. The masses of the B_c^* mesons are summarized in Table 2.1.

Table 2.1: Numerical values of B_c^* masses used in this analysis.

Type	Mass [GeV/c^2]
vector	6.337, 6.899, 7.012, 7.280
axial vector	6.7370, 6.736, 7.135, 7.142

The outer functions ϕ are defined as

$$\begin{aligned}
\phi_g(z) &= \sqrt{\frac{256 n_I}{3\pi\chi^T(+u)}} \frac{r^{*2}(1+z)^2(1-z)^{-1/2}}{[(1+r^*)(1-z)+2\sqrt{r^*}(1+z)]^4}, \\
\phi_f(z) &= \frac{1}{m_B^2}\sqrt{\frac{16 n_I}{3\pi\chi^T(-u)}} \frac{r^*(1+z)(1-z)^{3/2}}{[(1+r^*)(1-z)+2\sqrt{r^*}(1+z)]^4}, \\
\phi_{\mathcal{F}_1}(z) &= \frac{1}{m_B^3}\sqrt{\frac{8 n_I}{3\pi\chi^T(-u)}} \frac{r^*(1+z)(1-z)^{5/2}}{[(1+r^*)(1-z)+2\sqrt{r^*}(1+z)]^5},
\end{aligned} \tag{2.29}$$

where the effective number of light quarks $n_I = 2.6$, the value of the parameter $u = m_c/m_b$ used in subsequent calculations is 0.33, and $\chi^T(\pm u)$ is related to a perturbative calculation at $q^2 = 0$. The specific numerical values

$$\chi^T(+0.33) = 5.28 \times 10^{-4}\text{GeV}^{-2}, \qquad \chi^T(-0.33) = 3.07 \times 10^{-4}\text{GeV}^{-2} \tag{2.30}$$

are employed in the pole mass scheme, with negligible contributions from condensates.

2.4 Fully differential decay rate

The $\bar{B}^0 \to D^{*+}\ell^-\bar{\nu}_\ell$ decay rate is completely characterized by the recoil parameter w and three decay angles θ_ℓ, θ_V, and χ (see also Fig. 2.2). These angles are defined as follows.

- The angle θ_ℓ is defined by the direction of the charged lepton and the direction opposite to the B meson in the virtual W boson rest frame.

- The angle θ_V is defined by the direction of the D meson and the direction opposite to the B meson in the D^* meson rest frame.

- The angle χ is the azimuthal angle between the two decay planes spanned by the W boson and D^* meson decay products, and defined in the rest frame of the B meson.

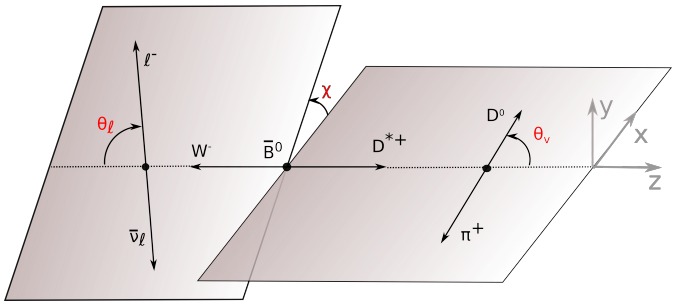

Figure 2.2: Illustration of the helicity angles θ_ℓ, θ_V, and χ that characterize the $\bar{B}^0 \to D^{*+}\ell^-\bar{\nu}_\ell$ decay.

The fully differential decay rate in terms of those kinematic variables is expressed as

$$\begin{aligned}\frac{\mathrm{d}\Gamma(\bar{B}^0 \to D^{*+}\ell^-\bar{\nu}_\ell)}{\mathrm{d}w\,\mathrm{d}\cos\theta_\ell\,\mathrm{d}\cos\theta_V\,\mathrm{d}\chi} =& \frac{3m_B m_{D^*}^2}{4(4\pi)^4}\eta_{\mathrm{ew}}^2 G_F^2 |V_{cb}|^2 \sqrt{w^2-1}(1-2wr^*+r^{*2})\times \\ & \Big[(1-\cos\theta_\ell)^2\sin^2\theta_V H_+^2(w) + (1+\cos\theta_\ell)^2\sin^2\theta_V H_-^2(w) \\ & + 4\sin^2\theta_\ell\cos^2\theta_V H_0^2(w) - 2\sin^2\theta_\ell\sin^2\theta_V\cos 2\chi H_+(w)H_-(w) \\ & - 4\sin\theta_\ell(1-\cos\theta_\ell)\sin\theta_V\cos\theta_V\cos\chi H_+(w)H_0(w)) \\ & + 4\sin\theta_\ell(1+\cos\theta_\ell)\sin\theta_V\cos\theta_V\cos\chi H_-(w)H_0(w)\Big].\end{aligned} \tag{2.31}$$

where the helicity amplitudes $H_0(w)$ and $H_\pm(w)$ are related to the form factors in the helicity basis through the following equations

$$H_0 = \mathcal{F}_1/\sqrt{q^2}, \tag{2.32}$$
$$H_+ = f - m_B|\vec{p}_{D^*}|g, \tag{2.33}$$
$$H_- = f + m_B|\vec{p}_{D^*}|g. \tag{2.34}$$

The helicity amplitudes $H_0(q^2)$ and $H_\pm(q^2)$ can be expanded in terms of form factors in the heavy quark basis as

$$H_0 = \frac{1}{2m_{D^*}\sqrt{q^2}}\left((m_B^2 - m_{D^*}^2 - q^2)(m_B + m_{D^*})A_1(q^2) - \frac{4m_B^2|\vec{p}_{D^*}|^2}{m_B + m_{D^*}}A_2(q^2)\right), \tag{2.35}$$

$$H_\pm = (m_B + m_{D^*})A_1(q^2) \mp \frac{2m_B}{m_B + m_{D^*}}|\vec{p}_{D^*}|V(q^2) \tag{2.36}$$

where

$$A_1(q^2) = \frac{w+1}{2}r' h_{A_1}(q^2), \tag{2.37}$$
$$A_2(q^2) = \frac{R_2(w)}{r'}h_{A_1}(q^2), \tag{2.38}$$
$$V(q^2) = \frac{R_1(w)}{r'}h_{A_1}(q^2), \tag{2.39}$$

with $r' = 2\sqrt{m_B m_{D^*}}/(m_B + m_{D^*})$.

CHAPTER 3

Belle II experiment

The Belle II experiment, operated by the High Energy Accelerator Research Organization in Tsukuba, Japan, is the successor to the Belle experiment. Its primary objectives are to search for new physics at the precision frontier and to measure the parameters of the SM with increased accuracy. In the experiment, electrons and positrons collide at an energy of 10.58 GeV in the center-of-mass frame, corresponding to the mass of the $\Upsilon(4S)$ resonance. These $\Upsilon(4S)$ particles predominantly decay into $B\bar{B}$ pairs. As a result, the Belle II experiment is often referred to as a B factory. The Belle II experimental configuration offers numerous advantages for physics analyses, and some of them are discussed below [33].

- The $\Upsilon(4S)$ resonance provides a clean sample of $B\bar{B}$ pairs, and a low-background environment allows for the reconstruction of particles that subsequently decay into photons, such as π^0, $\rho^{\pm}$, η, η', etc. Additionally, the reconstruction of K_L^0 mesons is achieved with relatively high efficiency.

- Since the initial state is known, "missing mass" analyses can be performed to infer the existence of new particles via energy and momentum conservation rather than reconstructing their final states.

- The asymmetric beam energies for electrons and positrons enable the measurements of lifetimes, mixing parameters, and time-dependent CP violation. This is because the beam asymmetry results in a significant Lorentz boost, allowing the produced B mesons and subsequent D mesons to travel a significant distance before decaying.

- A large number of τ leptons are also produced in collisions. This opens up numerous possibilities for studying rare τ decays, as well as investigating lepton flavor and lepton number conservation within the context of τ decays, all within a low-background environment.

In the remainder of this chapter, we will provide more details about the Belle II experiment. The introduction to the hardware can be found in Sec. 3.1 and Sec. 3.2 for the SuperKEKB accelerator and Belle II detector, respectively. Section 3.4 and Sec. 3.5 will discuss the collected collision data and simulated Monte Carlo (MC) samples, respectively.

3.1 SuperKEKB collider

The SuperKEKB collider is an asymmetric-energy and double-ring collider that was constructed through the upgrade of KEKB. A schematic representation of the SuperKEKB collider is depicted in Fig. 3.2. Electrons are initially generated in a triode-type thermionic electron gun at the beginning of the electron-positron injector linear accelerator (linac). After the acceleration to 7 GeV, they are used as the injection beam.

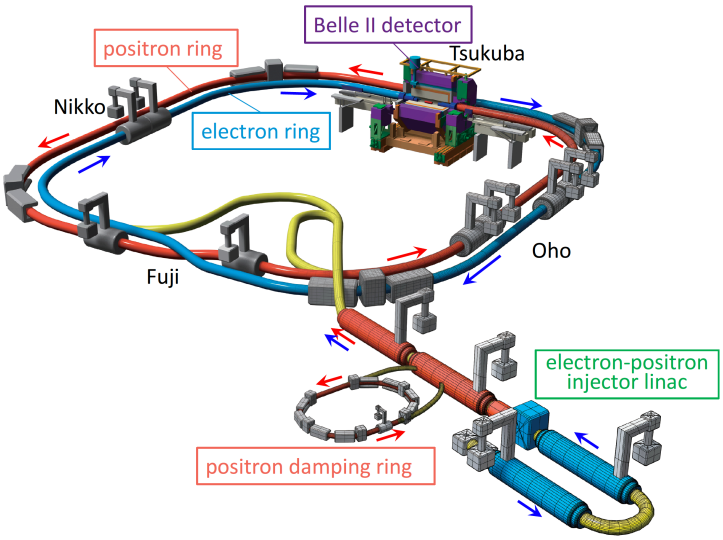

Figure 3.1: Schematic view of the SuperKEKB collider. Source: Ref. [34].

Additionally, electrons produced in the same pre-injector are accelerated up to 4 GeV to irradiate a tungsten target for positron generation [35]. However, positrons generated in this manner possess a significantly larger emittance compared to the electron beam, and their intensity is limited by the acceptance of the capture section.

To address these issues, the acceptance is expanded by introducing L-band accelerating structures in the capture section. Furthermore, a 1.1 GeV damping ring (DR) is installed as a collector ring, designed to accommodate a beam with a substantial energy spread and significant transverse emittance. Positrons, characterized by low emittance and a narrow energy spread after undergoing damping in the DR, are subsequently reinjected into the linac and accelerated to 4.0 GeV.

The SuperKEKB accelerator system stores electrons with an energy of 7 GeV in the high-energy electron ring (HER) and positrons with an energy of 4 GeV in the low-energy ring (LER). In contrast to a head-on collision scheme, the two beams intersect only at specific short and narrow sections near the interaction point (IP).

The SuperKEKB adopts the nano-beam collision scheme, initially proposed for the Super B factory in Italy [36]. A key characteristic of this approach is the significant horizontal crossing angle between the electron and positron beams, denoted as $\theta_x \approx 83$ mrad [37]. Additionally, the bunch length is much longer than the beta function at the IP $\sigma_z \approx 6\,\text{mm} \gg \beta_y^*$ [37]. This

configuration allows for the vertical beam sizes at the IP to be compressed to a range of 48 to 62 nm.

Utilizing the nano-beam collision technique, the SuperKEKB collider is poised to achieve an astounding instantaneous luminosity of 6×10^{35} $\mathrm{cm}^{-2}\mathrm{s}^{-1}$[38] — a remarkable 40-fold increase compared to what KEKB achieved. A new world record for peak luminosity, reaching 3.1×10^{34} $\mathrm{cm}^{-2}\mathrm{s}^{-1}$ [39], was established on June 22, 2021, bringing us closer to realizing our ambitious goals.

3.2 Belle II detector

Belle II comprises several concentric sub-detectors positioned around the 1-cm radius beryllium beam pipe enclosing the IP. As illustrated in Fig. 3.2, the closest sub-detector to the IP is the two-layer pixel detector (PXD). The first PXD layer (L1) features 16 modules, while the second layer (L2) is equipped with 4 modules, all of which have been successfully installed. As part of the plan during the long shutdown 1 (commencing in July 2022), a new, fully assembled two-layer PXD is currently being installed to enhance performance and increase tolerance for hit occupancy stemming from background interactions [40].

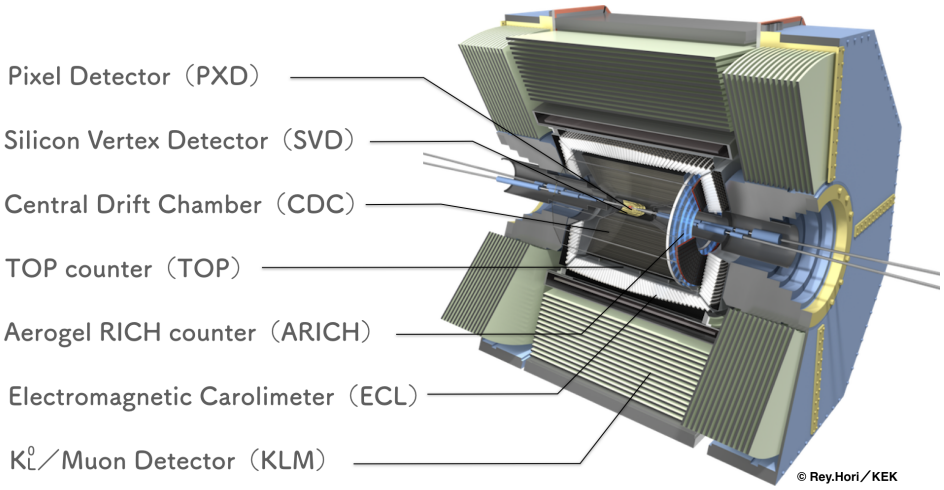

Figure 3.2: Schematic view of the Belle II detector. Source: Ref. [41]

Subsequent to the PXD, the next four layers (L3-L6) constitute the double-sided silicon strip vertex detector (SVD). Both the PXD and the SVD belong to vertex detectors, which are specifically designed to pinpoint the precise location where particle tracks intersect, allowing for the reconstruction of primary and secondary vertices in high-energy physics experiments.

Surrounding these vertex detectors is the central drift chamber (CDC), whose task is to accurately reconstruct the trajectories of charged particles. Outside the CDC, other two sub-detectors: the time-of-propagation (TOP) and the aerogel ring imaging Cherenkov counters (ARICH) are installed. These sub-detectors play a crucial role in identifying charged particles.

An electromagnetic calorimeter (ECL) is integrated to detect photons. In addition, it contributes to distinguishing electrons from hadrons, particularly pions.

All of the aforementioned subsystems are immersed within a uniform 1.5 T magnetic field. This magnetic field, generated by a superconducting solenoid located exterior to the calorimeter, is nearly aligned with the electron beam. In the laboratory frame, the z-axis is defined as the central axis of the solenoid, with the positive direction pointing in the direction of the electron beam. The polar angle θ as well as the longitudinal and transverse directions are defined with respect to this z-axis.

The K_L^0 and muon (KLM) detector serves as the outermost detector. As its name suggests, the KLM is designed for the detection of muons and K_L^0 particles. The latter particle hardly interacts with any other sub-detectors, except for very rare interactions with the ECL [42].

Further details regarding these sub-detectors will be elaborated on in the following sections. For information on the planned near-term and potential longer-term upgrades of the Belle II detector, one can refer to Ref. [40]

3.2.1 Pixel detector

The pixel sensor employed in the Belle II experiment leverages DEPleted p-channel Field Effect Transistor (DEPFET) technology [43, 44]. This advanced sensor is constructed from semiconductor materials, featuring a sensitive layer depleted of charge carriers and equipped with transistors for signal amplification and readout.

As charged particles traverse the DEPFET sensor, they interact with the silicon material, initiating the creation of electron-hole pairs. These electron-hole pairs are collected by the electrodes within each pixel of the DEPFET sensor. This collection process leads to a modification in the voltage of the transistor situated in every pixel, generating an electrical signal that is directly proportional to the energy deposited by the passing particle.

The precise position of the particle is determined by analyzing the distribution of these electrical signals across the pixel array. Thanks to the small pixel size, typically ranging from $50{\times}55\,\mu m^2$ to $50{\times}85\,\mu m^2$ [45], the DEPFET sensor enhances accurate measurements of charged particle trajectories.

The PXD is designed with two layers positioned at radii of 14 mm and 22 mm. The inner layer comprises 8 planar sensors, while the outer layer has 12 planar sensors. Together, these layers cover an angular acceptance range of $\theta \in [17°, 150°]$. For the most up-to-date status update on the PXD, one can consult the report in Ref. [46].

3.2.2 Silicon vertex detector

The SVD comprises four layers of double-sided silicon strip sensors. One of its primary function is to extrapolate particle tracks to the inner PXD, enabling the identification of hits within the PXD associated with these tracks. The combination of PXD and SVD is used for the precise determination of the positions of charged particle tracks and the reconstruction of both primary and secondary vertices. Moreover, the SVD provides standalone tracking capabilities for low-momentum tracks, enhancing the efficiency of reconstructing pions generated in D^*

meson decays. Additionally, its measurements of ionization energy loss can be used for particle identification. [47, 48].

For a more in-depth understanding of the PXD's operation and performance, as well as a novel approach to computing the time of collision based on SVD hit time information, one can refer to Ref. [49].

3.2.3 Central drift chamber

The CDC is filled with a gas mixture comprising 50% helium (He) and 50% ethane (C_2H_6). These components enable the CDC to record the trajectories of charged particles and make precise measurements of their momenta. Furthermore, within the CDC volume, the energy loss of charged particles is used for particle identification within the low momentum range, as well as providing essential level-1 trigger information for charged particles [50]. These functions are achieved through the measurement of specific ionization in the chamber gas, denoted as dE/dx.

Comprising a total of 56 layers and 14,336 wires arranged in cylindrical layers (ranging from 160 to 384 wires per layer), the CDC spans a length of 2.3 meters and has a diameter of 2.2 meters [51]. Its coverage extends across a polar angle range of $17° < \theta < 150°$. When charged particles traverse the CDC's gas-filled volume, they induce ionization of the gas atoms, generating positive ions and electrons. The electrons subsequently drift toward the positively charged wires, guided by the electric fields established between the wire electrodes. The signals induced by these electron drifts are recorded and utilized for the reconstruction of particle trajectories [52, 53].

3.2.4 Time-of-propagation detector

The TOP detector is installed in the barrel region, covering a polar angle $32.2° < \theta < 128.7°$, as an important component within Belle II's particle identification system, particularly for low-energy particles that may not generate sufficient ionization in the tracking detectors. Comprising a scintillation material, the TOP detector has a rapid response and a high photon yield associated with Cherenkov radiation. This phenomenon occurs when charged particles traverse the material at velocities exceeding the speed of light within it.

As these charged particles move through the scintillation material, they emit Cherenkov radiation photons determined by their velocities. An array of photon detectors captures these emitted photons, converting them into electrical signals. Time-measuring electronics then collect these signals, enabling precise measurements of photon arrival times. By considering the known path length in the detector, particle velocity and Cherenkov angle is determined through time-of-flight measurements.

Each type of particle possesses a unique mass-to-charge ratio, which establishes the relationship between velocities and Cherenkov angles. Consequently, particle identification becomes possible by comparing the measured Cherenkov angle with the anticipated angles associated with different particle species. The recent operation and performance of the TOP detector are summarized in Refs. [54, 55].

3.2.5 Aerogel ring imaging Cherenkov detector

The ARICH detector is positioned in the forward end-cap region, covering a range of polar angles within $\theta \in [12.4°, 31.4°]$. Much like the TOP detector, the ARICH system is designed to capture the Cherenkov light emitted by charged particles as they traverse the aerogel radiator at velocities exceeding that of light in the aerogel material. This emission of Cherenkov photons results in the formation of distinctive ring-like patterns within the detector plane, with the ring's radius directly correlating with the particle's velocity.

Aside from the contribution to the measurement particle velocity, the ARICH detector is also helpful for identifying various charged particle species, including pions, kaons, and others. Each particle type generates a unique and recognizable pattern of Cherenkov rings, facilitating particle identification [56].

3.2.6 Electromagnetic calorimeter

The ECL is installed in the barrel and forward end-cap regions and extends to the backward end-cap region. This latter region covers polar angles within the range of $\theta \in [130.7°, 155.1°]$. The ECL is used to study electromagnetic particles, including photons and electrons. Its core construction features CsI(Tl) crystals. When photons interact with the scintillation material, they directly deposit their energy, whereas electrons generate photons through processes like bremsstrahlung and pair production. The released energy is converted into scintillation light, which is subsequently captured, amplified, and analyzed to reconstruct the energy.

Ongoing advancements include the integration of a convolutional neural network (CNN) for the identification of light leptons and pions within the ECL [57, 58].

3.2.7 K_L and μ Detector

In the Belle experiment, K_L^0 and muon subsystems was developed using the resistive plate chambers (RPC) [59, 60]. For its successor the Belle II experiment is expected to face higher background rates, primarily stemming from neutrons produced in electromagnetic showers resulting from background reactions. To resolve this problem, the endcap RPCs have been replaced with scintillators [35].

To reach the KLM, particles must possess a minimum momentum of $|\vec{p}| \approx 600$ MeV/c. Since the KLM is located outside the superconducting solenoid, muons and charged hadrons follow a linear trajectory through the KLM until they either exit the system or undergo energy loss due to electromagnetic interactions.

It is important to point out that the KLM cluster is capable of providing only directions of K_L^0 candidates. Given the substantial variability in the development of showers during K_L^0-nuclear collisions, the number of hits within a cluster associated with a K_L^0 meson serves as an inadequate measure of the incident energy. Consequently, it is not feasible to reconstruct the energies of K_L particles [35].

3.3 Reconstruction and identification of final-state particles

The reconstruction of final state particles, such as electron, muons, pions, and kaons is carried out using the Belle II analysis software framework (basf2) [61, 62]. The reconstruction and identification of charged particles are detailed in Sec. 3.3.1 and Sec. 3.3.2, respectively. Additionally, in Sec. 3.3.3, we will provide an overview of reconstruction of neutral particles.

3.3.1 Reconstruction of charged particles

The reconstruction of charged particles primarily includes two key steps: track reconstruction and the subsequent determination of momentum based on the track's curvature in the magnetic field. Track reconstruction encompasses two main phases: track finding and track fitting. During the first phase, the software collects detector hits and generates initial track candidates. In the subsequent track fitting step, precise track trajectories are established for these initial candidates.

Various tracking algorithms have been developed to address the unique characteristics of the tracking detectors, namely the PXD, SVD, and CDC. The reconstruction process progresses from the CDC towards the inner vertex detectors.

Within the CDC, recorded signals are filtered and reconstructed via two different approaches: a global algorithm based on the Legendre transformation [63] and a local method relying on cellular automatons [64, 65]. These methods operate independently, but their outcomes are combined and refined using a deterministic annealing filter (DAF) [66]. Furthermore, the CDC tracks receive enrichment through a combinatorial Kalman filter (CKF) [67, 68], which extrapolates hits detected in the SVD. The resulting tracks originating from the CDC and SVD are then seamlessly integrated and refined with the aid of another DAF and subsequently extrapolated to the PXD using a second CKF.

Simultaneously, a standalone SVD track finder has been devised, leveraging a sector map technique [69] in conjunction with cellular automatons. This allows for the reconstruction of high-curvature tracks that may not have yielded sufficient hits in the CDC.

The track fitting process relies on a DAF provided by the GENFIT2 package [66]. To accurately account for energy loss and material effects, it is essential to employ a specific particle hypothesis. The available hypotheses in the Belle II experiment include electrons, muons, pions, kaons, and protons. Once trajectory information is established, the tracks are extrapolated to the point of closest approach (POCA) to the origin, where their helix parameters are extracted. A more comprehensive summary of the track reconstruction procedures can be found in Refs. [33, 70].

3.3.2 Identification of charged particles

Accurate and efficient particle identification (PID) is essential for the Belle II physics program. The PID system, which includes the TOP counter in the barrel region and the ARICH detector in the forward endcap region, combines information on charged particles across the entire kinematic spectrum. Data from these detectors are analyzed with specific ionization (dE/dx) measurements obtained from the CDC. The SVD also offers independent dE/dx measurements, although these are not currently integrated into the Belle II data processing as of the time of writing. For the

identification of charged leptons, the ECL and KLM detectors play important roles in electron and muon identification, respectively.

Identification of charged particle at Belle II employs likelihood-based selectors. Information from each PID system is independently analyzed to compute a likelihood score for each charged particle hypothesis. These PID likelihoods from each detector are aggregated to form a composite PID likelihood for each of the six long-lived charged particle hypotheses, which include electron, muon, pion, kaon, proton, and deuteron. For a given particle denoted as α, the PID quantity is defined as

$$\mathrm{PID}(\alpha) = \frac{\mathcal{L}_\alpha}{\mathcal{L}_e + \mathcal{L}_\mu + \mathcal{L}_\pi + \mathcal{L}_K + \mathcal{L}_p + \mathcal{L}_d}, \tag{3.1}$$

where $\mathcal{L}_\alpha$ represents the likelihood score for the particle hypothesis α. The specific details of likelihood construction for individual particle hypotheses and sub-detectors are elaborated in Ref. [33]. The performance of charged particle identification is discussed in Ref. [55].

3.3.3 Reconstruction of neutral particles

When photons interact with calorimeters, clusters are identified by clustering individual cells. With high backgrounds, it becomes challenging to discern the energy from a signal photon incidents amid the multitude of energy deposits originating from beam-induced backgrounds. To overcome this challenge, a specialized clustering algorithm has been developed [33].

The crystals with energy deposits are categorized into two distinct regions: connected and unconnected, based on specified energy criteria. The connected regions are isolated from each other, with the possibility of multiple clusters within a single connected region. These clusters are discerned by requiring that each cluster possesses only one local maximum. A local maximum is defined as a crystal with energy higher than its eight neighboring crystals.

The centroid position of a cluster is determined by computing the weighted sum of crystal positions, with each crystal's weight w_i calculated as $4 + \log(E_i/E_{\mathrm{sum}})$, where E_{sum} represents the total energy of the cluster. Cluster energy undergoes a calibration process to account for various factors, including energy loss beyond the calorimeter boundaries, losses within inactive materials, and the omission of energy deposits that do not meet specific criteria. The latter introduces a bias due to the trade-off between incorporating more photon energy and potentially including additional electronic noise and beam-related background.

Additionally, the cluster time, denoted as t_{cluster}, signifies the time of the highest energy crystal within a cluster relative to the collision time. This parameter is carefully studied to mitigate the impact of out-of-time beam backgrounds.

Notably, the recent work discussed in Ref. [71] explores the implementation of advanced graph neural networks (GNN) to enhance photon reconstruction efficiency. Overall, GNN-based reconstruction has demonstrated the potential to improve energy resolution, reduce tail artifacts in the reconstructed energy distribution.

The reconstruction of π^0 mesons relies on the combination of two photon candidates. For π^0 energies below approximately 2.5 GeV, it is reconstructed from two distinct photon candidates in the ECL, utilizing their respective photon 4-momenta. However, when dealing with π^0 energies exceeding about 2.5 GeV, the two photon induced showers frequently no longer exhibit separate

local maxima. In such cases, the energy is inferred from the shower's second moment shape variable [33].

The reconstruction of K_L^0 mesons utilizes information gathered from the KLM and ECL detectors. Multivariate classifiers, developed based on boosted decision trees, are applied separately to the KLM and ECL clusters to provide estimates of the probability that a given cluster originates from a K_L^0 meson. These classifiers significantly outperform the previous Belle K_L^0 identification method, achieving an improvement by a factor of ≈ 2 [33].

3.4 Collision data

The data collection for the Belle II experiment commenced in 2019, with the ultimate goal of achieving a target integrated luminosity of 50 ab^{-1}. By the time of the long shutdown 1, 424 fb^{-1} of integrated luminosity had been accumulated. For the analysis presented in this thesis, a subset of this data collected until 2021 is considered.

The on-resonance data sets are acquired at a center-of-mass (CM) energy of $\sqrt{s} = 10.58$ GeV, corresponding to the mass of the $\Upsilon(4S)$, and amounting to a total integrated luminosity of 189 fb^{-1}. Additionally, 18 fb^{-1} of off-resonance data sets are recorded at a CM energy of $\sqrt{s} = 10.52$ GeV, which is slightly below the $\Upsilon(4S)$ mass, preventing the production of B mesons. These non-$B\bar{B}$ events are commonly referred to as "continuum". The continuum component contains a variety of processes, including $e^+e^- \to \mu^+\mu^-$, $e^+e^- \to \tau^+\tau^-$, and $e^+e^- \to q\bar{q}$ processes, where q represents the u, d, s, c quarks. Notably, the cross-section magnitudes for these processes are comparable to that of the $e^+e^- \to \Upsilon(4S) \to B\bar{B}$ process.

The off-resonance data sets are utilized to determine the number of $B\bar{B}$ pairs within the data sets through the following equation,

$$N_{B\bar{B}} = \frac{N_{\text{had.}}^{\text{on-res.}} - N_{\text{had.}}^{\text{off-res.}} R_{\text{lumi.}} k}{\epsilon_{B\bar{B}}}, \tag{3.2}$$

where $N_{\text{had.}}^{\text{on-res.}}$ and $N_{\text{had.}}^{\text{off-res.}}$ are the numbers of selected hadronic events in the on-resonance and off-resonance data sets, respectively. In addition,

$$R_{\text{lumi.}} = \frac{\mathcal{L}^{\text{on-res.}}}{\mathcal{L}^{\text{off-res.}}}, \tag{3.3}$$

is the ratio of integrated luminosities between the on-resonance and off-resonance data sets. The efficiencies and cross sections for the non-$B\bar{B}$ events exhibit variations dependent on the beam energy. These variations are corrected using the factor k, which is expressed as

$$k = \frac{\sum_i \epsilon_i \sigma_i}{\sum_i \epsilon_i' \sigma_i'}, \tag{3.4}$$

where ϵ_i and σ_i represent the selection efficiencies and cross sections of continuum events at the on-resonance energy respectively, while the primed quantities, i.e., ϵ_i' and σ_i', denote those at the off-resonance energy. The B-counting study is conducted by the performance group. They

determine the number of $B\bar{B}$-pairs in the 189 fb^{-1} data set to be

$$N_{B\bar{B}} = (198 \pm 3) \times 10^6. \tag{3.5}$$

In addition to the B-counting study, the off-resonance data sets are employed to validate the Monte Carlo (MC) simulation of continuum events. More details can be found in Appendix A.

3.5 Simulated samples

In the Belle II experiment, all simulation processes begin with at least one event generator responsible for simulating the primary physics processes. This is followed by a detector simulation. In certain studies, the impact of beam background is also considered, and it is simulated separately in specialized background simulations before being incorporated into the physics event simulation.

Simulated MC samples of $\bar{B}^0 \to D^{*+}\ell^-\bar{\nu}_\ell$ signal events, with the subsequent decays $D^{*+} \to D^0\pi^+$ and $D^0 \to K^-\pi^+$, are used to obtain the template shapes for the signal extraction, determine reconstruction efficiencies and the signal kinematic distributions. These events are generated using the `EvtGen` package [72] with the other B meson in the event decays generically. `EvtGen` is controlled by means of a fairly complete decay table (DECAY.DEC), which provides a detailed listing of all potential decay processes, their associated branching ratios, and the utilized model (amplitude) for their decay. Samples of MC simulated background events are used to model the kinematic distributions of background processes. These include a sample of $e^+e^- \to B\overline{B}$ events with generic B meson decays, generated with `EvtGen`, which correspond to an integrated luminosity of 1 ab^{-1}.

A sample of continuum $e^+e^- \to q\bar{q}$ $(q = u, d, s, c)$ events is simulated with the `KKMC` generator [73] interfaced with `PYTHIA 8` [74]. Further, $e^+e^- \to \tau^+\tau^-$ events are simulated with `KKMC`, and interfaced with `TAUOLA` [75].

Interactions of detectors and particles are simulated by `GEANT4` [76]. All recorded data and simulated samples are processed and analyzed using the basf2.

CHAPTER 4

Event reconstruction, selection, and correction

4.1 Event reconstruction

We focus on reconstructing the signal $\bar{B}^0 \to D^{*+}\ell^-\bar{\nu}_\ell$ decays with $\ell = e, \mu$, while not explicitly reconstructing the decay of the other B meson in the same event. This is categorized as untagged reconstruction. In contrast, the tagged approach includes the reconstruction of hadronic or semileptonic decays of the accompanying B meson. At Belle II, the B-tagging process is facilitated by the full event interpretation algorithm [77], which utilizes boost decision trees [78].

Tagged reconstruction significantly improves the purity of the selected candidates and provides valuable kinematic information of the signal B meson. This is especially advantageous for analyses of semileptonic B decays, where the presence of neutrinos in the final state makes it challenging to infer the momentum of the B meson at Belle II. However, this improved purity comes at the cost of reduced efficiency. Consequently, compared to untagged measurements, tagged measurements from the same dataset always exhibit a larger statistical uncertainty.

Figure 4.1 illustrates a typical collision event containing the signal $\bar{B}^0 \to D^{*+}\ell^-\bar{\nu}_\ell$ decay. The reconstruction of the charge-conjugated mode is included without specific declaration. As shown in Fig. 4.1, a D^0 meson is reconstructed from a kaon and a pion with opposite charges, and then combined with a low-energy charged pion to form a D^{*+} meson. Subsequently, we reconstruct a $D^{*+}\ell^-$ system. The final-state neutrino cannot be detected by the Belle II detectors and is, therefore, represented by a dashed line. The remaining unused particles are considered to originate from the accompanying B meson and are referred to as the rest of the event (ROE).

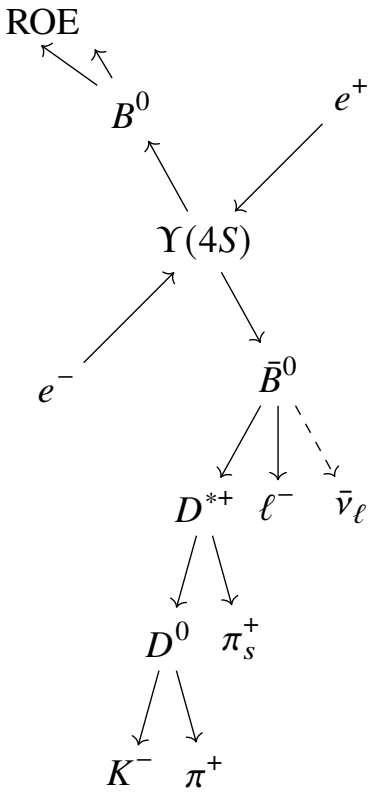

Figure 4.1: Illustration of a typical event containing the signal $\bar{B}^0 \to D^{*+}\ell^-\bar{\nu}_\ell$ decay.

4.2 Event selection

The selected events must firstly activate a hadronic high level trigger (HLT) [79], which conducts a full event reconstruction, excluding hits from the PXD, and filters out non-hadronic events using the Belle II analysis software framework (basf2) [61, 80]. In addition, charged tracks must satisfy certain criteria, including a requirement that their distance of closest approach to the interaction point is less than 4.0 cm along the z direction and less than 2.0 cm in the transverse $r - \phi$ plane. Further, all tracks must fall within the angular acceptance of the CDC.

Momenta of both electron and muon candidates in the CM frame are required to be larger than 1.2 GeV/c and smaller than 2.4 GeV/c. Electron candidates are selected using particle identification likelihoods based on CDC, ARICH, ECL and KLM information. To identify muon candidates, information from the TOP detector is also considered, in addition to information from the CDC, ARICH, ECL, and KLM detectors. The efficiencies to identify electrons and muons are 88% and 91%, respectively. The misidentifiation rates for hadrons, including pions and kaons, as electrons and muons are 0.2% and 3%, respectively.

Neutral D candidates are reconstructed from charged kaon and pion candidates, and their invariant masses are required to be within a range of 15 MeV/c^2 from the known D^0 mass, which corresponds to approximately ±3.4 units of mass resolution. To reconstruct D^{*+} candidates, we

combine the D^0 candidates with low-momentum pion candidates (referred to as slow pions) selected from the remaining charged particles with momenta below 0.4 GeV/c. To enhance the purity of the reconstructed D^{*+} candidates, we impose a requirement on the mass difference between D^{*+} and D^0 candidates, denoted as $\Delta M = M(K\pi\pi) - M(K\pi)$. This requirement stipulates that ΔM must be within the range of $[0.141, 0.156]$ GeV/c^2. Correctly reconstructed D^{*+} candidates exhibit a peak at a value of $m_{D^{*+}} = 2.010$ GeV/c^2, with a resolution of 5 MeV/c^2.

To suppress continuum backgrounds, such as $e^+e^- \to q\bar{q}$ with $q = u, d, s, c$ or $e^+e^- \to \tau^+\tau^-$ processes, we employ the requirement that the ratio between the second- and the zeroth-order Fox-Wolfram moments [81] be less than 0.3. Additionally, we set an upper limit on the momentum of D^{*+} in the CM frame, restricting it to $p^{\mathrm{CM}}_{D^{*+}} < 2.5$ GeV/c, which effectively rejects D^{*+} candidates originating from $e^+e^- \to c\bar{c}$ events. To enhance the separation from continuum background, we impose a requirement that the sum of reconstructed energy in the CM frame exceeds 4 GeV.

The signal B-meson energy and magnitude of the momentum in the CM frame is inferred from the beam energy $E^{\mathrm{CM}}_{\mathrm{Beam}} = \sqrt{s}/2$,

$$E^{\mathrm{CM}}_B = E^{\mathrm{CM}}_{\mathrm{Beam}}, \quad |\vec{p}^{\,\mathrm{CM}}_B| = \sqrt{(E^{\mathrm{CM}}_{\mathrm{Beam}})^2 - m_B^2 c^4}/c\,. \tag{4.1}$$

Here $m_B = 5.279\,\mathrm{GeV}/c^2$ is the B-meson mass. With this information, we reconstruct the cosine of the angle between the B meson and the $D^*\ell$ system (denoted by Y) via

$$\cos\theta_{BY} = \frac{2E^{\mathrm{CM}}_B E^{\mathrm{CM}}_Y - m_B^2 c^4 - m_Y^2 c^4}{2|\vec{p}^{\,\mathrm{CM}}_B||\vec{p}^{\,\mathrm{CM}}_Y|c^2}, \tag{4.2}$$

where E^{CM}_Y, $|\vec{p}^{\,\mathrm{CM}}_Y|$, and m_Y are the energy, magnitude of momentum, and mass of the reconstructed $D^*\ell$ system, respectively. If a $D^*\ell$ pair does not originate from a $\bar{B}^0 \to D^{*+}\ell^-\bar{\nu}_\ell$ decay, $|\cos\theta_{BY}|$ can exceed unity. We keep all candidates in the range $\cos\theta_{BY} \in [-4, 2]$ to separate signal decays and background processes.

Combining all of these selection criteria, we achieve efficiencies of 22.0% and 23.5% for the $\bar{B}^0 \to D^{*+}e^-\bar{\nu}_e$ and $\bar{B}^0 \to D^{*+}\mu^-\bar{\nu}_\mu$ decays, respectively. With an average of 1.06 candidates per event, our observed candidate multiplicity closely aligns with the multiplicity of candidates in simulated samples. We retain all candidates per event [82]. Importantly, our event selection strategy was optimized and tested using simulated samples, and no bias was observed on the selection efficiency.

All selection criteria discussed above are summarized in Table 4.1.

Table 4.1: Selection criteria employed in the analysis of the $\bar{B}^0 \to D^{*+}\ell^-\bar{\nu}_\ell$ decay.

	Variable	Selection criterion
Final-state particles	d_r	< 2 cm
	$\lvert d_z \rvert$	< 4 cm
	polar angle θ	$\in [17°, 150°]$
	e-ID (or μ-ID)	> 0.9
	p_ℓ^{CM}	$\in [1.2, 2.4]$ GeV/c
	$p_{\pi_s^+}^{\mathrm{CM}}$	< 0.4 GeV/c
Intermediate particles	$\lvert M(K\pi) - M_{D^0}^{\mathrm{PDG}} \rvert$	< 15 MeV/c^2
	ΔM	$\in [0.141, 0.156]$ GeV/c^2
Continuum suppression	$p_{D^{*+}}^{*}$	< 2.5 GeV/c
	R_2	< 0.3
Other selections	$\cos\theta_{BY}$	$\in [-4, 2]$
	E^{CM}	> 4 GeV
	High level trigger	hadronic events

4.3 Corrections for simulated samples

The efficiencies and fake rates of lepton identification, as well as the reconstruction efficiency of slow pions, can vary between collision data and simulated samples. These discrepancies are kinematics-dependent and affect not only the normalization but also the shape of the distributions. The latter plays a significant role in the signal extraction, as we will discuss later. Therefore, for precise measurements of $|V_{cb}|$ and form factor parameters, it is essential to carefully calibrate the simulated samples.

In the following sections, we will discuss the corrections for lepton ID efficiency and fake rate in Sec. 4.3.1, as well as the correction for slow pion reconstruction efficiency in Sec. 4.3.2. Additionally, Sec. 4.3.3 will cover the correction for background shapes.

4.3.1 Lepton ID efficiency and fake rate

The efficiencies and fake rates for electron and muon identification exhibit discrepancies between collision data and simulated samples. To address these differences, the lepton ID performance group conducts investigations using processes including $J/\psi \to \ell^+\ell^-$, $e^+e^- \to \ell^+\ell^-(\gamma)$, and $e^+e^- \to e^+e^-\ell^+\ell^-$, where $\ell = e, \mu$.

For pion fake rates, correction factors are derived from decays including $K_S^0 \to \pi^+\pi^-$, $D^{*+} \to D^0(\to K^-\pi^+)\pi^+$, and $e^+e^- \to \tau^+(1\text{-prong})\tau^-(3\text{-prong})$ processes. Additionally, the kaon fake rate is determined through the study of the $D^{*+} \to D^0(\to K^-\pi^+)\pi^+$ process.

The correction is assessed within the polar angle acceptance regions of the ECL for electrons

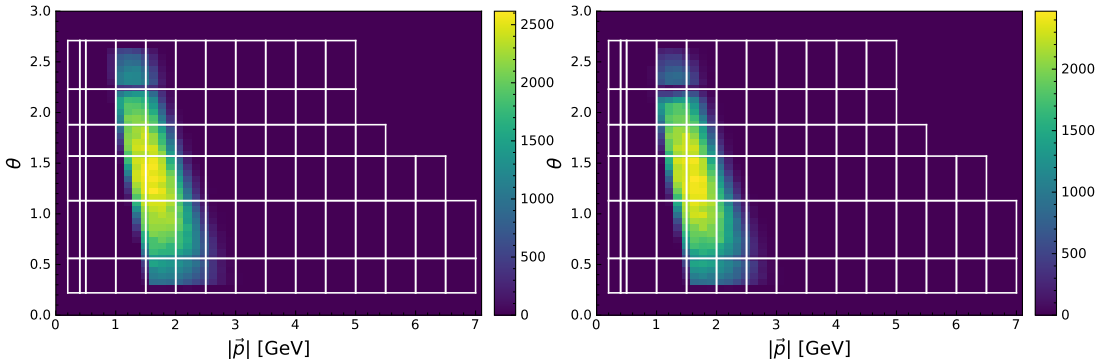

Figure 4.2: Heatmaps of the true electrons (left) and positrons (right). Brighter colors indicate a higher density of particles. The white grid areas represent the $|\vec{p}_{\text{lab}}|$-θ phase spaces available for efficiency correction.

(0.22 to 2.71 rad) and of the KLM for muons (0.40 to 2.60 rad). The comprehensive set of probe channels is combined to span a lab-frame momentum range of 0.4 GeV/c to 7.0 GeV/c for electrons and 0.4 GeV/c to 6.5 GeV/c for muons. In this study, correction factors are determined separately for positive and negative charges, and are binned based on the lepton polar angle θ and momentum in the lab frame $|\vec{p}|$.

If lepton candidates are correctly identified, they are assigned central correction values as weights according to the corresponding efficiency table. If they are reconstructed from pions or kaons, corrections are applied using the relevant fake rate table.

Figure 4.2 shows two-dimensional heatmaps illustrating correctly identified electrons, while Fig. 4.3 shows those that are identified incorrectly. The coverage of the respective correction tables is represented by the white grid.

Two types of candidates remain uncorrected due to insufficient studies on their efficiencies and fake rates:

- Particles, excluding pions and kaons, such as protons, that are misidentified as leptons, and beam background hits that are mistakenly interpreted as lepton tracks. They make up only 0.6% of the total reconstructed samples.
- Correctly identified leptons that fall outside the phase space of the efficiency study, and misidentified pions or kaons that are outside the phase space of the fake rate study. Together, they constitute only 0.5% of the total reconstructed samples.

Considering that these two types of events constitute a small fraction of the total events, we anticipate that they have a negligible impact on our analysis. We assign a weight of one to them, indicating that no correction for their efficiencies or fake rates is applied.

Both statistical and systematic uncertainties are estimated for efficiency and fake rate correction factors. In order to effectively assess uncertainties and correlations, we generate 400 variation weights w'_k for each event in bin k, following a multivariate Gaussian distribution.

$$w'_k = w_k + \mathcal{G}(0,\ \sigma^T_{\text{stat}}\rho_{\text{stat}}\sigma_{\text{stat}} + \sigma^T_{\text{sys}}\rho_{\text{sys}}\sigma_{\text{sys}})_k, \tag{4.3}$$

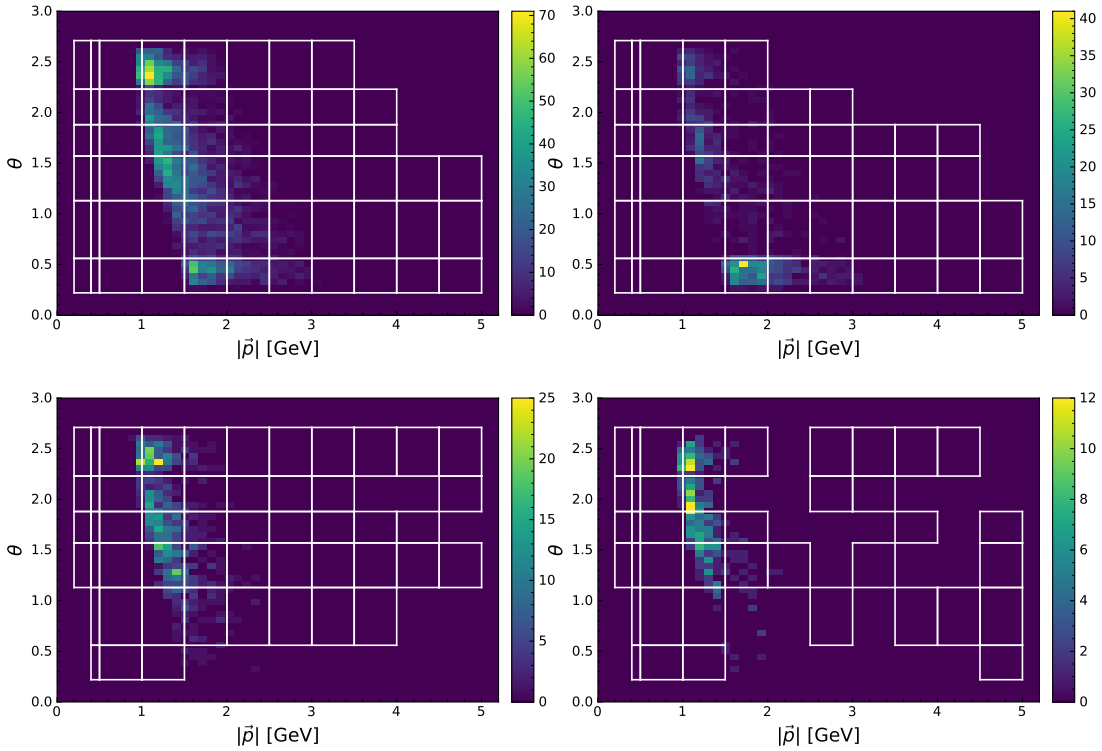

Figure 4.3: Heatmaps of pions (top) and kaons (bottom) that are misidentified as electrons (left) or positrons (right). The area in a brighter color implies a higher density of fake particles. Brighter colors indicate a higher density of particles. The white grid areas represent the $|\vec{p}_{\text{lab}}|$-θ phase spaces available for fake rate correction.

where w_k represents the correction weight for bin k, and $\mathcal{G}(0, \sigma^T \rho \sigma)_k$ refers to a sample generator that simulates statistical or systematic fluctuations for bin k following a multivariate Gaussian distribution with 0 means and a covariance matrix $\sigma^T \rho \sigma$. Here, ρ_{stat} is diagonal, indicating that statistical uncertainties between different bins are uncorrelated. In contrast, ρ_{sys} is a matrix with all elements equal to one, implying that systematic uncertainties are fully correlated across all bins. Additionally, σ corresponds to the standard deviations provided by the correction tables.

Regarding the candidates falling outside the phase space covered by the correction table, their variation weights are generated using the formula

$$w' = 1 + \mathcal{G}(0,\ \sigma_{\text{average}}), \tag{4.4}$$

where the σ_{average} is determined by

$$\sigma^2_{\text{average}} = \overline{\sigma}^2_{\text{stat+sys}} + \overline{1 - w}^2. \tag{4.5}$$

Here, $\overline{\sigma}_{\text{stat+sys}}$ represents the average of full uncertainties across the entire table, while $\overline{1 - w}$ is

the average of the differences between one and the correction factors across the entire table. The assignment of the correction weights and the generation of variation weights are carried out using the `PIDvar` package [83].

Due to the absence of performance studies, we are not able to assign uncertainties for the misidentified lepton candidates other than kaons and pions.

4.3.2 Slow pion reconstruction efficiency

The investigation of the slow pion reconstruction efficiency is an important part of my PhD research. This efficiency correction plays a critical role in measurements of semileptonic B decays involving D^{*+} mesons and typically contributes the leading-order uncertainty in measurements of $\bar{B}^0 \to D^{*+}\ell^-\bar{\nu}_\ell$ decays. Detailed information on how the correction factors for slow pion reconstruction efficiency are determined can be found in Appendix B. The resulting momentum-dependent correction factors for slow pions are summarized in Table 4.2. It's worth noting that no correction is applied to pions with momenta exceeding 0.20 GeV/c.

Table 4.2: Correction factors for the slow pion reconstruction efficiency, where the first uncertainty is uncorrelated between different momentum bins, while the second is correlated.

Momentum region	Correction factor
0.05-0.12 GeV/c	$0.909 \pm 0.032 \pm 0.020$
0.12-0.16 GeV/c	$1.033 \pm 0.026 \pm 0.022$
0.16-0.20 GeV/c	$0.971 \pm 0.027 \pm 0.021$
> 0.20 GeV/c	1

Similar to the lepton ID correction, we assign corresponding correction factors as weights for slow pion candidates according to their momenta. To properly estimate uncertainties and correlations, we adopt the same method as for lepton identification. We generate 400 variation weights for each candidate by

$$w'_{\text{slow}} = w + \mathcal{G}(0, \sigma_{\text{uncorr}}) + \mathcal{G}(0, \sigma_{\text{corr}}), \tag{4.6}$$

where w is the correction factor, and $\mathcal{G}(0, \sigma_{\text{uncorr}})$ and $\mathcal{G}(0, \sigma_{\text{corr}})$ denote sample generators that produce random numbers following Gaussian distributions with uncorrelated and correlated uncertainties, respectively. Particularly, we use the same seeds for generating correlated random numbers across different bins for both $\bar{B}^0 \to D^{*+}e^-\bar{\nu}_e$ and $\bar{B}^0 \to D^{*+}\mu^-\bar{\nu}_\mu$ decays. This strategy, implemented using the `NumPy` package [84], ensures full correlation of slow pions within the same momentum window between the electron and muon channels.

4.3.3 Background shape correction

The $\cos\theta_{BY}$ distribution holds significant importance as it is utilized for determining signal yields. Nevertheless, a discrepancy is observed between the reconstructed candidates and the simulated

samples in the region where $\cos\theta_{BY} > 2$, fully populated by background events. To address this issue, we decide to exclude the problematic $\cos\theta_{BY} > 2$ region from our analysis.

Moreover, we conduct an additional examination of background events with $\cos\theta_{BY} < 2$. This involves the reconstruction of reference data and samples by pairing D^* and lepton candidates with the same charge. The reconstructed samples are then categorized into two distinct groups: the true D^* component, where D^* mesons are accurately reconstructed, and the fake D^* component, where they are not.

Subsequently, we calculate a bin-by-bin correction for the fake D^* component in the $\cos\theta_{BY}$ spectrum by computing the ratios between data and MC samples originating from the sideband region $\Delta M > 0.152$ GeV/c^2. We then apply this correction to the fake D^* candidates in the $\Delta M < 0.152$ GeV/c^2 region of the same-sign samples and subtract this component from experimental data. Further, we determine the ratios of correctly reconstructed D^* candidates between reference data and samples in bins of the $\cos\theta_{BY}$ distribution, which are used as correction factors for the true D^* component.

The background samples with this correction applied will be utilized in the subsequent analysis. To maintain a conservative approach, the discrepancy in results when the correction is omitted is considered as the uncertainty arising from the background shape.

4.4 Comparison of collision data and simulated samples

After implementing the corrections that are described in this section, we present the distributions of the $\cos\theta_{BY}$ and ΔM variables in Fig. 4.4 for both $\bar{B}^0 \to D^{*+}e^-\bar{\nu}_e$ and $\bar{B}^0 \to D^{*+}\mu^-\bar{\nu}_\mu$ channels. In the figure, the simulated samples are categorized as follows

- Signal: the entire decay chain is reconstructed correctly.
- "True D^*" background: the D^* candidate is reconstructed correctly, but the $D^*\ell$ system is wrongly reconstructed due to the misidentification of the lepton candidate or the wrong combination of D^* and ℓ candidates. This arises from continuum, B-meson background, or signal processes.
- "Fake D^*" background: the D^* candidate is misreconstructed, arising from continuum, B-meson background, or signal processes.

In general, we observe a good agreement between the experimental data and the simulated samples. There is a slight deficit of the simulated samples in the high $\cos\theta_{BY}$ region, while the samples overshoot the data in the highest bin of the ΔM spectrum.

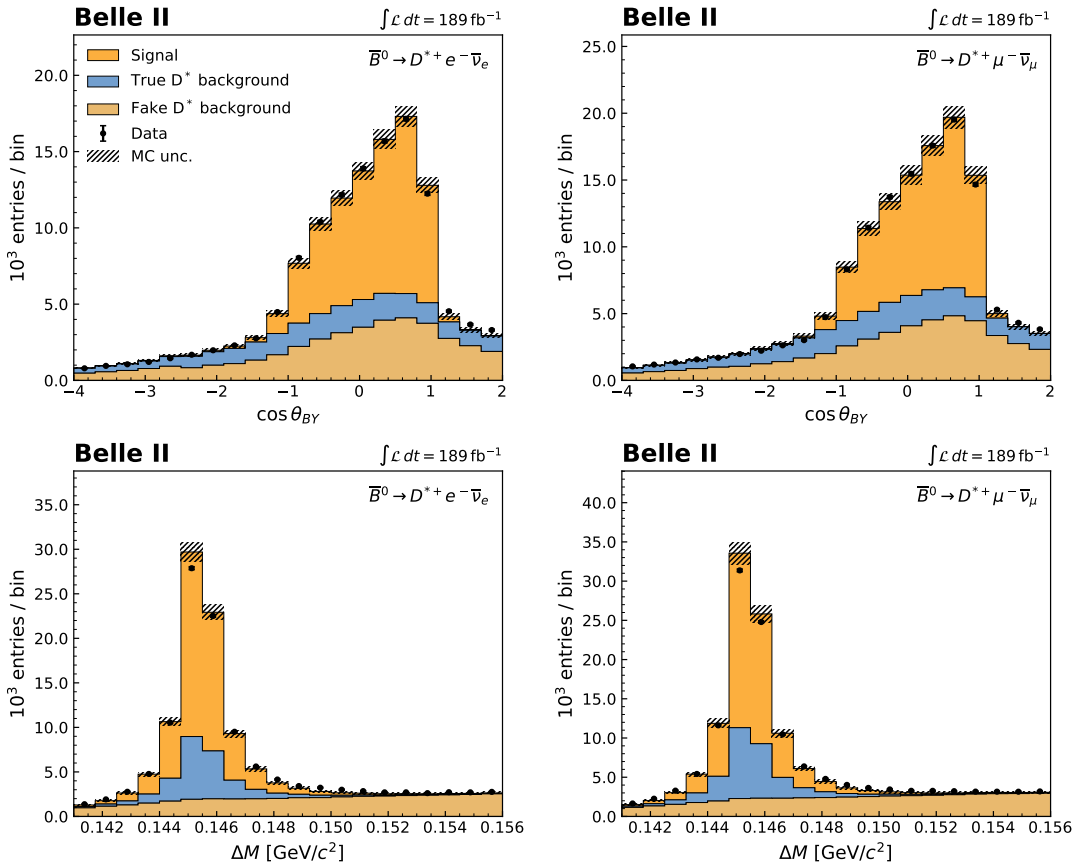

Figure 4.4: Distributions of reconstructed $\cos\theta_{BY}$ and ΔM for $\bar{B}^0 \to D^{*+} e^- \bar{\nu}_e$ (left) and $\bar{B}^0 \to D^{*+} \mu^- \bar{\nu}_\mu$ (right) candidates in data with expectations from simulation overlaid. The simulated samples are weighed based on integrated luminosities. The hatched area represents the uncertainty due to the finite size of the simulated sample, and the uncertainties arising from the lepton identification, slow-pion reconstruction, and tracking efficiency of K, π, and ℓ.

CHAPTER 5

Reconstruction of kinematic variables

To reconstruct the recoil parameter w and three decay angles θ_ℓ, θ_V, and χ, we must first determine momenta of B mesons. As previously mentioned in Chapter 4.2, we can estimate the energy and magnitude of the three-momentum of the B meson from the beam energy using Eq. (4.1). However, the next crucial question is how to ascertain the direction of the B meson's momentum.

We recognize that the $\cos\theta_{BY}$ variable indicates the angle between the B meson and the reconstructed $D^*\ell$ system. Consequently, the momentum of the B meson must lie on the lateral surface of a right circular cone, where the cone's axis aligns with the momentum of the $D^*\ell$ system, and the opening angle of the cone is defined as $2\theta_{BY}$. It's worth noting that there is no deterministic information available to definitively determine which direction on the cone corresponds to the actual B meson's orientation.

5.1 Reconstruction using B angular distribution

The "diamond frame" method was originally developed by the BaBar experiment [85, 86]. Its foundation lies in the fact that the electron and positron beams are effectively massless and completely polarized along the beam axis. Consequently, the resulting spin-1 $\Upsilon(4S)$ meson should have its spin aligned with the axis. This meson further decays into two spinless B mesons, and the distribution of their angle with respect to the beam axis, denoted as θ_B, follows a $\sin^2\theta_B$ distribution. Therefore, we can deduce the probability distribution of the B meson's polar angle.

In this approach, we begin with randomly selecting the first direction on the cone, and then we determine the other nine directions with equal spacing around the cone's lateral surface. Next, we calculate four kinematic variables for each of these ten directions. The weighted average of these ten samples is calculated, with the weight for the i-th sample written as

$$\omega_i = \sin^2\theta_{B\,i}, \tag{5.1}$$

with $\theta_{B\,i}$ denoting the polar angle of the i-th sampled B direction.

5.2 Reconstruction utilizing rest of event

This method was previously employed by the Belle experiment. In an untagged $\bar{B}^0 \to D^{*+}\ell^-\bar{\nu}_\ell$ measurement, the tracks and clusters that are not associated with the $D^*\ell$ system are regarded as originating from the companion B meson. Consequently, exploring the characteristics of the ROE proves valuable in reconstructing the kinematics of the partner B meson. With the known beam information, we can then deduce the kinematics of the signal B meson.

In this method, we aggregate all remaining tracks and clusters in the event to directly calculate the momentum of the ROE in the CM frame, denoted as $\vec{p}^*_{\mathrm{ROE}}$. This approximates the three-momentum vector of the partner B meson. Furthermore, in the CM frame, the two B mesons are emitted in opposite directions, and thus the opposite direction of the ROE momentum in the CM frame, denoted as $-\vec{p}^*_{\mathrm{ROE}}$, points in the direction of the signal B meson if all particles in the ROE are reconstructed and assigned perfectly.

With this assumption in mind, we select the direction on the cone that is closest to the $-\vec{p}^*_{\mathrm{ROE}}$ momentum, as illustrated in Fig. 5.1, and four kinematic variables are determined based on the chosen direction.

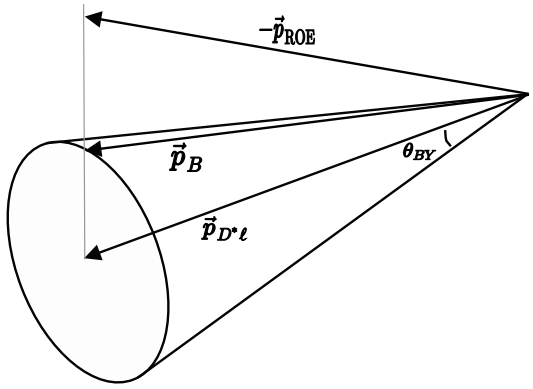

Figure 5.1: Illustration of how we choose the direction on the cone based on the ROE momentum.

5.3 Combination of two methods

Both of the approaches discussed above have their own disadvantages. For instance, in the first approach, while it's possible that the true B meson direction may be randomly selected as one of the ten samples, it will still be combined with the other nine incorrect directions when calculating the weighted average. This will lead to an inaccurate final estimate.

As for the second method, factors such as missing particles (like neutrinos and K^0_L mesons) and the limitations of detector resolution and acceptance impact the determination of the ROE direction. Consequently, the chosen direction on the cone may deviate from the actual B meson direction.

Inspired by these methods, we have developed a novel approach that leverages both the B angular distribution and ROE information. In this approach, we continue to select ten directions

on the cone, and calculate the weighted average of these ten samples, similar to the diamond frame method. However, the weight is now given by

$$\tilde{w}_i = (1 - \widehat{p}_{\mathrm{ROE}} \cdot \widehat{p}_{B_i}) \sin^2 \theta_{B_i} \tag{5.2}$$

where $\widehat{p}_{\mathrm{ROE}}$ and $\widehat{p}_{B_i}$ represent the unit vectors of the ROE momentum and the i-th sampled B meson momentum on the cone, respectively.

It is worth noting that, in comparison to the diamond frame method, the inclusion of the factor $(1 - \widehat{p}_{\mathrm{ROE}} \cdot \widehat{p}_{B_i})$ ensures that the direction on the cone closer to the vector $-\widehat{p}_{\mathrm{ROE}}$ will receive a larger weight, while those further away are suppressed.

Additionally, we confirm that selecting ten directions on the cone is adequate. There is no significant improvement observed by increasing the number of sampling.

5.4 Performance of three methods

In this section, we will compare the resolution and investigate migration properties of the three methods using simulated signal decays. Our objective is to identify the method that exhibits the best performance, and subsequently, this method will be used in the presented analysis.

We reconstruct the kinematic variables for the simulated samples with three methods, respectively. For each correctly reconstructed signal decay, we compute the difference, also referred to as the residual, between the reconstructed values and the values used to generate these events. The resulting distributions of these differences are shown in Fig. 5.2 for the kinematic variables w, $\cos\theta_\ell$, $\cos\theta_V$, and χ.

Generally, we observe that the ROE method produces distributions with the best core resolution. This phenomenon is as expected because, when there are no missing particles in the ROE and when tracks and clusters are accurately reconstructed, the ROE method provides a more precise estimation of the B direction compared to the other two methods.

On the other hand, we also note that the ROE method consistently yields distributions with the longest tails. This can be attributed to situations where the ROE reconstruction is influenced by missing particles and detector acceptance, leading to a substantial deviation between the chosen direction and the true B direction. As a result, the determination of kinematic variables based on this inaccurate direction becomes less precise when compared to the weighted average of the ten directions on the cone.

The distributions in Fig. 5.2 are not standard Gaussian distributions. To be resistant to skewness, we calculate and summarize medians as well as the 15.865% and 84.135% percentiles of the residuals in Table 5.1 and Table 5.2, respectively. While the medians from different methods exhibit minimal variation, the new combined method results in a narrower spread around the median, with 68.27% of events falling within this range, compared to the other two methods.

In addition to comparing medians and percentiles, we also assess the migration properties. In this context, elements of migration matrices are defined as conditional probabilities of events being reconstructed in a specific bin i of the recoil parameter or decay angle, given that the true

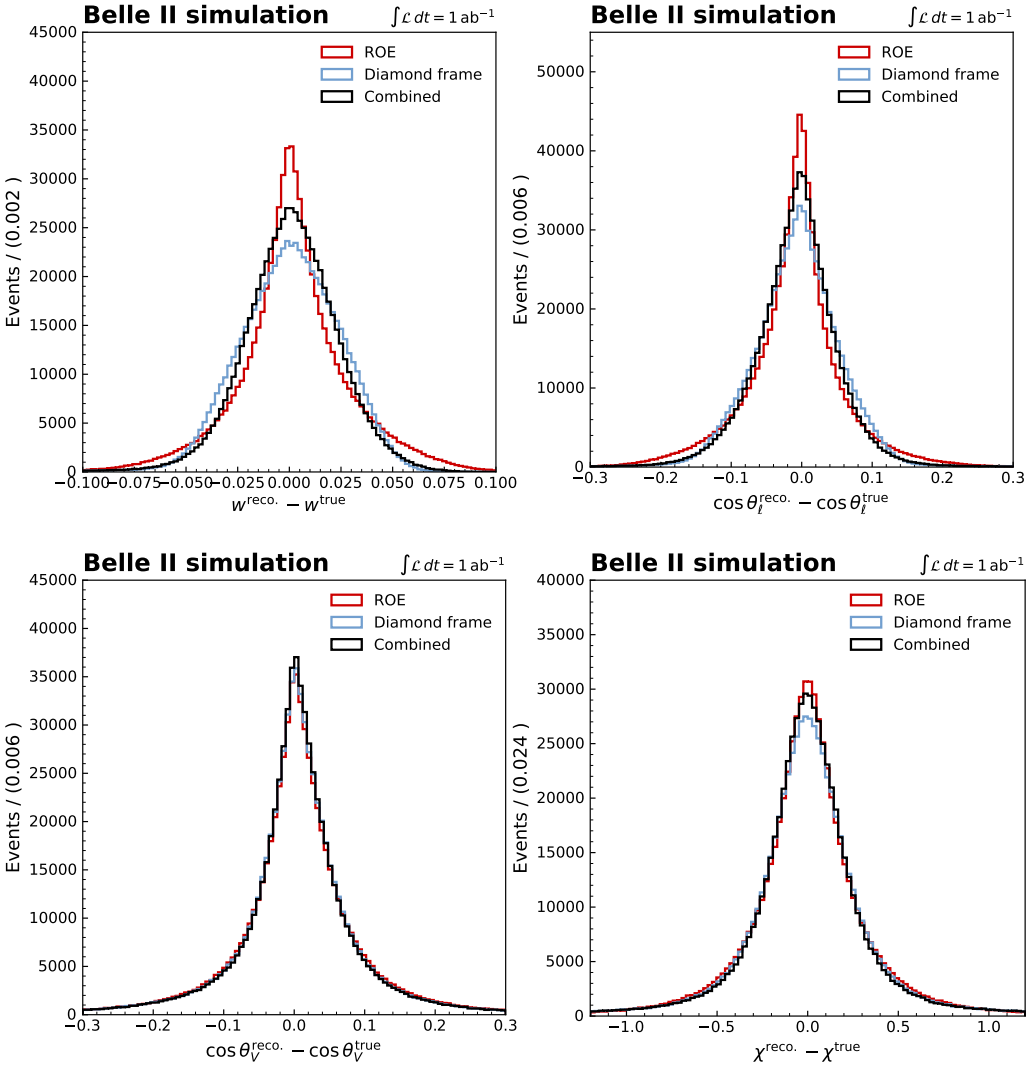

Figure 5.2: Distributions of residuals for kinematic variables w, $\cos\theta_\ell$, $\cos\theta_V$, and χ reconstructed using the diamond frame, ROE, and combined methods (including both $\bar{B}^0 \to D^{*+} e^- \bar{\nu}_e$ and $\bar{B}^0 \to D^{*+} \mu^- \bar{\nu}_\mu$ decays)

Table 5.1: Medians of residuals (in units of 10^{-3}) for kinematic variables w, $\cos\theta_\ell$, $\cos\theta_V$, and χ reconstructed using the diamond frame, ROE, and combined methods.

Variables	Diamond frame	ROE	Combined
w	0.8	1.1	1.0
$\cos\theta_\ell$	−4.9	−5.8	−5.2
$\cos\theta_V$	4.0	3.9	4.0
χ	0.8	1.1	1.0

Table 5.2: Summary of 15.865% and 84.135% percentiles of the residuals, presented as the first and second numbers in brackets, respectively, with their differences provided as the third number outside the brackets.

Variables	Diamond frame	ROE	Combined
w	[-0.024, 0.025], 0.049	[-0.021, 0.026], 0.047	[-0.020, 0.022], 0.043
$\cos\theta_\ell$	[-0.065, 0.051], 0.116	[-0.068, 0.045], 0.112	[-0.060, 0.044], 0.104
$\cos\theta_V$	[-0.061, 0.069], 0.130	[-0.064, 0.073], 0.137	[-0.059, 0.068], 0.127
χ	[-0.300, 0.301], 0.602	[-0.286, 0.287], 0.573	[-0.281, 0.282], 0.563

value falls within bin j,

$$\mathcal{M}_{ij} = P(\text{reconstructed value in bin } i | \text{true value in bin } j)\,. \tag{5.3}$$

The binning for kinematic variables w, $\cos\theta_\ell$, $\cos\theta_V$, and χ is summarized in Table 5.3. These bins are equidistant, except for the last bin of w, which extends slightly beyond 1.5, and the first bin of $\cos\theta_\ell$, which is made broader to increase the efficiency for signal decays. Furthermore, the bin widths are defined such that they are larger than the widths of the residuals, as summarized in Table 5.2. This ensures a relatively small migration across bins. In Chapter 6, we will measure partial decay rates using the same binning.

Table 5.3: Binning of kinematic variables w, $\cos\theta_\ell$, $\cos\theta_V$ and χ for partial decay rate measurement.

Variable	Bin edge
w	[1.00, 1.05, 1.10, 1.15, 1.20, 1.25, 1.30, 1.35, 1.40, 1.45, 1.504]
$\cos\theta_\ell$	[−1.0, −0.4, −0.2, 0.0, 0.2, 0.4, 0.6, 0.8, 1.0]
$\cos\theta_V$	[−1.0, −0.8, −0.6, −0.4, −0.2, 0.0, 0.2, 0.4, 0.6, 0.8, 1.0]
χ	[0, π/5, 2π/5, 3π/5, 4π/5, π, 6π/5, 7π/5, 8π/5, 9π/5, 2π]

The migration matrices for the $\bar{B}^0 \to D^{*+} e^- \bar{\nu}_e$ decay are shown in Fig. 5.3, Fig. 5.4, and

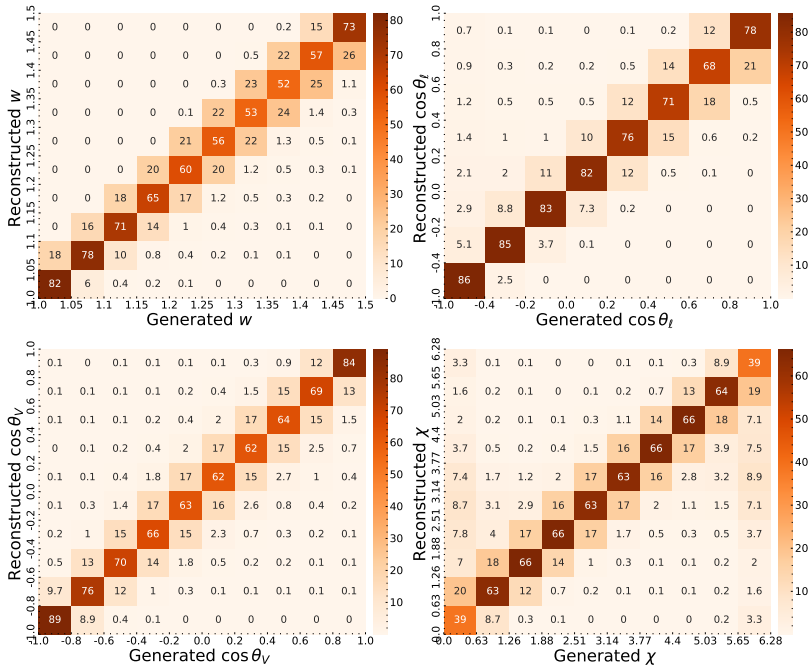

Figure 5.3: Migration matrices of kinematic variables w, $\cos\theta_\ell$, $\cos\theta_V$, and χ reconstructed using the diamond frame method for the $\bar{B}^0 \to D^{*+} e^- \bar{\nu}_e$ decay.

Fig. 5.5 corresponding to the diamond frame, ROE, and combined method, respectively. The $\bar{B}^0 \to D^{*+} \mu^- \bar{\nu}_\mu$ decay shows a similar migration pattern, which can be found in Appendix C.

For the χ angle, 0 rad and 2π rad represent the same angle. This explains the relatively large migration between the bin $[0, \pi/5]$ and bin $[9\pi/5, 2\pi]$ observed in Fig. 5.4. However, in the weighted average approaches (the diamond frame method and the novel combined method), 10 uniform directions are used in the calculation, which breaks this identity as no significant migration is observed between those two bins. Due to this, we reconstruct the χ angle using the ROE method. For the other observables, we use the novel combined method, which improves the resolutions.

The distributions of the reconstructed kinematic variables w, $\cos\theta_\ell$, $\cos\theta_V$, and χ of the analyzed Belle II data are shown in Fig. 5.6, with expectations from simulation overlaid, for both $\bar{B}^0 \to D^{*+} e^- \bar{\nu}_e$ and $\bar{B}^0 \to D^{*+} \mu^- \bar{\nu}_\mu$ decays. We observe that nearly all data points fluctuate within the prediction of the simulated samples. A small discrepancy shows around the low w region, where backgrounds are dominant. They can be constrained with the two-dimensional fits to the $\cos\theta_{BY}$ and ΔM distributions.

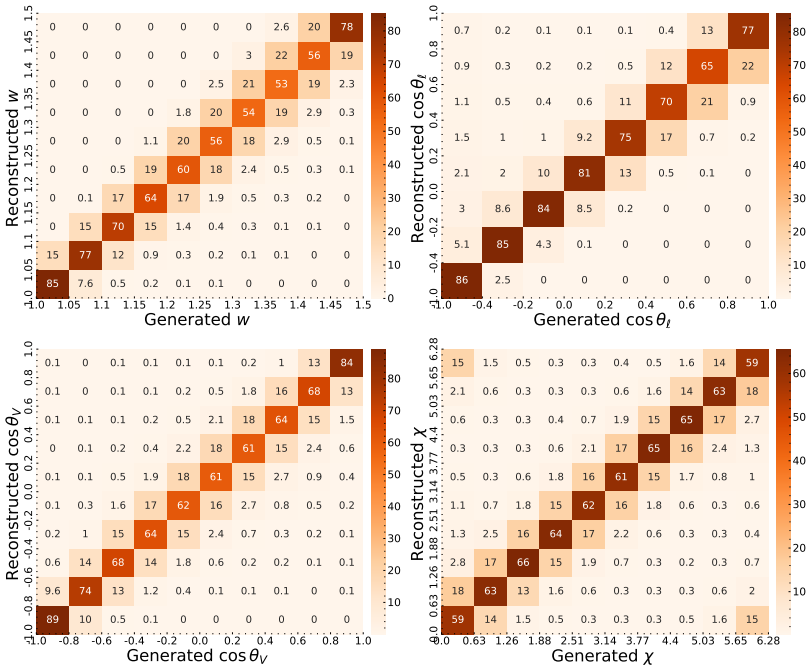

Figure 5.4: Migration matrices of kinematic variables w, $\cos\theta_\ell$, $\cos\theta_V$, and χ reconstructed using the ROE method for the $\bar{B}^0 \to D^{*+} e^- \bar{\nu}_e$ decay.

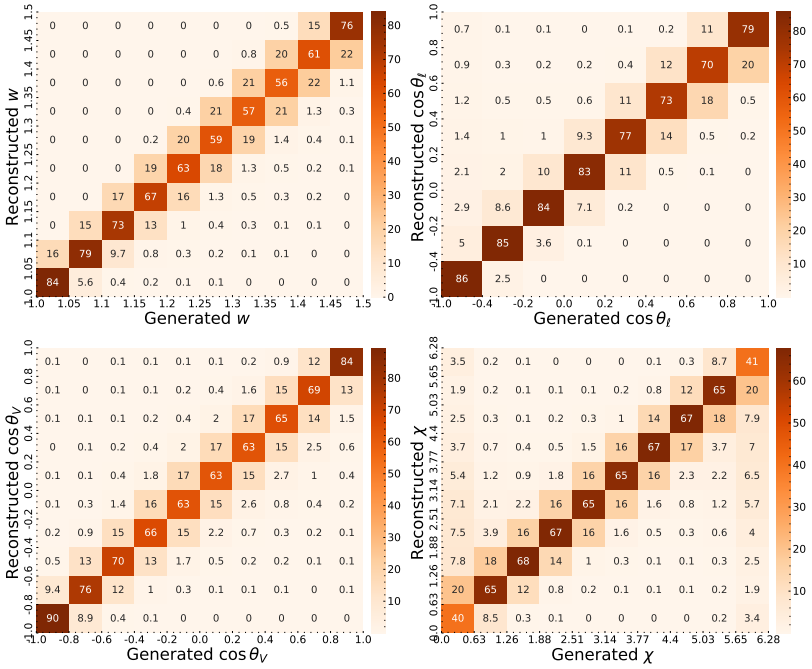

Figure 5.5: Migration matrices of kinematic variables w, $\cos\theta_\ell$, $\cos\theta_V$, and χ reconstructed using the combined method for the $\bar{B}^0 \to D^{*+} e^- \bar{\nu}_e$ decay.

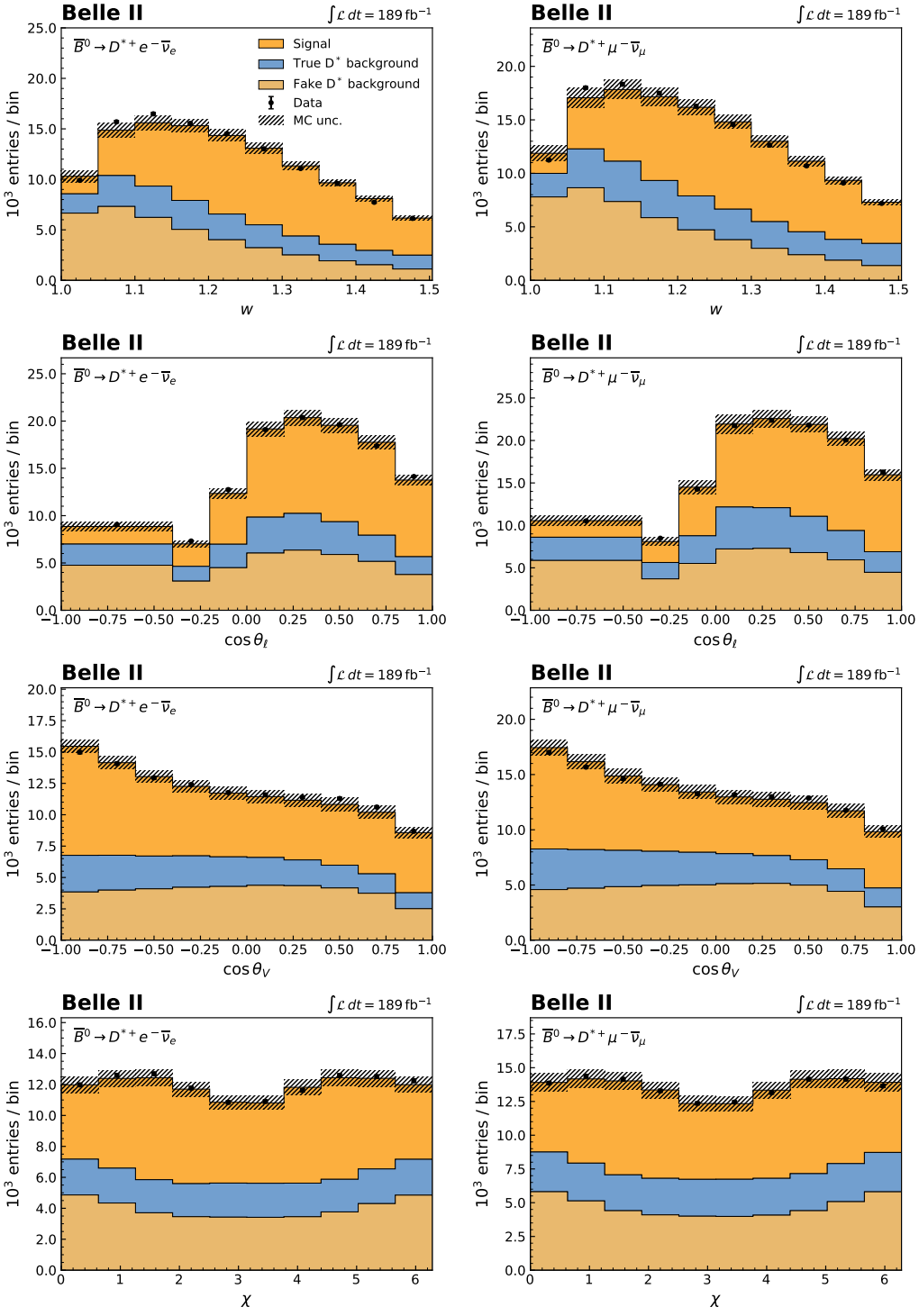

Figure 5.6: Distributions of observed kinematic variables for $\bar{B}^0 \to D^{*+} e^- \bar{\nu}_e$ (left) and $\bar{B}^0 \to D^{*+} \mu^- \bar{\nu}_\mu$ (right) candidates reconstructed in data with expected distributions from simulation overlaid. In all panels, simulated samples are shown separately for signal, true D^* background, and fake D^* background and weighted according to luminosities. The hatched area represents uncertainties due to the finite size of the simulated samples, lepton identification, slow pion reconstruction, and tracking efficiency of K, π, and ℓ.

CHAPTER 6

Measurement of partial decay rates

Presently, obtaining a measurement of the four-dimensional differential decay rate, as expressed in Eq. (2.31), is challenging. Consequently, we perform measurements of the differential decay rate in one dimension, integrated across different regions

$$\int_{X_{\min}}^{X_{\max}} \frac{d\Gamma}{dX} \quad \propto |V_{cb}|^2 \times \left|F(w, \cos\theta_\ell, \cos\theta_V, \chi)\right|^2 , \tag{6.1}$$

where $X = w,\ \cos\theta_\ell,\ \cos\theta_V,$ and χ. For $X_{\max}$ and $X_{\min}$, we use the binning outlined in Table 5.3.

The prediction of these partial decay rates depends on $|V_{cb}|$ and form factor parameters. In Chapter 8, We will establish a χ^2 fit to determine their values that best describe the observed partial decay rates.

6.1 Signal extraction

To experimentally measure the partial decay rates, we firstly need to determine the signal yield within each bin. This is achieved through two-dimensional binned maximum likelihood fits to $\cos\theta_{BY}$ and ΔM distributions.

As depicted in Fig. 6.1, most signal events are confined within the range $\cos\theta_{BY} \in [-1, 1]$, although some extend beyond this range due to the detector resolution and photon radiation (final state radiation or Bremsstrahlung), which affect the determination of the momentum and energy of the $D^*\ell$ system. The background component, which contains correctly reconstructed D^* candidates, is well-constrained in the ΔM variable but spans the entire $\cos\theta_{BY}$ space. In the case of fake D^* candidates, their momenta can be wrongly estimated due to the mis-reconstruction or wrong assignment. As a result, we observe them across the full ranges of the $\cos\theta_{BY}$ and ΔM variables, and no peak in the ΔM distribution.

The difference in density within the two-dimensional distributions serve as a prerequisite for the likelihood fits that we will introduce later. They lead to varying probabilities of finding events from different components, making them distinguishable. The ΔM variable effectively separates the fake D^* events from signals and backgrounds with correctly reconstructed D^* mesons, which

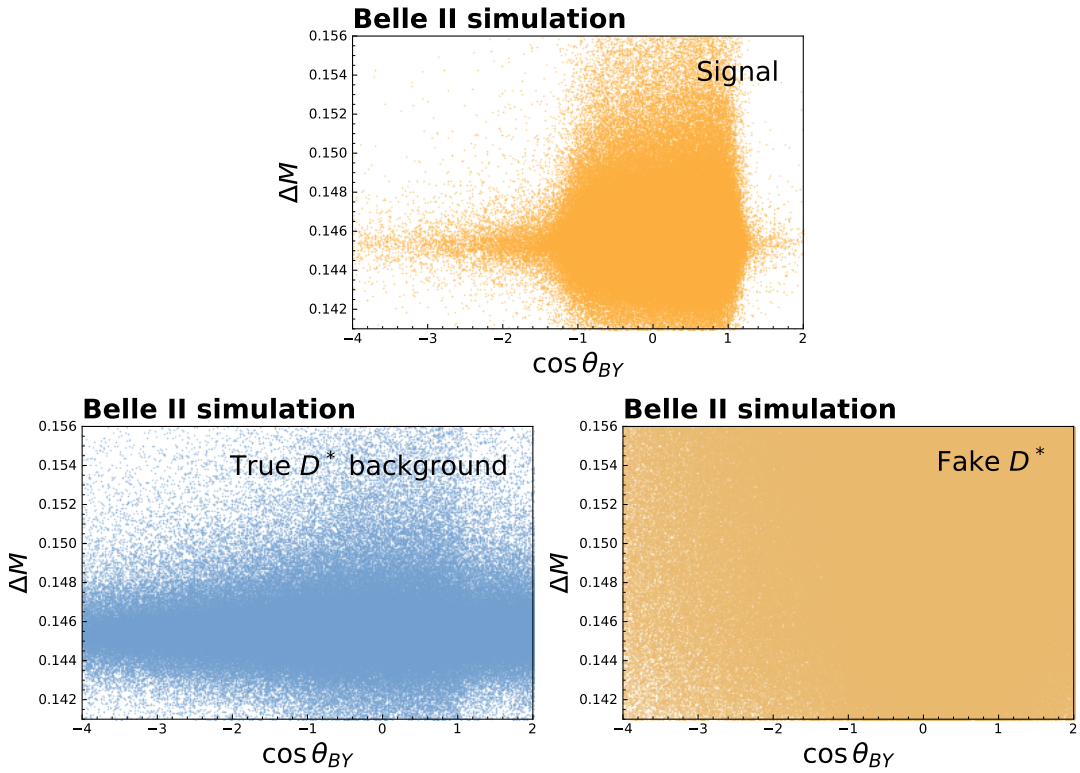

Figure 6.1: Scatter plots illustrate the signal (top), true D^* background (bottom left), and fake D^* background (bottom right) components on the coordinate plane defined by the $\cos\theta_{BY}$ and ΔM variables. Each point represents a reconstructed candidate.

peak near $\Delta M = 0.145$ GeV/c^2. Additionally, the $\cos\theta_{BY}$ variable distinguishes signal events from the true D^* backgrounds.

For each fit, we adopt the following bin granularity, consisting of a total of 16 bins across two dimensions:

- Four bins in $\cos\theta_{BY}$ spanning $[-4.0, -2.5, -1.0, 1.0, 2.0]$.
- Four equidistant ΔM bins spanning 0.141 GeV/c^2 to 0.156 GeV/c^2.

This coarse binning strategy mitigates the sensitivity to the exact modeling of the simulated detector response and resolution.

The histogram fits rely on simulated samples, where the expected number of events in bin i of $\cos\theta_{BY}$ and ΔM is represented as

$$\nu_i^{\text{exp}}(\nu_k, \boldsymbol{\theta}) = \sum_k \nu_k \, f_{ik}^{\text{MC}}(\boldsymbol{\theta}) \,, \tag{6.2}$$

where ν_k represents the yield for the event category k that we aim to determine. These event categories include the signal, true D^* background, and fake D^* background. Additionally, f_{ik}^{MC}

indicates the fraction of k-type events in bin i, and is expressed as

$$f_{ik}^{\mathrm{MC}}(\boldsymbol{\theta}) = \frac{p_{ik}^{\mathrm{MC}}(1+\epsilon_{ik}\theta_{ik})}{\sum_j p_{jk}^{\mathrm{MC}}(1+\epsilon_{jk}\theta_{jk})}\,. \tag{6.3}$$

Here, p_{ik}^{MC} is the probability of finding an event of category k in bin i, and it is determined based on simulations. The shapes of templates can vary based on the nuisance parameter θ_{ik} and the 1σ deviation ϵ_{ik}, whose magnitude is dominated by the uncertainty due to the limited size of the simulated samples.

It is important to note that the uncertainties arising from lepton ID efficiency and tracking efficiencies for final state particles, including leptons, slow pions, and other hadrons, are nearly fully correlated across all bins. Therefore, they tend to have a negligible impact on the template's shape.

The free parameters of the fit are the yields for three distinct categories (signal, true D^* background, and fake D^* background), and the bin-wise nuisance parameters θ_{ik} associated with each template.

The likelihood function for a specific bin of the recoil parameter or decay angle is expressed as follows,

$$-2\ln\mathcal{L}(\boldsymbol{\nu},\boldsymbol{\theta}) = -2\ln\prod_i \mathcal{P}(n_i^{\mathrm{reco.}},\,\nu_i^{\mathrm{exp}}) + \boldsymbol{\theta}^T C_\theta^{-1}\boldsymbol{\theta}, \tag{6.4}$$

where $n_i^{\mathrm{reco.}}$ represents the number of reconstructed events in data within a given bin i, $\boldsymbol{\nu}$ and $\boldsymbol{\theta}$ are the yields for three categories and nuisance parameters in the vector format, respectively, and $\mathcal{P}$ denotes the Poisson distribution. In addition, C_θ is the correlation matrix of the systematic nuisance parameters. The fit procedure is implemented with the `Binfit` package [87], which numerically minimizes the likelihood function using the `iminuit` package [88, 89].

Before conducting the fit on experimental data, we generate toy samples to perform a check for potential biases and to validate the accuracy of uncertainty estimates. More extensive information can be found in Appendix D. We observe no bias in the signal extraction and uncertainty estimation.

The signal yields obtained in bins of kinematic variables w, $\cos\theta_\ell$, $\cos\theta_V$, and χ, along with their associated statistical uncertainties, are summarized in Table 6.1. Post-fit comparisons between the collision data and simulated samples can be found in Appendix E.

Table 6.1: Observed signal yields with their associated statistical uncertainties in bins of kinematic variables.

Variables	Bin	$\bar{B}^0 \to D^{*+} e^- \bar{\nu}_e$	$\bar{B}^0 \to D^{*+} \mu^- \bar{\nu}_\mu$
w	[1.00, 1.05)	2 004 ± 84	2 055 ± 85
	[1.05, 1.10)	4 519 ± 120	4 927 ± 122
	[1.10, 1.15)	6 252 ± 126	6 807 ± 126
	[1.15, 1.20)	7 433 ± 127	7 806 ± 129
	[1.20, 1.25)	7 636 ± 125	8 180 ± 128
	[1.25, 1.30)	7 326 ± 121	7 686 ± 123
	[1.30, 1.35)	6 531 ± 112	7 016 ± 118
	[1.35, 1.40)	5 615 ± 106	6 091 ± 110
	[1.40, 1.45)	4 699 ± 100	4 924 ± 109
	[1.45, 1.51)	3 352 ± 99	3 626 ± 110
$\cos\theta_\ell$	[−1.00, −0.40)	1 811 ± 82	1 990 ± 87
	[−0.40, −0.20)	2 136 ± 81	2 368 ± 85
	[−0.20, 0.00)	5 085 ± 120	5 214 ± 127
	[0.00, 0.20)	8 901 ± 154	9 679 ± 159
	[0.20, 0.40)	10 163 ± 145	10 056 ± 146
	[0.40, 0.60)	10 020 ± 140	10 728 ± 141
	[0.60, 0.80)	9 286 ± 132	10 312 ± 139
	[0.80, 1.00)	8 018 ± 121	8 872 ± 129
$\cos\theta_V$	[−1.00, −0.80)	7 930 ± 126	8 802 ± 131
	[−0.80, −0.60)	6 963 ± 122	7 217 ± 126
	[−0.60, −0.40)	6 209 ± 117	6 481 ± 121
	[−0.40, −0.20)	5 297 ± 113	5 762 ± 117
	[−0.20, 0.00)	5 025 ± 112	5 321 ± 114
	[0.00, 0.20)	4 887 ± 110	5 194 ± 112
	[0.20, 0.40)	4 720 ± 108	5 235 ± 110
	[0.40, 0.60)	4 921 ± 106	5 234 ± 109
	[0.60, 0.80)	4 800 ± 103	4 935 ± 107
	[0.80, 1.00)	4 650 ± 98	5 038 ± 104
χ	[0.00, 0.63)	4 660 ± 107	4 992 ± 112
	[0.63, 1.26)	5 458 ± 115	6 033 ± 117
	[1.26, 1.88)	6 542 ± 117	6 741 ± 119
	[1.88, 2.51)	5 885 ± 114	6 358 ± 118
	[2.51, 3.14)	5 063 ± 107	5 362 ± 113
	[3.14, 3.77)	5 222 ± 109	5 516 ± 112
	[3.77, 4.40)	5 815 ± 112	6 188 ± 116
	[4.40, 5.03)	6 361 ± 117	6 930 ± 120
	[5.03, 5.65)	5 653 ± 112	6 240 ± 116
	[5.65, 6.28)	4 726 ± 106	4 831 ± 110

6.2 Unfolding

Due to the detector resolution, as well as limitations in detector acceptance and other contributing factors, the measured kinematic values in each event exhibit deviations from their true values. Consequently, the resulting distributions are subject to smearing and distortions. The signal yields, as summarized in Table 6.1, are determined based on the reconstructed observables. To estimate the underlying true spectra, we rely on simulated samples to establish the connection between observed distributions and their non-distorted counterparts. This restorative process is commonly referred to as "unfolding".

Various unfolding methods exist, including bin-by-bin unfolding [90], iterative Bayesian approaches [91, 92], and other techniques. In this study, we compare two widely-used methods: matrix inversion and singular value decomposition (SVD) [93]. Both approaches aim to correct the measurements using migration matrices, which were discussed in detail in Sec. 5.4.

In the matrix inversion method, it is important to note that the reconstructed values exhibit a linear relationship with the underlying true values, as expressed by the equation,

$$x^{\text{reco.}} = \mathcal{M} y^{\text{true}}, \tag{6.5}$$

where $\mathcal{M}$ is the migration matrix, and $x^{\text{reco.}}$ and y^{true} represent reconstructed spectra and underlying true spectra, respectively. Consequently, we can straightforwardly obtain the true distribution by simply inverting the migration matrix

$$y^{\text{true}} = \mathcal{M}^{-1} x^{\text{reco.}}. \tag{6.6}$$

The SVD unfolding introduces a regularization parameter, denoted as k, to mitigate statistical fluctuations. It is important to fine-tune this parameter appropriately, considering the specific number of bins and the size of the sample through the use of MC samples: If k is set too small, the unfolded results become overly reliant on the input MC shape. Conversely, an excessively large k introduces heightened statistical fluctuations, resulting in larger uncertainties and (anti-)correlations between adjacent bins. The optimization of the parameter k will be discussed in detail in Section 6.2.1. For unfolding processes, we employ the `PyRooUnfold` package [94], which serves as a Python wrapper for `RooUnfold` [95, 96]. This toolkit also facilitates bias tests and toy studies, as we will detail later.

The signal yields from each projection will undergo separate unfolding procedures. In these procedures, we use a diagonal covariance matrix for error propagation, implying that statistical and systematic uncertainties on the signal yields are uncorrelated. This choice is supported by the following reasons. First, in terms of statistical uncertainties, the signal extraction is performed bin-by-bin independently, and there is no statistical overlap between bins within a given kinematic variable. Second, systematic uncertainties arise from variations in the template shapes due to finite statistics. These uncertainties are also uncorrelated across different bins.

6.2.1 Optimization of parameter k in SVD

The simulation of the signal decay relies on a model with form factor parameters obtained in previous measurements. However, the precision of these parameter values might be limited or biased, leading to discrepancies between the simulation and the actual physics process. These discrepancies can introduce biases in the unfolding procedure as the determination of migration matrices relies on the simulated signal decay.

To investigate potential biases, a benchmark test is conducted using reweighted signal decay simulations. We utilize the form factor values and uncertainties from Ref. [97]. In this analysis, we intentionally inflate the uncertainties of the form factor parameters by a factor of 10 to assess bias under an extreme scenario. We calculate the eigenvalues λ_i and eigenvectors $\vec{e}_i$ of the covariance matrix and determine the eigen-variations of the form factor parameters as follows,

$$\vec{x}^{\pm}_{\mathrm{var},i} = \vec{x} \pm \sqrt{\lambda_i}\vec{e}_i, \tag{6.7}$$

where $\vec{x}$ represents the central values of the form factor parameters as obtained in Ref. [97].

Using these orthogonal variations, we reweight the simulated signal decay along one of eigen-directions. Candidate-wise weights are computed based on the kinematic variables at the generator level, as expressed in the equation,

$$w_{\mathrm{FF}}(w, \cos\theta_\ell, \cos\theta_V, \chi) = \frac{\Gamma^{\mathrm{cen}}}{\Gamma_i^{\pm}} \times \frac{\dfrac{\mathrm{d}^4\Gamma_i^{\pm}}{\mathrm{d}w\,\mathrm{d}\cos\theta_\ell\,\mathrm{d}\cos\theta_V\,\mathrm{d}\chi}}{\dfrac{\mathrm{d}^4\Gamma^{\mathrm{cen}}}{\mathrm{d}w\,\mathrm{d}\cos\theta_\ell\,\mathrm{d}\cos\theta_V\,\mathrm{d}\chi}}, \tag{6.8}$$

where Γ^{cen} represents the integrated decay rate with the central values of form factor parameters, and $\Gamma_i^{\pm}$ represents the integrated decay rate with the orthogonal variations of the form factor parameters. The ratio between two integrated decay rates ensures that the total rate remains the same after reweighting. In the second fraction, the numerator and denominator correspond to the differential decay rates calculated with the central values of form factor parameters and their orthogonal variations, respectively. This reweighting procedure is implemented using the `eFFORT` package [98].

We generate ten thousand toy spectra using Gaussian distributions, where the mean corresponds to the number of events in each bin after reweighting, and the standard deviation corresponds to the input uncertainty for unfolding. Subsequently, we perform the unfolding process on these toy samples using the SVD method with various values of the regularization parameter k, and the matrix inversion method. In this step, we use the nominal migration matrix, which remains unchanged across all toy spectra. We calculate the mean and root-mean-square deviation of the post-unfolding results and compare them, as illustrated in Fig. 6.2.

Our observations reveal significant deviations from the true spectrum when using a small k value, such as $k = 2$ or 3. In these cases, the non-closures cannot be adequately accounted for by the uncertainties. This behavior can be attributed to the strong dependence on the simulated spectrum. As we progressively decrease the level of regularization applied in the SVD method, the observed bias reduces. Furthermore, the unfolded distributions approach closer to the unfolded

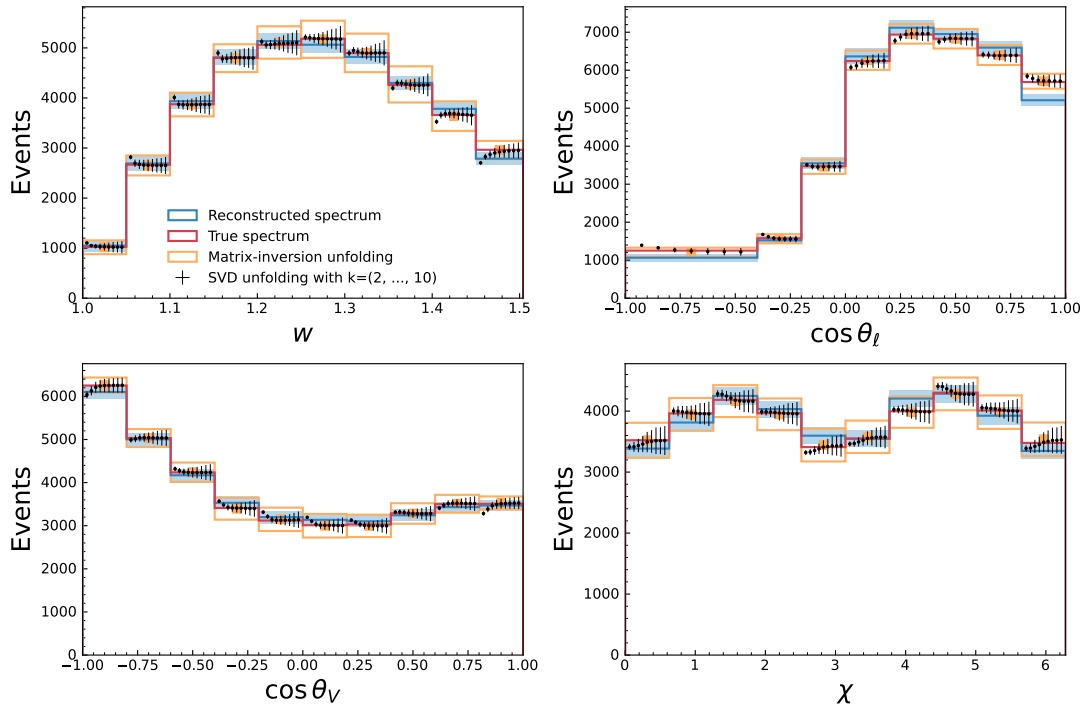

Figure 6.2: Comparison of SVD unfolding with various k values and matrix inversion methods. The data points represent the means of unfolded toy spectra, and the lengths of the error bars correspond to the root-mean-square deviations. The data points in a bin, from left to right, correspond to increasing values of k. The post-unfolding uncertainties with the matrix inversion method are depicted as orange boxes.

spectra derived from the matrix inversion method.

An optimal unfolding method must result in minimal biases and not overestimated uncertainties. To determine which unfolding method is ideal, we evaluate various figure-of-merits listed in Table 6.2. We perform unfolding on reweighted signal distributions using the nominal migration matrices and assess both biases and the resulting post-unfolding covariance matrices. The results for w, $\cos\theta_\ell$, $\cos\theta_V$, and χ are presented in Table 6.3 to Table 6.6, respectively.

In comparison to the matrix inversion method, the SVD method leads to larger total biases when k values are less than 5, with the largest biases consistently observed when using $k = 2$. However, as the regularization is reduced, the total biases can decrease to values smaller than those obtained with the matrix inversion method. Simultaneously, the sum of elements in the post-unfolding covariance matrix increases with respect to the increasing k value.

We opt for the SVD method with k values of 7, 6, 6, and 7 for w, $\cos\theta_\ell$, $\cos\theta_V$, and χ, respectively. These choices ensure that the total bias remains smaller than the one obtained through the inversion of the migration matrices. Furthermore, with these selected k values, the ratios of bias to unfolding uncertainty are relatively low and stable.

We conduct a validation of the unfolding procedure on toy samples for both the matrix inversion method and SVD method with the chosen regularization parameters. Further details can be found

Table 6.2: Summary of the metrics used to evaluate unfolding algorithms and parameters.

Figure of merit	Description
$\sum_i \lvert b_i \rvert$	The sum of absolute biases, with $b_i = N_i^{\text{unfoled}} - N_i^{\text{true}}$ (i is the bin index).
$\sqrt{\sum_{i,j} Cov_{i,j}}$	The square root of the sum of all covariances.
$\frac{\sum_i \lvert b_i \rvert}{\sqrt{\sum_{i,j} Cov_{i,j}}}$	The ratio between the sum of absolute biases and the sum of covariances. This is used to assess whether the total bias resulting from the unfolding can be accommodated by the uncertainties across the entire distribution.
$\sum_i \frac{\lvert b_i \rvert}{\sqrt{Cov_{i,i}}}$	The sum of ratios between bin-wise absolute biases and post-unfolding uncertainties.

Table 6.3: Resulting metrics values for the unfolded w spectrum using the matrix inversion method, and the SVD method with various k parameters.

	$\sum_i \lvert b_i \rvert$	$\sqrt{\sum_{i,j} Cov_{i,j}}$	$\frac{\sum_i \lvert b_i \rvert}{\sqrt{\sum_{i,j} Cov_{i,j}}}$	$\sum_i \frac{\lvert b_i \rvert}{\sqrt{Cov_{i,i}}}$
Matrix inversion	132	913	0.1	0.5
SVD ($k = 2$)	1015	162	6.3	24.3
SVD ($k = 3$)	340	216	1.6	5.6
SVD ($k = 4$)	234	263	0.9	3.0
SVD ($k = 5$)	164	315	0.5	1.7
SVD ($k = 6$)	131	373	0.3	1.1
SVD ($k = 7$)	116	442	0.3	0.9
SVD ($k = 8$)	103	516	0.2	0.7
SVD ($k = 9$)	97	555	0.2	0.6
SVD ($k = 10$)	104	671	0.2	0.5

in Appendix F.

Table 6.4: Resulting metrics values for the unfolded $\cos\theta_\ell$ spectrum using the matrix inversion method, and the SVD method with various k parameters.

	$\sum_i \lvert b_i \rvert$	$\sqrt{\sum_{i,j} Cov_{i,j}}$	$\frac{\sum_i \lvert b_i \rvert}{\sqrt{\sum_{i,j} Cov_{i,j}}}$	$\sum_i \frac{\lvert b_i \rvert}{\sqrt{Cov_{i,i}}}$
Matrix inversion	141	606	0.2	0.8
SVD ($k = 2$)	864	184	4.7	17.5
SVD ($k = 3$)	433	241	1.8	5.6
SVD ($k = 4$)	168	294	0.6	1.6
SVD ($k = 5$)	136	352	0.4	1.2
SVD ($k = 6$)	121	410	0.3	1.0
SVD ($k = 7$)	118	448	0.3	1.0
SVD ($k = 8$)	123	488	0.3	0.9

Table 6.5: Resulting metrics values for the unfolded $\cos\theta_V$ spectrum using the matrix inversion method, and the SVD method with various k parameters.

	$\sum_i \lvert b_i \rvert$	$\sqrt{\sum_{i,j} Cov_{i,j}}$	$\frac{\sum_i \lvert b_i \rvert}{\sqrt{\sum_{i,j} Cov_{i,j}}}$	$\sum_i \frac{\lvert b_i \rvert}{\sqrt{Cov_{i,i}}}$
Matrix inversion	142	725	0.2	0.6
SVD ($k = 2$)	1318	159	8.3	28.8
SVD ($k = 3$)	662	213	3.1	10.6
SVD ($k = 4$)	204	257	0.8	2.5
SVD ($k = 5$)	106	301	0.4	1.2
SVD ($k = 6$)	87	351	0.2	0.9
SVD ($k = 7$)	101	399	0.3	0.9
SVD ($k = 8$)	109	452	0.2	0.8
SVD ($k = 9$)	116	511	0.2	0.7
SVD ($k = 10$)	121	568	0.2	0.7

Table 6.6: Resulting metrics values for the unfolded χ spectrum using the matrix inversion method, and the SVD method with various k parameters.

	$\sum_i \lvert b_i \rvert$	$\sqrt{\sum_{i,j} Cov_{i,j}}$	$\frac{\sum_i \lvert b_i \rvert}{\sqrt{\sum_{i,j} Cov_{i,j}}}$	$\sum_i \frac{\lvert b_i \rvert}{\sqrt{Cov_{i,i}}}$
Matrix inversion	240	850	0.3	0.9
SVD ($k = 2$)	719	162	4.4	14.5
SVD ($k = 3$)	678	227	3.0	9.9
SVD ($k = 4$)	485	285	1.7	5.5
SVD ($k = 5$)	280	332	0.8	2.7
SVD ($k = 6$)	90	416	0.2	0.6
SVD ($k = 7$)	116	467	0.2	0.8
SVD ($k = 8$)	161	567	0.3	0.9
SVD ($k = 9$)	166	580	0.3	0.9
SVD ($k = 10$)	191	641	0.3	0.9

6.3 Determination of partial decay rates

The partial decay rate in bin x is determined based on the unfolded yield ν_x^{unfolded} using the equation,

$$\Delta\Gamma_x = \frac{\nu_x^{\text{unfolded}}}{\epsilon_x \tau_{B^0} N_{B^0} \mathcal{B}(D^{*+} \to D^0\pi^+)\mathcal{B}(D^0 \to K^-\pi^+)}, \tag{6.9}$$

with $\tau_{B^0} = 1.519 \pm 0.004$ ps [1] denoting the B^0 meson lifetime, and N_{B^0} denoting the number of B^0 mesons in the analyzed data set, which will be further discussed in Sec. 7.6. The branching fractions $\mathcal{B}(D^{*+} \to D^0\pi^+)$ and $\mathcal{B}(D^0 \to K^-\pi^+)$ will be discussed in Sec. 7.7. Additionally, ϵ_x represents the reconstruction efficiency in bin x. These efficiencies are studied using simulated signal events and are calculated as the ratios between the numbers of reconstructed events in bin x that meet the selection criteria and the generated events that fall into bin x. The resulting values are summarized in Table 6.7 and Table 6.8 for $\bar{B}^0 \to D^{*+}e^-\bar{\nu}_e$ and $\bar{B}^0 \to D^{*+}\mu^-\bar{\nu}_\mu$ decays, respectively.

Table 6.7: Reconstruction efficiencies, along with their statistical uncertainties (expressed in %) for the $\bar{B}^0 \to D^{*+}e^-\bar{\nu}_e$ decay within each bin of kinematic variables.

	w	$\cos\theta_\ell$	$\cos\theta_V$	χ
1st bin	12.1 ± 0.1	4.32 ± 0.04	23.8 ± 0.1	22.3 ± 0.1
2nd bin	18.4 ± 0.1	9.5 ± 0.1	25.0 ± 0.1	21.7 ± 0.1
3rd bin	21.7 ± 0.1	18.2 ± 0.1	26.1 ± 0.1	21.5 ± 0.1
4th bin	24.1 ± 0.1	29.4 ± 0.1	26.7 ± 0.2	21.8 ± 0.1
5th bin	25.1 ± 0.1	31.0 ± 0.1	27.1 ± 0.2	22.4 ± 0.1
6th bin	25.1 ± 0.1	30.8 ± 0.1	25.7 ± 0.2	22.5 ± 0.1
7th bin	24.4 ± 0.1	30.0 ± 0.1	23.1 ± 0.1	22.0 ± 0.1
8th bin	22.9 ± 0.1	29.4 ± 0.1	20.0 ± 0.1	21.5 ± 0.1
9th bin	20.9 ± 0.1		16.6 ± 0.1	21.9 ± 0.1
10th bin	17.6 ± 0.1		13.0 ± 0.1	22.4 ± 0.1

Inserting all numerical values and obtaining the corresponding partial decay rates is a straightforward process. The results, along with their uncertainties, are summarized in Table 6.9.

Table 6.8: Reconstruction efficiencies, along with their statistical uncertainties (expressed in %) for the $\bar{B}^0 \to D^{*+}\mu^-\bar{\nu}_\mu$ decay within each bin of kinematic variables.

	w	$\cos\theta_\ell$	$\cos\theta_V$	χ
1st bin	35.2 ± 0.1	4.01 ± 0.04	25.4 ± 0.1	22.9 ± 0.1
2nd bin	24.7 ± 0.1	9.7 ± 0.1	26.7 ± 0.1	22.9 ± 0.1
3rd bin	22.9 ± 0.1	19.6 ± 0.1	27.8 ± 0.1	23.1 ± 0.1
4th bin	19.5 ± 0.1	31.2 ± 0.1	29.1 ± 0.2	24.0 ± 0.1
5th bin	16.2 ± 0.1	32.3 ± 0.1	28.9 ± 0.2	24.7 ± 0.1
6th bin	16.5 ± 0.1	32.9 ± 0.1	27.3 ± 0.2	24.8 ± 0.1
7th bin	20.8 ± 0.1	33.2 ± 0.1	24.6 ± 0.2	23.7 ± 0.1
8th bin	24.6 ± 0.1	32.6 ± 0.1	21.5 ± 0.1	23.2 ± 0.1
9th bin	25.3 ± 0.1		17.8 ± 0.1	23.1 ± 0.1
10th bin	23.3 ± 0.1		13.8 ± 0.1	22.7 ± 0.1

Table 6.9: Measured partial decay rates $\Delta\Gamma$ (in units of 10^{-15} GeV) and average of normalized partial decay rates $\Delta\Gamma/\Gamma$ over $\bar{B}^0 \to D^{*+} e^- \bar{\nu}_e$ and $\bar{B}^0 \to D^{*+} \mu^- \bar{\nu}_\mu$ decays in bins of kinematic variables. The normalized partial decay rate in the last bin of each projection is excluded in the $|V_{cb}|$ determination to subtract the redundant degrees of freedom. The full (statistical and systematic) uncertainties are provided.

Variable	Bin	$\Delta\Gamma$		$\Delta\Gamma/\Gamma$ average (in %)
		$\bar{B}^0 \to D^{*+} e^- \bar{\nu}_e$	$\bar{B}^0 \to D^{*+} \mu^- \bar{\nu}_\mu$	$\bar{B}^0 \to D^{*+} \ell^- \bar{\nu}_\ell$
w	[1.00, 1.05)	1.34 ± 0.10	1.30 ± 0.09	6.19 ± 0.21
	[1.05, 1.10)	2.08 ± 0.12	2.11 ± 0.12	9.86 ± 0.22
	[1.10, 1.15)	2.40 ± 0.13	2.45 ± 0.13	11.39 ± 0.20
	[1.15, 1.20)	2.61 ± 0.14	2.60 ± 0.14	12.18 ± 0.19
	[1.20, 1.25)	2.60 ± 0.13	2.60 ± 0.13	12.16 ± 0.17
	[1.25, 1.30)	2.49 ± 0.12	2.43 ± 0.12	11.50 ± 0.17
	[1.30, 1.35)	2.30 ± 0.11	2.29 ± 0.11	10.72 ± 0.17
	[1.35, 1.40)	2.07 ± 0.10	2.07 ± 0.10	9.67 ± 0.18
	[1.40, 1.45)	1.83 ± 0.09	1.80 ± 0.09	8.47 ± 0.17
	[1.45, 1.51)	1.67 ± 0.09	1.70 ± 0.10	
$\cos\theta_\ell$	[−1.00, −0.40)	3.89 ± 0.33	4.10 ± 0.39	18.94 ± 0.79
	[−0.40, −0.20)	2.00 ± 0.14	2.07 ± 0.16	9.60 ± 0.27
	[−0.20, 0.00)	2.28 ± 0.12	2.26 ± 0.14	10.63 ± 0.19
	[0.00, 0.20)	2.51 ± 0.12	2.56 ± 0.14	11.86 ± 0.24
	[0.20, 0.40)	2.73 ± 0.13	2.63 ± 0.13	12.54 ± 0.25
	[0.40, 0.60)	2.70 ± 0.13	2.70 ± 0.13	12.68 ± 0.24
	[0.60, 0.80)	2.54 ± 0.12	2.57 ± 0.12	12.01 ± 0.24
	[0.80, 1.00)	2.52 ± 0.12	2.49 ± 0.12	
$\cos\theta_V$	[−1.00, −0.80)	2.89 ± 0.13	3.02 ± 0.14	13.86 ± 0.27
	[−0.80, −0.60)	2.38 ± 0.10	2.32 ± 0.11	11.00 ± 0.18
	[−0.60, −0.40)	1.98 ± 0.09	1.93 ± 0.09	9.14 ± 0.13
	[−0.40, −0.20)	1.67 ± 0.08	1.65 ± 0.08	7.75 ± 0.11
	[−0.20, 0.00)	1.54 ± 0.08	1.53 ± 0.08	7.18 ± 0.10
	[0.00, 0.20)	1.56 ± 0.08	1.58 ± 0.09	7.37 ± 0.11
	[0.20, 0.40)	1.73 ± 0.09	1.77 ± 0.10	8.20 ± 0.12
	[0.40, 0.60)	2.05 ± 0.11	2.04 ± 0.11	9.59 ± 0.14
	[0.60, 0.80)	2.48 ± 0.13	2.42 ± 0.14	11.48 ± 0.17
	[0.80, 1.00)	3.07 ± 0.17	3.09 ± 0.18	
χ	[0.00, 0.63)	1.82 ± 0.11	1.85 ± 0.11	8.59 ± 0.21
	[0.63, 1.26)	2.20 ± 0.11	2.24 ± 0.12	10.42 ± 0.16
	[1.26, 1.88)	2.55 ± 0.13	2.50 ± 0.13	11.82 ± 0.18
	[1.88, 2.51)	2.24 ± 0.11	2.24 ± 0.11	10.51 ± 0.16
	[2.51, 3.14)	1.85 ± 0.09	1.83 ± 0.10	8.62 ± 0.15
	[3.14, 3.77)	1.89 ± 0.10	1.85 ± 0.10	8.75 ± 0.14
	[3.77, 4.40)	2.19 ± 0.11	2.21 ± 0.11	10.31 ± 0.16
	[4.40, 5.03)	2.47 ± 0.12	2.56 ± 0.13	11.82 ± 0.17
	[5.03, 5.65)	2.24 ± 0.11	2.30 ± 0.12	10.67 ± 0.15
	[5.65, 6.28)	1.88 ± 0.11	1.75 ± 0.10	

6.4 Statistical correlations

Statistical correlations between bins within the same kinematic variable are derived from the post-unfolding covariance matrix. To fit all four spectra simultaneously, we also require statistical correlations between bins of different variables. These cross-variable correlations are assessed using a bootstrapping approach.

Ten thousand replicas are generated by resampling collision data with replacement. In each replica, the total number of events is allowed to fluctuate according to the statistical uncertainty of the entire data set. For each replica, the signal extraction and unfolding are repeated using the nominal templates (with the nuisance parameters fixed at their values from the nominal fits) and nominal migration matrices.

Pearson correlation coefficients are derived from the unfolded yields of the replicas. The resulting statistical correlations among the partial decay rates are shown in Fig. 6.3 and Fig. 6.4 for $\bar{B}^0 \to D^{*+} e^- \bar{\nu}_e$ and $\bar{B}^0 \to D^{*+} \mu^- \bar{\nu}_\mu$ decays, respectively.

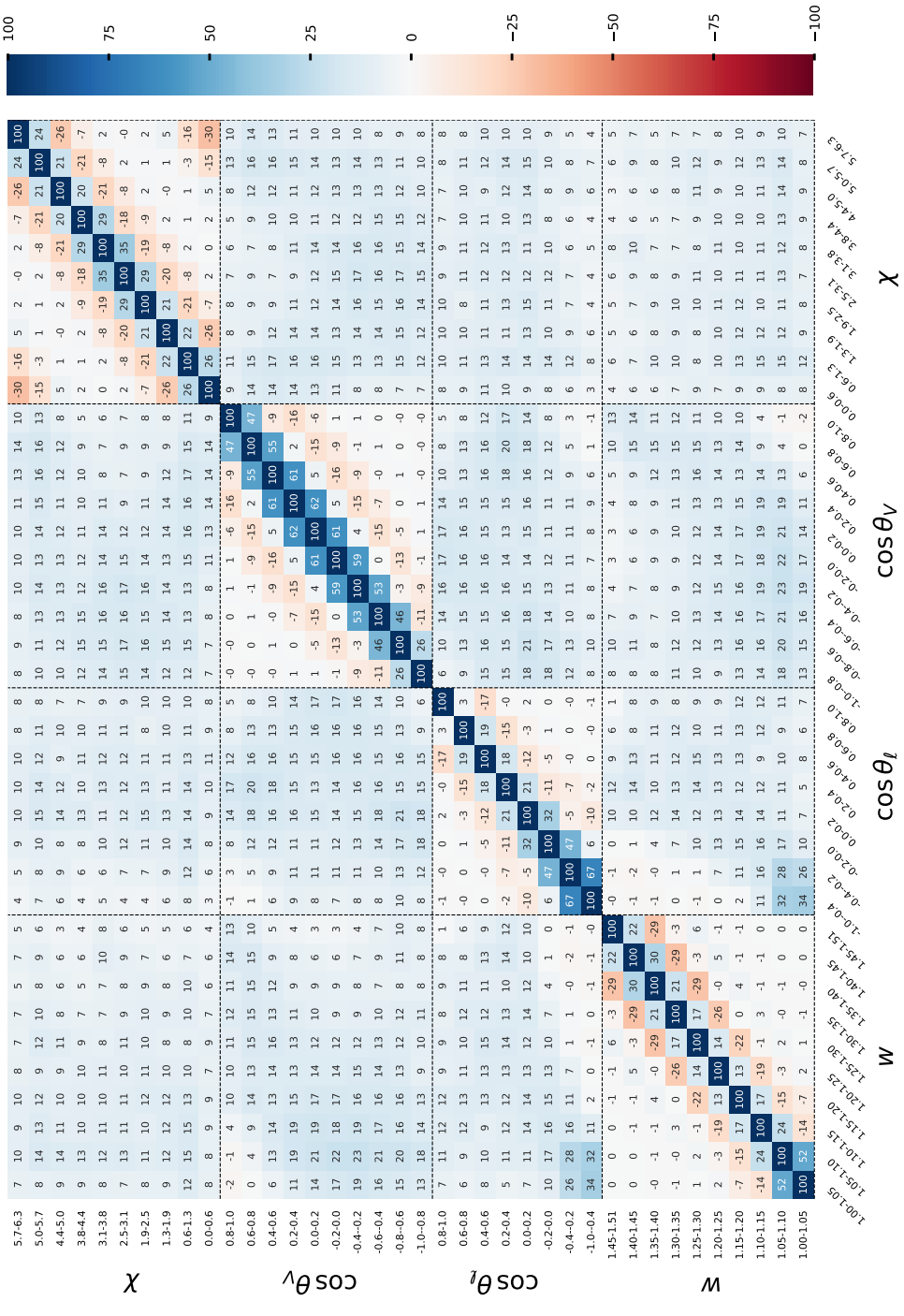

Figure 6.3: Statistical correlations (in %) of the partial decay rates for the $\bar{B}^0 \to D^{**+} e^- \bar{\nu}_e$ decay.

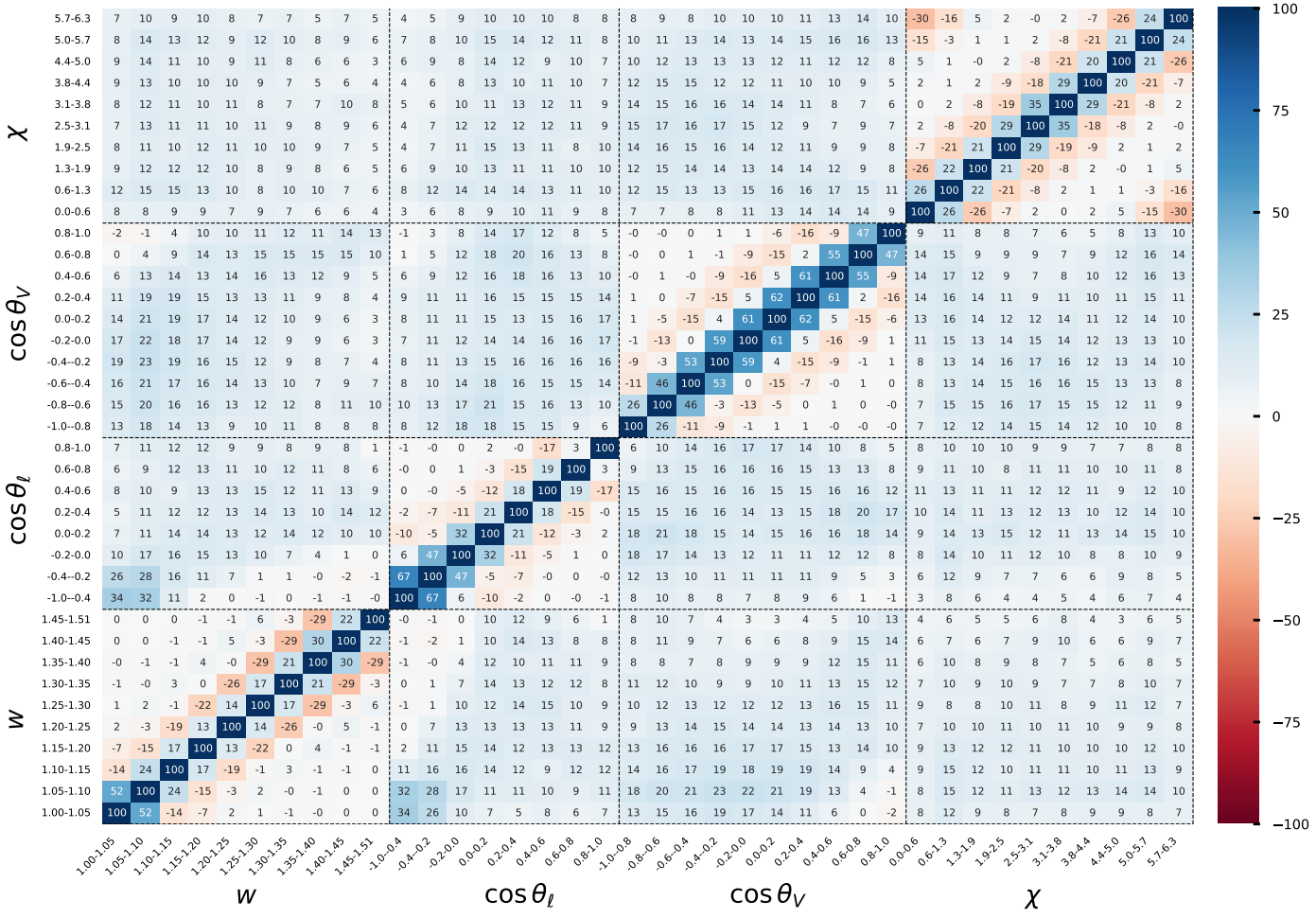

Figure 6.4: Statistical correlations (in %) of the partial decay rates for the $\bar{B}^0 \to D^{*+}\mu^-\bar{\nu}_\mu$ decay.

CHAPTER 7

Systematic uncertainties

7.1 Background subtraction

As outlined in Sec. 4.3.3, a background shape correction is introduced due to the discrepancies between simulated samples and collision data, observed in the region where $\cos\theta_{BY} > 2$, which is populated by background events. To account for this effect in a conservative manner, we introduce an uncertainty associated with the background shape. This is achieved by extracting signal yields twice: once using templates that incorporate the background shape correction, and once without it. The signal yields obtained with the corrected templates are considered as the nominal results, and the difference between the two sets of yields is treated as the uncertainty, which is subsequently propagated to the partial decay rates.

7.2 Size of simulated samples

We propagate the statistical uncertainty resulting from the limited size of the simulated sample into various aspects, including the signal and background shapes, migration matrices, and signal efficiencies. To account for the statistical uncertainties in the signal and background shapes, we introduce nuisance parameters that allow the template shapes in $\cos\theta_{BY}$ and ΔM to vary within their respective statistical uncertainties. Note that these uncertainties arising from the finite size of the simulated samples are treated as uncorrelated before unfolding, as they are determined independently bin-by-bin.

7.3 Mid to high momentum tracking efficiency

The efficiency of track reconstruction are determined through analyses conducted by the performance group using $e^+e^- \to \tau^+\tau^-$ events. In these events, one of the τ leptons decays leptonically, $\tau^\pm \to \ell^\pm \nu_\ell \bar{\nu}_\tau$, while the other τ lepton decays hadronically, producing three charged pions, $\tau^\pm \to 3\pi^\pm(n\pi^0)\nu_\tau$. These decay modes are commonly referred to as 1-prong and 3-prong τ decays, respectively.

The momenta of τ-pairs span a wide range, from 200 MeV/c to approximately 3.5 GeV/c. To evaluate the tracking efficiency, the tag-and-probe method which was initially developed by the BaBar experiment [99] is used. In this approach, three high-quality tracks are selected, with a combined charge of ± 1, to tag the τ pair events. The presence of an additional track in the event, referred to as the probe track, can be deduced from the charge conservation principle. It can be verified whether the probe track is successfully reconstructed or not, and express the tracking efficiency ϵ_{track} as follows

$$\epsilon_{\text{track}} \cdot A = \frac{N_4}{N_4 + N_3}. \tag{7.1}$$

Here, A is the geometric acceptance of the Belle II detector, N_4 represents the number of events in which all four tracks are detected, while N_3 corresponds to the number of events where only the 3-prong decay is found, without any 1-prong decay.

A calibration study has been conducted on the simulated samples to establish a relationship between the measured inefficiency Δ^{meas} and the underlying true inefficiency Δ^*. Initially, known per-track inefficiencies are introduced into the signal MC, specifically, $\Delta^* = 0.025, 0.05, 0.075$, and 0.1. The efficiency can be estimated using the formula

$$\begin{aligned} \epsilon^{\text{meas}} &= \frac{N_4}{N_4 + N_3} \\ &= \epsilon^*(1 - \Delta^{\text{meas}}), \end{aligned} \tag{7.2}$$

where ϵ^* is the true efficiency for simulated samples. This relationship leads to the expression of Δ^{meas} in terms of ϵ^{meas} and ϵ^*,

$$\Delta^{\text{meas}} = 1 - \frac{\epsilon^{\text{meas}}}{\epsilon^*}. \tag{7.3}$$

The resulting Δ^{meas} demonstrates a linear relationship with the generated inefficiency Δ^* across the entire kinematic range under investigation. Therefore, Δ^{meas} and Δ^* are related with a scaling factor k

$$\Delta^{\text{meas}} = k \cdot \Delta^*. \tag{7.4}$$

It is noteworthy that the obtained values of k are consistent regardless of the lepton flavors and charges.

Regardless of the respective efficiencies in collision data and simulated samples, the discrepancy between them is of greater significance for physics analyses. This discrepancy is used to estimate the corresponding systematic uncertainty for physics measurements and is defined as

$$\begin{aligned} \delta &= 1 - \frac{\epsilon^{\text{Data}}_{\text{track}}}{\epsilon^{\text{MC}}_{\text{track}}} \\ &= 1 - \frac{\epsilon^{\text{Data}}_{\text{track}} \cdot A}{\epsilon^{\text{MC}}_{\text{track}} \cdot A} = 1 - \left(\frac{N_4^{\text{Data}}}{N_4^{\text{Data}} + N_3^{\text{Data}}} \right) \cdot \left(\frac{N_4^{\text{MC}} + N_3^{\text{MC}}}{N_4^{\text{MC}}} \right). \end{aligned} \tag{7.5}$$

The calibrated discrepancy is expressed as

$$\delta^* = 1 - \frac{\epsilon^*_{\text{Data}}}{\epsilon^*_{\text{MC}}} = \frac{1}{k}\left(1 - \frac{\epsilon^{\text{meas}}_{\text{Data}}}{\epsilon^{\text{meas}}_{\text{MC}}}\right). \tag{7.6}$$

A value of

$$\delta^* = \left(0.217 \pm 0.037_{\text{stat.}} \pm 0.167_{\text{syst.}}\right)\,\% \tag{7.7}$$

is found.

Based on this study, we assign a track selection uncertainty of 0.3% per track on kaon, pion, and lepton tracks. This uncertainty is fully correlated across all bins of all kinematic variables.

7.4 Slow pion tracking efficiency

The details of calibration of the slow pion tracking efficiency are provided in Appendix B. The tracking efficiency of slow pions has a dual impact, affecting both the reconstruction of signal decays and migration matrices. To study these effects, we utilize 400 candidate-wise variation weights, generated as described in Sec. 4.3.2. With each set of these weights, we update the corresponding migration matrices and reconstruction efficiencies. Subsequently, we perform an unfolding of the nominal signal yields using the modified migration matrices and calculate the partial decay rates based on the new reconstruction efficiencies. In the end, we extract Pearson correlation coefficients from the resulting 400 partial decay rates for each bin of kinematic variables. We observe strong correlations across all bins, with the smallest correlation approximately equal to 0.7.

7.5 Lepton ID efficiency and fake rate

The uncertainty associated with lepton ID is treated in a manner similar to that of the slow pion tracking efficiency, using the variation weights generated based on the lepton ID uncertainties, which is described in Sec. 4.3.1. Note that the identifications of electrons and muons are entirely uncorrelated.

7.6 Number of B^0 in the data set

The determination of the number of $B\bar{B}$ pairs was described in Sec. 3.4. The number of neutral B mesons in the data set is given by

$$N_{B^0} = 2N_{B\bar{B}}\,(1 + f_{+0})^{-1}, \tag{7.8}$$

with $f_{+0} = \mathcal{B}(\Upsilon(4S) \to B^+B^-)/\mathcal{B}(\Upsilon(4S) \to B^0\bar{B}^0) = 1.065 \pm 0.052$ [100]. The uncertainties from both $N_{B\bar{B}}$ and f_{+0} are propagated into the measured partial decay rates, and they are fully correlated across all bins.

7.7 External inputs

In Eq. (6.9), the values of $\mathcal{B}(D^{*+} \to D^0\pi^+) = (67.7 \pm 0.5)\%$, $\mathcal{B}(D^0 \to K^-\pi^+) = (3.947 \pm 0.030)\%$, and the B^0 lifetime $\tau_{B^0} = (1.519 \pm 0.004)$ ps are taken from Ref. [1]. The uncertainties from each source across bins of kinematic variables are treated as fully correlated.

7.8 Dependence of signal model

The simulation of the signal $\bar{B}^0 \to D^{*+}\ell^-\bar{\nu}_\ell$ decay is used to determine the migration matrices and efficiencies. However, this simulation relies on a specific model and its associated parameters, introducing a residual dependence on the assumed model into the results.

To assess the magnitude of this uncertainty, we utilize the form factor parameters and their corresponding 3σ uncertainties from Ref. [97]. We reweight the simulated samples using Eq. (6.8) and examine the resulting variations in partial decay rates. We find that the size of this uncertainty is generally smaller than the experimental uncertainties and, in most bins, does not exceed 1%. However, in the $\cos\theta_\ell$ bin of $[-1.0, -0.4]$, it reaches 4%, which is comparable to other uncertainties. This sizable uncertainty is primarily attributed to the low reconstruction efficiency in this region of phase space.

In Table 7.1 and Table 7.2, we summarize the fractional uncertainties from various sources, along with the statistical uncertainty in each bin of w, $\cos\theta_\ell$, $\cos\theta_V$, and χ for the $\bar{B}^0 \to D^{*+}e^-\bar{\nu}_e$ and $\bar{B}^0 \to D^{*+}\mu^-\bar{\nu}_\mu$ decays, respectively. The full (statistical + systematic) correlations of the partial decay rates for the $\bar{B}^0 \to D^{*+}e^-\bar{\nu}_e$ and $\bar{B}^0 \to D^{*+}\mu^-\bar{\nu}_\mu$ decays are provided in Fig. 7.1 and Fig. 7.2, respectively.

Table 7.1: Fractional uncertainties (in %) of the partial decay rate in each bin for the $\bar{B}^0 \to D^{*+} e^- \bar{\nu}_e$ decay.

Variable	Bin	Statistical	Simulated sample size	Signal modeling	Background substraction	Lepton ID efficiency	Slow-pion efficiency	Tracking of K, π, ℓ	$N_{B\bar{B}}$	f_{+0}	$\mathcal{B}(D^* \to D\pi)$	$\mathcal{B}(D^0 \to K\pi)$	B^0 lifetime
w	[1.00, 1.05)	3.56	1.48	0.57	2.53	0.65	4.24	0.90	1.52	2.52	0.74	0.76	0.26
	[1.05, 1.10)	2.25	0.96	0.26	1.72	0.53	3.72	0.90	1.52	2.52	0.74	0.76	0.26
	[1.10, 1.15)	1.94	0.82	0.55	1.27	0.51	3.34	0.90	1.52	2.52	0.74	0.76	0.26
	[1.15, 1.20)	1.74	0.74	0.87	1.07	0.45	3.17	0.90	1.52	2.52	0.74	0.76	0.26
	[1.20, 1.25)	1.72	0.70	0.80	0.98	0.44	2.88	0.90	1.52	2.52	0.74	0.76	0.26
	[1.25, 1.30)	1.75	0.73	0.70	0.87	0.46	2.73	0.90	1.52	2.52	0.74	0.76	0.26
	[1.30, 1.35)	1.81	0.84	0.94	0.85	0.45	2.54	0.90	1.52	2.52	0.74	0.76	0.26
	[1.35, 1.40)	1.94	0.78	1.05	0.83	0.46	2.27	0.90	1.52	2.52	0.74	0.76	0.26
	[1.40, 1.45)	2.02	0.85	0.92	0.80	0.47	2.10	0.90	1.52	2.52	0.74	0.76	0.26
	[1.45, 1.51)	2.97	1.36	1.27	0.24	0.51	1.93	0.90	1.52	2.52	0.74	0.76	0.26
$\cos\theta_\ell$	[−1.00, −0.40)	3.58	1.40	3.96	1.99	0.53	3.57	0.90	1.52	2.52	0.74	0.76	0.26
	[−0.40, −0.20)	2.50	1.02	3.08	1.44	0.62	3.27	0.90	1.52	2.52	0.74	0.76	0.26
	[−0.20, 0.00)	1.95	0.80	1.23	1.18	0.58	2.88	0.90	1.52	2.52	0.74	0.76	0.26
	[0.00, 0.20)	1.56	0.62	0.66	0.97	0.56	2.59	0.90	1.52	2.52	0.74	0.76	0.26
	[0.20, 0.40)	1.37	0.61	0.66	0.91	0.62	2.62	0.90	1.52	2.52	0.74	0.76	0.26
	[0.40, 0.60)	1.37	0.54	0.59	0.93	0.64	2.67	0.90	1.52	2.52	0.74	0.76	0.26
	[0.60, 0.80)	1.41	0.58	0.76	0.95	0.46	2.73	0.90	1.52	2.52	0.74	0.76	0.26
	[0.80, 1.00)	1.54	0.68	0.81	1.10	0.30	2.79	0.90	1.52	2.52	0.74	0.76	0.26
$\cos\theta_V$	[−1.00, −0.80)	1.53	0.70	0.47	0.89	0.53	2.07	0.90	1.52	2.52	0.74	0.76	0.26
	[−0.80, −0.60)	1.36	0.58	0.42	0.86	0.52	2.27	0.90	1.52	2.52	0.74	0.76	0.26
	[−0.60, −0.40)	1.49	0.66	0.64	1.01	0.50	2.54	0.90	1.52	2.52	0.74	0.76	0.26
	[−0.40, −0.20)	1.60	0.68	0.91	1.04	0.47	2.65	0.90	1.52	2.52	0.74	0.76	0.26
	[−0.20, 0.00)	1.66	0.72	1.24	0.98	0.45	2.85	0.90	1.52	2.52	0.74	0.76	0.26
	[0.00, 0.20)	1.67	0.71	1.44	0.87	0.45	3.07	0.90	1.52	2.52	0.74	0.76	0.26
	[0.20, 0.40)	1.66	0.72	1.46	0.77	0.44	3.17	0.90	1.52	2.52	0.74	0.76	0.26
	[0.40, 0.60)	1.61	0.67	1.38	0.66	0.46	3.40	0.90	1.52	2.52	0.74	0.76	0.26
	[0.60, 0.80)	1.51	0.63	1.24	0.54	0.45	3.55	0.90	1.52	2.52	0.74	0.76	0.26
	[0.80, 1.00)	1.98	0.86	1.18	0.12	0.49	3.65	0.90	1.52	2.52	0.74	0.76	0.26
χ	[0.00, 0.63)	3.02	1.31	1.02	1.87	0.46	3.05	0.90	1.52	2.52	0.74	0.76	0.26
	[0.63, 1.26)	1.96	0.82	0.87	1.29	0.46	2.89	0.90	1.52	2.52	0.74	0.76	0.26
	[1.26, 1.88)	1.87	0.81	0.76	1.20	0.46	2.73	0.90	1.52	2.52	0.74	0.76	0.26
	[1.88, 2.51)	1.96	0.83	0.86	1.22	0.51	2.62	0.90	1.52	2.52	0.74	0.76	0.26
	[2.51, 3.14)	2.06	0.91	1.10	1.19	0.49	2.44	0.90	1.52	2.52	0.74	0.76	0.26
	[3.14, 3.77)	2.03	0.85	1.06	1.02	0.51	2.55	0.90	1.52	2.52	0.74	0.76	0.26
	[3.77, 4.40)	1.98	0.87	0.88	0.88	0.51	2.62	0.90	1.52	2.52	0.74	0.76	0.26
	[4.40, 5.03)	1.92	0.78	0.67	0.76	0.51	2.77	0.90	1.52	2.52	0.74	0.76	0.26
	[5.03, 5.65)	1.89	0.80	0.72	0.63	0.46	2.93	0.90	1.52	2.52	0.74	0.76	0.26
	[5.65, 6.28)	2.89	1.20	1.04	0.51	0.43	2.94	0.90	1.52	2.52	0.74	0.76	0.26

Table 7.2: Fractional uncertainties (in %) of the partial decay rate in each bin for the $\bar{B}^0 \to D^{*+}\mu^-\bar{\nu}_\mu$ decay.

Variable	Bin	Statistical	Simulated sample size	Signal modeling	Background subtraction	Lepton ID efficiency	Slow-pion efficiency	Tracking of K, π, ℓ	$N_{B\bar{B}}$	f_{+0}	$\mathcal{B}(D^* \to D\pi)$	$\mathcal{B}(D^0 \to K\pi)$	B^0 lifetime
w	[1.00, 1.05)	3.35	1.32	0.49	1.46	2.00	4.28	0.90	1.52	2.52	0.74	0.76	0.26
	[1.05, 1.10)	2.04	0.79	0.30	0.97	1.91	3.73	0.90	1.52	2.52	0.74	0.76	0.26
	[1.10, 1.15)	1.74	0.70	0.69	0.78	1.69	3.33	0.90	1.52	2.52	0.74	0.76	0.26
	[1.15, 1.20)	1.64	0.72	0.87	0.67	1.62	3.08	0.90	1.52	2.52	0.74	0.76	0.26
	[1.20, 1.25)	1.61	0.67	0.80	0.61	1.58	2.87	0.90	1.52	2.52	0.74	0.76	0.26
	[1.25, 1.30)	1.67	0.70	0.84	0.63	1.53	2.64	0.90	1.52	2.52	0.74	0.76	0.26
	[1.30, 1.35)	1.72	0.68	0.96	0.62	1.57	2.50	0.90	1.52	2.52	0.74	0.76	0.26
	[1.35, 1.40)	1.85	0.70	1.04	0.59	1.63	2.24	0.90	1.52	2.52	0.74	0.76	0.26
	[1.40, 1.45)	1.99	0.78	1.00	0.66	1.72	2.06	0.90	1.52	2.52	0.74	0.76	0.26
	[1.45, 1.51)	2.96	1.15	1.55	0.16	1.81	1.86	0.90	1.52	2.52	0.74	0.76	0.26
$\cos\theta_\ell$	[−1.00, −0.40)	3.36	1.28	4.20	1.85	3.56	3.76	0.90	1.52	2.52	0.74	0.76	0.26
	[−0.40, −0.20)	2.37	0.95	2.99	1.35	3.42	3.14	0.90	1.52	2.52	0.74	0.76	0.26
	[−0.20, 0.00)	1.88	0.74	1.11	1.11	3.42	2.89	0.90	1.52	2.52	0.74	0.76	0.26
	[0.00, 0.20)	1.45	0.61	0.59	0.90	2.95	2.59	0.90	1.52	2.52	0.74	0.76	0.26
	[0.20, 0.40)	1.34	0.52	0.64	0.89	2.02	2.56	0.90	1.52	2.52	0.74	0.76	0.26
	[0.40, 0.60)	1.27	0.55	0.53	0.88	1.14	2.65	0.90	1.52	2.52	0.74	0.76	0.26
	[0.60, 0.80)	1.29	0.56	0.68	0.87	0.42	2.67	0.90	1.52	2.52	0.74	0.76	0.26
	[0.80, 1.00)	1.47	0.59	0.70	1.04	0.15	2.75	0.90	1.52	2.52	0.74	0.76	0.26
$\cos\theta_V$	[−1.00, −0.80)	1.43	0.64	0.50	0.43	2.04	2.04	0.90	1.52	2.52	0.74	0.76	0.26
	[−0.80, −0.60)	1.35	0.55	0.45	0.58	1.77	2.21	0.90	1.52	2.52	0.74	0.76	0.26
	[−0.60, −0.40)	1.48	0.62	0.66	0.68	1.56	2.46	0.90	1.52	2.52	0.74	0.76	0.26
	[−0.40, −0.20)	1.55	0.64	0.95	0.68	1.46	2.69	0.90	1.52	2.52	0.74	0.76	0.26
	[−0.20, 0.00)	1.60	0.68	1.23	0.67	1.32	2.89	0.90	1.52	2.52	0.74	0.76	0.26
	[0.00, 0.20)	1.58	0.66	1.44	0.63	1.34	3.07	0.90	1.52	2.52	0.74	0.76	0.26
	[0.20, 0.40)	1.56	0.66	1.46	0.57	1.38	3.14	0.90	1.52	2.52	0.74	0.76	0.26
	[0.40, 0.60)	1.56	0.63	1.40	0.52	1.56	3.30	0.90	1.52	2.52	0.74	0.76	0.26
	[0.60, 0.80)	1.50	0.61	1.27	0.46	1.82	3.46	0.90	1.52	2.52	0.74	0.76	0.26
	[0.80, 1.00)	1.94	0.81	1.21	0.07	2.03	3.60	0.90	1.52	2.52	0.74	0.76	0.26
χ	[0.00, 0.63)	2.88	1.20	1.15	1.02	1.57	2.90	0.90	1.52	2.52	0.74	0.76	0.26
	[0.63, 1.26)	1.83	0.74	0.82	0.77	1.74	2.91	0.90	1.52	2.52	0.74	0.76	0.26
	[1.26, 1.88)	1.79	0.77	0.68	0.80	1.78	2.77	0.90	1.52	2.52	0.74	0.76	0.26
	[1.88, 2.51)	1.84	0.75	0.89	0.77	1.63	2.60	0.90	1.52	2.52	0.74	0.76	0.26
	[2.51, 3.14)	1.98	0.84	1.11	0.79	1.60	2.50	0.90	1.52	2.52	0.74	0.76	0.26
	[3.14, 3.77)	1.95	0.79	1.10	0.74	1.56	2.46	0.90	1.52	2.52	0.74	0.76	0.26
	[3.77, 4.40)	1.86	0.80	0.89	0.65	1.69	2.58	0.90	1.52	2.52	0.74	0.76	0.26
	[4.40, 5.03)	1.75	0.69	0.74	0.52	1.68	2.73	0.90	1.52	2.52	0.74	0.76	0.26
	[5.03, 5.65)	1.78	0.72	0.81	0.54	1.70	2.83	0.90	1.52	2.52	0.74	0.76	0.26
	[5.65, 6.28)	3.00	1.18	0.93	0.32	1.59	2.98	0.90	1.52	2.52	0.74	0.76	0.26

Figure 7.1: Full experimental (statistical and systematic) correlations (in %) of the partial decay rates for the $\bar{B}^0 \to D^{*+} e^- \bar{\nu}_e$ decay.

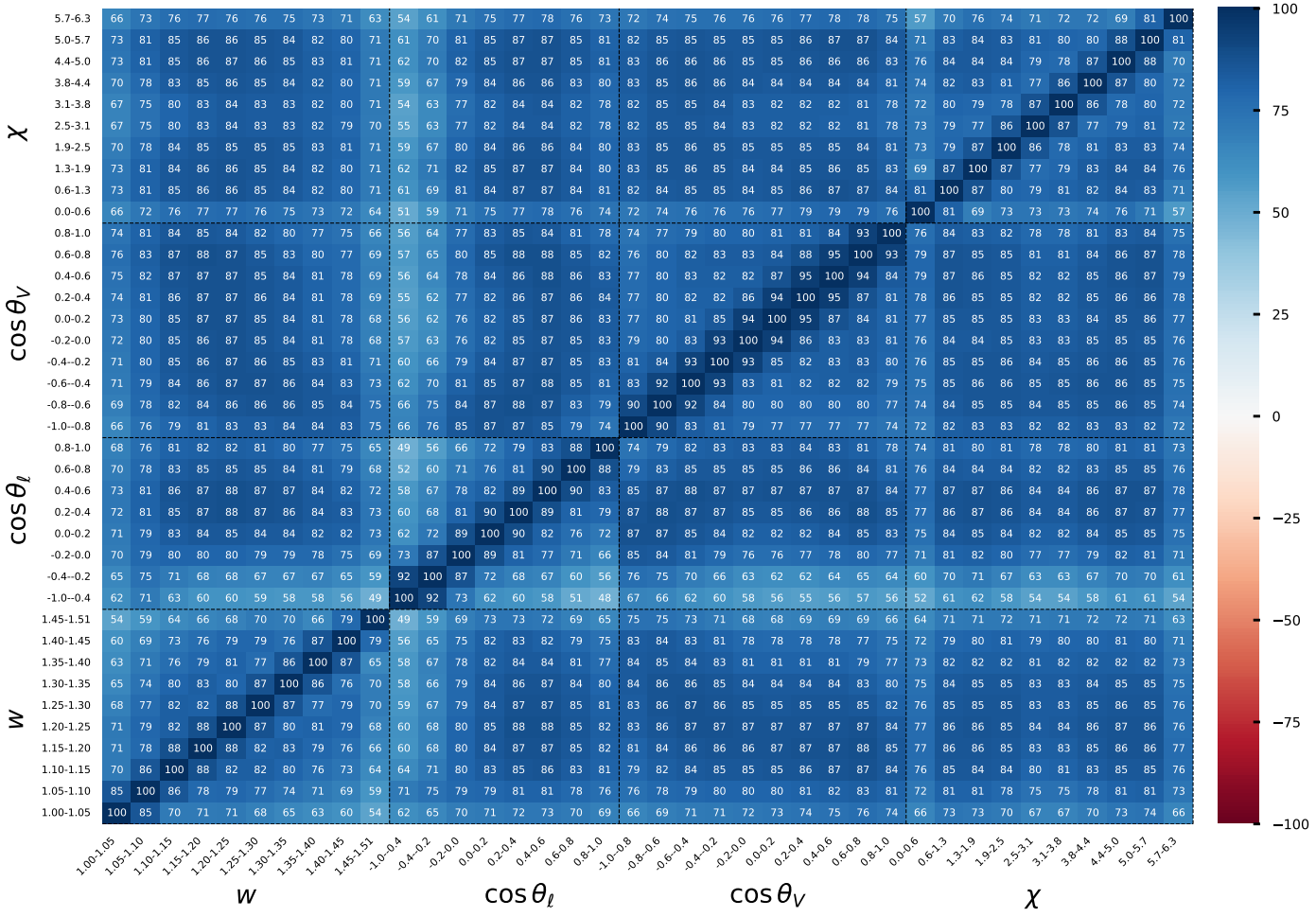

Figure 7.2: Full experimental (statistical and systematic) correlations (in %) of the partial decay rates for the $\bar{B}^0 \to D^{*+}\mu^-\bar{\nu}_\mu$ decays.

CHAPTER 8

Determination of form factors and $|V_{cb}|$

8.1 Fit setup

As we investigate partial decay rates of the same data set, the measured total decay rate is highly correlated on four projections. These are redundant degrees of freedom in the measured partial decay rates within electrons and muons. They are removed before analyzing the observed distributions: we calculate normalized partial decay rates $\Delta\Gamma/\Gamma$ and exclude the last bin of each kinematic variable in the determination of form factors and $|V_{cb}|$. The total decay rate is determined as the average over four projections

$$\Gamma = \left(\sum_{i=1}^{10} \Delta\Gamma_i^{w} + \sum_{i=1}^{8} \Delta\Gamma_i^{\cos\theta_\ell} + \sum_{i=1}^{10} \Delta\Gamma_i^{\cos\theta_V} + \sum_{i=1}^{10} \Delta\Gamma_i^{\chi} \right) /4, \tag{8.1}$$

where $\Delta\Gamma_i^X$ represents the partial decay rate in bin i of variable X. Furthermore, we average the normalized partial decay rates over the $\bar{B}^0 \to D^{*+} e^- \bar{\nu}_e$ and $\bar{B}^0 \to D^{*+} \mu^- \bar{\nu}_\mu$ decays, as summarized in Table 6.9. The correlations between these averages are visualized in Fig. 8.1.

The extraction of $|V_{cb}|$ and form factor parameters involves the construction of a χ^2 function, defined as

$$\chi^2 = \sum_{i,j}^{34} \left(\frac{\Delta\Gamma_i^{\text{obs}}}{\Gamma^{\text{obs}}} - \frac{\Delta\Gamma_i^{\text{pre}}}{\Gamma^{\text{pre}}} \right) C_{ij}^{-1} \left(\frac{\Delta\Gamma_j^{\text{obs}}}{\Gamma^{\text{obs}}} - \frac{\Delta\Gamma_j^{\text{pre}}}{\Gamma^{\text{pre}}} \right) + \frac{(\Gamma^{\text{obs}} - \Gamma^{\text{pre}})^2}{\sigma_\Gamma^2}. \tag{8.2}$$

In this equation, i and j denote the indices of the bins in the observables w, $\cos\theta_\ell$, $\cos\theta_V$, and χ, and $\Delta\Gamma_i^{\text{pre}}/\Gamma^{\text{pre}}$ and Γ^{pre} are the predicted values expressed as functions of the form-factor parameters and $|V_{cb}|$ [30–32]. Further, C is the covariance matrix on the normalized rates, and σ_Γ is the uncertainty on the total rate.

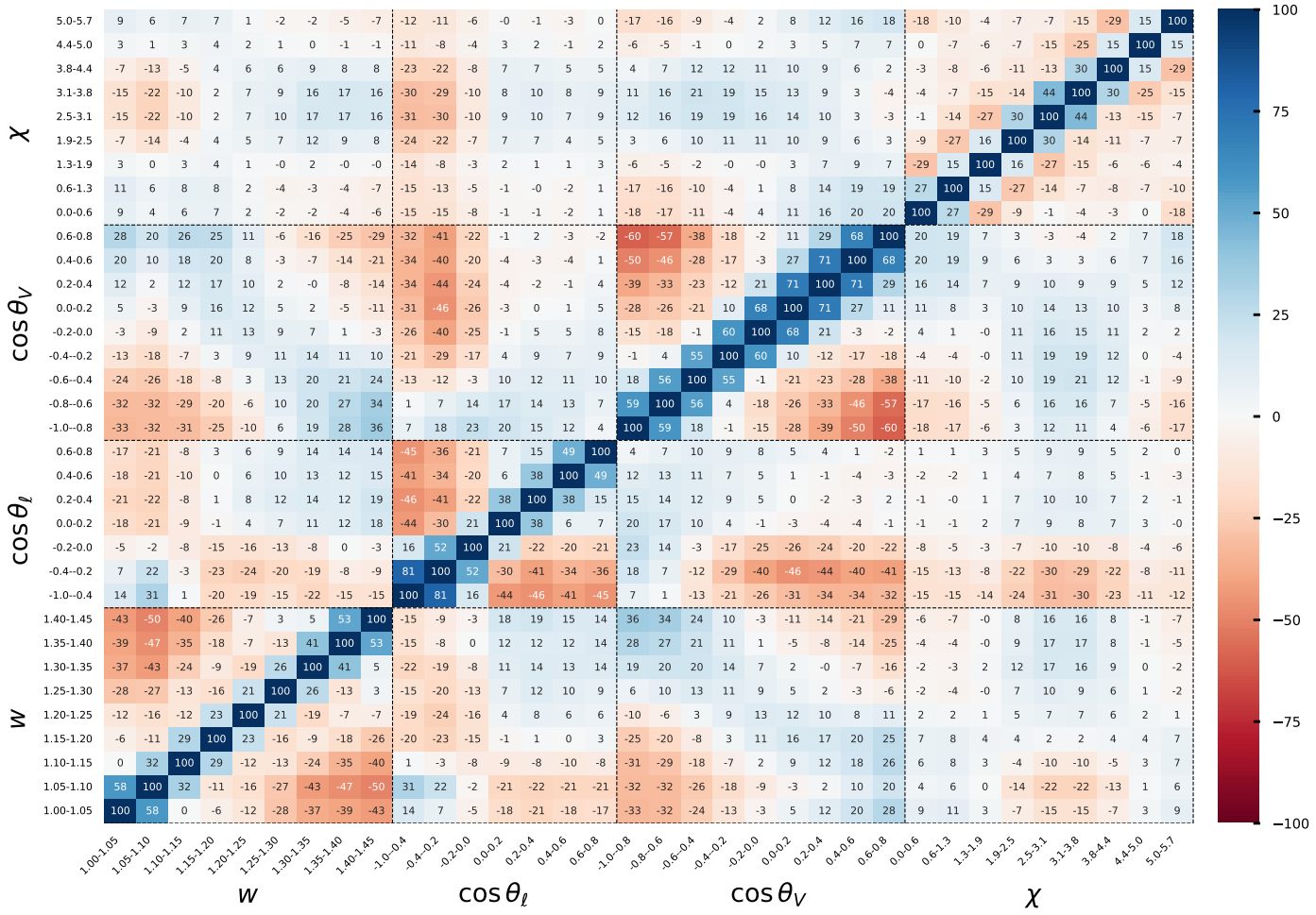

Figure 8.1: Full experimental (statistical and systematic) correlations (in %) for the average of the normalized partial decay rates. The last bin of each projection is excluded in the determination of $|V_{cb}|$ value, thus it is not shown.

8.2 Results of BGL parametrization

The form factors $g(z)$, $f(z)$, and $\mathcal{F}_1(z)$ in the BGL parametrization are expanded in terms of the z parameter, as discussed in Eq. (2.25). The expansion can be of infinite order, and must be truncated carefully. In this work, the truncation is specifically investigated using a nested hypothesis test (NHT) method initially proposed in Ref. [101]. Further details on this truncation analysis will be provided in Section 8.2.1. The results of the fit, based on the selected truncation, will be presented in Section 8.2.2.

8.2.1 Truncation of BGL expansion

We initiate the fitting process with the expansion of $g(z)$, $f(z)$, and $\mathcal{F}_1(z)$, each with only one degree of freedom. Subsequently, we extend the expansion to the next order for each of $g(z)$, $f(z)$, and $\mathcal{F}_1(z)$ and repeat the $|V_{cb}|$ fit. To accept an extension, we require that the minimum χ^2 value decreases by one unit or more when adding one more degree of freedom to the form factors. Any extension that does not lead to such improvement is rejected.

Moreover, as strong correlations between the form factor parameters suggest reduced independence among them, we reject expansions that result in correlations exceeding 0.95. This process iterates until all attempted extensions in the next generation prove to be dead ends.

The search processes are illustrated in Fig. 8.2. In addition, Table 8.1 summarizes the corresponding $|V_{cb}|$ value, the largest off-diagonal correlation coefficient, the minimized χ^2 value, the degree of freedom in the fit, and the p-value of the fit for each configuration of the expansion. Following the rules of acceptance and rejection, we choose (1, 2, 2) as the optimal pattern.

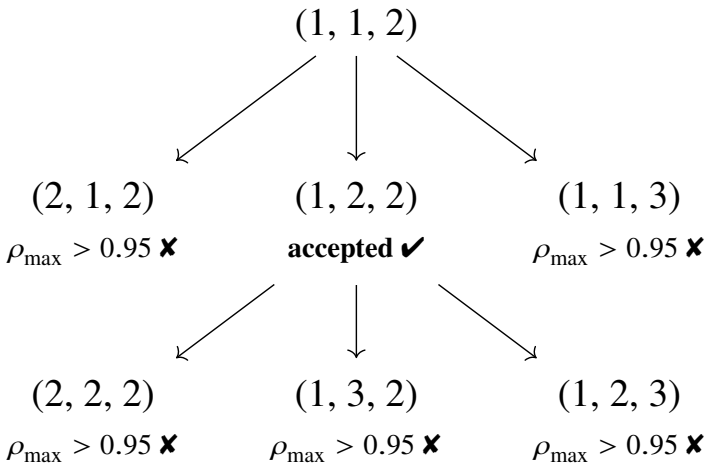

Figure 8.2: Search process in a nested hypothesis test. The numbers (n_a, n_b, n_c) represent the expansion orders of the form factors $g(z)$, $f(z)$ and $\mathcal{F}_1(z)$ introduced in Eq. (2.25).

Table 8.1: Summary of the nested hypothesis test without LQCD input. The $\rho_{\max}$ column records the largest off-diagonal correlation coefficients. The optimal expansion order is highlighted with a gray background.

(n_a, n_b, n_c)	$\lvert V_{cb}\rvert \times 10^3$	$\rho_{\max}$	χ^2	Ndf	p-value
$(1,1,2)$	40.2 ± 1.1	0.43	40	32	16%
$(2,1,2)$	40.1 ± 1.1	0.97	38.6	31	16%
$(1,2,2)$	40.6 ± 1.2	0.57	38.9	31	16%
$(1,1,3)$	40.1 ± 1.1	0.96	39.5	31	14%
$(2,2,2)$	40.3 ± 1.3	0.99	38.6	30	13%
$(1,3,2)$	40.0 ± 1.3	0.98	38	30	15%
$(1,2,3)$	40.5 ± 1.2	0.96	38.8	30	13%

Table 8.2: Results of the determination of the BGL expansion coefficients and their correlations.

	Value	Correlation				χ^2/ndf
$\tilde{a}_0 \times 10^3$	0.88 ± 0.05	1.00	0.26	−0.28	0.19	39/31
$\tilde{b}_0 \times 10^3$	0.54 ± 0.01	0.26	1.00	−0.37	−0.43	
$\tilde{b}_1 \times 10^3$	-0.31 ± 0.30	−0.28	−0.37	1.00	0.57	
$\tilde{c}_1 \times 10^3$	-0.04 ± 0.03	0.19	−0.43	0.57	1.00	

8.2.2 Fit result

In the fits, we incorporate $|V_{cb}|$ into the expansion coefficients x_i as follows

$$\tilde{x}_i = |V_{cb}|\,\eta_{\rm EW}\,x_i\,. \tag{8.3}$$

The resulting values and correlations are summarized in Table 8.2, and $|V_{cb}|$ is further determined using the relationship:

$$|V_{cb}|\eta_{\rm EW}\mathcal{F}(1) = \frac{1}{\sqrt{m_B m_{D^*}}}\left(\frac{|\tilde{b}_0|}{P_f(0)\phi_f(0)}\right). \tag{8.4}$$

Using $\mathcal{F}(1) = 0.906 \pm 0.013$ [102] and $\eta_{\rm EW} = 1.0066$ [25], we determine

$$|V_{cb}|_{\rm BGL} = (40.57 \pm 0.31 \pm 0.95 \pm 0.58) \times 10^{-3}, \tag{8.5}$$

where the first, second, and third contributions to the uncertainty are statistical, systematic, and from the prediction of $\mathcal{F}(1)$, respectively. We find a p-value of 15% for the fit.

To decompose the uncertainties from different sources, we generate 3000 normalized decay

rates and total rates based on multivariate Gaussian distributions, where the input covariance matrix is constructed for each individual source, respectively. We fit these toy samples and study the deviations of the fitted values. The relative uncertainties of various sources are summarized in Table 8.3. The largest uncertainty on $|V_{cb}|$ stems from the knowledge of the slow pion reconstruction efficiency, followed by the uncertainty in the external input f_{+0}, which is used to convert the number of counted B-meson pairs into the number of B^0 mesons.

Table 8.3: Fractional contributions to the uncertainties of the BGL form factors from a fit of the $\bar{B}^0 \to D^{*+}\ell^-\bar{\nu}_\ell$ decay. Because of the absorption of $|V_{cb}|$ into the coefficients (see Eq. (8.3)), the fitted parameters $\tilde{x}_i$ are affected by the uncertainties that only have an impact on the overall normalization.

	$\tilde{a}_0$	$\tilde{b}_0$	$\tilde{b}_1$	$\tilde{c}_1$
Statistical	3.7	0.8	65.1	50.8
Background subtraction	2.1	0.4	31.3	21.8
Size of simulated samples	1.5	0.3	26.4	20.5
Lepton ID efficiency	1.6	0.3	3.4	2.8
Tracking of K, π, ℓ	0.4	0.4	0.5	0.4
Slow-pion efficiency	1.6	1.5	23.8	24.7
$N_{B\bar{B}}$	0.8	0.8	0.8	0.8
f_{+0}	1.3	1.3	1.3	1.2
$\mathcal{B}(D^{*+} \to D^0\pi^+)$	0.4	0.4	0.4	0.4
$\mathcal{B}(D^0 \to K^-\pi^+)$	0.4	0.4	0.4	0.4
B^0 lifetime	0.1	0.1	0.1	0.1
Signal modeling	2.3	0.5	52.1	35.0
Total	5.8	2.5	96.0	73.0

Additionally, we conduct an examination of the D'Agostini-type bias, and our findings indicate that our results are unbiased. Further information can be found in Appendix G.

8.3 Results of CLN parametrization

We also minimize Eq. (8.2) with $\Delta\Gamma^{\text{pre}}$ and Γ^{pre} expressed in the CLN parametrization. We find

$$|V_{cb}|_{\text{CLN}} = (40.13 \pm 0.27 \pm 0.93 \pm 0.58) \times 10^{-3}, \tag{8.6}$$

with a p-value of 16%. The resulting values of $|V_{cb}|$ and form factor parameters, along with their correlations, are summarized in Table 8.4. Furthermore, we break down the uncertainties on the fitted values using the same approach as for the BGL parametrization. The obtained relative uncertainties are provided in Table 8.5.

Table 8.4: Results of the determination of the CLN parameters, $|V_{cb}|$ and their correlations.

	Value	Correlation				χ^2/ndf
ρ^2	1.22 ± 0.05	1.00	0.36	-0.81	0.29	39/31
$R_1(1)$	1.14 ± 0.07	0.36	1.00	-0.60	-0.10	
$R_2(1)$	0.89 ± 0.03	-0.81	-0.60	1.00	-0.08	
$\|V_{cb}\| \times 10^3$	40.1 ± 1.1	0.29	-0.10	-0.08	1.00	

Table 8.5: Fractional contributions to the uncertainties of the CLN form factors from a fit of the $\bar{B}^0 \to D^{*+}\ell^-\bar{\nu}_\ell$ decay. The uncertainties originating from tracking efficiency, the number of B^0 mesons, the B^0 lifetime, and the charm branching fractions only affect the overall normalization but do not contribute to the parameters related to the shape.

	ρ^2	$R_1(1)$	$R_2(1)$	$\|V_{cb}\|$
Statistical	3.0	4.1	2.8	0.7
Background subtraction	1.4	2.2	1.2	0.3
Size of simulated samples	1.2	1.7	1.1	0.3
Lepton ID efficiency	0.2	1.6	0.1	0.3
Slow pion efficiency	1.0	0.9	0.8	1.5
Tracking of K, π, ℓ				0.4
$N_{B\bar{B}}$				0.8
f_{+0}				1.3
$\mathcal{B}(D^{*+} \to D^0\pi^+)$				0.4
$\mathcal{B}(D^0 \to K^-\pi^+)$				0.4
B^0 lifetime				0.1
Signal modeling	2.6	2.6	2.0	0.5
Total	4.5	5.9	3.9	2.4

We plot the partial decay rates with the fitted values and 1σ deviation in both BGL and CLN parametrizations. They predict nearly identical differential decay rates. Meanwhile, they describe the measured four spectra very well.

In addition to the results obtained through the SVD method, we also implement the matrix inversion method to unfold the signal yields and extract values for $|V_{cb}|$ and form factor parameters. The results in these two cases are compatible with each other. More details are provided in Appendix H.

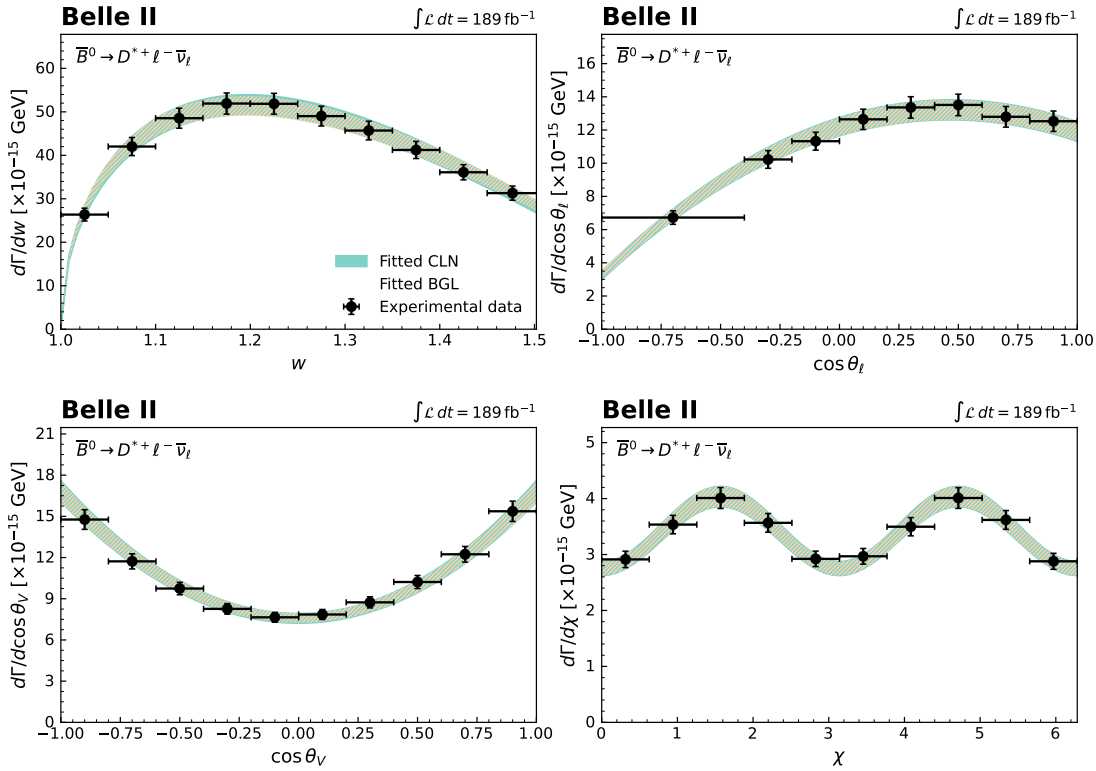

Figure 8.3: Comparison of the fitted partial decay rates with 1σ uncertainties in the BGL and CLN parametrizations to the unfolded experimental data (shown as points with error bars). Note that the BGL (hatched) band almost completely overlays the CLN (solid) band.

8.4 Sensitivity to FNAL/MILC lattice results at nonzero recoil

In Ref. [103], the Fermilab Lattice and MILC (FNAL/MILC) Collaborations reported predictions for the $\bar{B}^0 \to D^{*+}\ell^-\bar{\nu}_\ell$ form factors at nonzero recoil. We compare our data with these predictions using two scenarios:

- Inclusion of predictions beyond zero recoil for $h_{A_1}(w)$ at $w = [1.03, 1.10, 1.17]$. This scenario allows a comparison with the zero-recoil result when information on the w dependence of h_{A_1} is included.
- Inclusion of predictions beyond zero recoil for $h_{A_1}(w)$, $R_1(w)$, and $R_2(w)$ at $w = [1.03, 1.10, 1.17]$. This scenario includes the full LQCD information.

To include beyond zero recoil information, we add to Eq. (8.2) a term of the form

$$\chi^2_{\mathrm{LQCD}} = \sum_{ij} (F_i^{\mathrm{LQCD}} - F_i^{\mathrm{pre}}) C_{ij}^{-1} (F_j^{\mathrm{LQCD}} - F_j^{\mathrm{pre}}) \,. \tag{8.7}$$

Here, F_i^{LQCD} denotes the lattice data on $h_{A_1}(w)$ or on $h_{A_1}(w)$, $R_1(w)$, $R_2(w)$. The parameter

F_i^{pre} represents the corresponding value expressed in terms of form-factor parameters. As we now explicitly include normalization information on the form factors into the fit, we directly fit for the BGL coefficients without absorbing $|V_{cb}|$ and η_{EW}.

The fitted results in BGL and CLN parametrizations are summarized in Tables 8.6 and 8.7, respectively. The inclusion of beyond-zero-recoil information for h_{A_1} results in a small decrease on the central value for $|V_{cb}|$ if we use the BGL form-factor expansion. The CLN fits show a small increase. The inclusion of the full beyond-zero-recoil information shifts $|V_{cb}|$ significantly and the resulting fit shapes in h_{A_1}, R_1, and R_2 show disagreements with the FNAL/MILC lattice predictions with a poor p-value of 0.04%. This is consistent with the results of Ref. [104]. The BGL fits of both scenarios are shown in Fig. 8.4 with the nonzero recoil FNAL/MILC predictions of Ref. [103]. The agreement can be improved if more BGL expansion parameters are included: in Appendix I we repeat the nested hypothesis test to determine the appropriate truncation order when full lattice information is included and find $n_a = 3$, $n_b = 1$, $n_c = 3$. With 6 expansion coefficients we find a p-value of 16%.

Table 8.6: Values of BGL form factors and $|V_{cb}|$ resulting from a fit that includes nonzero recoil lattice information.

	Constraints on $h_{A_1}(w)$	Constraints on $h_{A_1}(w)$, $R_1(w)$, $R_2(w)$
$a_0 \times 10^3$	21.7 ± 1.3	25.6 ± 0.8
$b_0 \times 10^3$	13.19 ± 0.24	13.61 ± 0.23
$b_1 \times 10^3$	−6 ± 6	2 ± 6
$c_1 \times 10^3$	−0.9 ± 0.7	0.0 ± 0.7
$\|V_{cb}\| \times 10^3$	40.3 ± 1.2	38.3 ± 1.1
χ^2/ndf	39/33	75/39
p-value	21%	0.04%

Table 8.7: Values of CLN form factors and $|V_{cb}|$ resulting from a fit that includes nonzero recoil lattice information.

	Constraints on $h_{A_1}(w)$	Constraints on $h_{A_1}(w)$, $R_1(w)$, $R_2(w)$
$h_{A_1}(1)$	0.91 ± 0.02	0.94 ± 0.02
ρ^2	1.22 ± 0.05	1.21 ± 0.04
$R_1(1)$	1.14 ± 0.07	1.26 ± 0.04
$R_2(1)$	0.88 ± 0.03	0.88 ± 0.03
$\lvert V_{cb}\rvert \times 10^3$	40.3 ± 1.2	38.7 ± 1.1
χ^2/ndf	39/33	70/39
p-value	23%	0.2%

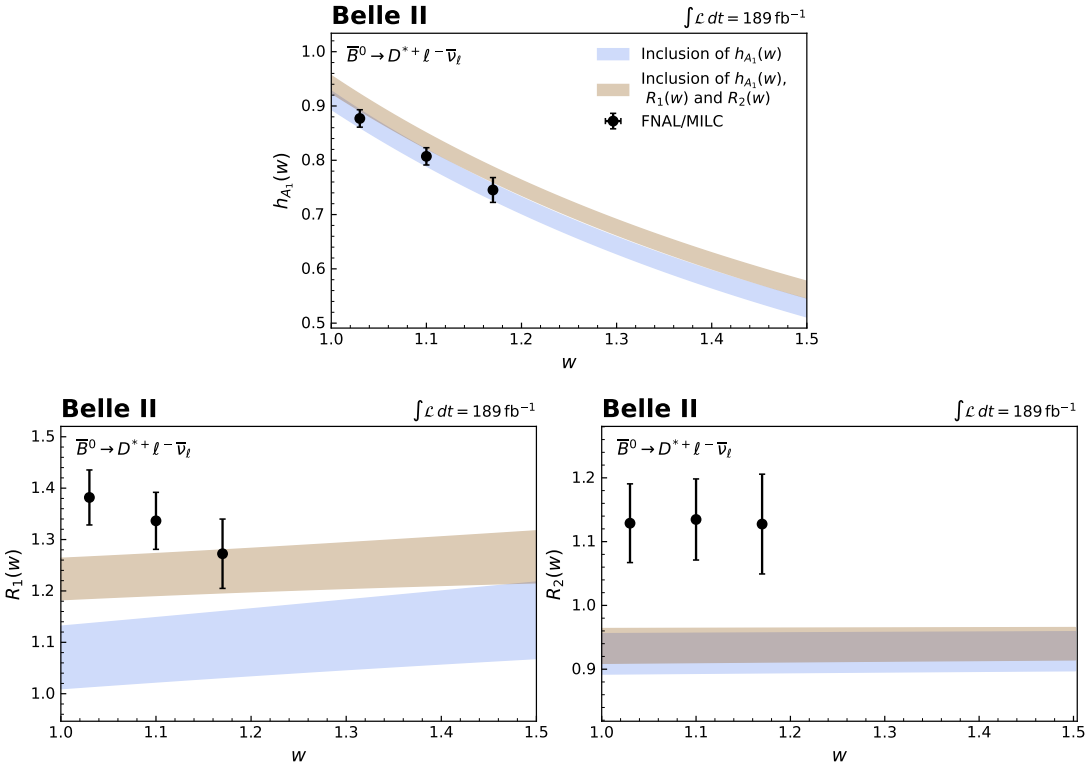

Figure 8.4: Comparison of the fitted $h_{A_1}(w)$, $R_1(w)$ and $R_2(w)$ for the BGL fits.

CHAPTER 9

Lepton flavour universality tests

9.1 Ratio of branching fractions

By summing the partial decay rates of all kinematic variables we obtain the total rate. The total decay rates averaged over w, $\cos\theta_\ell$, $\cos\theta_V$, and χ are converted to branching fractions using the B^0 lifetime. We find

$$\mathcal{B}(\bar{B}^0 \to D^{*+} e^- \bar{\nu}_e) = (4.92 \pm 0.03 \pm 0.22)\%\,, \tag{9.1}$$

$$\mathcal{B}(\bar{B}^0 \to D^{*+} \mu^- \bar{\nu}_\mu) = (4.93 \pm 0.03 \pm 0.24)\%\,, \tag{9.2}$$

where the first and second uncertainties are statistical and systematic, respectively. The average is calculated as

$$\mathcal{B}(\bar{B}^0 \to D^{*+} \ell^- \bar{\nu}_\ell) = (4.922 \pm 0.023 \pm 0.220)\%\,, \tag{9.3}$$

which is compatible with the current world average: $(4.97 \pm 0.12)\%$ [1].

In addition, we report a value for the ratio of the $\bar{B}^0 \to D^{*+} e^- \bar{\nu}_e$ and $\bar{B}^0 \to D^{*+} \mu^- \bar{\nu}_\mu$ branching fractions

$$R_{e/\mu} = 0.998 \pm 0.009 \pm 0.020, \tag{9.4}$$

where the first contribution to the uncertainty is statistical and the second systematic. The ratio is compatible with the predictions of Refs. [24, 105] (see Table 9.1 for a summary) assuming LFU and with previous measurements [23, 106]. The fully correlated systematic uncertainties, e.g., the tracking efficiency, the number of B^0 mesons, and the branching fractions of the D^{*+} and D^0 decays cancel in the ratio.

Table 9.1: Summary of the SM predictions taken from Refs. [24, 105] for the observables regarding the lepton flavor universality tests. Note that the F_L in Ref. [105] is only reported with $m_\ell = 0$ for the light leptons $\ell = e, \mu$.

	Ref. [105]	Ref. [24]
$R_{e/\mu}$	1.0041 ± 0.0001	1.0026 ± 0.0001
$\mathcal{A}_{\rm FB}^{e}$	0.244 ± 0.004	0.204 ± 0.012
$\mathcal{A}_{\rm FB}^{\mu}$	0.239 ± 0.004	0.198 ± 0.012
$\Delta\mathcal{A}_{\rm FB} \times 10^3$	-5.7 ± 0.1	-5.33 ± 0.24
F_L^e	0.516 ± 0.003	0.541 ± 0.011
F_L^μ	0.516 ± 0.003	0.542 ± 0.012
$\Delta F_L \times 10^4$	1.2 ± 0.1	5.43 ± 0.36

9.2 Angular asymmetry

The angular asymmetry $\mathcal{A}_{FB}$ is defined as the difference of partial decay rate in the forward and backward regions in the $\cos\theta_\ell$ spectrum normalized by the total decay rate:

$$\mathcal{A}_{\rm FB} = \frac{\int_0^1 \mathrm{d}\cos\theta_\ell \mathrm{d}\Gamma/\mathrm{d}\cos\theta_\ell - \int_{-1}^0 \mathrm{d}\cos\theta_\ell \mathrm{d}\Gamma/\mathrm{d}\cos\theta_\ell}{\int_0^1 \mathrm{d}\cos\theta_\ell \mathrm{d}\Gamma/\mathrm{d}\cos\theta_\ell + \int_{-1}^0 \mathrm{d}\cos\theta_\ell \mathrm{d}\Gamma/\mathrm{d}\cos\theta_\ell}. \tag{9.5}$$

With $\mathcal{A}_{\rm FB}$, we test LFU using the difference

$$\Delta\mathcal{A}_{\rm FB} = \mathcal{A}_{\rm FB}^{\mu} - \mathcal{A}_{\rm FB}^{e}\,. \tag{9.6}$$

We find

$$\begin{aligned} \mathcal{A}_{\rm FB}^{e} &= 0.228 \pm 0.012 \pm 0.017\,, \\ \mathcal{A}_{\rm FB}^{\mu} &= 0.211 \pm 0.011 \pm 0.021\,, \end{aligned} \tag{9.7}$$

and

$$\Delta\mathcal{A}_{\rm FB} = (-17 \pm 16 \pm 16) \times 10^{-3}\,. \tag{9.8}$$

The correlated uncertainties between the $\bar{B}^0 \to D^{*+} e^- \bar{\nu}_e$ and $\bar{B}^0 \to D^{*+} \mu^- \bar{\nu}_\mu$ decays, e.g., the number of B^0 mesons, the B^0 lifetime, and others cancel in $\Delta\mathcal{A}_{\rm FB}$. Note that due to the selection requirement on the lepton momentum in the c.m. system, the unfolded yields in the negative $\cos\theta_\ell$ region receive a large correction based on the SM assumption. Consequently, the measured value of $\Delta\mathcal{A}_{\rm FB}$ would change in the presence of non-SM physics, and should only be used to check for consistency with the SM expectation.

To minimize the extrapolation, we also measure $\mathcal{A}_{\rm FB}$ in the phase space of $p_\ell^B > 1.2\,\mathrm{GeV}/c$,

with p_ℓ^B denoting the lepton momentum in the B meson rest frame. We find

$$\mathcal{A}_{\rm FB}^e(p_\ell^B > 1.2\,{\rm GeV}/c) = 0.611 \pm 0.006 \pm 0.005\,, \tag{9.9}$$

$$\mathcal{A}_{\rm FB}^\mu(p_\ell^B > 1.2\,{\rm GeV}/c) = 0.604 \pm 0.006 \pm 0.008\,, \tag{9.10}$$

$$\Delta\mathcal{A}_{\rm FB}(p_\ell^B > 1.2\,{\rm GeV}/c) = (-7 \pm 9 \pm 9) \times 10^{-3}\,. \tag{9.11}$$

9.3 Longitudinal D^{*+} polarization

From the observed $\cos\theta_V$ distribution, we determine the longitudinal D^* polarization fraction F_L via

$$\frac{1}{\Gamma}\frac{{\rm d}\Gamma}{{\rm d}\cos\theta_V} = \frac{3}{2}\left(F_L\cos^2\theta_V + \frac{1-F_L}{2}\sin^2\theta_V\right)\,, \tag{9.12}$$

and find

$$F_L^e = 0.520 \pm 0.005 \pm 0.005\,, \tag{9.13}$$

$$F_L^\mu = 0.527 \pm 0.005 \pm 0.005\,, \tag{9.14}$$

and

$$\Delta F_L = 0.006 \pm 0.007 \pm 0.005\,, \tag{9.15}$$

with $\Delta F_L = F_L^\mu - F_L^e$. The correlated uncertainties between the $\bar{B}^0 \to D^{*+}e^-\bar{\nu}_e$ and $\bar{B}^0 \to D^{*+}\mu^-\bar{\nu}_\mu$ decays cancel in ΔF_L.

The resulting angular asymmetry and longitudinal polarization for $\bar{B}^0 \to D^{*+}e^-\bar{\nu}_e$ and $\bar{B}^0 \to D^{*+}\mu^-\bar{\nu}_\mu$ decays and their difference between the e channel and μ channel agree with the SM predictions of Refs. [24, 105], which are summarized in Table 9.1. Note that $\mathcal{A}_{\rm FB}$ in Ref. [24] is determined from a slightly reduced phase space corresponding to $1.0 < w < 1.5$. However, the impact of this restriction on the SM expectations is at order 10^{-4} [105].

Our values are compatible with the determination of $\Delta\mathcal{A}_{\rm FB}$ and ΔF_L of Refs. [23, 24] within 2.3 and 1.2 standard deviations, respectively. Recently Ref. [104] also determined these quantities and we observe good agreement for $\mathcal{A}_{\rm FB}$ and F_L for electron and muon final states and their differences.

CHAPTER 10

Summary and outlook

This thesis presents a measurement of exclusive $\bar{B}^0 \to D^{*+}\ell^-\bar{\nu}_\ell$ decays using collision data corresponding to a luminosity of $189\,\text{fb}^{-1}$ collected by the Belle II experiment. We develop a novel method to reconstruct the kinematic variables w, $\cos\theta_\ell$, $\cos\theta_V$, and χ that describe the differential decay rate of $\bar{B}^0 \to D^{*+}\ell^-\bar{\nu}_\ell$ processes. The signal yields in these bins of kinematic variables are determined by binned likelihood fits to two-dimensional distributions in $\cos\theta_{BY}$ and ΔM, and are further unfolded to correct for migration across bins.

After unfolding the yields in each bin of kinematic variables, we calculate the corresponding partial decay rates and average them over $\bar{B}^0 \to D^{*+}e^-\bar{\nu}_e$ and $\bar{B}^0 \to D^{*+}\mu^-\bar{\nu}_\mu$ decays. These results are then used to determine the values of $|V_{cb}|$ and the form factor parameters for $\bar{B}^0 \to D^{*+}\ell^-\bar{\nu}_\ell$ decays. We find

$$|V_{cb}|_{\text{BGL}} = (40.57 \pm 0.31 \pm 0.95 \pm 0.58) \times 10^{-3}, \tag{10.1}$$

within the BGL parametrization, which is in good agreement with the world average of the exclusive approach and the inclusive determination of Refs. [107, 108]. Using the CLN parametrization results in a similar, but lower value,

$$|V_{cb}|_{\text{CLN}} = (40.13 \pm 0.27 \pm 0.93 \pm 0.58) \times 10^{-3}\,. \tag{10.2}$$

The obtained $|V_{cb}|$ values of BGL and CLN parametrizations agree with the recent Belle measurement [104].

We also test the impact of including FNAL/MILC lattice predictions at nonzero recoil from Ref. [103] with the same order of BGL expansion in two scenarios: when nonzero recoil information for h_{A_1} is included, the resulting value of $|V_{cb}|$ decreases slightly. With the full information on all form factors included, the resulting functional dependence on h_{A_1}, R_1 and R_2 is in tension with the FNAL/MILC lattice predictions, and the BGL fit results in a poor p-value of 0.04% if one uses the same number of BGL expansion parameters as for the data only fit. Repeating the fits with more parameters can provide better agreement, but the predicted functional dependence of $R_2(w)$ is in tension with the FNAL/MILC LQCD predictions.

We test the electron-muon LFU by determining the ratio of branching fractions. The result

$$R_{e/\mu} = 0.998 \pm 0.009 \pm 0.020, \tag{10.3}$$

is in good agreement with unity. To further test LFU, we also measure the forward-backward asymmetry and the D^{*+} polarization, and find

$$\Delta\mathcal{A}_{\rm FB} = (-17 \pm 16 \pm 16) \times 10^{-3} \tag{10.4}$$

and

$$\Delta F_L = 0.006 \pm 0.007 \pm 0.005 \tag{10.5}$$

in good agreement with the SM expectations.

As the Belle II experiment is still in its early stages, the amount of collision data collected is less than that accumulated in the Belle experiment. Therefore, the uncertainty on $|V_{cb}|$ in the current measurement is slightly larger than that in a similar analysis carried out by the Belle experiment [23]. However, with a rapid increase in integrated luminosity, the Belle II experiment is poised to improve its precision and surpass previous measurements.

For future untagged measurements of $\bar{B}^0 \to D^{*+}\ell^-\bar{\nu}_\ell$ decays, it would be advantageous to improve the identification of low-momentum leptons. In our current analysis, we require $p_\ell^{\rm CM} > 1.2$ GeV/c to effectively reject the imperfect description of collision data, where misidentified leptons are primarily found. This selection criterion, however, leads to a lower efficiency in the first two bins of the $\cos\theta_\ell$ distribution, as indicated in Table6.7 and Table 6.8. It introduces a dependence on the signal model, which is considered in our uncertainties. Furthermore, it has a notable impact on the precision of determining $\mathcal{A}_{\rm FB}$ and $\Delta\mathcal{A}_{\rm FB}$, as these values are calculated based on the $\cos\theta_\ell$ spectrum. Hence, the enhancement of lepton identification is beneficial for improving the precision of angular asymmetry measurements.

In addition to the measurements of $|V_{cb}|$ from the partial decay rates discussed in this thesis, it is worth noting that the four-dimensional differential decay rate can be expressed in terms of 12 angular coefficients denoted as $J_i(w)$. These coefficients can be measured in bins of w and offer an avenue for extracting form factors and $|V_{cb}|$. The feasibility of this approach has been demonstrated in a prior, not yet published Belle study. This method is considered as an alternative means to cross-verify the value of $|V_{cb}|$ obtained from one-dimensional partial rates. In comparison to one-dimensional partial rates, these angular coefficients capture a more comprehensive set of angular information related to $\bar{B}^0 \to D^{*+}\ell^-\bar{\nu}_\ell$ decays. It is anticipated that these angular coefficients will be measured using Belle II data in the near future.

APPENDIX A

Validation of simulated continuum events

The simulated $e^+e^- \to q\bar{q}$ and $e^+e^- \to \tau^+\tau^-$ events are significant components of the backgrounds. We reconstruct the signal decay chain using collected 18 fb^{-1} of off-resonance data recorded at a CM energy of $\sqrt{s} = 10.52$ GeV, applying the same criteria outlined in Table 4.1 for the candidate selection. We then compare the distributions of $\cos\theta_{BY}$, ΔM, w, $\cos\theta_\ell$, $\cos\theta_V$, and χ with the corresponding distributions from simulated samples. The results are presented in Fig. A.1 and Fig. A.2 for the $\bar{B}^0 \to D^{*+}e^-\bar{\nu}_e$ and $\bar{B}^0 \to D^{*+}\mu^-\bar{\nu}_\mu$ decays, respectively. Most data points from the two channels fluctuate within the predicted statistical uncertainties of the simulated samples.

exhibit excellent agreement between the collected data and simulated samples.

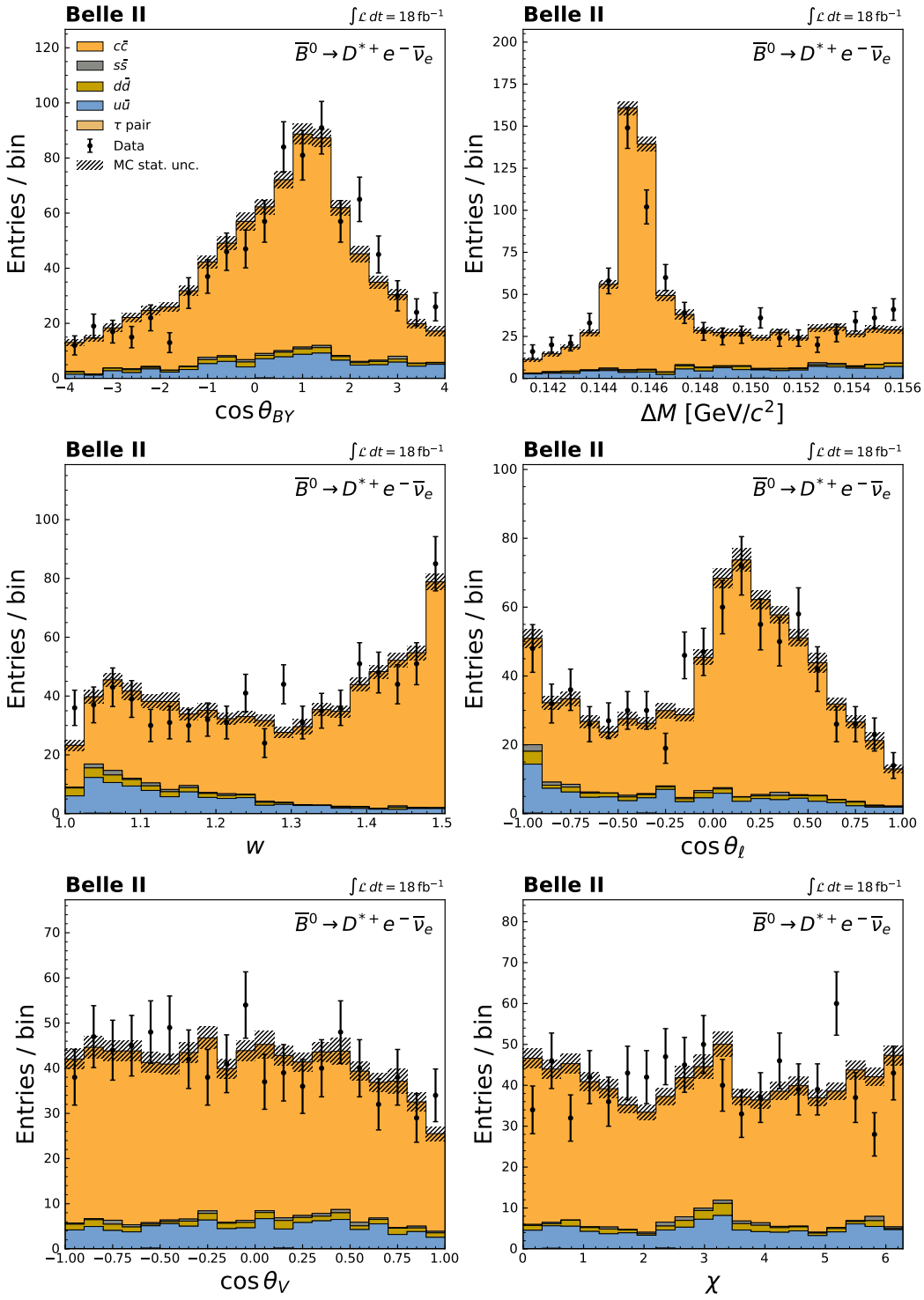

Figure A.1: Distributions of $\cos\theta_{BY}$, ΔM, w, $\cos\theta_\ell$, $\cos\theta_V$, and χ for the $\bar{B}^0 \to D^{*+} e^- \bar{\nu}_e$ decay reconstructed using off-resonance experimental data and simulated $e^+e^- \to q\bar{q}$ and $e^+e^- \to \tau^+\tau^-$ events. The simulated samples are normalized to match the number of events in the data. The hashed area represents the statistical uncertainty.

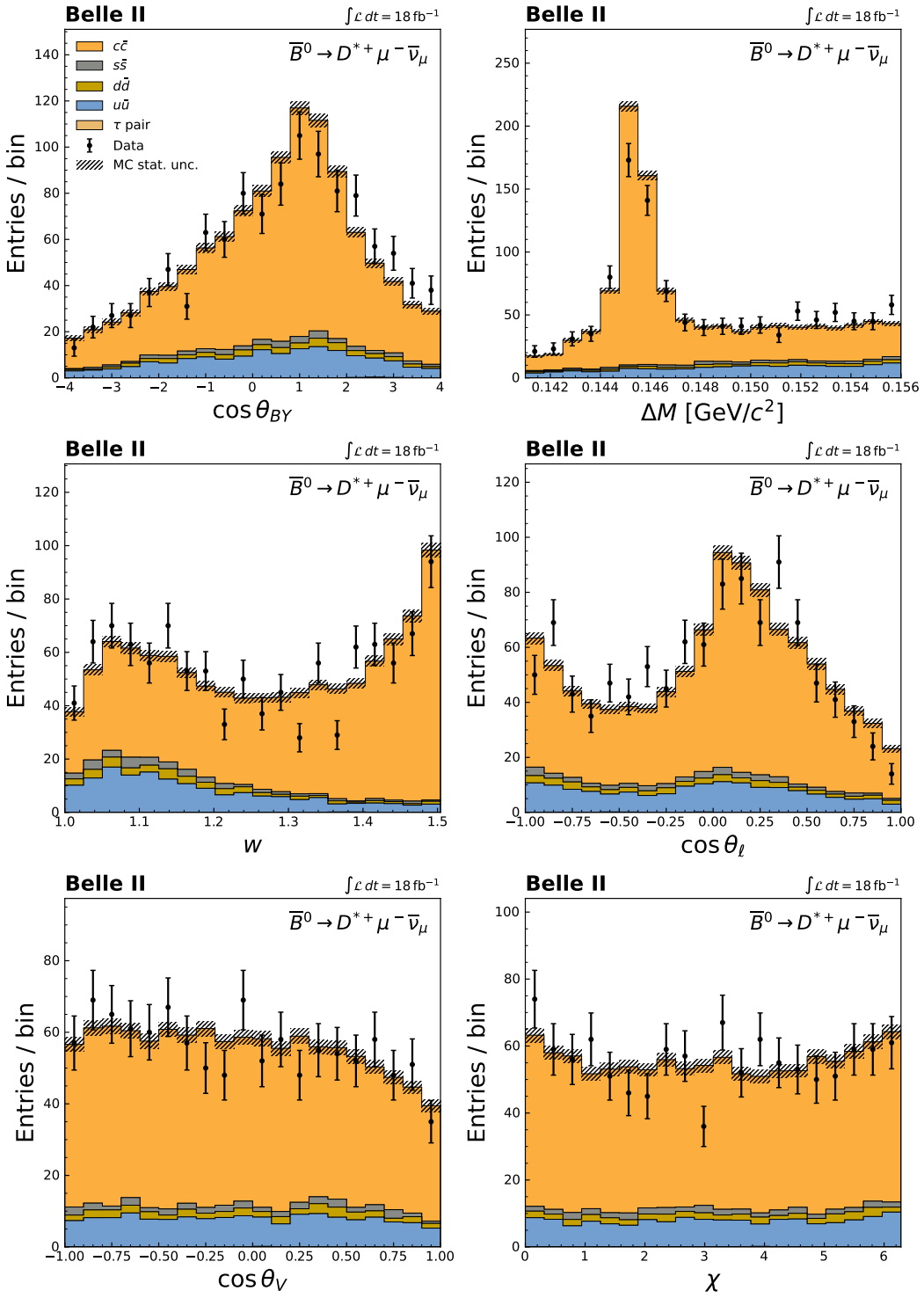

Figure A.2: Distributions of $\cos\theta_{BY}$, ΔM, w, $\cos\theta_\ell$, $\cos\theta_V$, and χ for the $\bar{B}^0 \to D^{*+}\mu^-\bar{\nu}_\mu$ decay reconstructed using off-resonance experimental data and simulated $e^+e^- \to q\bar{q}$ and $e^+e^- \to \tau^+\tau^-$ events. The simulated samples are normalized to match the number of events in the data. The hashed area represents the statistical uncertainty.

APPENDIX B

Slow pion tracking efficiency

In this study, our focus is on pions with momenta below 200 MeV/c. This is because the reconstruction of particles with low momenta is challenging. Such particles are significantly influenced by multiple Coulomb scattering and energy loss in the material, making their trajectories difficult to reconstruct accurately. Additionally, most of these tracks are recorded by only four layers of the SVD, while within the CDC volume, these particles curve multiple times, generating hundreds of hits. Calibration of their tracking efficiencies is important for the physics analyses of $\bar{B}^0 \to D^{*+}\ell^-\bar{\nu}_\ell$ decays and is part of my PhD research.

D^{*+} mesons produced in $e^+e^- \to c\bar{c}$ events are more energetic than those in $B\bar{B}$ events, as are their daughter pions. To focus exclusively on pions with similar momentum, We reconstruct the $\bar{B}^0 \to D^{*+}\pi^-$ decay, where the D^{*+} meson subsequently decay to the D^0 meson and the slow pion π_s^+. Further, D^0 candidates are reconstructed from the $K^-\pi^+$, $K^-\pi^+\pi^+\pi^-$, and $K_S^0\pi^+\pi^-$ final states.

To ensure the purity of the reconstructed events, we apply the selection criteria outlined in Table B.1. All tracks corresponding to kaons and pions must have a distance of closest approach to the interaction point of less than 4.0 cm along the z direction (d_z) and less than 2.0 cm in the transverse $r-\phi$ plane (d_r). Additionally, the binary likelihood ratio for kaon (pion) identification, $\mathcal{L}_{K/\pi}$ ($\mathcal{L}_{\pi/K}$), must exceed 0.4.

To minimize the fraction of incorrectly reconstructed D^0 and D^{*+} meson candidates, we require the invariant mass of the $K^-\pi^+$ system to fall within a window of ± 40 MeV/c^2 from the known D^0 mass. Furthermore, the mass difference between D^{*+} and D^0 candidates, ΔM, must lie within the range of $[0.143, 0.147]$ GeV/c^2.

Since the $e^+e^- \to c\bar{c}$ process significantly contributes to the reconstructed events, we suppress these contributions by imposing restrictions: the momentum of D^{*+} candidates in the CM frame must be less than 2.5 GeV/c, and the ratio of the second and the zeroth order Fox-Wolfram moments, R_2, must be below 0.3.

In addition, two beam energy related variables are calculated for each event:

$$M_{bc} = \sqrt{E_{\text{beam}}^2 - \vec{p}_B^{\,2}}, \tag{B.1}$$

and

$$\Delta E = E_B - E_{\text{beam}}, \tag{B.2}$$

with $E_{\text{beam}} = \sqrt{s}/2$, and $\vec{p}_B^{\,2}$ and E_B denoting the 3-momenta and energies of B candidates, respectively. Events with values of M_{bc} outside the range $[5.27, 5.29]$ GeV/c^2, or absolute values of ΔE greater than 0.2 GeV/c, are excluded from the subsequent analysis.

Moreover, it is observed that some final-state kaons and pions originating from the $D^0 \to K^-\pi^+\pi^+\pi^-$ decay have momenta below 200 MeV/c. To guarantee the presence of, at most, only one "slow" track per event, events containing such particles are excluded from the analysis.

Table B.1: Selection criteria employed in the study of slow pion tracking efficiency.

Variable	Range
d_r	< 2 cm
$\lvert d_z \rvert$	< 4 cm
$\mathcal{L}_{K/\pi}$ (for K)	> 0.4
$\mathcal{L}_{\pi/K}$ (for π)	> 0.4
$\lvert M_{K\pi} - M_{D^0}^{\text{PDG}} \rvert$	< 0.04 GeV/c^2
ΔM	$\in [0.143, 0.147]$ GeV/c^2
$p^*_{D^{*+}}$	< 2.5 GeV/c
R_2	< 0.3
M_{bc}	$\in [5.27, 5.29]$ GeV/c^2
$\lvert \Delta E \rvert$	< 0.2 GeV/c

The simulated samples are then categorized into the signal, $B\bar{B}$ background, and continuum background as follows

- Signal: the entire decay chain is reconstructed correctly.
- $B\bar{B}$ background: reconstructed events correspond to the simulated $e^+e^- \to \Upsilon(4S) \to B\bar{B}$ processes; however, the signal decay chain is not completely reconstructed correctly.
- Continuum background: reconstructed events correspond to the simulated continuum processes.

The simulated samples are compared to the experimental data concerning the distributions of ΔE and slow pion momentum in the lab frame, as depicted in Fig. B.1. The pull in each bin is defined as

$$\text{Pull} = \frac{N^{\text{Data}} - N^{\text{MC}}}{\sqrt{\sigma^{\text{Data}} + \sigma^{\text{MC}}}}, \tag{B.3}$$

where N^{Data} and N^{MC} represent the numbers of events in collision data and simulated samples, respectively, and σ^{Data} and σ^{MC} denote the uncertainties of data and simulated samples,

respectively.

The simulated distributions agree well with the experimental data in terms of their shapes. However, a noticeable deficit in the data is observed around the signal-enriched region in the ΔE distribution across all three reconstructed decay channels. This discrepancy implies a reduced efficiency in signal reconstruction when compared to the simulated results.

We divide the slow pion momentum into four bins spanning [0.05, 0.12, 0.16, 0.2, 0.32] GeV/c to assess efficiency differences across these momentum ranges. The agreement between experimental data and simulated samples in the last momentum bin serves as a reference point for deriving the relative efficiency in the low momentum range.

The expected values of the simulation are derived directly from the luminosity ratio

$$N_{\mathrm{MC}}^{\mathrm{exp}} = N_{\mathrm{MC}}^{\mathrm{sig}} \frac{\mathcal{L}_{\mathrm{data}}}{\mathcal{L}_{\mathrm{MC}}}, \tag{B.4}$$

where $N_{\mathrm{MC}}^{\mathrm{sig}}$ denotes the number of selected signal events. The signal yield in each bin for experimental data is independently determined through a binned likelihood fit of the ΔE spectrum similarly to the fit described in Sec. 6.1. In this fit, the signal component peaks near zero, while the other two components have a broader span. The post-fit plots for the four bins are shown in Fig. B.2.

The expected number of signal events in simulated samples and the fitted yields for experimental data are summarized in Table B.2. The reconstruction efficiency of slow pions is defined as the ratio of the reconstructed tracks ($N^{\mathrm{reco.}}$) and all the slow pion tracks (N^{all}) in the data set,

$$\epsilon = \frac{N^{\mathrm{reco.}}}{N^{\mathrm{all}}}. \tag{B.5}$$

The ratio of efficiencies between data and MC can be approximated as

$$r = \frac{\epsilon_{\mathrm{data}}}{\epsilon_{\mathrm{MC}}} = \frac{N_{\mathrm{data}}^{\mathrm{reco.}}}{N_{\mathrm{data}}^{\mathrm{all}}} \frac{N_{\mathrm{MC}}^{\mathrm{all}}}{N_{\mathrm{MC}}^{\mathrm{exp}}} \simeq \frac{N_{\mathrm{data}}^{\mathrm{reco.}}}{N_{\mathrm{MC}}^{\mathrm{exp}}}, \tag{B.6}$$

where the total number of slow pion tracks in experimental data does not significantly differ from the simulation with the same luminosity. The ratio $N_{\mathrm{data}}^{\mathrm{fit}}/N_{\mathrm{MC}}^{\mathrm{exp}}$ is thus calculated for each bin.

The mid to high momentum tracking efficiency has been extensively studied independently using a tag-and-probe method with τ-pair events (see Sec. 7.3). In these events, the kinematics of the τ leptons cover a wide track momentum range from 200 MeV/c up to 3.5 GeV/c. The analysis reveals that the ratio of reconstruction efficiencies between calibrated experimental data and simulation is consistent with unity. Therefore, the deviation of the ratio $N_{\mathrm{data}}^{\mathrm{fit}}/N_{\mathrm{MC}}^{\mathrm{exp}}$ from unity in the momentum bin of [0.2, 0.32] GeV/c is attributed to differences in particle identification efficiencies and K_S^0 reconstruction. Assuming these differences are uncorrelated with the slow pion track momentum, a relative efficiency ratio (f) is calculated by normalizing the $N_{\mathrm{data}}^{\mathrm{fit}}/N_{\mathrm{MC}}^{\mathrm{exp}}$ ratios in the first three bins to the last bin. The uncertainties of f that are uncorrelated and

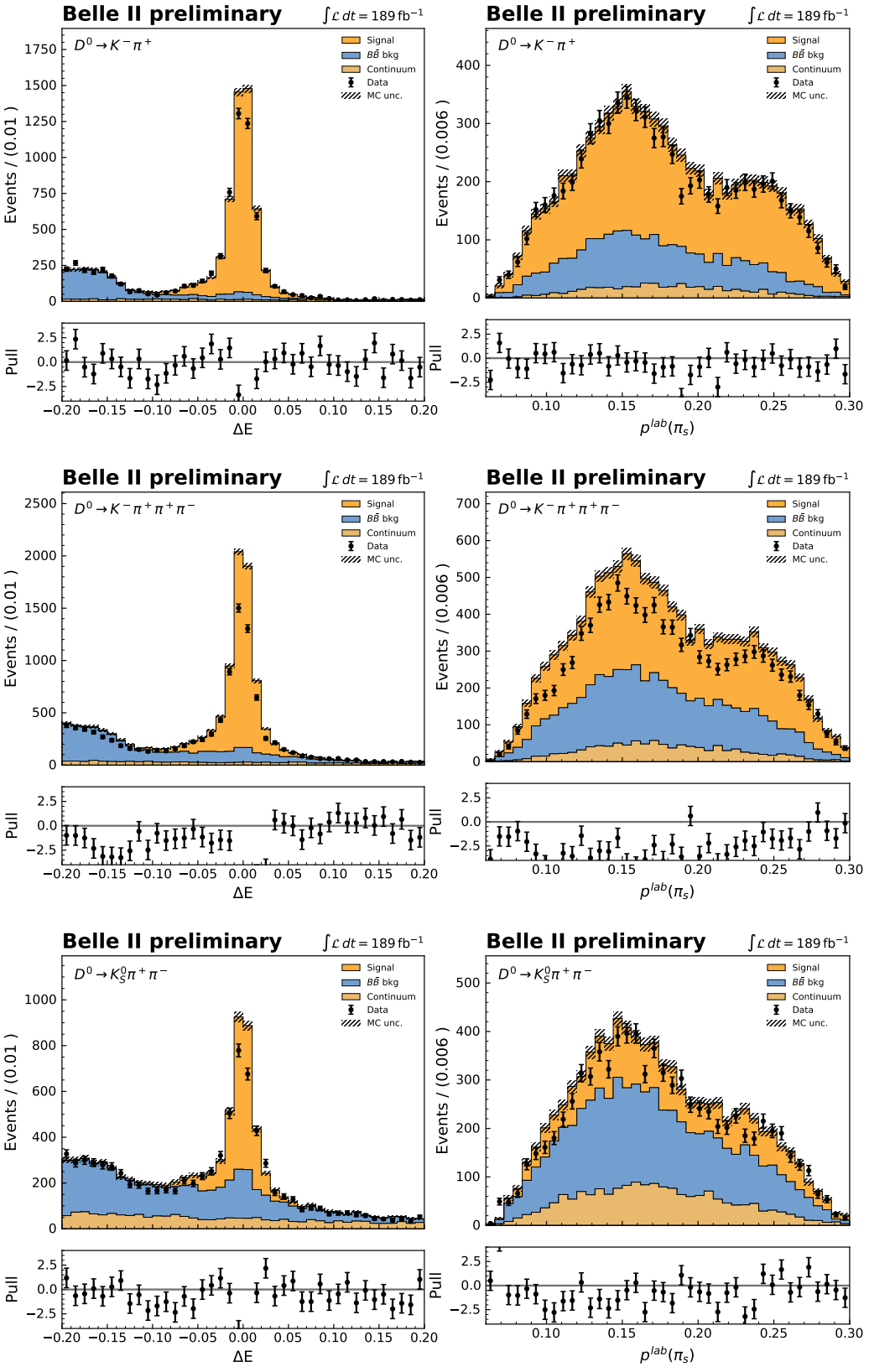

Figure B.1: Distributions of ΔE (left) and slow pion momentum $p^{\mathrm{lab}}_{\pi_s}$ (right) for the $D^0 \to K^-\pi^+$, $D^0 \to K^-\pi^+\pi^+\pi^-$, and $D^0 \to K^0_S\pi^+\pi^-$ decays, arranged from top to bottom, respectively. The simulated samples are weighted according to integrated luminosity. The error bars represent the statistical uncertainties for data, while the hashed areas represent the corresponding uncertainties for simulated samples.

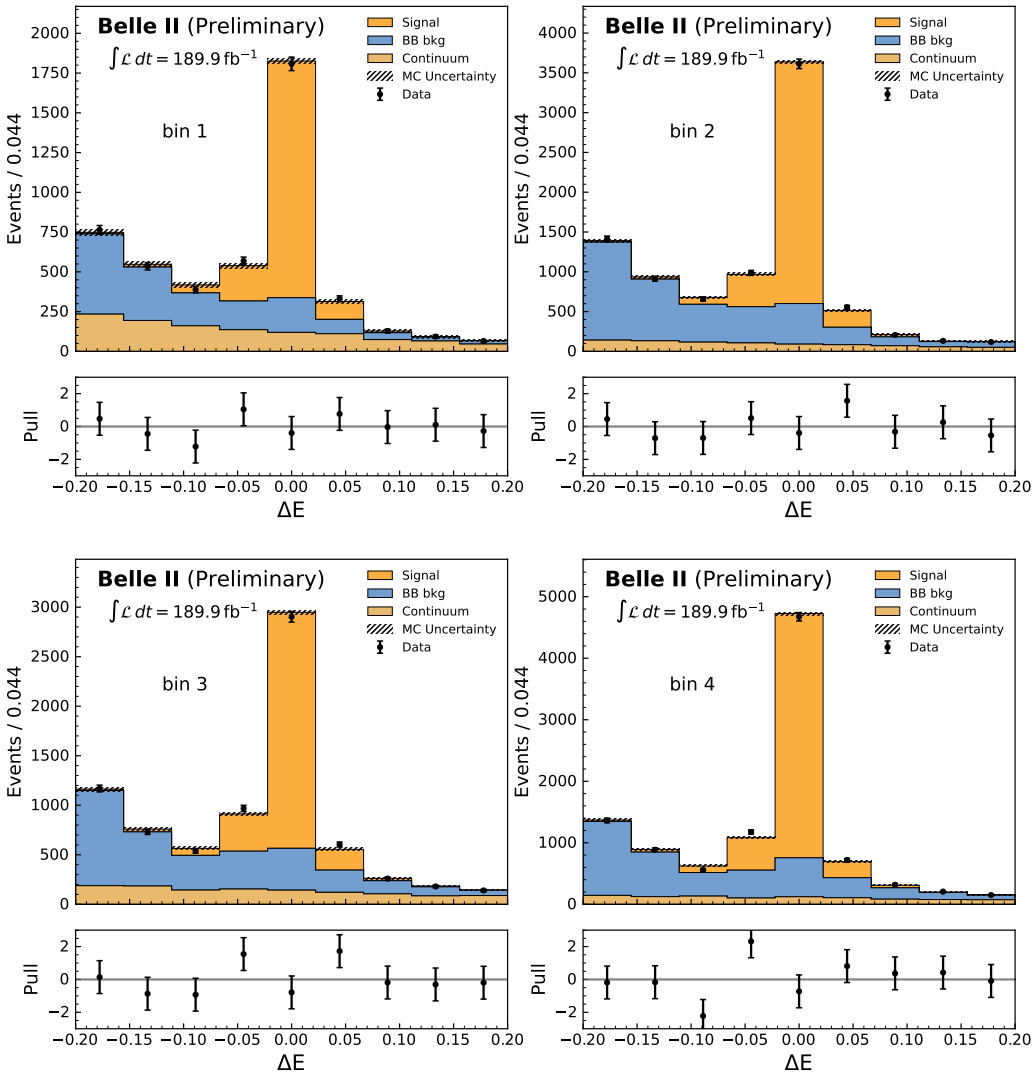

Figure B.2: Post-fit plots of the ΔE distribution for the determination of signal yields in bins of the slow pion momentum.

Table B.2: Summary of expected numbers of signal events in the simulated samples and the fitted yields for the experimental data. The uncertainties associated with the expectations for MC are purely statistical, while the uncertainties on the fitted yields encompass both statistical and systematic uncertainties originating from the finite MC samples. Furthermore, the relative efficiency f in the low momentum range, along with its uncorrelated (σ_f^{uncor}) and correlated (σ_f^{cor}) uncertainties, is provided.

Momentum bin (in GeV)	$[0.05, 0.12]$	$[0.12, 0.16]$	$[0.16, 0.20]$	$[0.20, 0.32]$
$N_{\text{MC}}^{\text{exp}}$	$2\,551 \pm 51$	$4\,486 \pm 67$	$3\,886 \pm 62$	$6\,047 \pm 78$
$N_{\text{data}}^{\text{fit}}$	$1\,914 \pm 55$	$3\,824 \pm 76$	$3\,115 \pm 72$	$4\,989 \pm 87$
$r = N_{\text{data}}^{\text{fit}}/N_{\text{MC}}^{\text{exp}}$	0.750 ± 0.026	0.852 ± 0.021	0.802 ± 0.022	0.825 ± 0.018
f	0.909	1.033	0.971	1
σ_f^{uncor}	0.032	0.026	0.027	
σ_f^{cor}	0.020	0.022	0.021	

correlated between different momentum ranges are derived using the following equations,

$$\sigma_{f_i}^{\text{uncor}} = \frac{1}{r_4}\sigma_{r_i}, \tag{B.7}$$

and

$$\sigma_{f_i}^{\text{cor}} = \frac{r_i}{r_4^2}\sigma_{r_4}, \tag{B.8}$$

where σ_{r_i} represents the uncertainty of the ratio $N_{\text{data}}^{\text{fit}}/N_{\text{MC}}^{\text{exp}}$ in the i-th bin. The obtained values are summarized in Table B.2.

The simulated reconstruction efficiencies of tracks in the momentum ranges of [0.12, 0.16] and [0.16, 0.20] GeV/c align with the experimental data within their uncertainties. However, in the first momentum bin, the simulated efficiency is approximately 10% higher than the experimental data. These results are utilized to correct for slow pions produced in $\bar{B}^0 \to D^{*+}\ell^-\bar{\nu}_\ell$ decays.

APPENDIX C

Migration matrices

The migration matrices for the $\bar{B}^0 \to D^{*+}\mu^-\bar{\nu}_\mu$ decay with the w, $\cos\theta_\ell$, $\cos\theta_V$, and χ are reconstructed using the diamond frame, ROE, and combined methods are shown in Fig. C.1, Fig. C.2, and Fig. C.3, respectively.

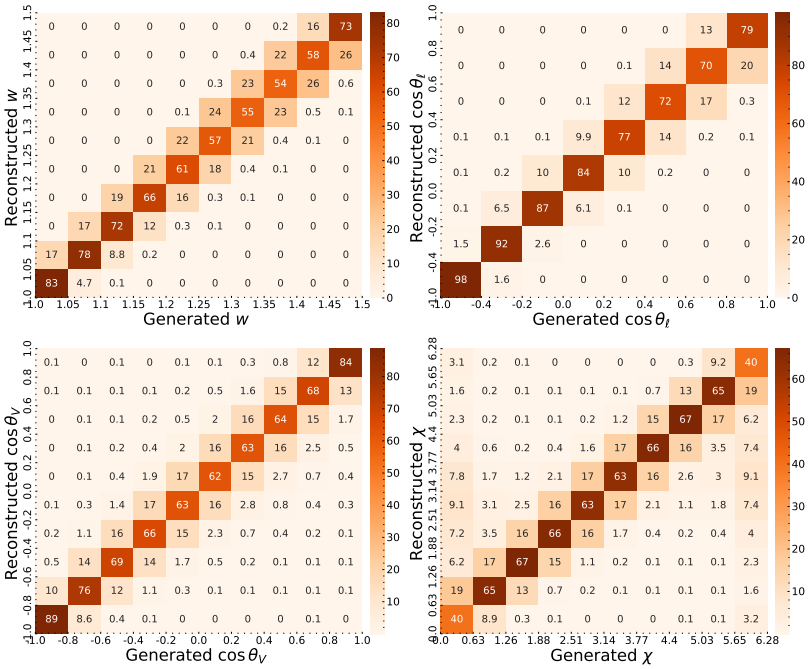

Figure C.1: The migration matrices of kinematic variables w, $\cos\theta_\ell$, $\cos\theta_V$, and χ reconstructed by the diamond frame method for the $\bar{B}^0 \to D^{*+}\mu^-\bar{\nu}_\mu$ decay.

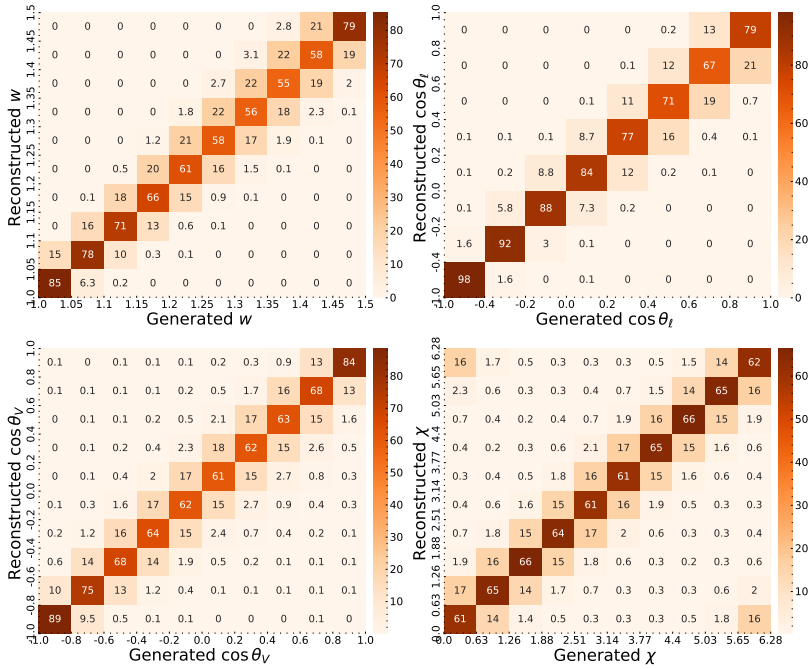

Figure C.2: The migration matrices of kinematic variables w, $\cos\theta_\ell$, $\cos\theta_V$, and χ reconstructed by the ROE approach for the $\bar{B}^0 \to D^{*+}\mu^-\bar{\nu}_\mu$ decay.

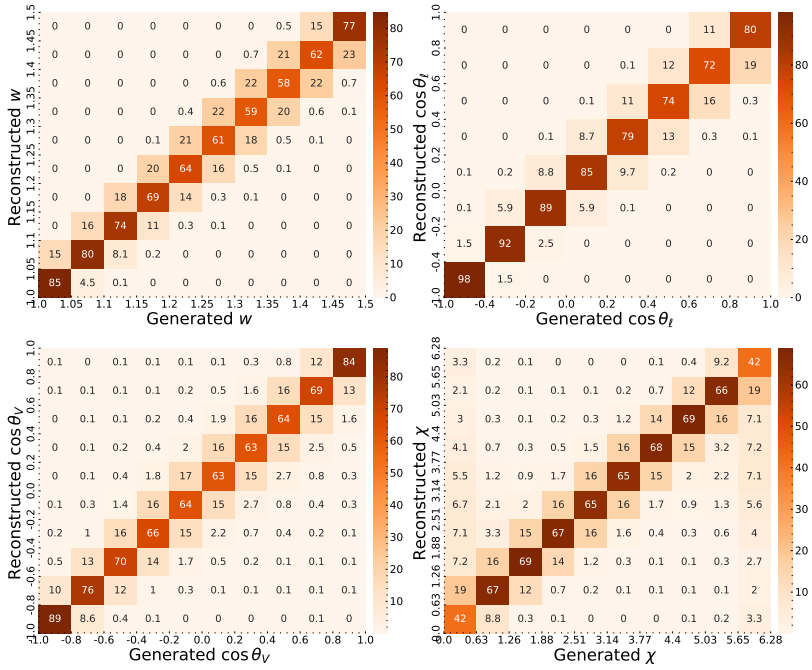

Figure C.3: The migration matrices of kinematic variables w, $\cos\theta_\ell$, $\cos\theta_V$, and χ reconstructed by the combined approach for the $\bar{B}^0 \to D^{*+}\mu^-\bar{\nu}_\mu$ decay.

APPENDIX D

Robustness of signal extraction

D.1 Linearity check

In this test, we apply 20 distinct weights ranging from 0.5 to 2.0 with uniform intervals to the reconstructed signal decays, keeping the backgrounds unchanged. Subsequently, we perform fits on the resulting toy distributions using the original, non-weighted signal and background templates. To validate the correctness of the fitted yields, we examine the relationship between the applied weights and the ratios $N^{\text{fit}}/N^{\text{sel}}$, where N^{fit} represents the fitted yields, and N^{sel} represents the count of selected signal decays before any reweighting.

In addition, we explore an alternative scenario where the reconstructed background events are weighted with values ranging from 0.5 to 2.0. We then fit to resulting distributions using the original, non-weighted signal and background templates, and crosscheck the consistency between these applied weights and the ratios of the fitted signal yield to the input signal events $N^{\text{fit}}/N^{\text{sel}}$.

We present the results corresponding to those two scenarios in Fig. D.1. In the first scenario, the relationship between the reweighing factor and the ratio $N^{\text{fit}}/N^{\text{sel}}$ can be represented by a straight line with a slope $m = 1$ and an offset $b = 0$, indicating that the fitted yields remain consistent with respect to the weights. It is observed that, in the second case, the fitted yields show no variation in response to changes in backgrounds.

This test has also been conducted separately for each bin of kinematic variables, although the detailed plots are not included here due to space constraints. In summary, the linear relationship holds consistently across all these scenarios, aligning with our expectations.

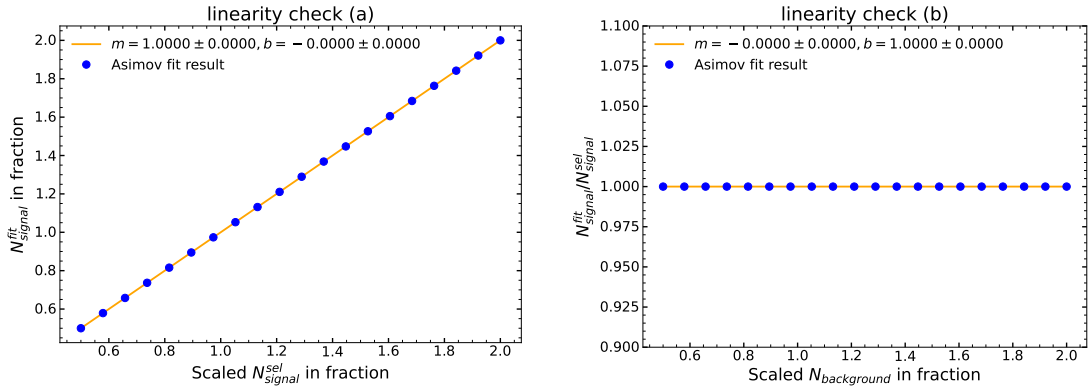

Figure D.1: Linearity check for fits. The left plot illustrates the variations in ratios $N^{\text{fit}}_{\text{signal}}/N^{\text{sel}}_{\text{signal}}$ corresponding to the weights applied on the signal template. Conversely, the right plot demonstrates how ratios $N^{\text{fit}}_{\text{signal}}/N^{\text{sel}}_{\text{signal}}$ vary concerning the weights applied on the background template.

D.2 Toy study

The toy fits are conducted to ensure the unbiasedness of the signal extraction and the accurate estimation of uncertainties. In this test, we generate 10000 pseudo-distributions by assigning random candidate-wise weights drawn from a Poisson distribution with $\lambda = 1$. Importantly, we guarantee that multiple candidates within the same event share identical weights, establishing full correlation among these candidates.

We apply random weights to the simulated samples and fit the resulting $\cos\theta_{BY}$ and ΔM distributions using the three templates, with the nuisance parameters fixed at zero. This procedure is carried out separately for samples within each bin of kinematic variables. The pull value is computed using the formula:

$$\text{Pull} = \frac{N^{\text{toy}} - N^{\text{Asimov}}}{\sigma^{\text{stat.}}}. \tag{D.1}$$

In this equation, N^{toy} and N^{Asimov} represent the fitted yields in the toy data set and Asimov data set, respectively. Here, $\sigma^{\text{stat.}}$ represents the statistical uncertainty associated with the fitted yields.

The normalized pull distributions for w, $\cos\theta_\ell$, $\cos\theta_V$, and χ are depicted in Fig. D.2 to Fig. D.5 respectively. These distributions are fitted using Gaussian functions, and the resulting means and standard deviations are provided above the respective plots. In the absence of bias, we anticipate the peak of each distribution to be centered at zero. If the uncertainties are neither overestimated nor underestimated, we expect to observe a standard deviation of $\sigma = 1$. Overall, our observations indicate that the fitted values align with our expectations.

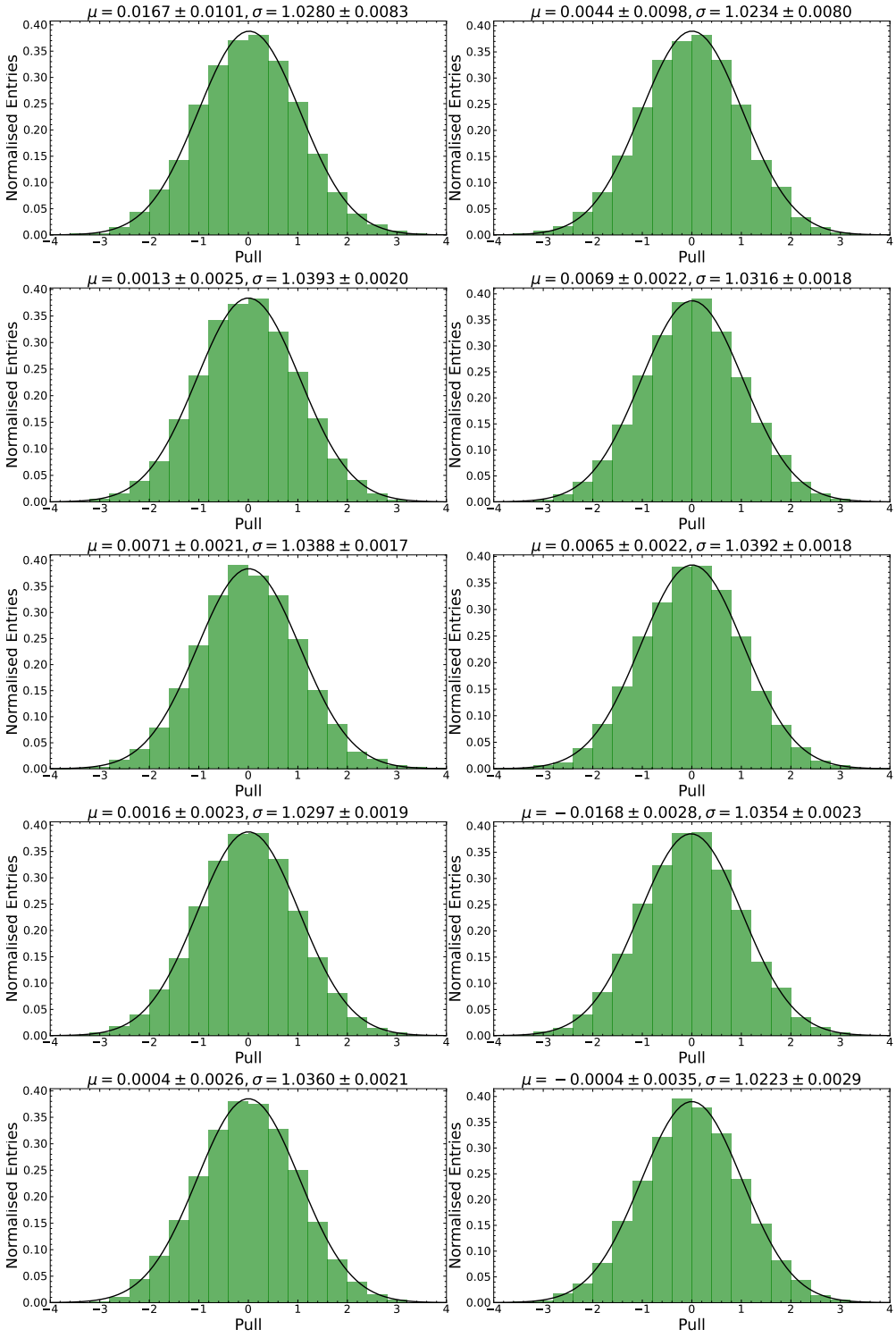

Figure D.2: Pull distributions that validate fits for signal extraction in w bins, and Gaussian parameters that describe the distributions are provided.

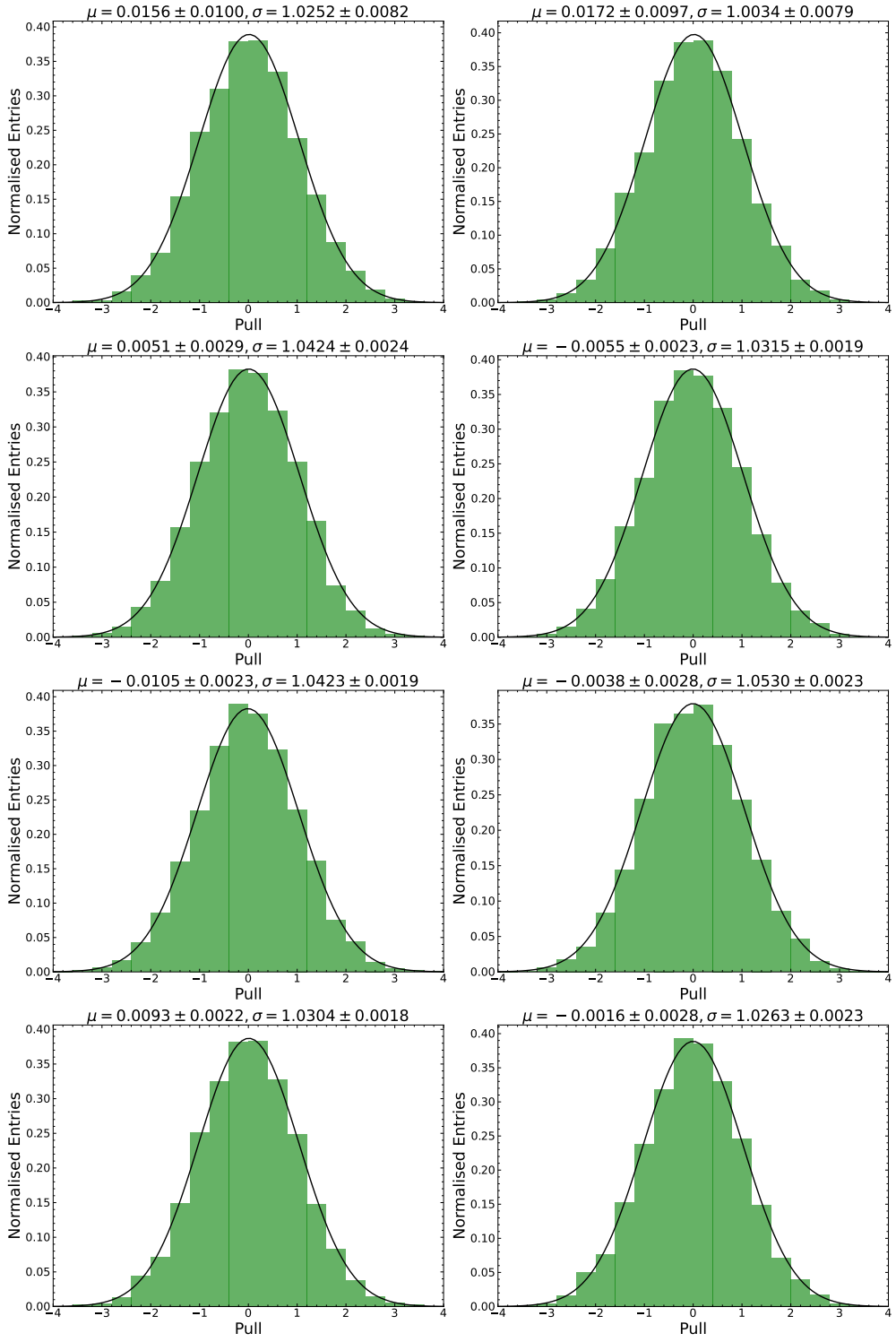

Figure D.3: Pull distributions that validate fits for signal extraction in $\cos\theta_\ell$ bins, and Gaussian parameters that describe the distributions are provided.

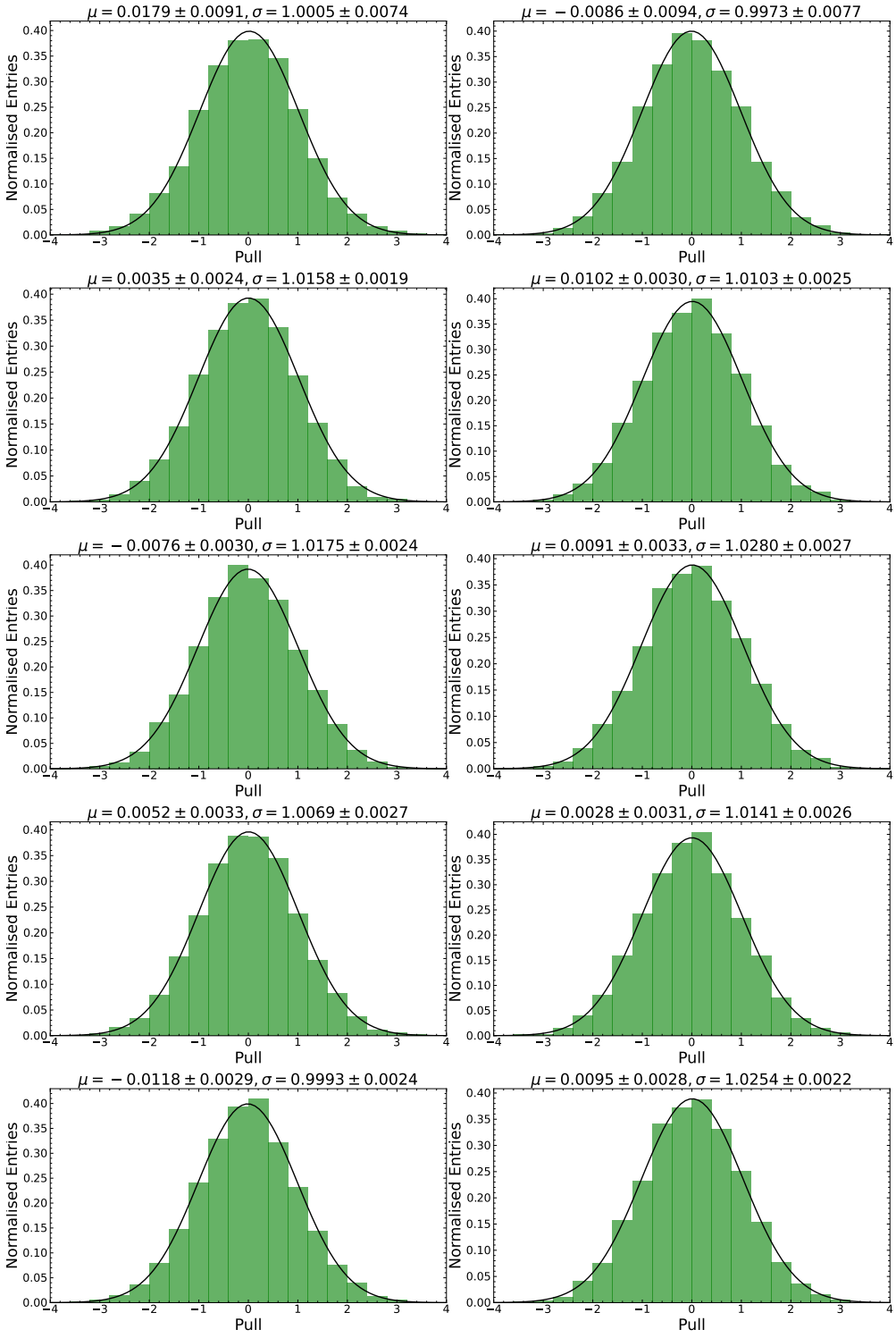

Figure D.4: Pull distributions that validate fits for signal extraction in $\cos\theta_V$ bins, and Gaussian parameters that describe the distributions are provided.

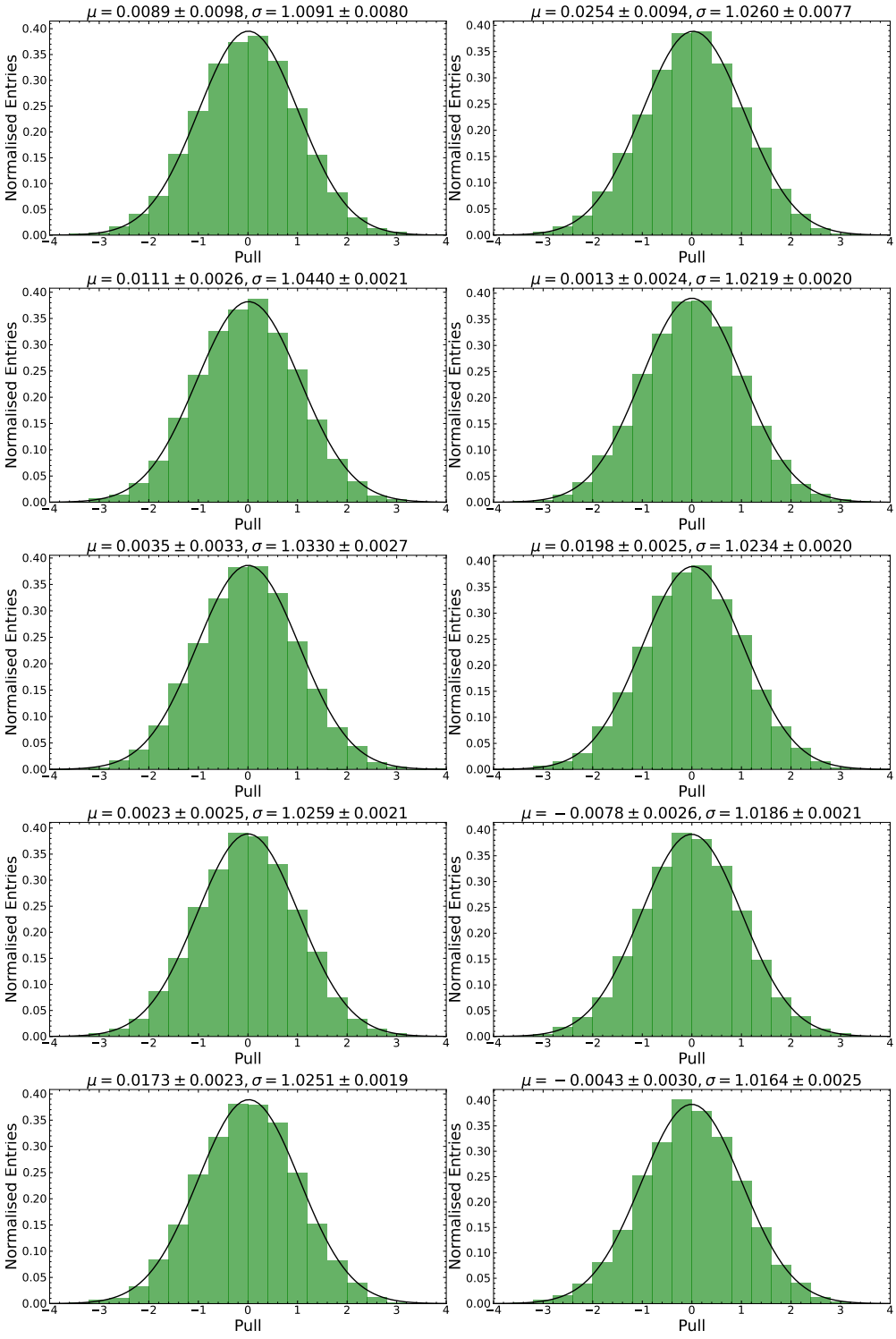

Figure D.5: Pull distributions that validate fits for signal extraction in χ bins, and Gaussian parameters that describe the distributions are provided.

APPENDIX E

Post-fit plots of $\cos\theta_{BY}$ and ΔM

In this section, we present post-fit plots of $\cos\theta_{BY}$ and ΔM distributions, depicted in Figs. E.2 to E.9 for the $\bar{B}^0 \to D^{*+} e^- \bar{\nu}_e$ decay, and Figs. E.10 to E.17 for the $\bar{B}^0 \to D^{*+} \mu^- \bar{\nu}_\mu$ decay, respectively. In these plots, the fractions of the simulated components in each bin have been adjusted based on binned likelihood fits described in Eq. (6.4). Note that we determine the $\cos\theta_{BY}$ and ΔM plots on projection of the two-dimensional fit templates Additionally, χ^2/ndf values for two-dimensional fits, along with their corresponding p-values, are provided to assess the goodness of the fits. These p-values are summarized in a distribution shown in Fig. E.1, demonstrating compatibility with the expected uniform behavior.

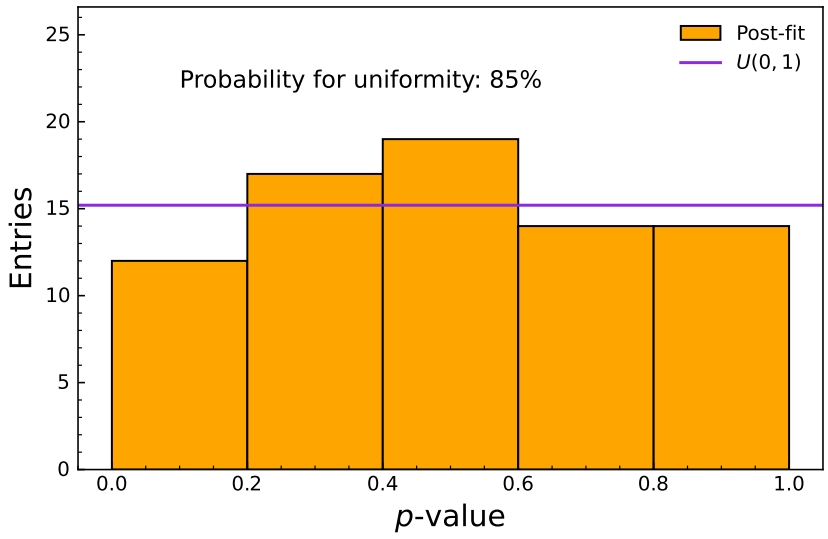

Figure E.1: Distribution of the p-values derived from a total of 76 fits conducted across 2 decay channels and 38 kinematic regions. This distribution conforms to the anticipated uniformity of a $U(0,1)$ distribution, as evidenced by the calculated probability of uniformity.

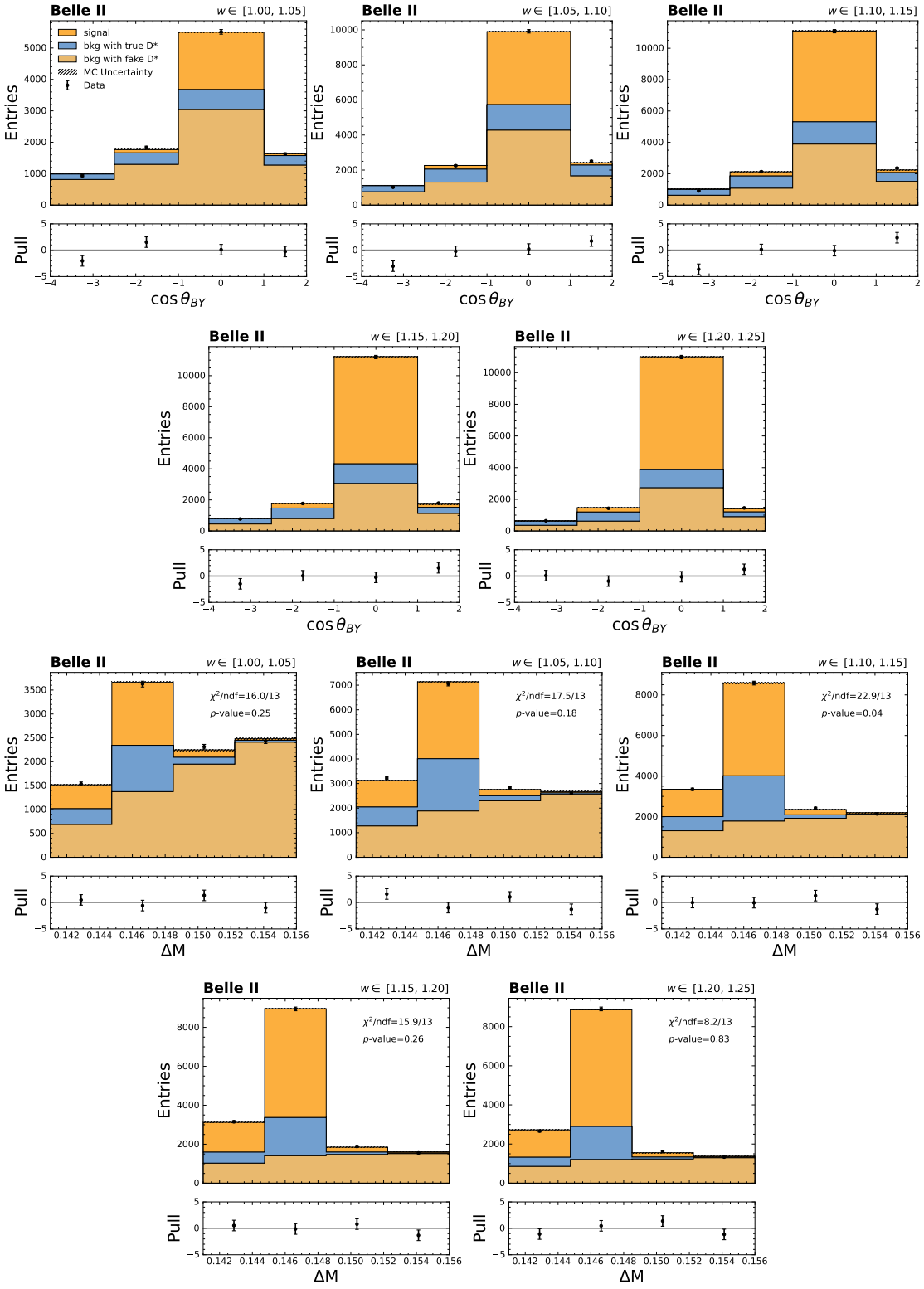

Figure E.2: Post-fit plots of $\cos\theta_{BY}$ (first 2 rows) and ΔM (last 2 rows) distributions for the first 5 w bins of the $\bar{B}^0 \to D^{*+} e^- \bar{\nu}_e$ decay.

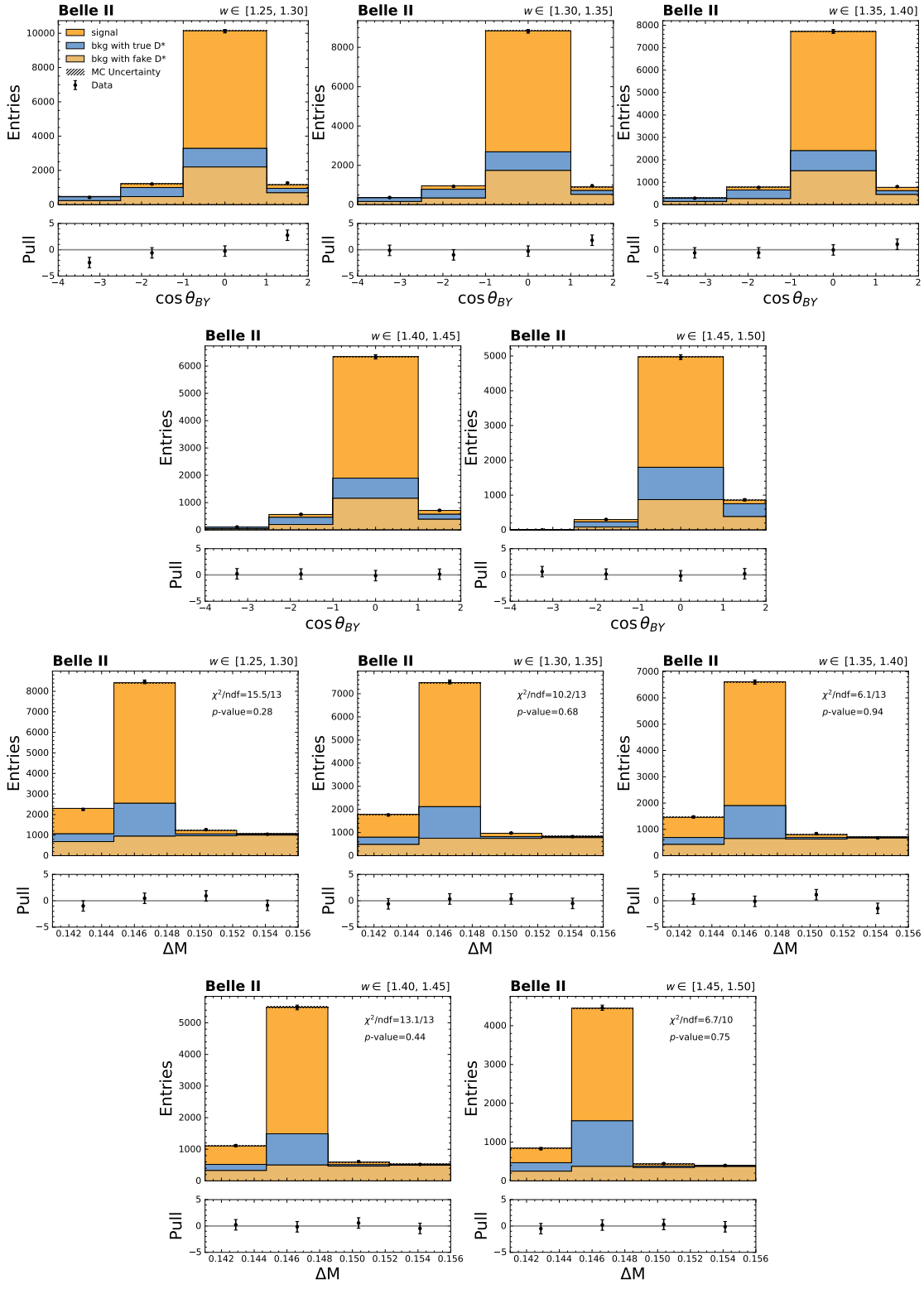

Figure E.3: Post-fit plots of $\cos\theta_{BY}$ (first 2 rows) and ΔM (last 2 rows) distributions for the last 5 w bins of the $\bar{B}^0 \to D^{*+} e^- \bar{\nu}_e$ decay.

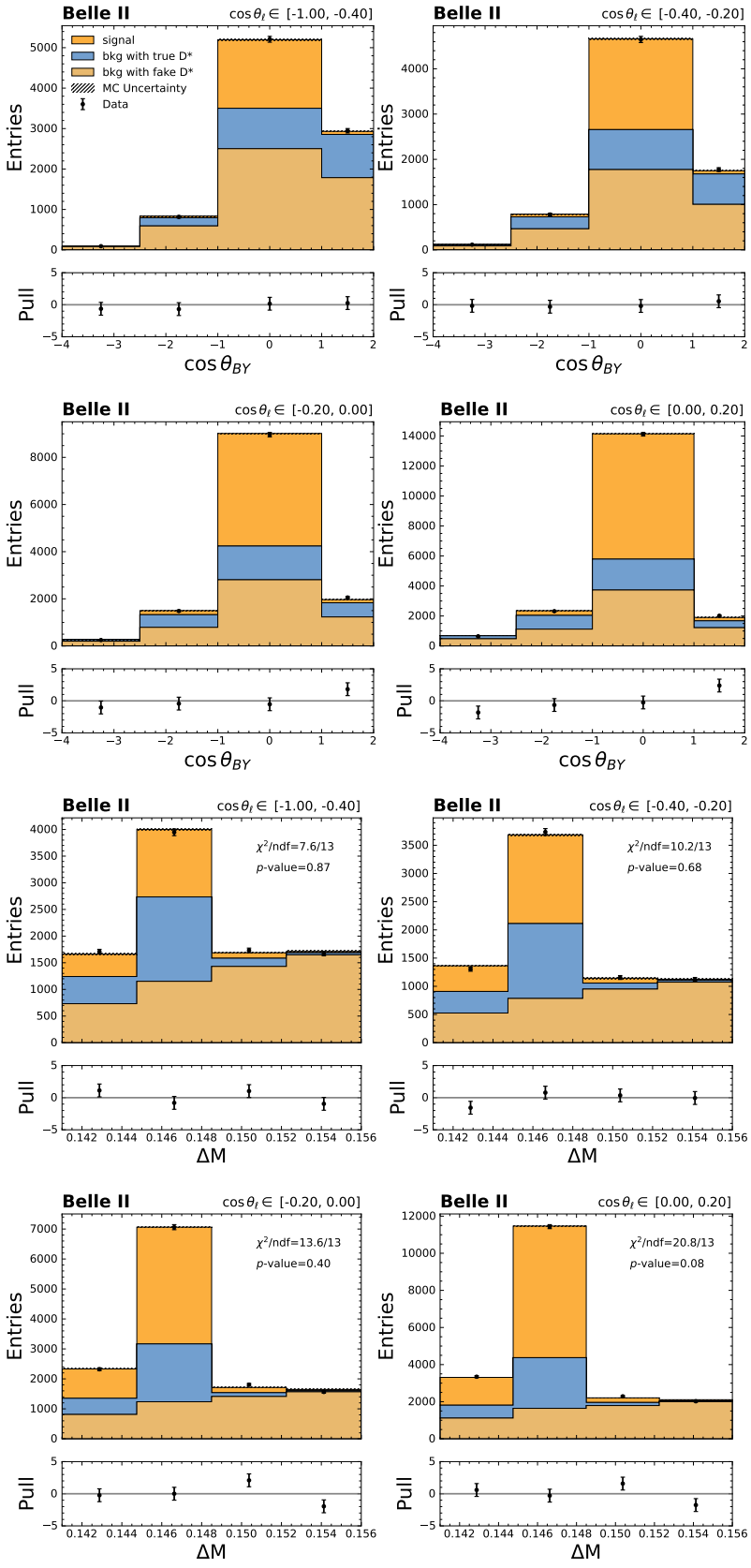

Figure E.4: Post-fit plots of $\cos\theta_{BY}$ (first 2 rows) and ΔM (last 2 rows) distributions for the first 4 $\cos\theta_\ell$ bins of the $\bar{B}^0 \to D^{*+} e^- \bar{\nu}_e$ decay.

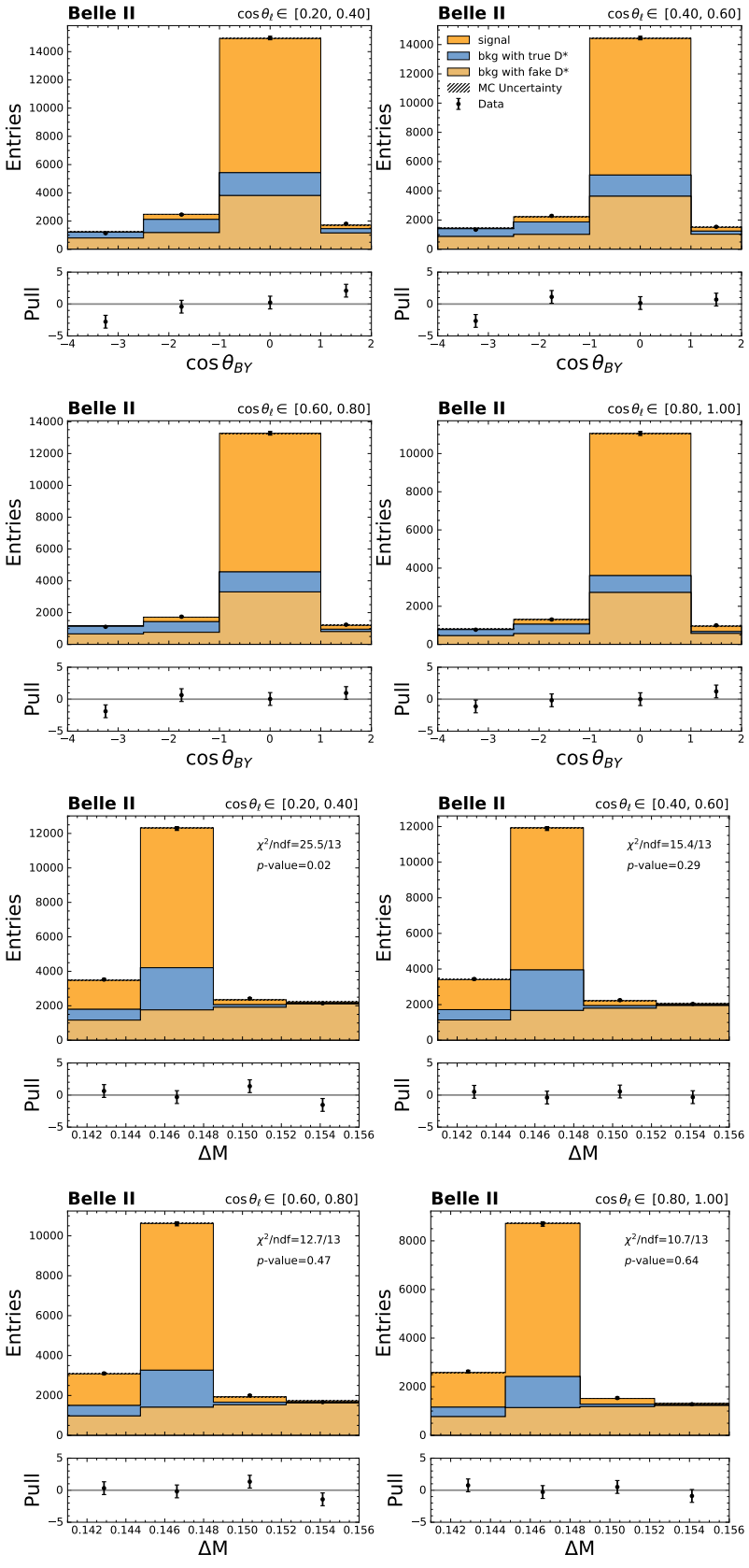

Figure E.5: Post-fit plots of $\cos\theta_{BY}$ (first 2 rows) and ΔM (last 2 rows) distributions for the last 4 $\cos\theta_\ell$ bins of the $\bar{B}^0 \to D^{*+} e^- \bar{\nu}_e$ decay.

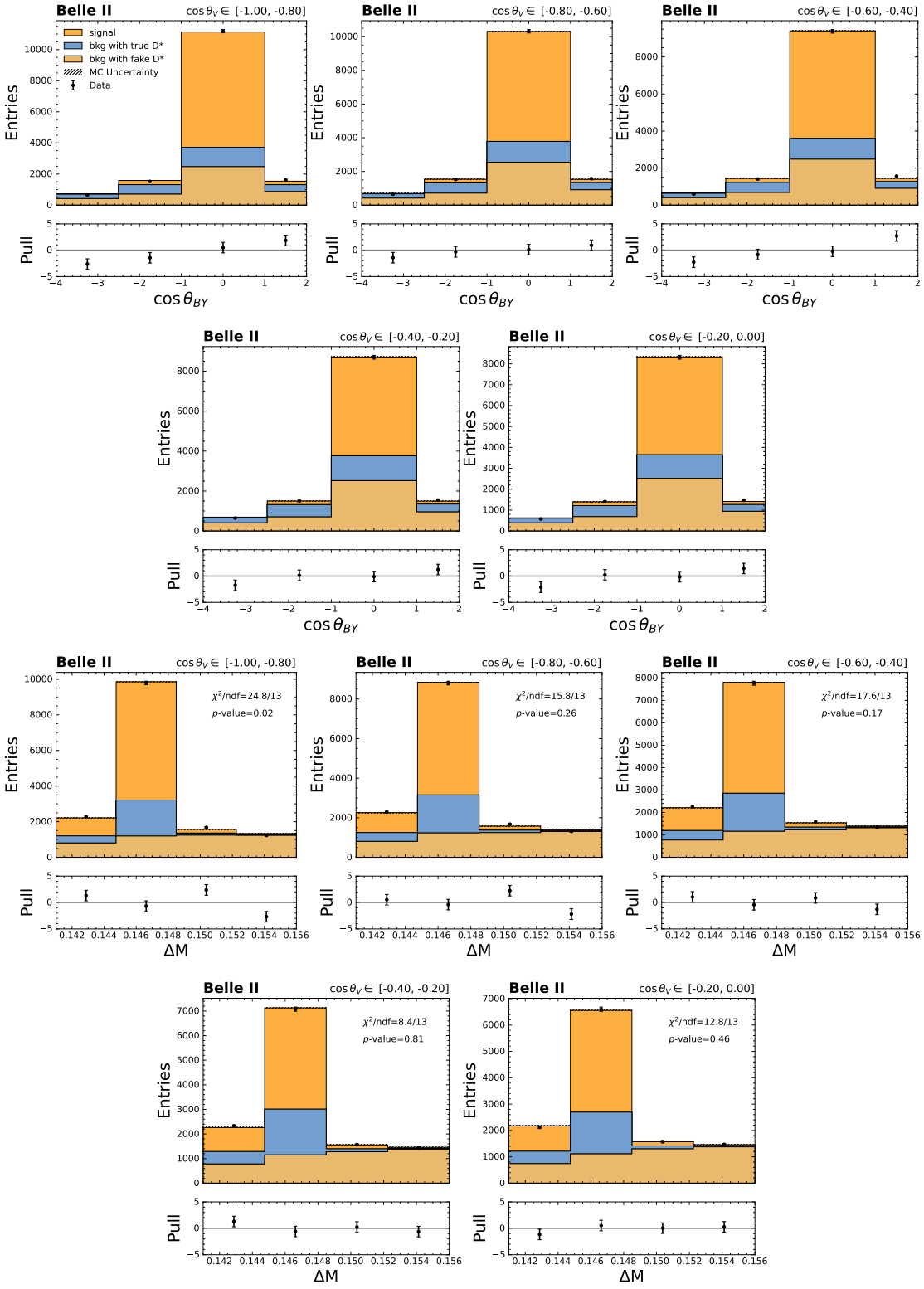

Figure E.6: Post-fit plots of $\cos\theta_{BY}$ (first 2 rows) and ΔM (last 2 rows) distributions for the first 5 $\cos\theta_V$ bins of the $\bar{B}^0 \to D^{*+} e^- \bar{\nu}_e$ decay.

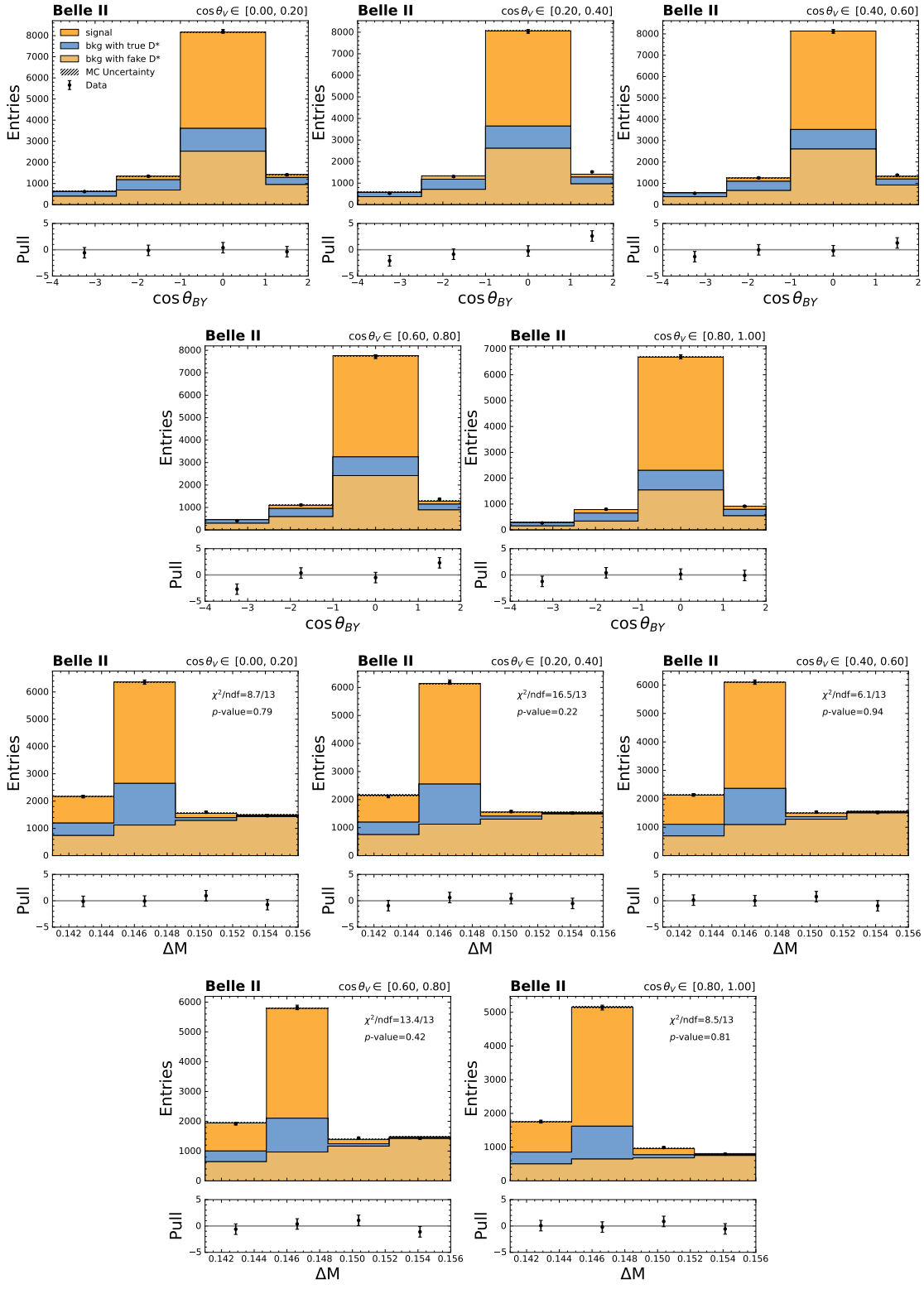

Figure E.7: Post-fit plots of $\cos\theta_{BY}$ (first 2 rows) and ΔM (last 2 rows) distributions for the last 5 $\cos\theta_V$ bins of the $\bar{B}^0 \to D^{*+} e^- \bar{\nu}_e$ decay.

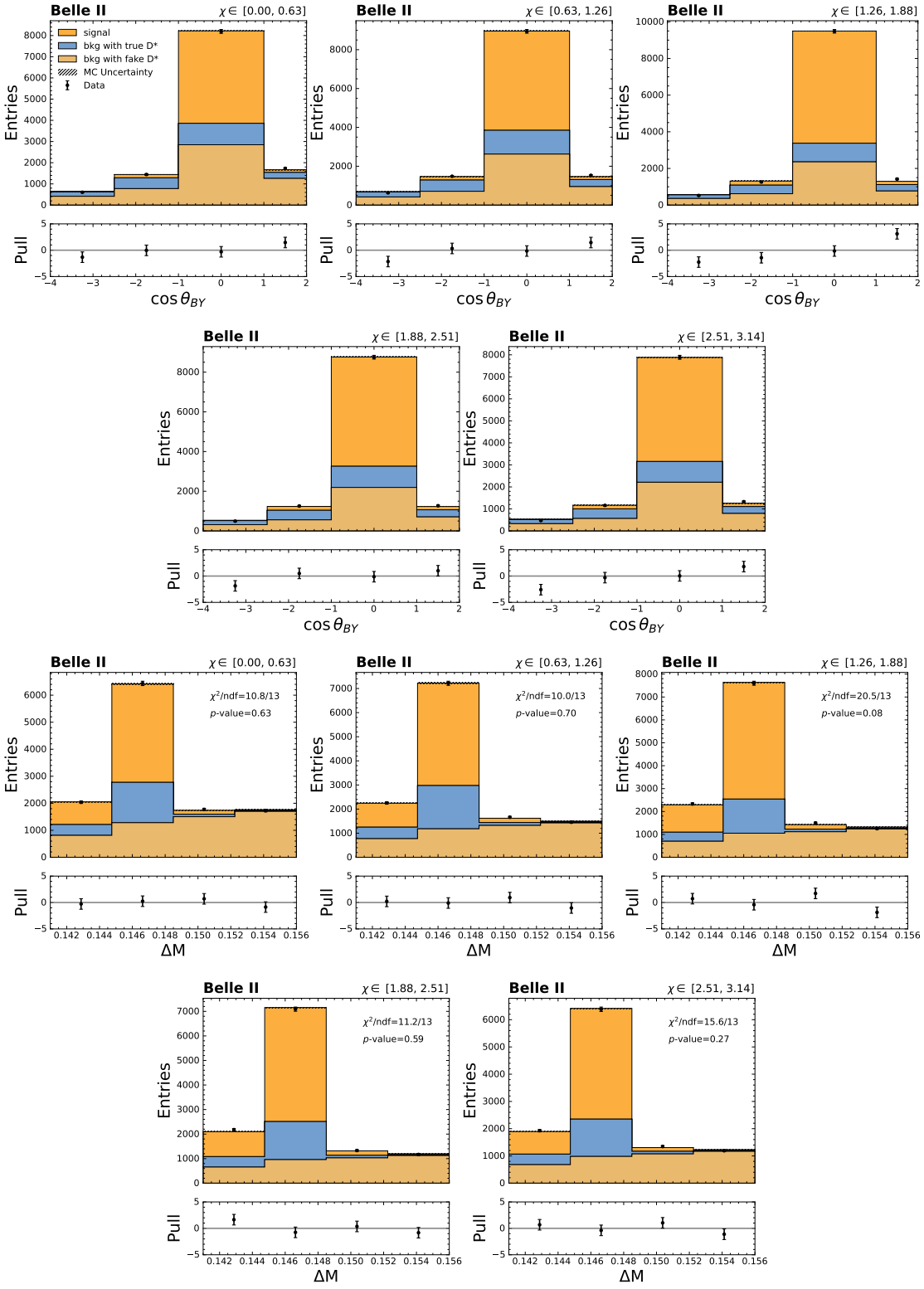

Figure E.8: Post-fit plots of $\cos\theta_{BY}$ (first 2 rows) and ΔM (last 2 rows) distributions for the first 5 χ bins of the $\bar{B}^0 \to D^{*+} e^- \bar{\nu}_e$ decay.

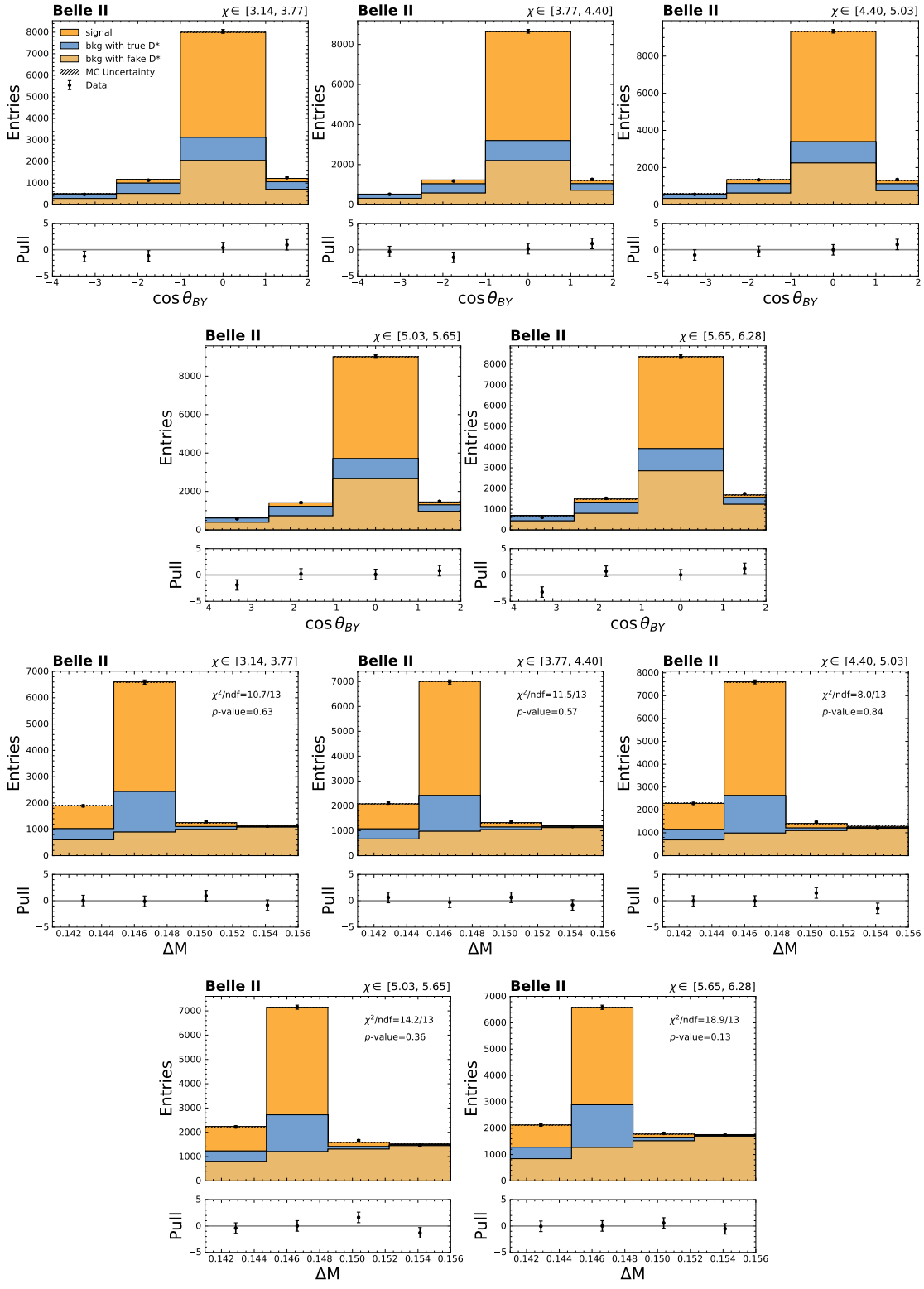

Figure E.9: Post-fit plots of $\cos\theta_{BY}$ (first 2 rows) and ΔM (last 2 rows) distributions for the last 5 χ bins of the $\bar{B}^0 \to D^{*+} e^- \bar{\nu}_e$ decay.

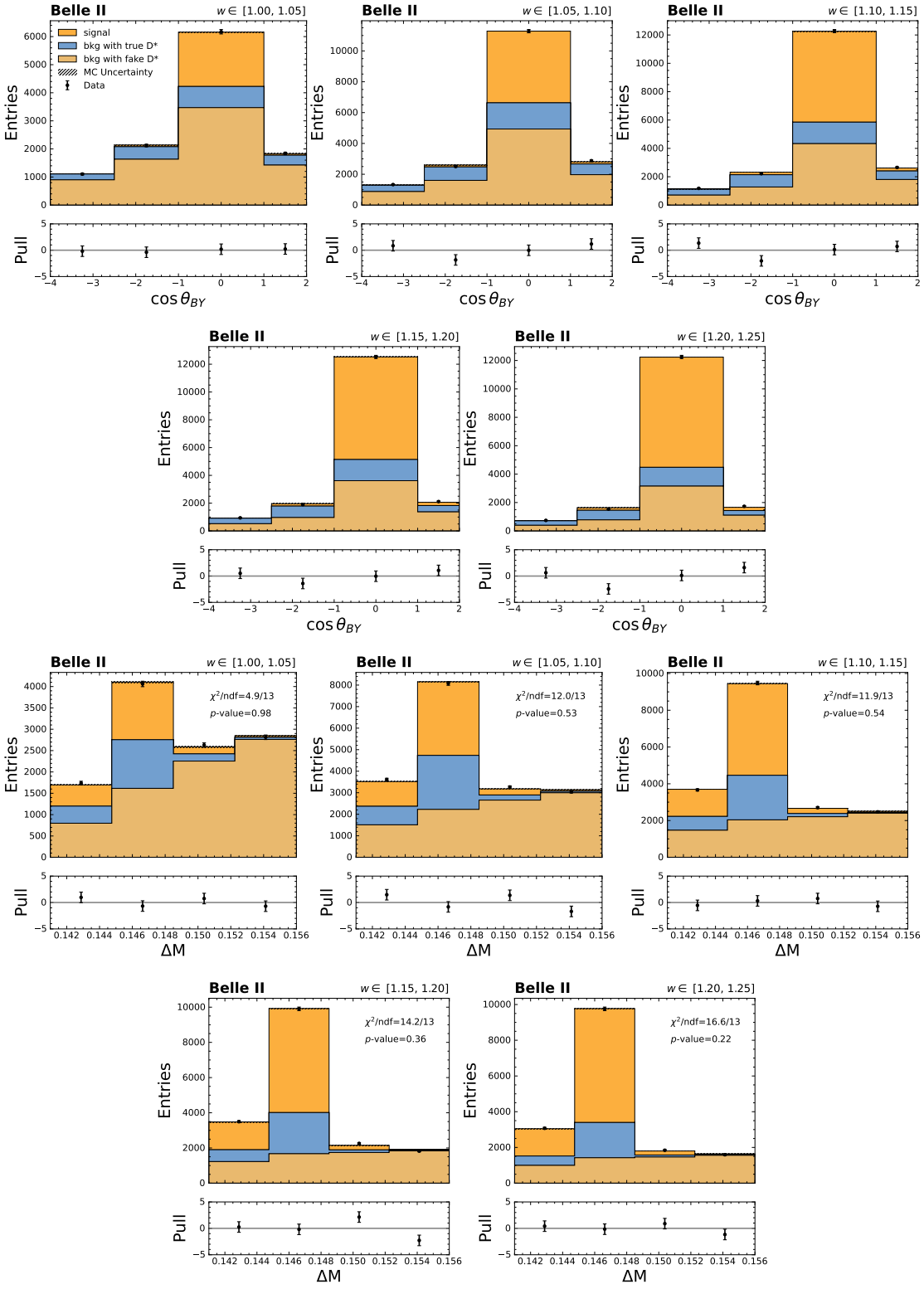

Figure E.10: Post-fit plots of $\cos\theta_{BY}$ (first 2 rows) and ΔM (last 2 rows) distributions for the first 5 w bins of the $\bar{B}^0 \to D^{*+}\mu^-\bar{\nu}_\mu$ decay.

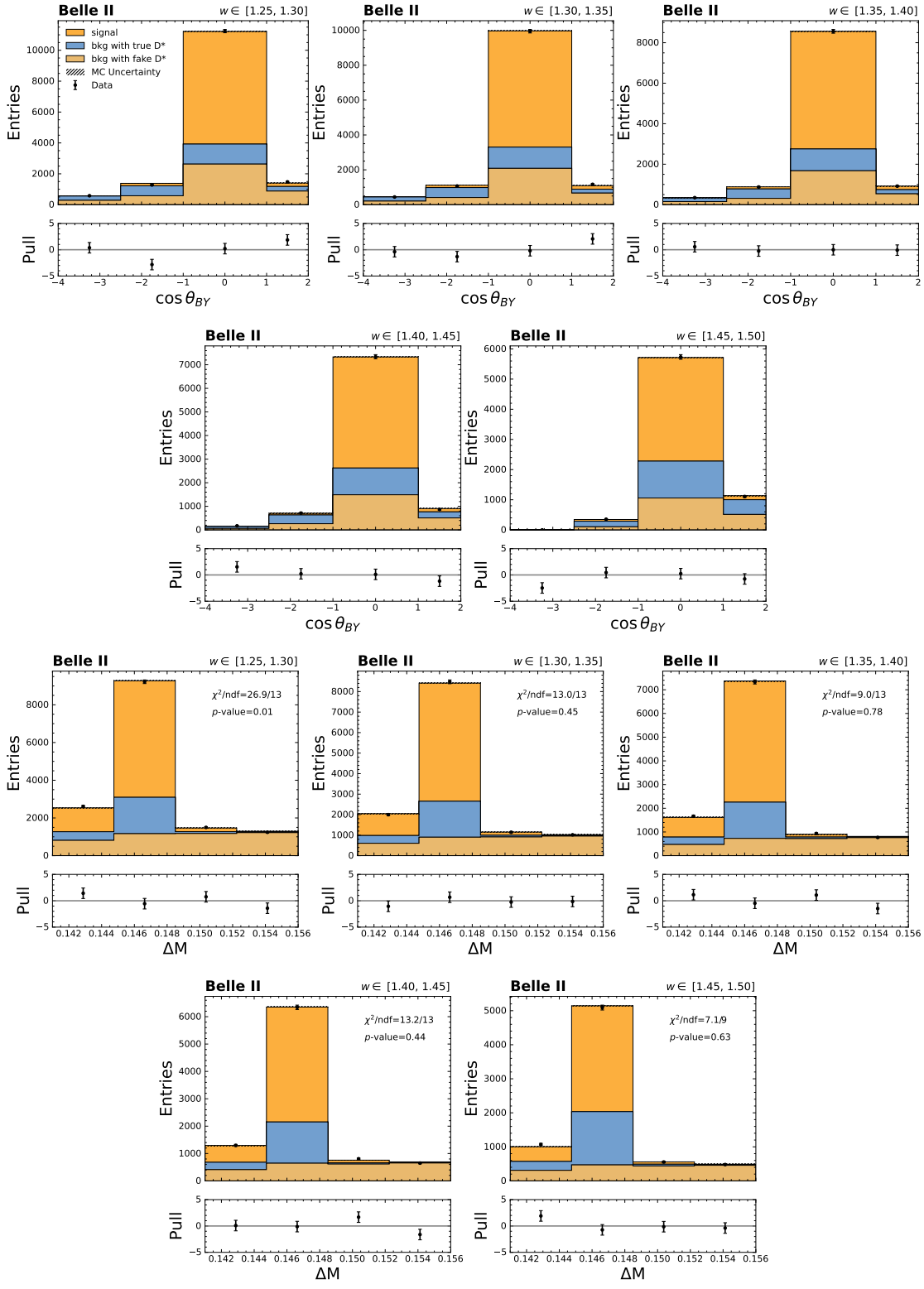

Figure E.11: Post-fit plots of $\cos\theta_{BY}$ (first 2 rows) and ΔM (last 2 rows) distributions for the last 5 w bins of the $\bar{B}^0 \to D^{*+}\mu^-\bar{\nu}_\mu$ decay.

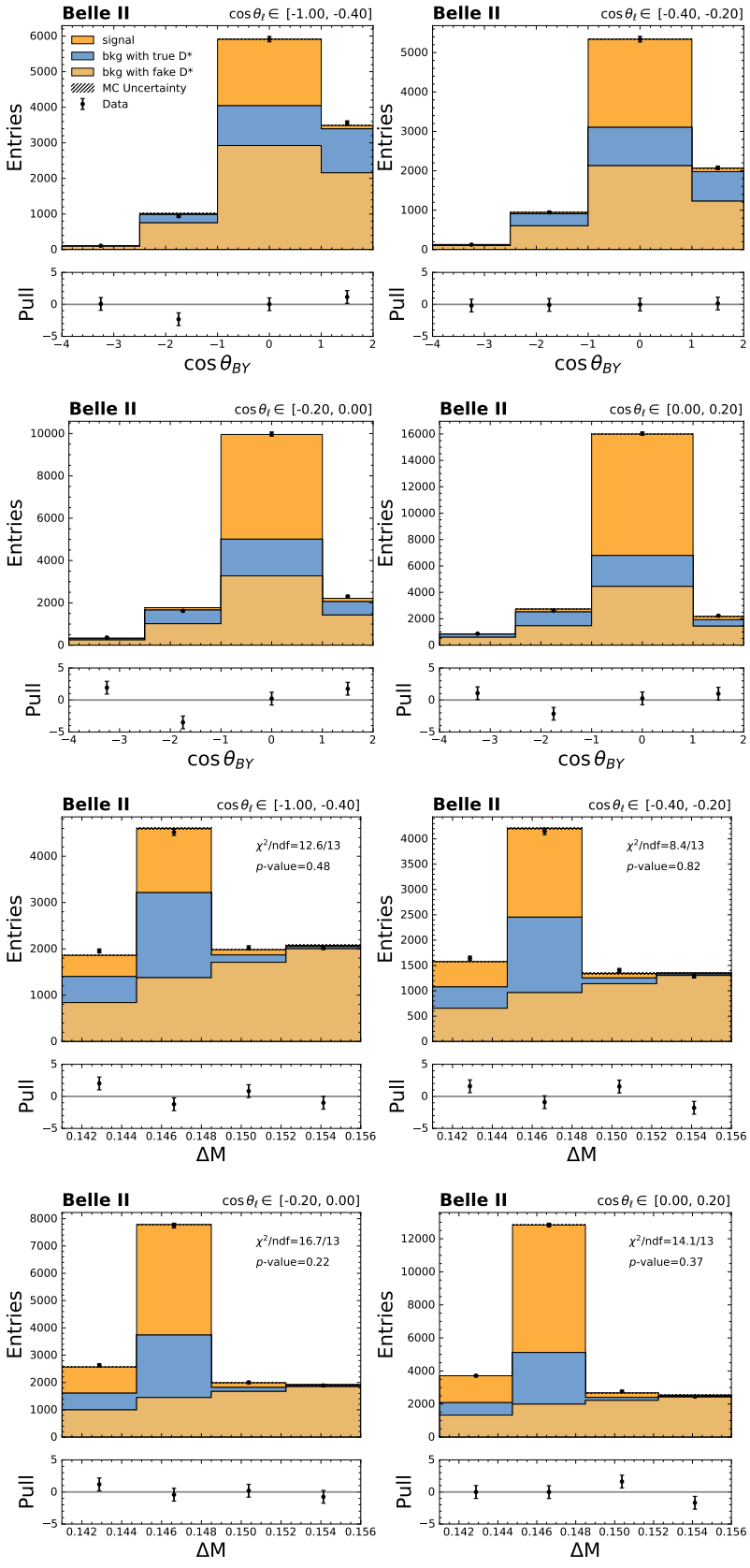

Figure E.12: Post-fit plots of $\cos\theta_{BY}$ (first 2 rows) and ΔM (last 2 rows) distributions for the first 4 $\cos\theta_\ell$ bins of the $\bar{B}^0 \to D^{*+}\mu^-\bar{\nu}_\mu$ decay.

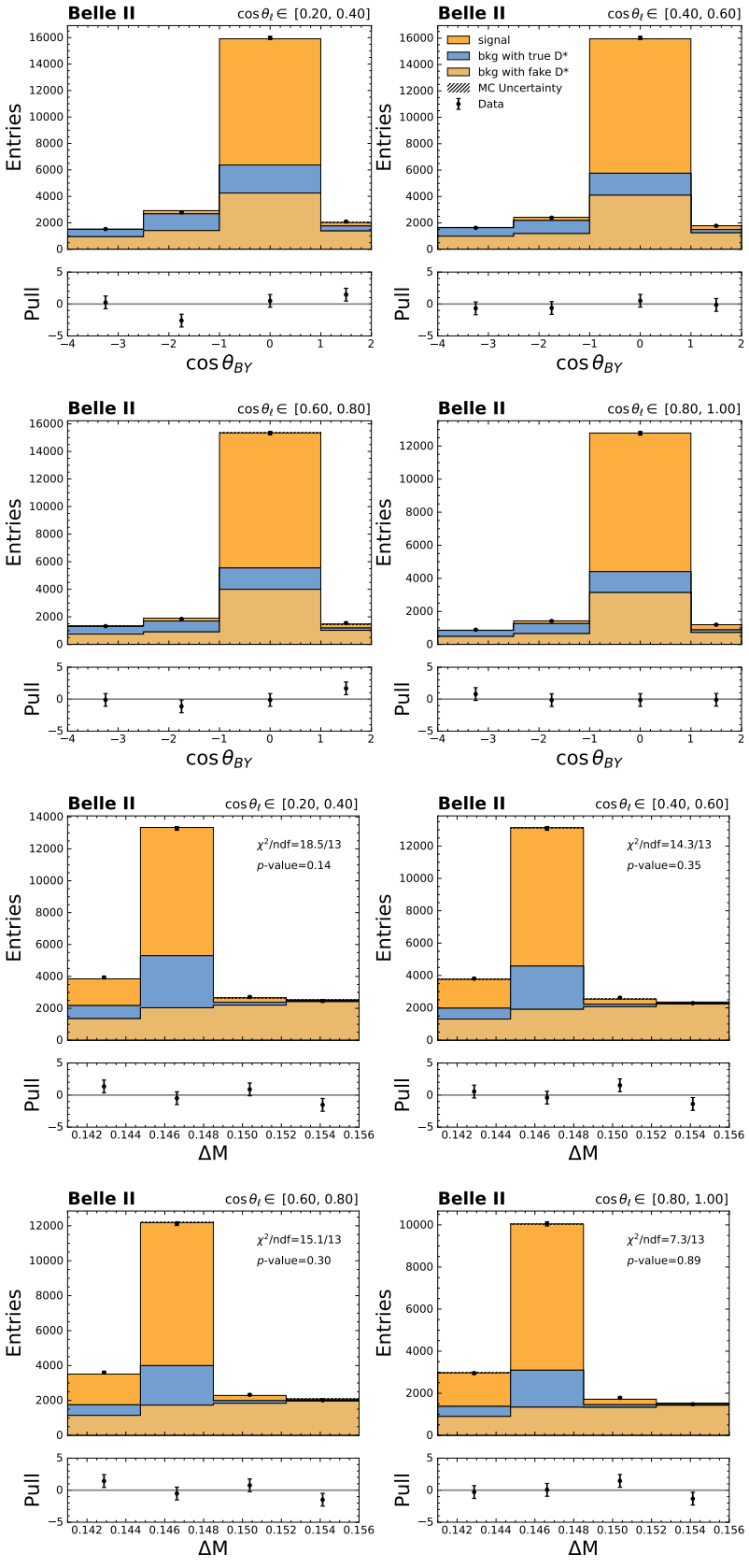

Figure E.13: Post-fit plots of $\cos\theta_{BY}$ (first 2 rows) and ΔM (last 2 rows) distributions for the last 4 $\cos\theta_\ell$ bins of the $\bar{B}^0 \to D^{*+}\mu^-\bar{\nu}_\mu$ decay.

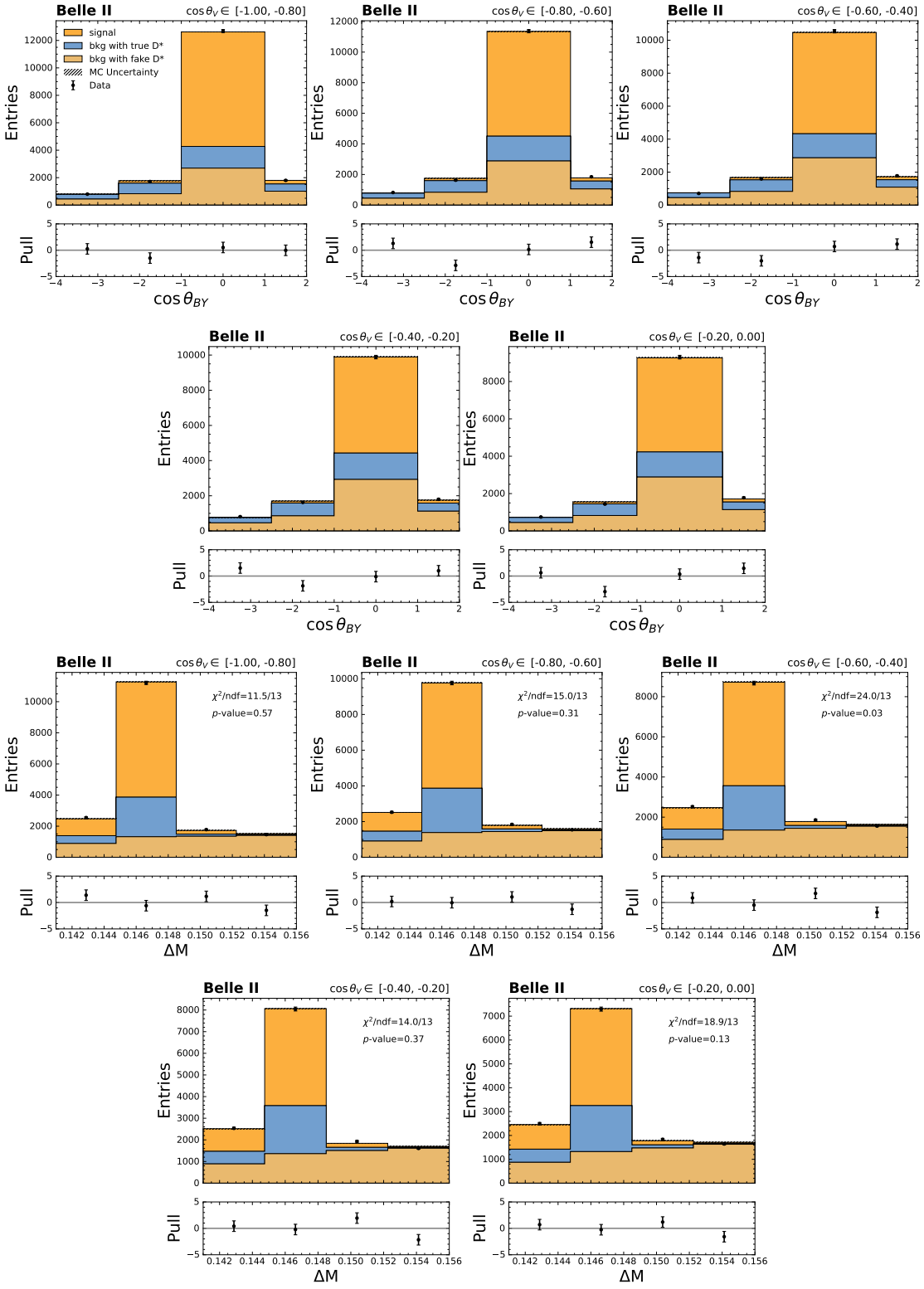

Figure E.14: Post-fit plots of $\cos\theta_{BY}$ (first 2 rows) and ΔM (last 2 rows) distributions for the first 5 $\cos\theta_V$ bins of the $\bar{B}^0 \to D^{**}\mu^-\bar{\nu}_\mu$ decay.

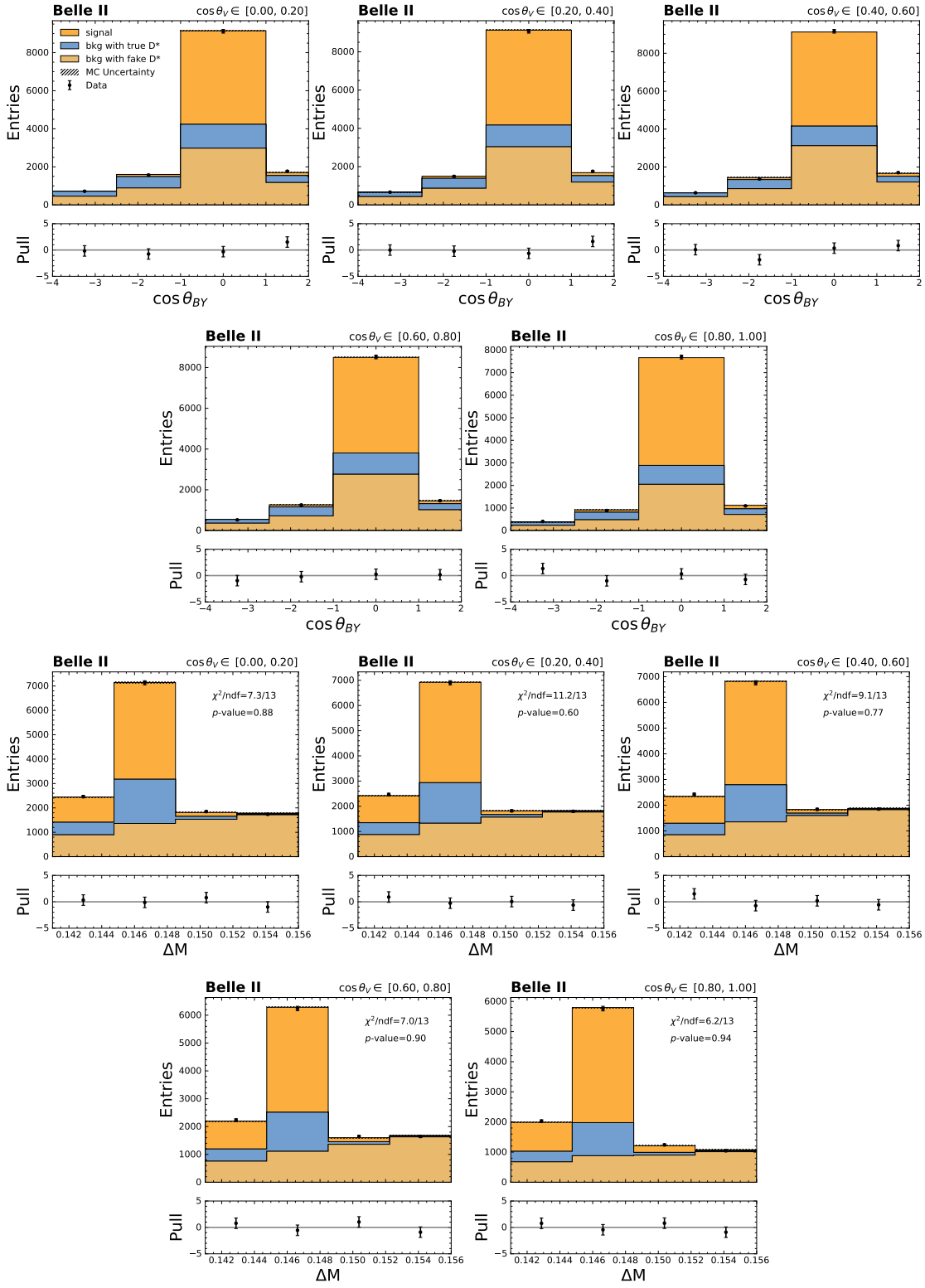

Figure E.15: Post-fit plots of $\cos\theta_{BY}$ (first 2 rows) and ΔM (last 2 rows) distributions for the last 5 $\cos\theta_V$ bins of the $\bar{B}^0 \to D^{*+}\mu^-\bar{\nu}_\mu$ decay.

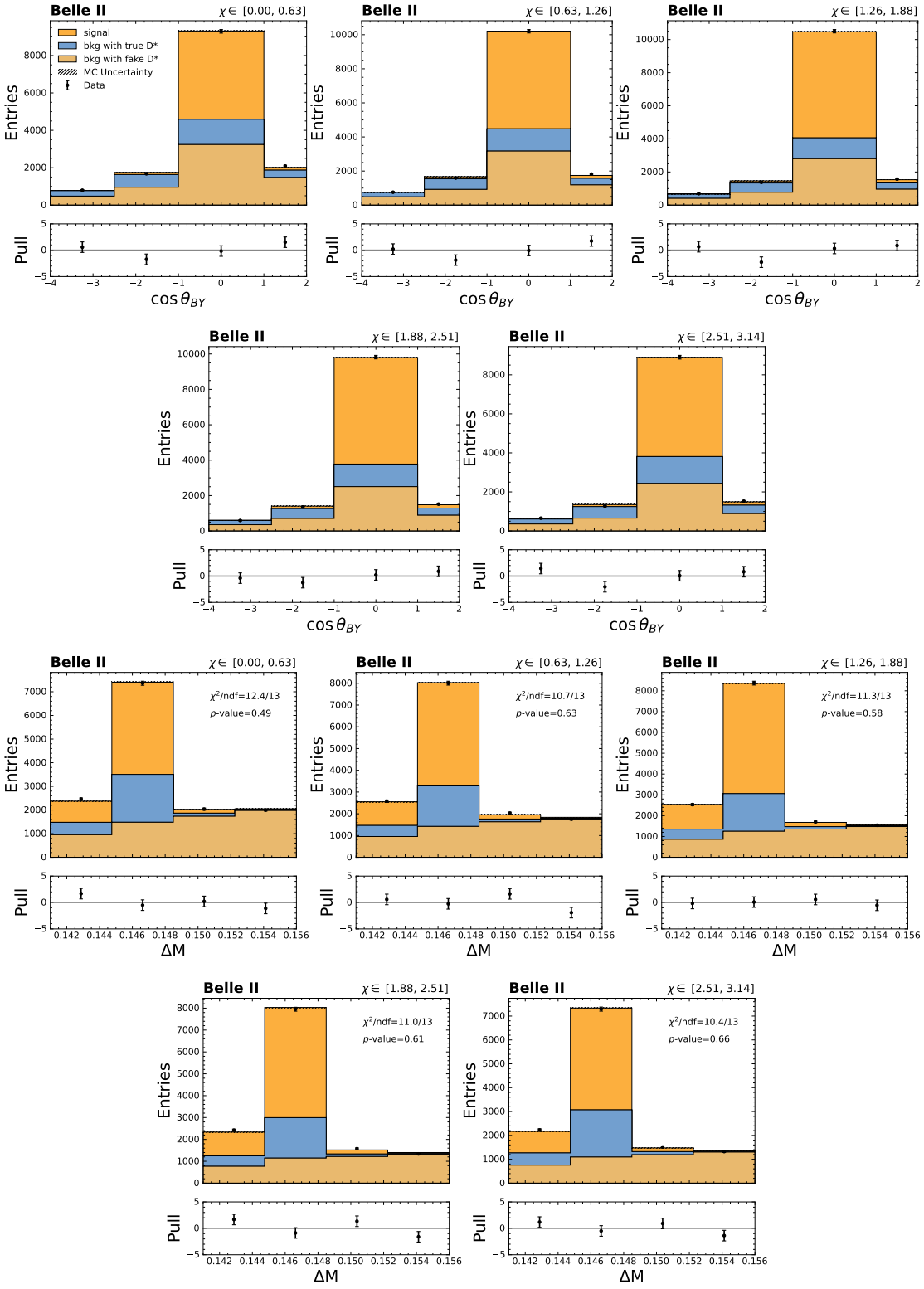

Figure E.16: Post-fit plots of $\cos\theta_{BY}$ (first 2 rows) and ΔM (last 2 rows) distributions for the first 5 χ bins of the $\bar{B}^0 \to D^{*+}\mu^-\bar{\nu}_\mu$ decay.

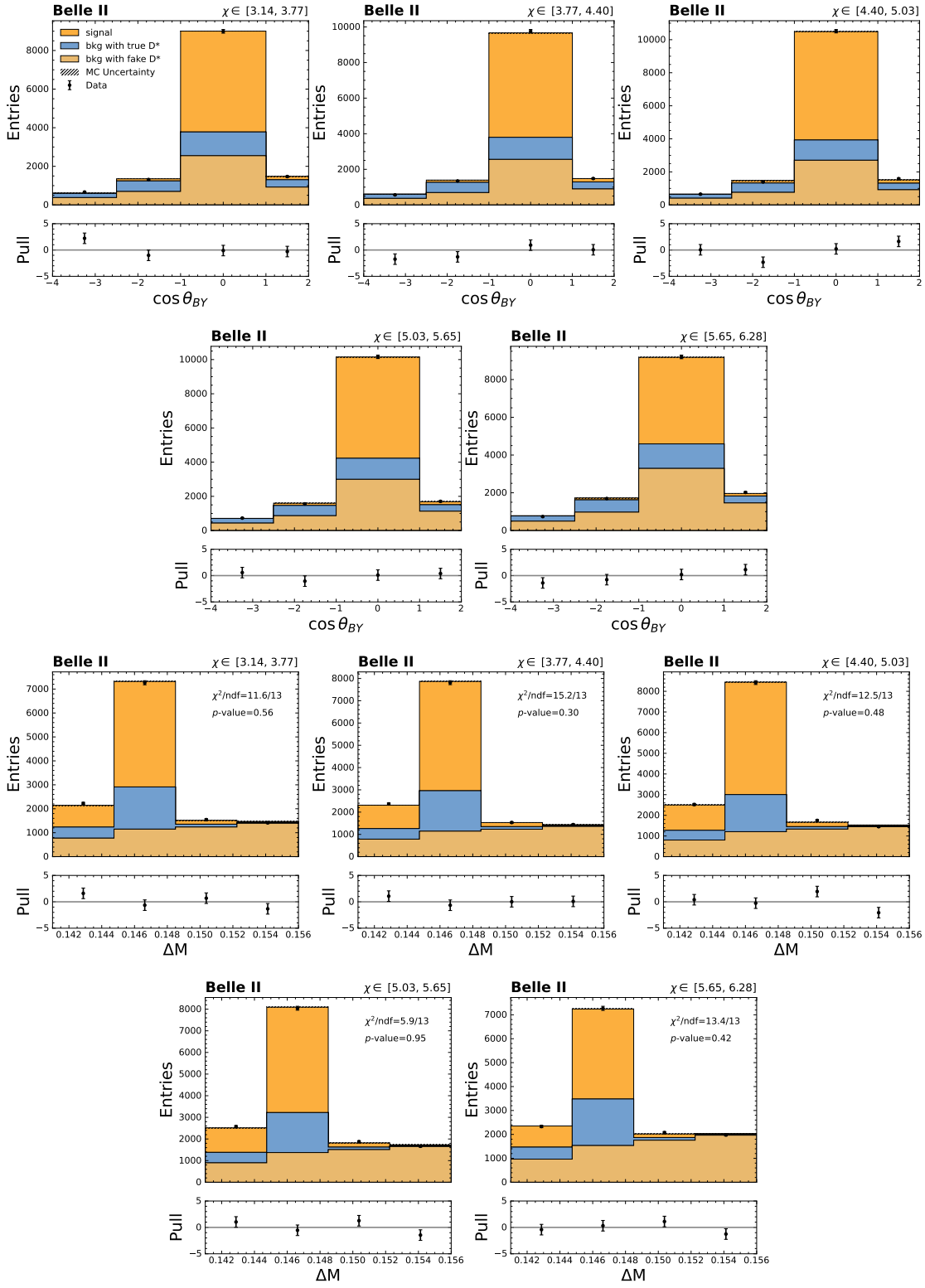

Figure E.17: Post-fit plots of $\cos\theta_{BY}$ (first 2 rows) and ΔM (last 2 rows) distributions for the last 5 χ bins of the $\bar{B}^0 \to D^{*+}\mu^-\bar{\nu}_\mu$ decay.

APPENDIX F

Validation of unfolding

To validate the unfolding procedure, 50000 pseudo signal yields are generated for each kinematic bin using multivariate Gaussian distributions, where the means correspond to the nominal fitted yields, and the covariance matrix on these yields is applied. These sampled yields are then unfolded using the nominal migration matrices. For each bin and each sample, we calculate the pull using the formula:

$$\text{Pull} = \frac{N^{\text{toy}} - N^{\text{nominal}}}{\sigma}, \tag{F.1}$$

where N^{toy} and N^{nominal} represent the unfolded yields in the toy sample and the nominal procedure, respectively, and σ denotes the nominal post-unfolding uncertainty. The validation is conducted for both matrix inversion and SVD unfolding methods.

The normalized pull distributions in each bin of kinematic variables are illustrated in Figs. F.1 to F.8. These distributions are fitted with Gaussian functions, and the resulting values of mean and standard deviation are provided with the plots. If the fits are unbiased and the post-unfolding uncertainties are estimated accurately, we expect the peak of the distribution to be centered at zero with a standard deviation of $\sigma = 1$. Overall, our observations indicate a good agreement between the fitted values and the expected outcomes.

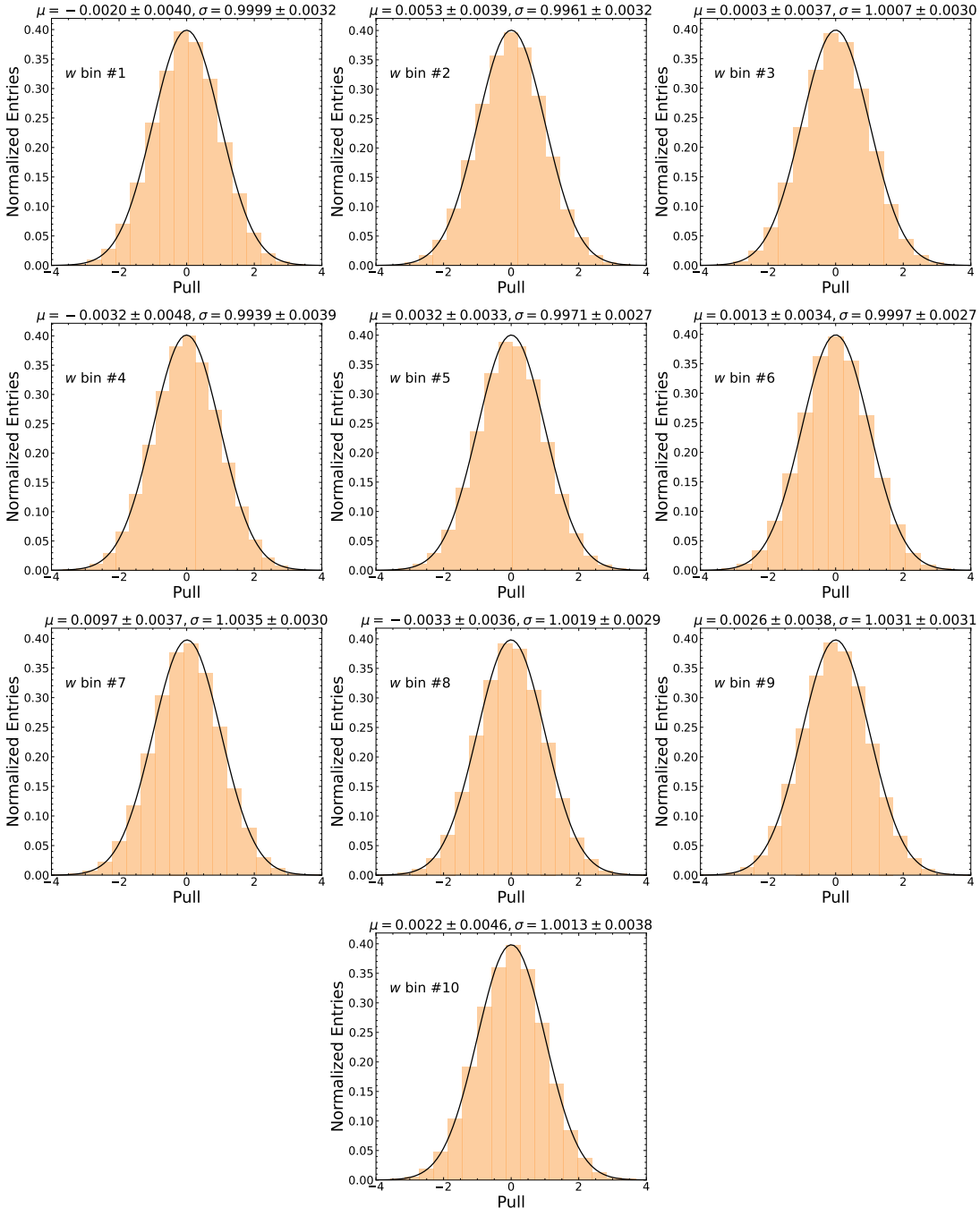

Figure F.1: Pull distributions of unfolded pseudo signal yields in w bins, derived using the matrix inversion method. The corresponding Gaussian parameters describing the distributions are provided.

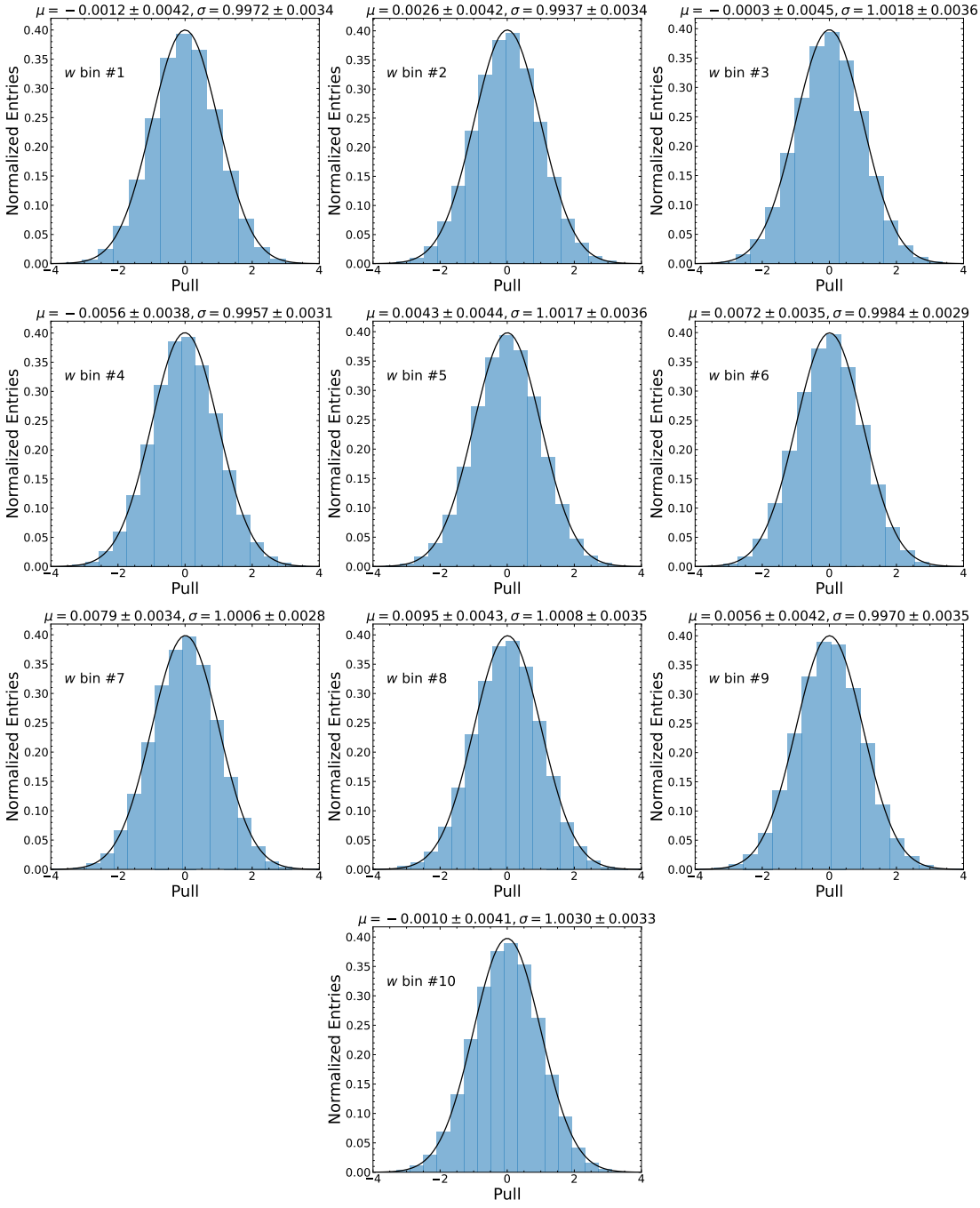

Figure F.2: Pull distributions of unfolded pseudo signal yields in w bins, derived using the SVD method. The corresponding Gaussian parameters describing the distributions are provided.

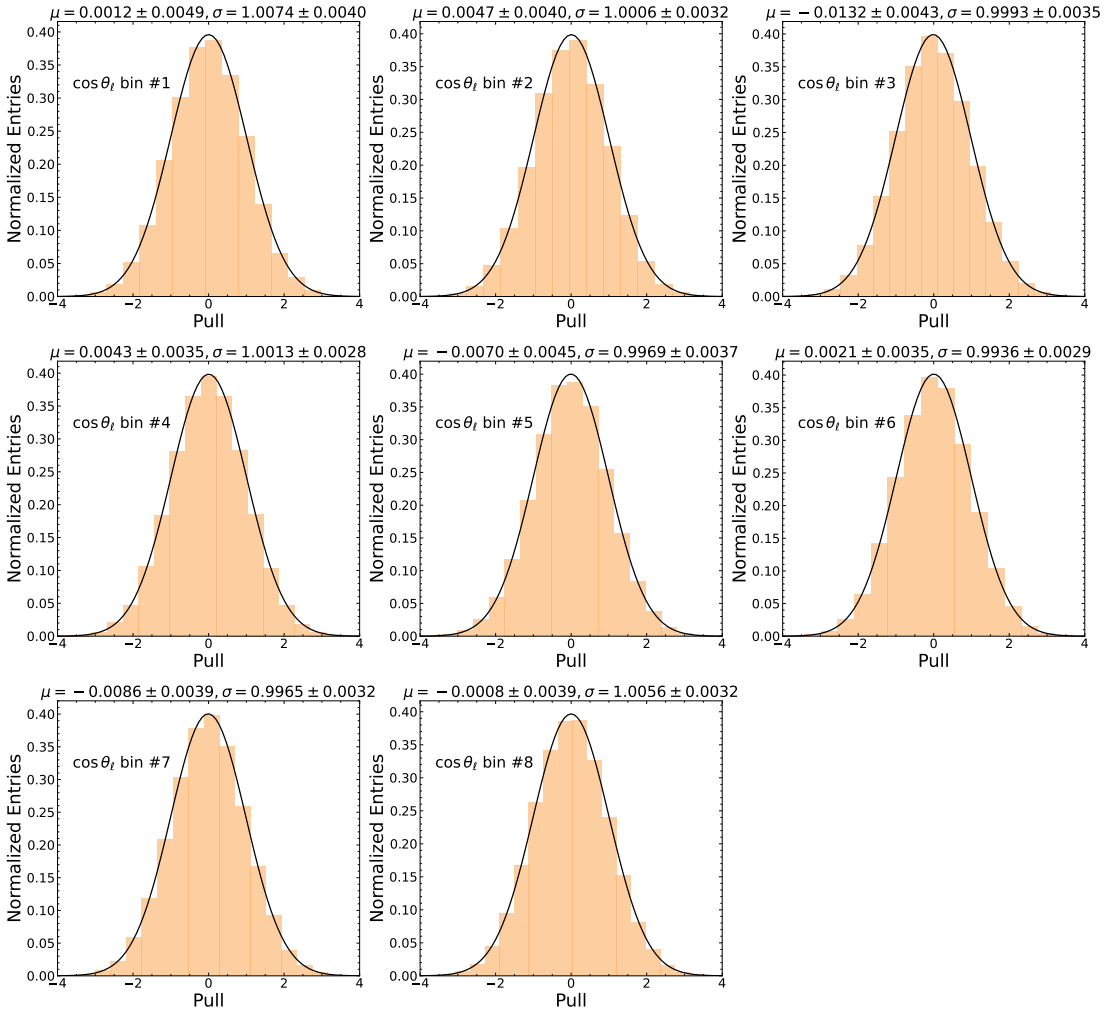

Figure F.3: Pull distributions of unfolded pseudo signal yields in $\cos\theta_\ell$ bins, derived using the matrix inversion method. The corresponding Gaussian parameters describing the distributions are provided.

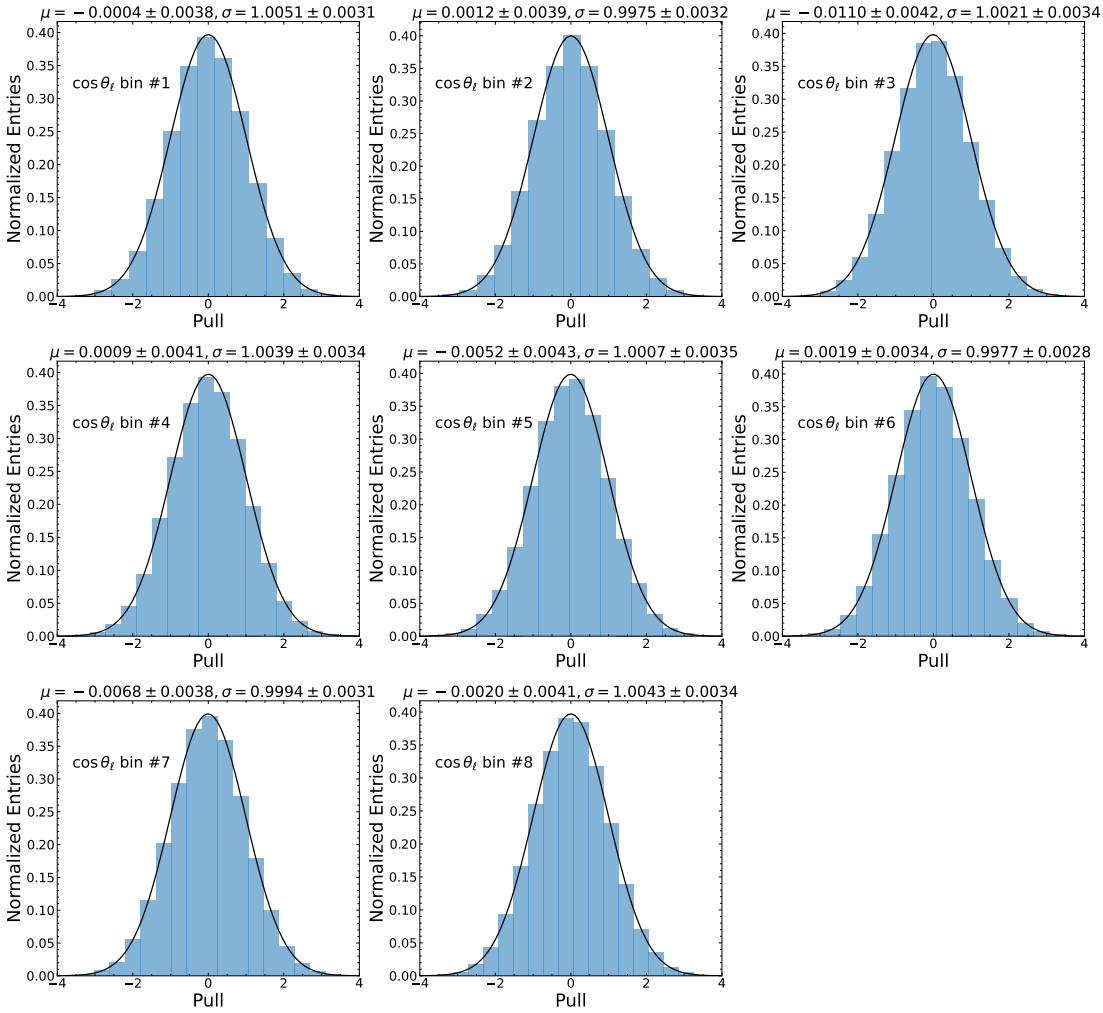

Figure F.4: Pull distributions of unfolded pseudo signal yields in $\cos\theta_\ell$ bins, derived using the SVD method. The corresponding Gaussian parameters describing the distributions are provided.

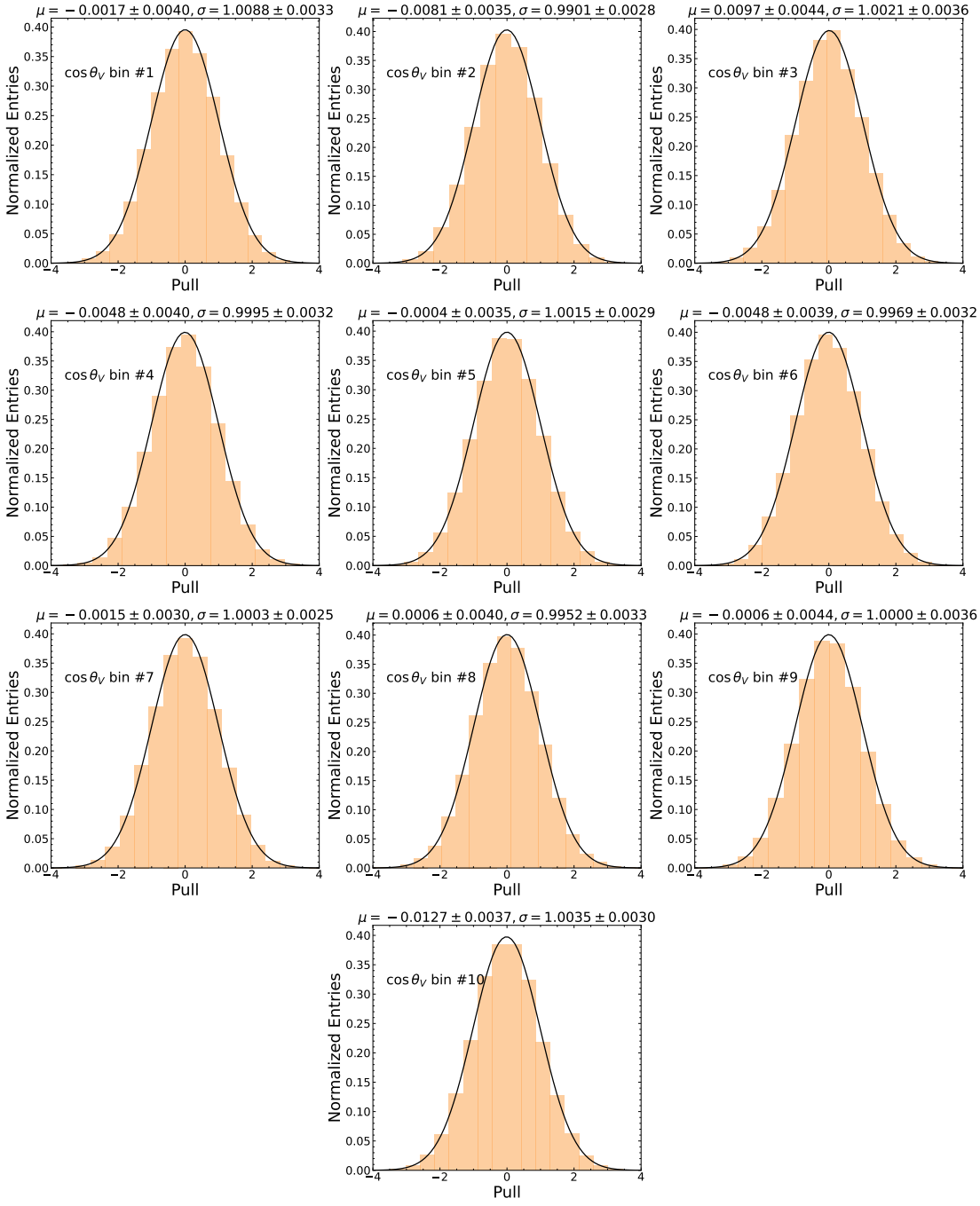

Figure F.5: Pull distributions of unfolded pseudo signal yields in $\cos\theta_V$ bins, derived using the matrix inversion method. The corresponding Gaussian parameters describing the distributions are provided.

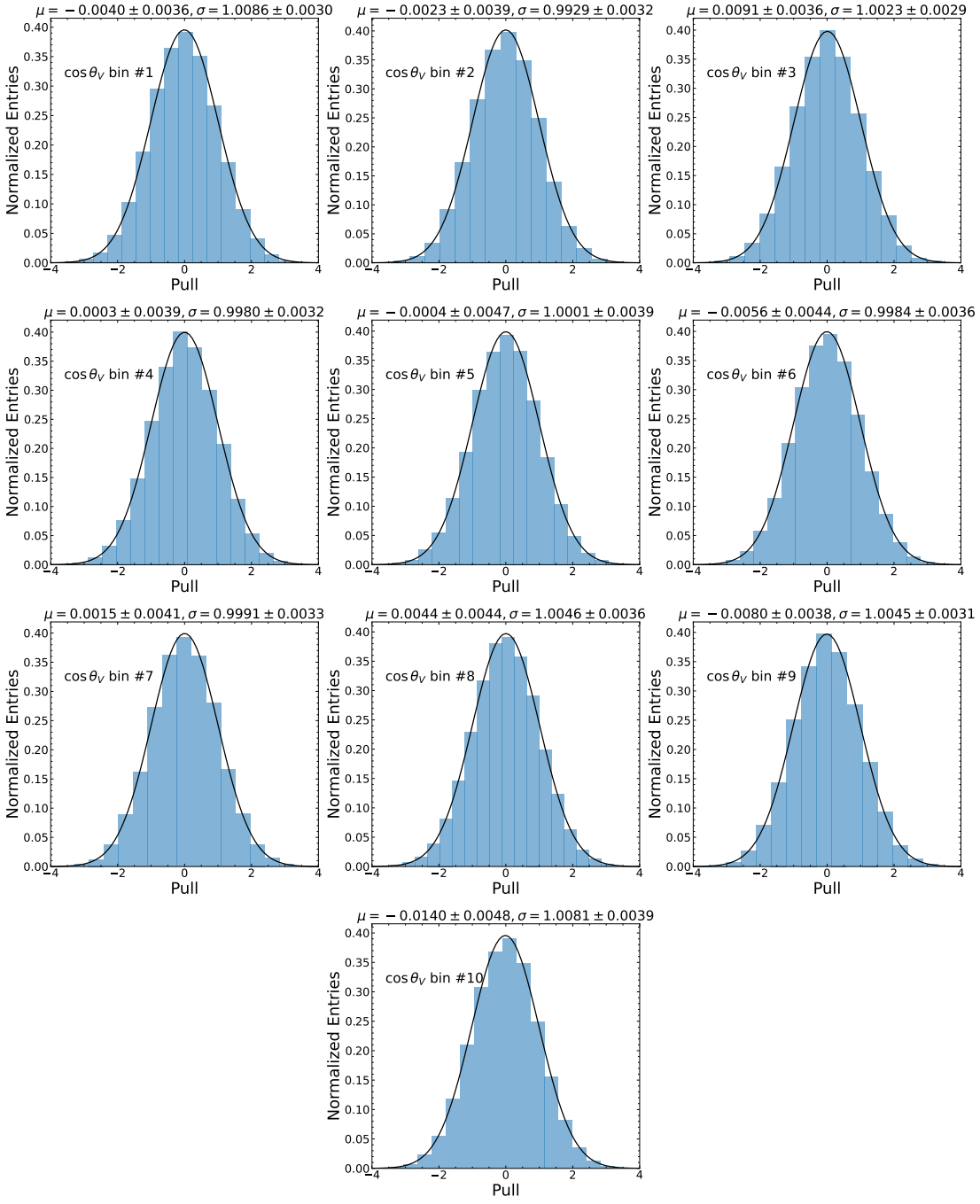

Figure F.6: Pull distributions of unfolded pseudo signal yields in $\cos\theta_V$ bins, derived using the SVD method. The corresponding Gaussian parameters describing the distributions are provided.

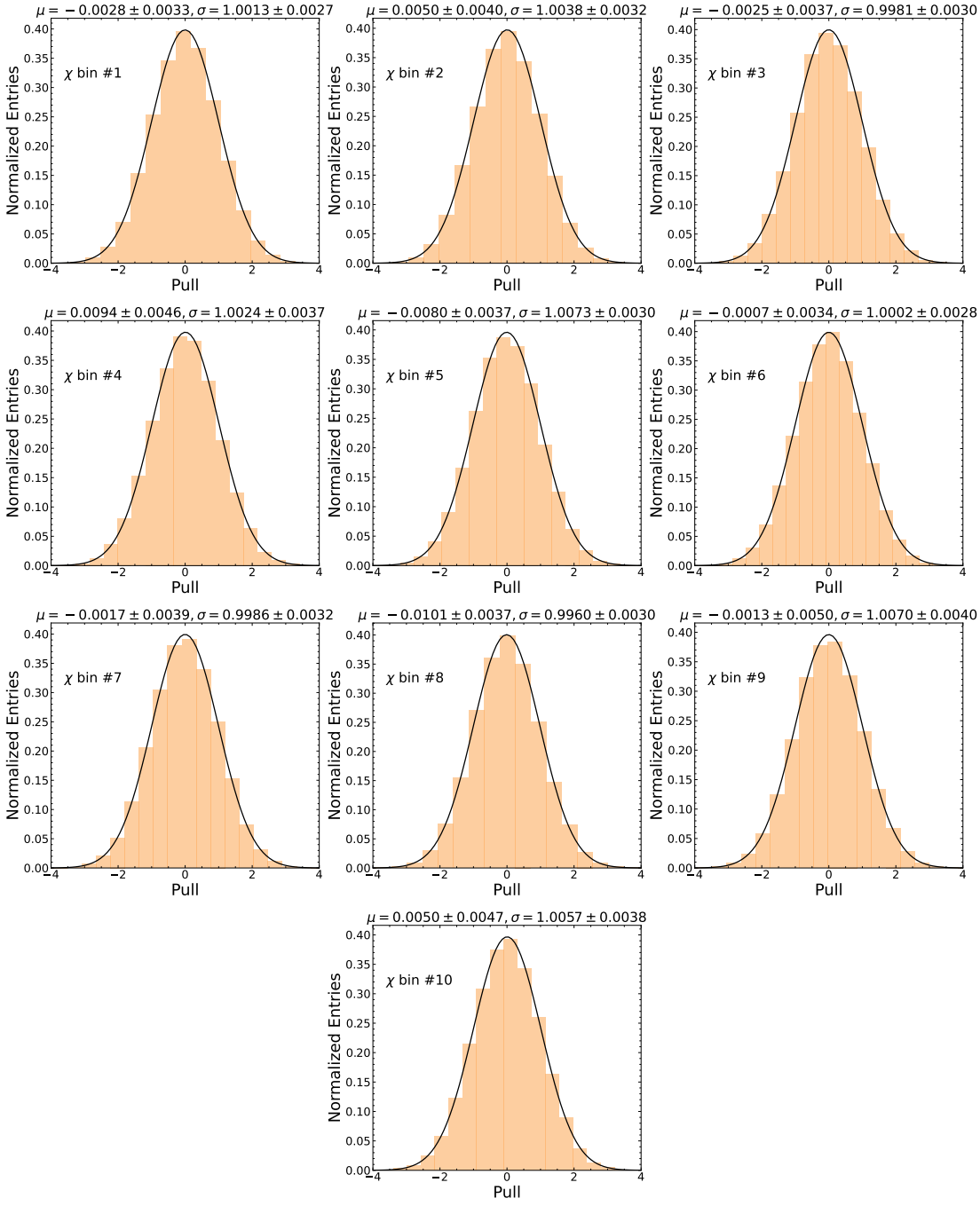

Figure F.7: Pull distributions of unfolded pseudo signal yields in χ bins, derived using the matrix inversion method. The corresponding Gaussian parameters describing the distributions are provided.

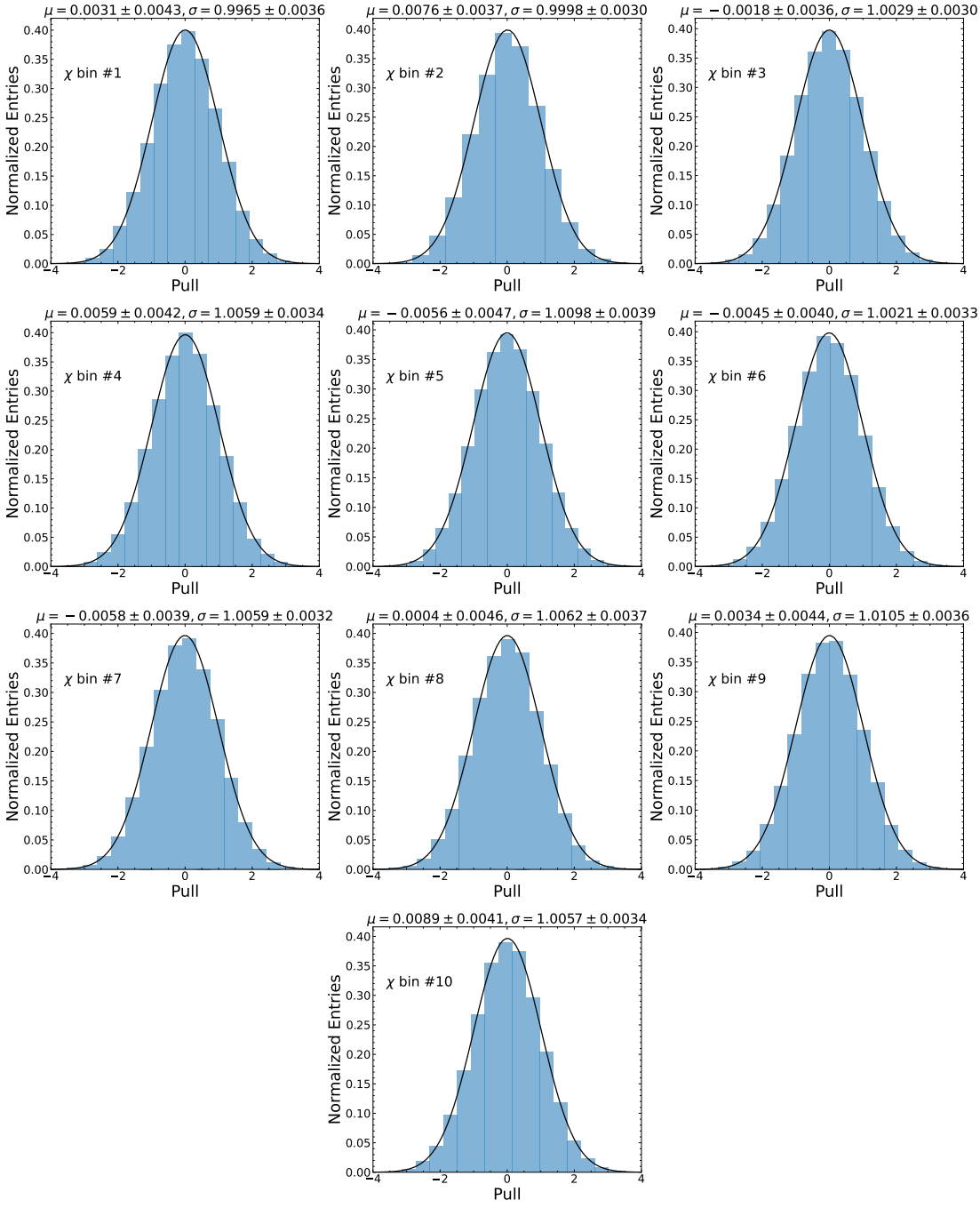

Figure F.8: Pull distributions of unfolded pseudo signal yields in χ bins, derived using the SVD method. The corresponding Gaussian parameters describing the distributions are provided.

APPENDIX G

Examination of D'Agostini type bias

Reference [109] demonstrates a potential bias in a χ^2 fit when there exists a large normalization uncertainty affecting all data points. The size of this bias varies based on the fitted function, the magnitude of the overall uncertainty, and the number of data points. It has been demonstrated that this bias arises from the linearization applied in usual error propagation methods.

In this measurement, the leading order uncertainty originates from the slow pion tracking efficiency, which exhibits strong correlations across all kinematic bins and primarily affects the normalization. The secondary uncertainty arises from the determination of the number of B^0 mesons, which is fully correlated across all bins of kinematic variables. These uncertainties have the potential to introduce bias, as discussed in Ref. [109]. Therefore, we examine our results and rule out any D'Agostini type bias.

In this test, we begin by weighting the covariance matrix of normalized decay rates. The weight applied to the systematic component of the matrix element C_{ij}, is expressed as:

$$w_{ij} = \frac{\Delta\Gamma_i^{\text{theo.}}}{\Delta\Gamma_i^{\text{obs.}}} \times \frac{\Delta\Gamma_j^{\text{theo.}}}{\Delta\Gamma_j^{\text{obs.}}}. \tag{G.1}$$

Here, $\Delta\Gamma_i^{\text{theo.}}$ represents the partial decay rate calculated using fitted $|V_{cb}|$ and form factor parameters for bin i, and $\Delta\Gamma_i^{\text{obs.}}$ denotes the experimentally observed partial decay rate in bin i.

Then, we substitute the nominal covariance matrix with the weighted matrix in the χ^2 fit, and re-extract values of $|V_{cb}|$ and form factor parameters. We find the resulting values and their correlations remain unchanged compared to those in Table 8.2, and thus no D'Agostini type bias is observed.

APPENDIX H

Results with matrix inversion unfolding

In addition to unfolding signal yields using the SVD method with the chosen k values, we also employ the matrix inversion unfolding method, where no regularization is applied. The results are presented and compared with those obtained from the SVD approach in this section.

The signal yields summarized in Table 6.1 are unfolded using the matrix inversion method and then converted into partial decay rates through Eq. (6.9). The resulting values in bins of kinematic variables, are provided in Table H.1.

The statistical correlations of partial decay rates are determined using the bootstrapping method, as detailed in Sec. 6.4. The obtained correlation matrices are illustrated in Fig. H.1 and Fig. H.2 for $\bar{B}^0 \to D^{*+} e^- \bar{\nu}_e$ and $\bar{B}^0 \to D^{*+} \mu^- \bar{\nu}_\mu$ decays, respectively. Since no regularization is applied to dampen statistical fluctuations in the unfolded distributions, neighboring bins present a negative correlation pattern, which is distinct from the SVD method. Additionally, we observe larger statistical uncertainties resulted from the matrix inversion method.

The partial decay rates measured for $\bar{B}^0 \to D^{*+} e^- \bar{\nu}_e$ and $\bar{B}^0 \to D^{*+} \mu^- \bar{\nu}_\mu$ decays are normalized, and further averaged over two decay channels. The full (statistical and systematic) correlations of these normalized decays rates are illustrated in Fig. H.3.

Utilizing the normalized decay rates and total rate obtained from the matrix inversion unfolding method, we determine the values of $|V_{cb}|$ and form factor parameters through a χ^2 fit outlined in Eq. (8.2). The resulting p-values are 14% and 13% for the BGL and CLN parametrizations, respectively, and the fitted values, along with their correlations, are summarized in Table H.2 and Table H.3. The results do not show significant deviation from those obtained with the SVD unfolding approach.

Using the fitted values and their corresponding 1σ uncertainties, we plot one-dimensional differential decay rates with respect to individual kinematic variables w, $\cos\theta_\ell$, $\cos\theta_V$, and χ in Fig. H.4. We observe a strong consistency between the plotted spectra and the measured data points.

Similarly, we observe a disagreement with low p-values of 0.2% and 0.4% when incorporating the FNAL/MILC predictions on $h_{A_1}(w)$, $R_1(w)$, $R_2(w)$ in the fits. The corresponding results are summarized in Table H.4 and Table H.5 for the BGL and CLN parametrizations, respectively.

Table H.1: Measured partial decay rates $\Delta\Gamma$ (in units of 10^{-15} GeV) and average of normalized partial decay rates $\Delta\Gamma/\Gamma$ over $\bar{B}^0 \to D^{*+} e^- \bar{\nu}_e$ and $\bar{B}^0 \to D^{*+} \mu^- \bar{\nu}_\mu$ decays in bins of kinematic variables. The normalized partial decay rate in the last bin of each projection is excluded in the $|V_{cb}|$ determination to subtract the redundant degrees of freedom. The full (statistical and systematic) uncertainties are provided.

Variable	Bin	$\Delta\Gamma$		$\Delta\Gamma/\Gamma$ average (in %)
		$\bar{B}^0 \to D^{*+} e^- \bar{\nu}_e$	$\bar{B}^0 \to D^{*+} \mu^- \bar{\nu}_\mu$	$\bar{B}^0 \to D^{*+} \ell^- \bar{\nu}_\ell$
w	[1.00, 1.05)	1.42 ± 0.12	1.32 ± 0.11	6.37 ± 0.30
	[1.05, 1.10)	2.02 ± 0.14	2.09 ± 0.14	9.66 ± 0.32
	[1.10, 1.15)	2.40 ± 0.15	2.46 ± 0.15	11.41 ± 0.30
	[1.15, 1.20)	2.63 ± 0.16	2.57 ± 0.15	12.16 ± 0.31
	[1.20, 1.25)	2.57 ± 0.16	2.65 ± 0.16	12.24 ± 0.33
	[1.25, 1.30)	2.51 ± 0.16	2.38 ± 0.15	11.37 ± 0.36
	[1.30, 1.35)	2.29 ± 0.16	2.30 ± 0.15	10.74 ± 0.40
	[1.35, 1.40)	2.07 ± 0.16	2.12 ± 0.15	9.79 ± 0.41
	[1.40, 1.45)	1.83 ± 0.14	1.71 ± 0.14	8.28 ± 0.38
	[1.45, 1.51)	1.67 ± 0.10	1.76 ± 0.11	
$\cos\theta_\ell$	[−1.00, −0.40)	4.00 ± 0.41	4.19 ± 0.45	19.23 ± 1.03
	[−0.40, −0.20)	1.93 ± 0.16	2.09 ± 0.17	9.44 ± 0.37
	[−0.20, 0.00)	2.31 ± 0.14	2.19 ± 0.15	10.48 ± 0.30
	[0.00, 0.20)	2.47 ± 0.13	2.62 ± 0.15	11.94 ± 0.30
	[0.20, 0.40)	2.76 ± 0.14	2.57 ± 0.14	12.43 ± 0.30
	[0.40, 0.60)	2.73 ± 0.14	2.77 ± 0.14	12.89 ± 0.32
	[0.60, 0.80)	2.47 ± 0.14	2.51 ± 0.13	11.70 ± 0.33
	[0.80, 1.00)	2.55 ± 0.14	2.51 ± 0.14	
$\cos\theta_V$	[−1.00, −0.80)	2.88 ± 0.13	3.06 ± 0.15	13.92 ± 0.31
	[−0.80, −0.60)	2.38 ± 0.12	2.24 ± 0.12	10.74 ± 0.27
	[−0.60, −0.40)	2.03 ± 0.12	2.01 ± 0.11	9.45 ± 0.26
	[−0.40, −0.20)	1.61 ± 0.11	1.62 ± 0.11	7.56 ± 0.26
	[−0.20, 0.00)	1.55 ± 0.12	1.51 ± 0.11	7.18 ± 0.27
	[0.00, 0.20)	1.59 ± 0.12	1.59 ± 0.12	7.46 ± 0.28
	[0.20, 0.40)	1.67 ± 0.12	1.78 ± 0.12	8.11 ± 0.29
	[0.40, 0.60)	2.12 ± 0.14	2.11 ± 0.14	9.91 ± 0.31
	[0.60, 0.80)	2.44 ± 0.16	2.28 ± 0.15	11.06 ± 0.32
	[0.80, 1.00)	3.07 ± 0.18	3.17 ± 0.20	
χ	[0.00, 0.63)	1.86 ± 0.14	1.88 ± 0.13	8.76 ± 0.32
	[0.63, 1.26)	2.11 ± 0.15	2.23 ± 0.14	10.24 ± 0.35
	[1.26, 1.88)	2.64 ± 0.16	2.49 ± 0.15	11.96 ± 0.33
	[1.88, 2.51)	2.20 ± 0.15	2.27 ± 0.14	10.50 ± 0.32
	[2.51, 3.14)	1.81 ± 0.13	1.77 ± 0.12	8.39 ± 0.32
	[3.14, 3.77)	2.00 ± 0.13	1.93 ± 0.13	9.21 ± 0.31
	[3.77, 4.40)	2.08 ± 0.13	2.12 ± 0.13	9.86 ± 0.29
	[4.40, 5.03)	2.53 ± 0.15	2.59 ± 0.15	12.02 ± 0.29
	[5.03, 5.65)	2.21 ± 0.13	2.35 ± 0.14	10.72 ± 0.29
	[5.65, 6.28)	1.88 ± 0.13	1.68 ± 0.12	

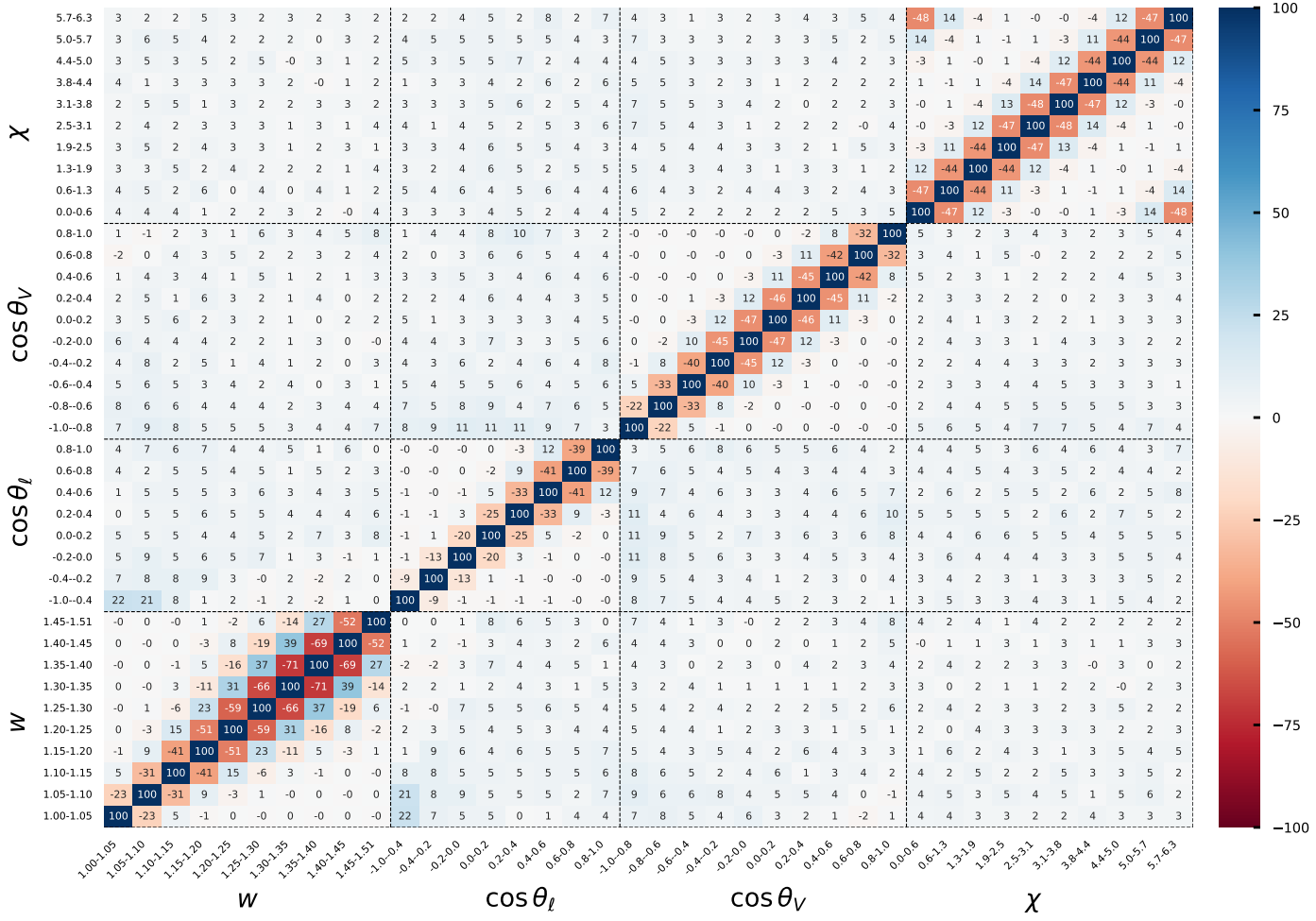

Figure H.1: Statistical correlations (in %) of the partial decay rates for the $\bar{B}^0 \to D^{*+} e^- \bar{\nu}_e$ decay.

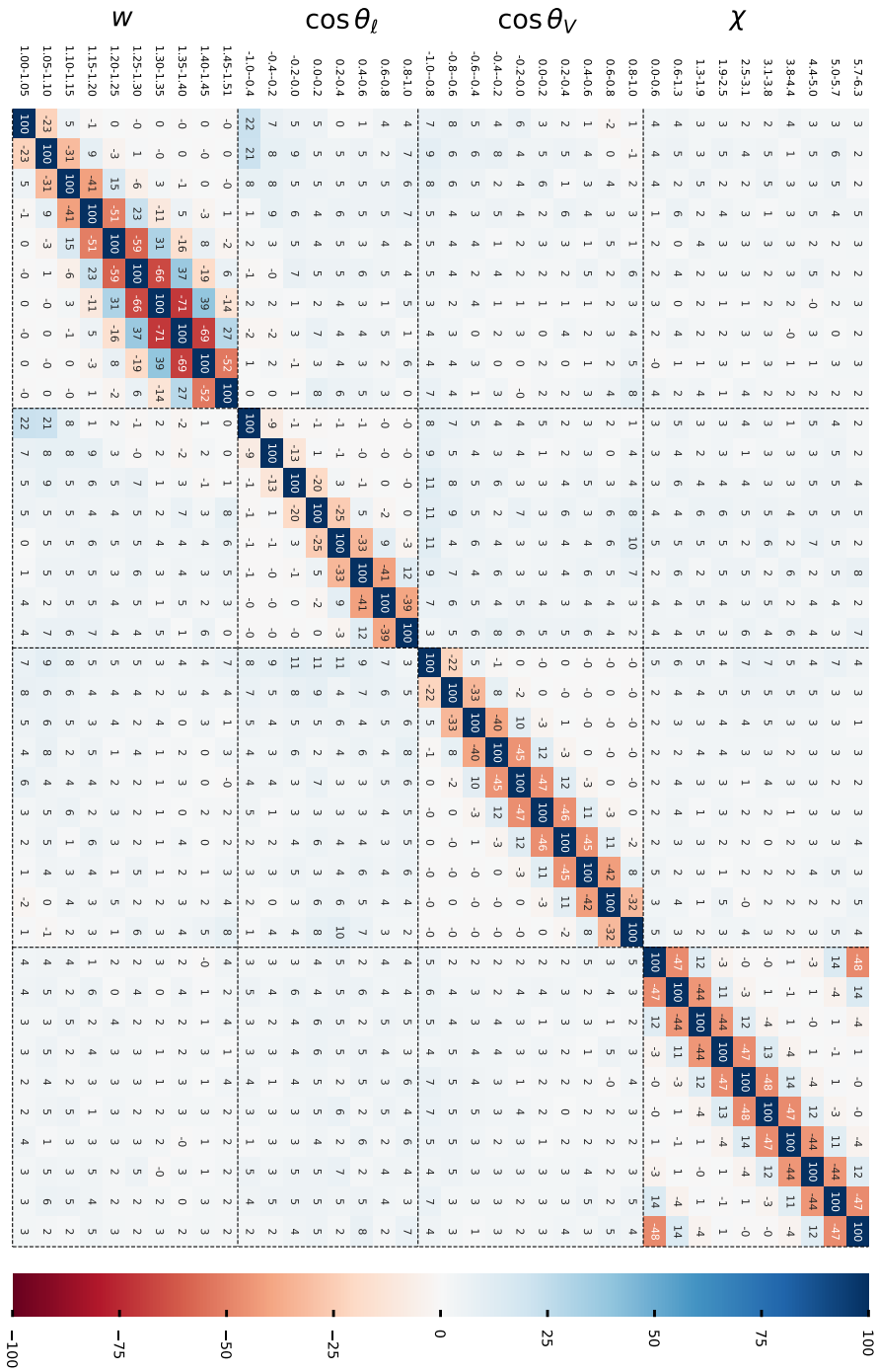

Figure H.2: Statistical correlations (in %) of the partial decay rates for the $\bar{B}^0 \to D^{*+}\mu^-\bar{\nu}_\mu$ decay.

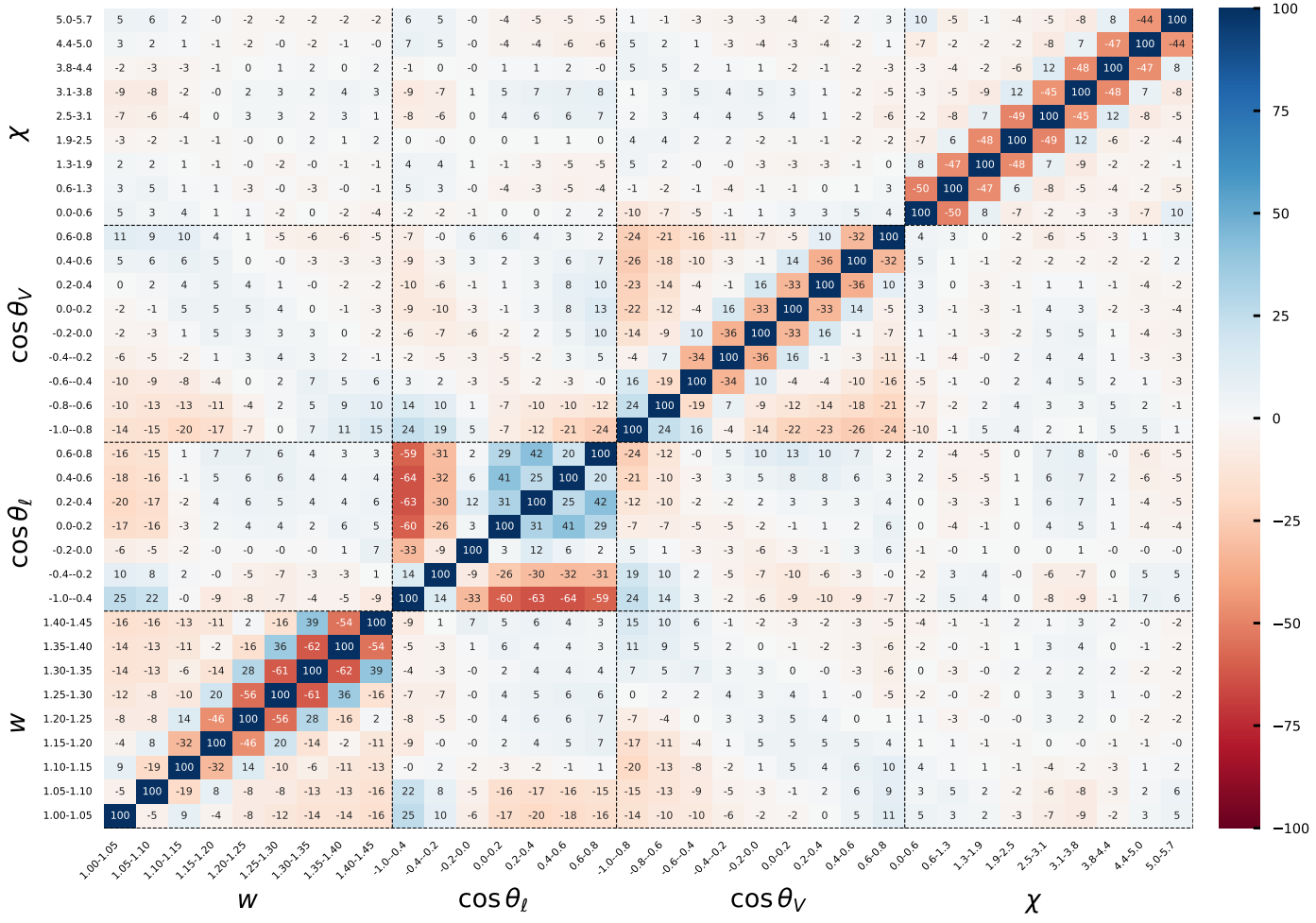

Figure H.3: Full experimental (statistical and systematic) correlations (in %) for the average of the normalized partial decay rates. The last bin of each projection is excluded in the determination of $|V_{cb}|$ value, thus it is not shown.

Table H.2: Results of the determination of the BGL expansion coefficients and their correlations.

	Value		Correlation			χ^2/ndf
$\tilde{a}_0 \times 10^3$	0.86 ± 0.06	1.00	0.17	−0.15	0.07	39/31
$\tilde{b}_0 \times 10^3$	0.54 ± 0.01	0.17	1.00	−0.35	−0.39	
$\tilde{b}_1 \times 10^3$	−0.18 ± 0.32	−0.15	−0.35	1.00	0.42	
$\tilde{c}_1 \times 10^3$	−0.04 ± 0.03	0.07	−0.39	0.42	1.00	

Table H.3: Results of the determination of the CLN parameters, $|V_{cb}|$ and their correlations.

	Value		Correlation			χ^2/ndf
ρ^2	1.19 ± 0.06	1.00	0.24	−0.83	0.28	40/31
$R_1(1)$	1.11 ± 0.08	0.24	1.00	−0.33	−0.12	
$R_2(1)$	0.90 ± 0.04	−0.83	−0.33	1.00	−0.09	
$\|V_{cb}\| \times 10^3$	40.1 ± 1.1	0.28	−0.12	−0.09	1.00	

Table H.4: Values of BGL form factors and $|V_{cb}|$ resulting from a fit that includes nonzero recoil lattice information.

	Constraints on $h_{A_1}(w)$	Constraints on $h_{A_1}(w)$, $R_1(w)$, $R_2(w)$
$a_0 \times 10^3$	21.2 ± 1.6	26.1 ± 0.9
$b_0 \times 10^3$	13.18 ± 0.24	13.50 ± 0.23
$b_1 \times 10^3$	−3 ± 6	6 ± 6
$c_1 \times 10^3$	−0.9 ± 0.7	−0.6 ± 0.7
$\|V_{cb}\| \times 10^3$	40.3 ± 1.2	38.6 ± 1.1
χ^2/ndf	40/33	69/39
p-value	20%	0.2%

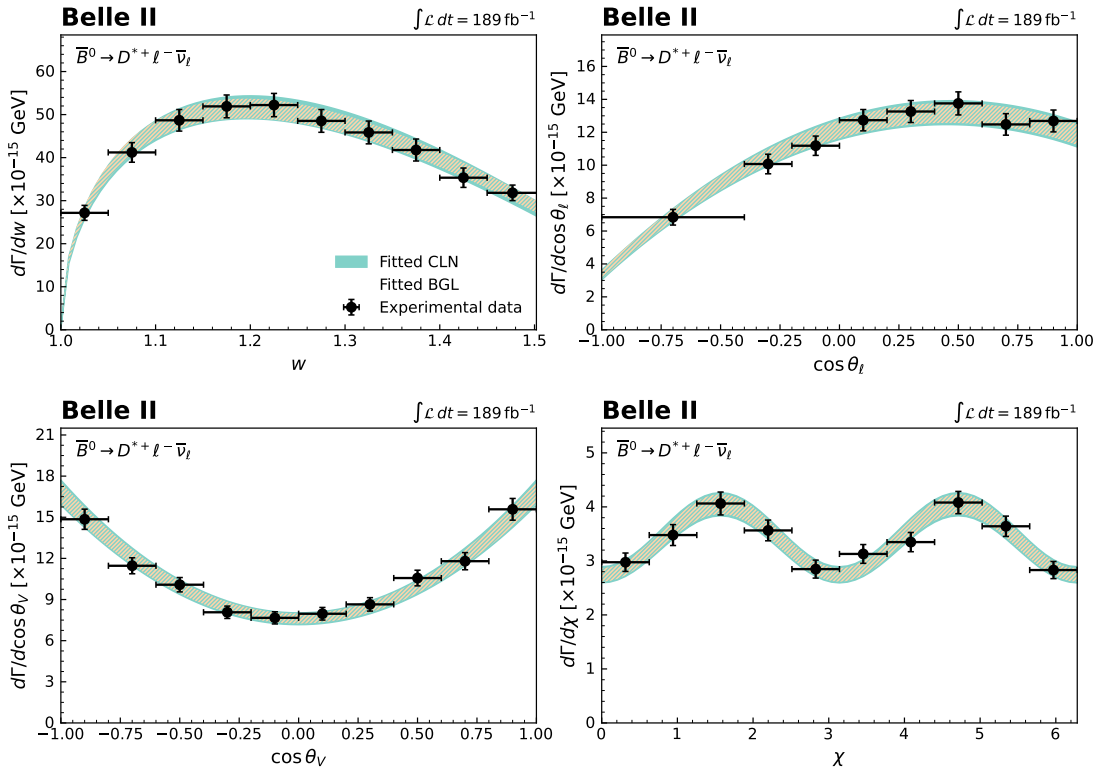

Figure H.4: Comparison of the fitted partial decay rates with 1σ uncertainties in the BGL and CLN parametrizations to the unfolded experimental data (shown as points with error bars). Note that the BGL (hatched) band almost completely overlays the CLN (solid) band.

Table H.5: Values of CLN form factors and $|V_{cb}|$ resulting from a fit that includes nonzero recoil lattice information.

	Constraints on $h_{A_1}(w)$	Constraints on $h_{A_1}(w)$, $R_1(w)$, $R_2(w)$
$h_{A_1}(1)$	0.91 ± 0.02	0.93 ± 0.02
ρ^2	1.20 ± 0.05	1.17 ± 0.05
$R_1(1)$	1.11 ± 0.08	1.29 ± 0.04
$R_2(1)$	0.90 ± 0.04	0.92 ± 0.03
$\lvert V_{cb}\rvert \times 10^3$	40.2 ± 1.2	38.9 ± 1.1
χ^2/ndf	40/33	67/39
p-value	19%	0.4%

APPENDIX I

Nested hypothesis tests with LQCD inputs

I.1 Test with LQCD constraints on h_{A_1}

In this scenario, we fit experimental data and the FNAL/MILC predictions on $h_{A_1}(w)$ at $w = [1.03, 1.10, 1.17]$ simultaneously. The obtained $|V_{cb}|$ values, minima of the χ^2, and numbers of degrees of freedom corresponding to various truncations are summarized in Table I.1. $n_a = 1$, $n_b = 1$, and $n_c = 2$ is determined as the optimal expansion order. The fitted parameters and their correlations are summarized in Table I.2.

Table I.1: Summary of the nested hypothesis test when FNAL/MILC predictions on $h_{A_1}(w)$ are taken into account. The chosen expansion is highlighted in a gray background.

(n_a, n_b, n_c)	$\lvert V_{cb}\rvert \times 10^3$	$\rho_{\max}$	χ^2	Ndf	p-value
$(1, 1, 2)$	40.0 ± 1.2	0.62	40.1	34	22%
$(2, 1, 2)$	40.0 ± 1.2	0.97	38.6	33	23%
$(1, 2, 2)$	40.3 ± 1.2	0.59	39.2	33	21%
$(1, 1, 3)$	40.0 ± 1.2	0.96	39.5	33	20%

Table I.2: Fitted parameters and their correlations using the optimal BGL expansion determined with FNAL/MILC constraints on $h_{A_1}(w)$.

	Value		Correlation			
$\lvert V_{cb}\rvert \times 10^3$	40.0	± 1.2	1.00	−0.36	−0.62	−0.19
$a_0 \times 10^3$	21.5	± 1.3	−0.36	1.00	0.31	0.51
$b_0 \times 10^3$	13.2	± 0.2	−0.62	0.31	1.00	−0.02
$c_1 \times 10^3$	−0.5	± 0.6	−0.19	0.51	−0.02	1.00

I.2 Test with LQCD constraints on h_{A_1}, R_1, and R_2

In this test, we fit experimental data and the FNAL/MILC predictions on $h_{A_1}(w)$, $R_1(w)$, and $R_2(w)$ at $w = [1.03, 1.10, 1.17]$ simultaneously. The obtained $|V_{cb}|$ values, minima of the χ^2, and numbers of degrees of freedom with various truncations are summarized in Table I.3. $n_a = 1$, $n_b = 3$, and $n_c = 2$ is determined as the optimal expansion order. The corresponding fitted parameters and their correlations are summarized in Table I.4.

By comparing the results in three scenarios, we find the inclusion of FNAL/MILC lattice results requires more BGL form-factor parameters to reach an acceptable χ^2 value. Using the fitted parameters and 1σ deviation summarized in Table I.2 and Table I.4, we plot the $h_{A_1}(w)$, $R_1(w)$ and $R_2(w)$ spectra in Fig. I.1. The re-optimized truncation results in a better description of lattice data, while the shapes of partial decay rates remain unchanged.

Table I.3: Summary of the nested hypothesis test when FNAL/MILC predictions on $h_{A_1}(w)$, $R_1(w)$, and $R_2(w)$ are taken into account. The chosen expansion is highlighted in a gray background.

(n_a, n_b, n_c)	$\lvert V_{cb}\rvert \times 10^3$	$\rho_{\max}$	χ^2	Ndf	p-value
$(1,1,2)$	38.3 ± 1.1	0.57	75.3	40	0.1%
$(2,1,2)$	39.2 ± 1.1	0.59	52.4	39	7%
$(1,2,2)$	38.3 ± 1.1	0.61	75.2	39	0.1%
$(1,1,3)$	38.5 ± 1.1	0.92	73.6	39	0.1%
$(3,1,2)$	39.5 ± 1.1	0.85	48.7	38	11%
$(2,2,2)$	39.2 ± 1.1	0.59	52.3	38	6%
$(2,1,3)$	39.4 ± 1.1	0.92	50.2	38	9%
$(4,1,2)$	39.4 ± 1.1	0.98	48.4	37	10%
$(3,2,2)$	39.3 ± 1.1	0.87	47.5	37	12%
$(3,1,3)$	39.7 ± 1.1	0.92	45.4	37	16%
$(4,2,2)$	39.2 ± 1.1	0.98	46.8	36	11%
$(3,3,2)$	39.3 ± 1.1	0.87	46.4	36	11%
$(3,2,3)$	39.6 ± 1.2	0.91	45.2	36	14%
$(4,3,2)$	39.3 ± 1.1	0.98	46	35	10%
$(3,4,2)$	39.3 ± 1.1	0.86	46.2	35	10%
$(3,3,3)$	39.6 ± 1.2	0.93	45	35	12%
$(4,1,3)$	39.7 ± 1.1	0.98	44.1	36	17%
$(3,1,4)$	39.7 ± 1.1	0.91	45.3	36	14%
$(2,2,3)$	39.5 ± 1.2	0.91	50.1	37	7%
$(2,1,4)$	39.4 ± 1.1	0.91	50.1	37	7%
$(1,2,3)$	38.5 ± 1.1	0.91	73.6	38	0.1%
$(1,1,4)$	38.5 ± 1.1	0.91	73.4	38	0.1%

Table I.4: Fitted parameters and their correlations using the optimal BGL expansion determined with FNAL/MILC constraints on $h_{A_1}(w)$, $R_1(w)$, and $R_2(w)$.

	Value		Correlation						
$\lvert V_{cb}\rvert \times 10^3$	39.7	± 1.1	1.00	−0.16	0.03	−0.11	−0.61	−0.16	0.11
$a_0 \times 10^3$	28.1	± 1.0	−0.16	1.00	−0.10	−0.19	0.17	0.12	−0.03
$a_1 \times 10^3$	−44.2	± 65.8	0.03	−0.10	1.00	−0.85	−0.04	−0.08	0.11
a_2	−5.1	± 2.4	−0.11	−0.19	−0.85	1.00	0.11	0.12	−0.12
$b_0 \times 10^3$	13.3	± 0.2	−0.61	0.17	−0.04	0.11	1.00	0.10	−0.12
$c_1 \times 10^3$	−2.7	± 1.3	−0.16	0.12	−0.08	0.12	0.10	1.00	−0.92
$c_2 \times 10^3$	50.8	± 27.7	0.11	−0.03	0.11	−0.12	−0.12	−0.92	1.00

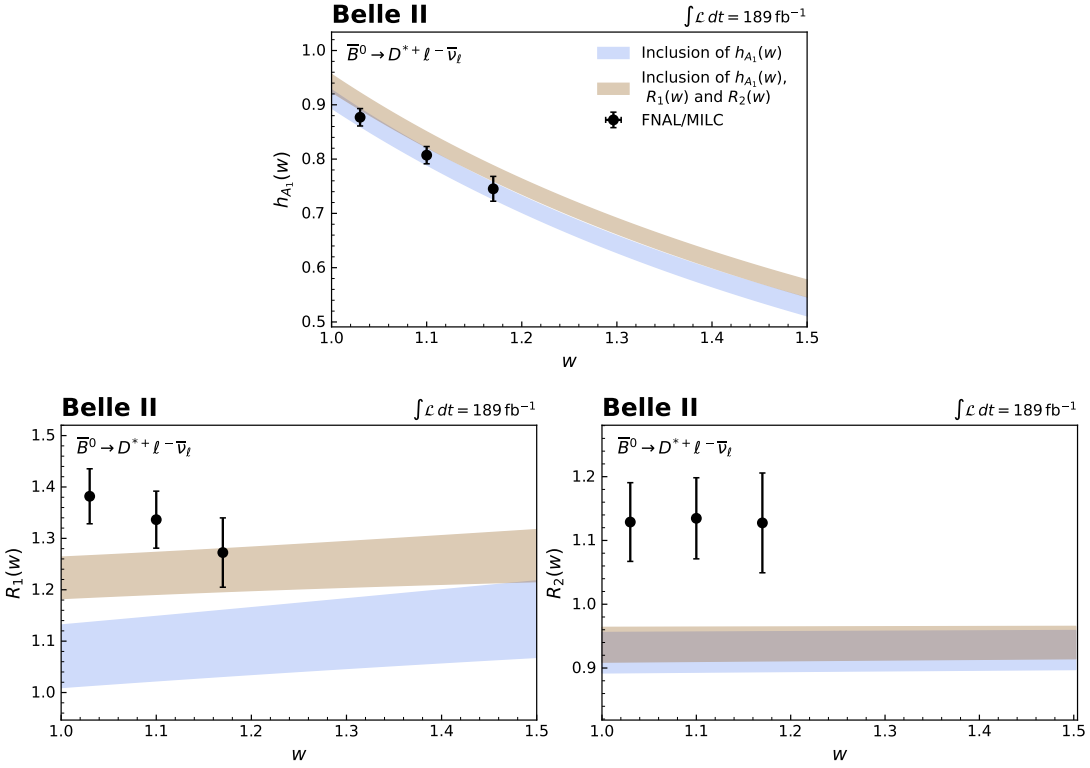

Figure I.1: Comparison of the $h_{A_1}(w)$, $R_1(w)$ and $R_2(w)$ spectra with the parameters determined in the nested hypothesis tests when FNAL/MILC lattice predictions are taken into account.

Bibliography

[1] R. L. Workman et al., *Review of Particle Physics*, PTEP **2022** (2022) 083C01 (cit. on pp. iii, 1, 65, 74, 89).

[2] J. W. Rohlf, *Modern Physics from α to Z^0*, 1st ed., Wiley, 1994 (cit. on p. 1).

[3] D. Griffiths, *Introduction to elementary particles*, 2008, ISBN: 978-3-527-40601-2 (cit. on p. 1).

[4] *The standard model*, URL: https://en.wikipedia.org/wiki/Standard_Model (cit. on p. 2).

[5] H.-X. Chen, W. Chen, X. Liu, Y.-R. Liu, and S.-L. Zhu, *An updated review of the new hadron states*, Rept. Prog. Phys. **86** (2023) 026201, arXiv: 2204.02649 [hep-ph] (cit. on p. 3).

[6] N. Brambilla et al., *The XYZ states: experimental and theoretical status and perspectives*, Phys. Rept. **873** (2020) 1, arXiv: 1907.07583 [hep-ex] (cit. on p. 3).

[7] T. P. Gorringe and D. W. Hertzog, *Precision Muon Physics*, Prog. Part. Nucl. Phys. **84** (2015) 73, arXiv: 1506.01465 [hep-ex] (cit. on p. 3).

[8] G. W. Bennett et al., *Final Report of the Muon E821 Anomalous Magnetic Moment Measurement at BNL*, Phys. Rev. D **73** (2006) 072003, arXiv: hep-ex/0602035 (cit. on p. 3).

[9] T. Aoyama et al., *The anomalous magnetic moment of the muon in the Standard Model*, Phys. Rept. **887** (2020) 1, arXiv: 2006.04822 [hep-ph] (cit. on p. 3).

[10] A. Pich, *Precision Tau Physics*, Prog. Part. Nucl. Phys. **75** (2014) 41, arXiv: 1310.7922 [hep-ph] (cit. on p. 3).

[11] Z.-z. Xing and S. Zhou, *Neutrinos in particle physics, astronomy and cosmology*, 2011, ISBN: 978-3-642-17559-6, 978-7-308-08024-8 (cit. on p. 3).

[12] J. Lesgourgues and S. Pastor, *Massive neutrinos and cosmology*, Phys. Rept. **429** (2006) 307, arXiv: astro-ph/0603494 (cit. on p. 3).

[13] M. D. Schwartz, *Quantum Field Theory and the Standard Model*, Cambridge University Press, 2014, ISBN: 978-1-107-03473-0, 978-1-107-03473-0 (cit. on p. 4).

[14] M. E. Peskin and D. V. Schroeder, *An Introduction to quantum field theory*, Reading, USA: Addison-Wesley, 1995, ISBN: 978-0-201-50397-5 (cit. on p. 4).

[15] M. Schumann, *Direct Detection of WIMP Dark Matter: Concepts and Status*, J. Phys. G **46** (2019) 103003, arXiv: 1903.03026 [astro-ph.CO] (cit. on p. 13).

[16] G. Bertone and T. Tait M. P., *A new era in the search for dark matter*, Nature **562** (2018) 51, arXiv: 1810.01668 [astro-ph.CO] (cit. on p. 13).

[17] Y. Amhis et al., *Averages of b-hadron, c-hadron, and τ-lepton properties as of 2021*, Phys. Rev. D **107** (2023) 052008, arXiv: 2206.07501 [hep-ex] (cit. on pp. 14–16).

[18] L. Lee, C. Ohm, A. Soffer, and T.-T. Yu, *Collider Searches for Long-Lived Particles Beyond the Standard Model*, Prog. Part. Nucl. Phys. **106** (2019) 210, [Erratum: Prog.Part.Nucl.Phys. 122, 103912 (2022)], arXiv: 1810.12602 [hep-ph] (cit. on p. 15).

[19] A. Canepa, *Searches for Supersymmetry at the Large Hadron Collider*, Rev. Phys. **4** (2019) 100033 (cit. on p. 15).

[20] S. Dawson, C. Englert, and T. Plehn, *Higgs Physics: It ain't over till it's over*, Phys. Rept. **816** (2019) 1, arXiv: 1808.01324 [hep-ph] (cit. on p. 15).

[21] G. Bhattacharyya and D. Das, *Scalar sector of two-Higgs-doublet models: A minireview*, Pramana **87** (2016) 40, arXiv: 1507.06424 [hep-ph] (cit. on p. 15).

[22] I. Doršner, S. Fajfer, A. Greljo, J. F. Kamenik, and N. Košnik, *Physics of leptoquarks in precision experiments and at particle colliders*, Phys. Rept. **641** (2016) 1, arXiv: 1603.04993 [hep-ph] (cit. on p. 15).

[23] E. Waheed et al., *Measurement of the CKM matrix element $|V_{cb}|$ from $B^0 \to D^{*-}\ell^+\nu_\ell$ at Belle*, Phys. Rev. D **100** (2019) 052007, [Erratum: Phys.Rev.D 103, 079901 (2021)], arXiv: 1809.03290 [hep-ex] (cit. on pp. 16, 89, 91, 94).

[24] C. Bobeth, M. Bordone, N. Gubernari, M. Jung, and D. van Dyk, *Lepton-flavour non-universality of $\bar{B} \to D^*\ell\bar{\nu}$ angular distributions in and beyond the Standard Model*, Eur. Phys. J. C **81** (2021) 984, arXiv: 2104.02094 [hep-ph] (cit. on pp. 16, 17, 89–91).

[25] A. Sirlin, *Large m(W), m(Z) Behavior of the O(alpha) Corrections to Semileptonic Processes Mediated by W*, Nucl. Phys. B **196** (1982) 83 (cit. on pp. 21, 82).

[26] A. V. Manohar and M. B. Wise, *Heavy quark physics*, vol. 10, 2000, ISBN: 978-0-521-03757-0 (cit. on p. 21).

[27] M. Neubert, *Heavy quark symmetry*, Phys. Rept. **245** (1994) 259, arXiv: hep-ph/9306320 (cit. on p. 21).

[28] A. F. Falk, *Hadrons of arbitrary spin in the heavy quark effective theory*, Nucl. Phys. B **378** (1992) 79 (cit. on p. 22).

[29] N. Isgur and M. B. Wise, *Weak Decays of Heavy Mesons in the Static Quark Approximation*, Phys. Lett. B **232** (1989) 113 (cit. on p. 23).

[30] I. Caprini, L. Lellouch, and M. Neubert,
Dispersive bounds on the shape of anti-B —> D(*) lepton anti-neutrino form-factors,
Nucl. Phys. B **530** (1998) 153, arXiv: hep-ph/9712417 (cit. on pp. 23, 79).

[31] C. G. Boyd, B. Grinstein, and R. F. Lebed, *Model independent determinations of anti-B —> D (lepton), D* (lepton) anti-neutrino form-factors*, Nucl. Phys. B **461** (1996) 493,
arXiv: hep-ph/9508211 (cit. on pp. 24, 79).

[32] C. G. Boyd, B. Grinstein, and R. F. Lebed,
Precision corrections to dispersive bounds on form-factors, Phys. Rev. D **56** (1997) 6895,
arXiv: hep-ph/9705252 (cit. on pp. 24, 79).

[33] W. Altmannshofer et al., *The Belle II Physics Book*, PTEP **2019** (2019) 123C01, ed. by E. Kou and P. Urquijo, [Erratum: PTEP 2020, 029201 (2020)],
arXiv: 1808.10567 [hep-ex] (cit. on pp. 27, 33–35).

[34] K. Akai, K. Furukawa, and H. Koiso, *SuperKEKB Collider*,
Nucl. Instrum. Meth. A **907** (2018) 188, arXiv: 1809.01958 [physics.acc-ph]
(cit. on p. 28).

[35] T. Abe et al., *Belle II Technical Design Report*, (2010),
arXiv: 1011.0352 [physics.ins-det] (cit. on pp. 28, 32).

[36] M. Bona et al., *SuperB: A High-Luminosity Asymmetric e+ e- Super Flavor Factory. Conceptual Design Report*, (2007), arXiv: 0709.0451 [hep-ex] (cit. on p. 28).

[37] V. Shiltsev and F. Zimmermann, *Modern and Future Colliders*,
Rev. Mod. Phys. **93** (2021) 015006, arXiv: 2003.09084 [physics.acc-ph]
(cit. on p. 28).

[38] K. Lalwani, *The Belle II experiment: Status and prospects*,
SciPost Phys. Proc. **8** (2023) 176 (cit. on p. 29).

[39] *SuperKEKB raises the bar*,
URL: https://cerncourier.com/a/superkekb-raises-the-bar (cit. on p. 29).

[40] F. Forti, "Snowmass Whitepaper: The Belle II Detector Upgrade Program,"
Snowmass 2021, 2022, arXiv: 2203.11349 [hep-ex] (cit. on pp. 29, 30).

[41] *The Belle II detector*,
URL: https://www.kek.jp/en/newsroom/2018/04/26/0700/ (cit. on p. 29).

[42] L. Stötzer,
Optimization of long-lived neutral kaon detection and rejection at the Belle II experiment,
PhD thesis: University of Bonn, 2022 (cit. on p. 30).

[43] P. Fischer et al., *Progress towards a large area, thin DEPFET detector module*,
Nucl. Instrum. Meth. A **582** (2007) 843, ed. by G. Ambrosi et al. (cit. on p. 30).

[44] J. Kemmer, E. Belau, U. Prechtel, W. Welser, and G. Lutz,
LOW CAPACITY DRIFT DIODE, Nucl. Instrum. Meth. A **253** (1987) 378 (cit. on p. 30).

[45] K. Dort et al., *Comparison of supervised and unsupervised anomaly detection in Belle II pixel detector data*, Eur. Phys. J. C **82** (2022) 587, arXiv: 2202.07935 [hep-ex] (cit. on p. 30).

[46] G. Giakoustidis et al., *Status of the BELLE II Pixel Detector*, PoS **Pixel2022** (2023) 005 (cit. on p. 30).

[47] L. Zani et al., *The Silicon Vertex Detector of the Belle II experiment*, Nucl. Instrum. Meth. A **1038** (2022) 166952, arXiv: 2206.11648 [physics.ins-det] (cit. on p. 31).

[48] K. Lautenbach et al., *The Silicon Vertex Detector of the Belle II Experiment*, PoS **ICHEP2022** (2022) 328 (cit. on p. 31).

[49] C. Irmler et al., *The silicon vertex detector of the Belle II experiment*, Nucl. Instrum. Meth. A **1045** (2023) 167578 (cit. on p. 31).

[50] Y. T. Lai et al., *Development of the Level-1 track trigger with Central Drift Chamber detector in Belle II experiment and its performance in SuperKEKB 2019 Phase 3 operation*, JINST **15** (2020) C06063 (cit. on p. 31).

[51] N. Taniguchi, *Central Drift Chamber for Belle-II*, JINST **12** (2017) C06014, ed. by L. Shekhtman (cit. on p. 31).

[52] Y. Sue et al., *The Event Timing Finder for the Central Drift Chamber Level-1 Trigger at the Belle II experiment*, J. Phys. Conf. Ser. **2374** (2022) 012103 (cit. on p. 31).

[53] S. Skambraks et al., *A 3D track finder for the Belle II CDC L1 trigger*, J. Phys. Conf. Ser. **1525** (2020) 012102 (cit. on p. 31).

[54] K. Kojima, *The operation and performance of the TOP detector at the Belle II experiment*, PoS **EPS-HEP2021** (2022) 803 (cit. on p. 31).

[55] S. Sandilya, A. Schwartz, and U. Tamponi, *Charged particle identification performance of the TOP counters in Belle II*, J. Phys. Conf. Ser. **2374** (2022) 012107 (cit. on pp. 31, 34).

[56] L. Santelj, "Recent developments in data reconstruction for aerogel RICH at Belle II," 2023, arXiv: 2305.18347 [physics.ins-det] (cit. on p. 32).

[57] A. N. Charan, *Particle identification with the Belle II calorimeter using machine learning*, J. Phys. Conf. Ser. **2438** (2023) 012111, arXiv: 2301.11654 [hep-ex] (cit. on p. 32).

[58] A. Novosel et al., "Identification of light leptons and pions in the electromagnetic calorimeter of Belle II," *11th International Workshop on Ring Imaging Cherenkov Detectors*, 2023, arXiv: 2301.05074 [hep-ex] (cit. on p. 32).

[59] A. Abashian et al., *The Belle Detector*, Nucl. Instrum. Meth. A **479** (2002) 117 (cit. on p. 32).

[60] A. Abashian et al.,
The K(L) / mu detector subsystem for the BELLE experiment at the KEK B factory,
Nucl. Instrum. Meth. A **449** (2000) 112 (cit. on p. 32).

[61] T. Kuhr, C. Pulvermacher, M. Ritter, T. Hauth, and N. Braun, *The Belle II Core Software*,
Comput. Softw. Big Sci. **3** (2019) 1, arXiv: 1809.04299 [physics.comp-ph]
(cit. on pp. 33, 38).

[62] T. B. I. Collaboration, *Belle II Analysis Software Framework (basf2)*,
version release-06-00-09, If you use this software, please cite it using the metadata from this file and https://doi.org/10.1007/s41781-018-0017-9., 2022,
URL: https://doi.org/10.5281/zenodo.6949513 (cit. on p. 33).

[63] T. Alexopoulos, M. Bachtis, E. Gazis, and G. Tsipolitis, *Implementation of the Legendre Transform for track segment reconstruction in drift tube chambers*,
Nucl. Instrum. Meth. A **592** (2008) 456 (cit. on p. 33).

[64] A. Glazov, I. Kisel, E. Konotopskaya, and G. Ososkov,
Filtering tracks in discrete detectors using a cellular automaton,
Nucl. Instrum. Meth. A **329** (1993) 262 (cit. on p. 33).

[65] I. Abt, I. Kisel, S. Masciocchi, and D. Emelyanov,
CATS: A cellular automaton for tracking in silicon for the HERA-B vertex detector,
Nucl. Instrum. Meth. A **489** (2002) 389 (cit. on p. 33).

[66] T. Bilka et al.,
Implementation of GENFIT2 as an experiment independent track-fitting framework,
(2019), arXiv: 1902.04405 [physics.data-an] (cit. on p. 33).

[67] R. Mankel and A. Spiridonov, *The Concurrent track evolution algorithm: Extension for track finding in the inhomogeneous magnetic field of the HERA-B spectrometer*,
Nucl. Instrum. Meth. A **426** (1999) 268, arXiv: hep-ex/9809021 (cit. on p. 33).

[68] R. Mankel, *Pattern recognition and event reconstruction in particle physics experiments*,
Rept. Prog. Phys. **67** (2004) 553, arXiv: physics/0402039 (cit. on p. 33).

[69] R. Frühwirth, R. Glattauer, J. Lettenbichler, W. Mitaroff, and M. Nadler,
Track finding in silicon trackers with a small number of layers,
Nucl. Instrum. Meth. A **732** (2013) 95, ed. by T. Bergauer et al. (cit. on p. 33).

[70] V. Bertacchi et al., *Track finding at Belle II*, Comput. Phys. Commun. **259** (2021) 107610,
arXiv: 2003.12466 [physics.ins-det] (cit. on p. 33).

[71] F. Wemmer et al.,
Photon Reconstruction in the Belle II Calorimeter Using Graph Neural Networks, (2023),
arXiv: 2306.04179 [hep-ex] (cit. on p. 34).

[72] D. J. Lange, *The EvtGen particle decay simulation package*,
Nucl. Instrum. Meth. A **462** (2001) 152, ed. by S. Erhan, P. Schlein, and Y. Rozen
(cit. on p. 36).

[73] S. Jadach, B. F. L. Ward, and Z. Was, *The Precision Monte Carlo event generator K K for two fermion final states in e+ e- collisions*, Comput. Phys. Commun. **130** (2000) 260, arXiv: hep-ph/9912214 (cit. on p. 36).

[74] T. Sjostrand, S. Mrenna, and P. Z. Skands, *A Brief Introduction to PYTHIA 8.1*, Comput. Phys. Commun. **178** (2008) 852, arXiv: 0710.3820 [hep-ph] (cit. on p. 36).

[75] S. Jadach, J. H. Kuhn, and Z. Was, *TAUOLA: A Library of Monte Carlo programs to simulate decays of polarized tau leptons*, Comput. Phys. Commun. **64** (1990) 275 (cit. on p. 36).

[76] S. Agostinelli et al., *GEANT4–a simulation toolkit*, Nucl. Instrum. Meth. A **506** (2003) 250 (cit. on p. 36).

[77] T. Keck et al., *The Full Event Interpretation: An Exclusive Tagging Algorithm for the Belle II Experiment*, Comput. Softw. Big Sci. **3** (2019) 6, arXiv: 1807.08680 [hep-ex] (cit. on p. 37).

[78] Y. Freund and R. E. Schapire, *A Decision-Theoretic Generalization of On-Line Learning and an Application to Boosting*, Journal of Computer and System Sciences **55** (1997) 119, ISSN: 0022-0000, URL: https://www.sciencedirect.com/science/article/pii/S002200009791504X (cit. on p. 37).

[79] M. T. Prim et al., *Design and Performance of the Belle II High Level Trigger*, PoS **ICHEP2020** (2021) 769 (cit. on p. 38).

[80] T. B. I. Collaboration, *Belle II Analysis Software Framework (basf2)*, version release-06-00-07, If you use this software, please cite it using the metadata from this file and https://doi.org/10.1007/s41781-018-0017-9., 2022, URL: https://doi.org/10.5281/zenodo.6949466 (cit. on p. 38).

[81] G. C. Fox and S. Wolfram, *Observables for the Analysis of Event Shapes in e^+e^- Annihilation and Other Processes*, Phys. Rev. Lett. **41** (23 1978) 1581, URL: https://link.aps.org/doi/10.1103/PhysRevLett.41.1581 (cit. on p. 39).

[82] P. Koppenburg, *Statistical biases in measurements with multiple candidates*, (2017), arXiv: 1703.01128 [hep-ex] (cit. on p. 39).

[83] *A package for offline particle ID efficiency and fake rate corrections*, URL: https://stash.desy.de/users/sutclw/repos/pidvar/browse (cit. on p. 43).

[84] C. R. Harris et al., *Array programming with NumPy*, Nature **585** (2020) 357, URL: https://doi.org/10.1038/s41586-020-2649-2 (cit. on p. 43).

[85] M. S. Gill, *Measurement of $B \to D$ Form Factors in the Semileptonic Decay $B^0 \to D^* \ell \nu$ at BaBar*, PhD thesis: Stanford University, 2004 (cit. on p. 47).

[86] B. Aubert et al., *Measurements of the $B \to D^*$ form-factors using the decay $\bar{B}^0 \to D^{*+} e^-$ electron-neutrino*, Phys. Rev. D **74** (2006) 092004, arXiv: hep-ex/0602023 (cit. on p. 47).

[87] *A package for template fit*, URL: https://stash.desy.de/users/sutclw/repos/binfit/browse (cit. on p. 57).

[88] F. James and M. Roos, *Minuit: A System for Function Minimization and Analysis of the Parameter Errors and Correlations*, Comput. Phys. Commun. **10** (1975) 343 (cit. on p. 57).

[89] H. Dembinski and P. O. et al., *scikit-hep/iminuit*, (2020), URL: https://doi.org/10.5281/zenodo.3949207 (cit. on p. 57).

[90] S. Schmitt, *Data Unfolding Methods in High Energy Physics*, EPJ Web Conf. **137** (2017) 11008, ed. by Y. Foka, N. Brambilla, and V. Kovalenko, arXiv: 1611.01927 [physics.data-an] (cit. on p. 59).

[91] G. D'Agostini, "Improved iterative Bayesian unfolding," *Alliance Workshop on Unfolding and Data Correction*, 2010, arXiv: 1010.0632 [physics.data-an] (cit. on p. 59).

[92] A. Andreassen, P. T. Komiske, E. M. Metodiev, B. Nachman, and J. Thaler, *OmniFold: A Method to Simultaneously Unfold All Observables*, Phys. Rev. Lett. **124** (2020) 182001, arXiv: 1911.09107 [hep-ph] (cit. on p. 59).

[93] A. Hocker and V. Kartvelishvili, *SVD approach to data unfolding*, Nucl. Instrum. Meth. A **372** (1996) 469, arXiv: hep-ph/9509307 (cit. on p. 59).

[94] *A Python wrapper of RooUnfold.* URL: https://github.com/lucao-git/PyRooUnfold (cit. on p. 59).

[95] *A framework for unfolding within the ROOT environment, implementing a number of specific algorithms.* URL: https://gitlab.cern.ch/RooUnfold/RooUnfold (cit. on p. 59).

[96] T. Adye, "Unfolding algorithms and tests using RooUnfold," *PHYSTAT 2011*, Geneva: CERN, 2011 313, arXiv: 1105.1160 [physics.data-an] (cit. on p. 59).

[97] D. Ferlewicz, P. Urquijo, and E. Waheed, *Revisiting fits to $B^0 \to D^{*-} \ell^+ \nu_\ell$ to measure $|V_{cb}|$ with novel methods and preliminary LQCD data at nonzero recoil*, Phys. Rev. D **103** (2021) 073005, arXiv: 2008.09341 [hep-ph] (cit. on pp. 60, 74).

[98] M. Prim, *b2-hive/eFFORT v0.1.0*, version v0.1.0, 2020, URL: https://doi.org/10.5281/zenodo.3965699 (cit. on p. 60).

[99] T. Allmendinger et al., *Track Finding Efficiency in BaBar*, Nucl. Instrum. Meth. A **704** (2013) 44, arXiv: 1207.2849 [hep-ex] (cit. on p. 72).

[100] S. Choudhury et al., *Measurement of the B+/B0 production ratio in e+e- collisions at the $\Upsilon(4S)$ resonance using $B \to J/\psi(\ell\ell)K$ decays at Belle*, Phys. Rev. D **107** (2023) L031102, arXiv: 2207.01194 [hep-ex] (cit. on p. 73).

[101] F. U. Bernlochner, Z. Ligeti, and D. J. Robinson,
$N = 5, 6, 7, 8$: Nested hypothesis tests and truncation dependence of $|V_{cb}|$,
Phys. Rev. D **100** (2019) 013005, arXiv: 1902.09553 [hep-ph] (cit. on p. 81).

[102] J. A. Bailey et al., *Update of $|V_{cb}|$ from the $\bar{B} \to D^* \ell \bar{\nu}$ form factor at zero recoil with three-flavor lattice QCD*, Phys. Rev. D **89** (2014) 114504,
arXiv: 1403.0635 [hep-lat] (cit. on p. 82).

[103] A. Bazavov et al., *Semileptonic form factors for $B \to D^* \ell \nu$ at nonzero recoil from 2 + 1-flavor lattice QCD: Fermilab Lattice and MILC Collaborations*,
Eur. Phys. J. C **82** (2022) 1141, [Erratum: Eur.Phys.J.C 83, 21 (2023)],
arXiv: 2105.14019 [hep-lat] (cit. on pp. 85, 86, 93).

[104] M. T. Prim et al.,
Measurement of Differential Distributions of $B \to D^* \ell \bar{\nu}_\ell$ and Implications on $|V_{cb}|$,
(2023), arXiv: 2301.07529 [hep-ex] (cit. on pp. 86, 91, 93).

[105] F. U. Bernlochner et al.,
Constrained second-order power corrections in HQET: R(D(*)), |Vcb|, and new physics,
Phys. Rev. D **106** (2022) 096015, arXiv: 2206.11281 [hep-ph] (cit. on pp. 89–91).

[106] L. Aggarwal et al., *Test of Light-Lepton Universality in the Rates of Inclusive Semileptonic B-Meson Decays at Belle II*, Phys. Rev. Lett. **131** (2023) 051804,
arXiv: 2301.08266 [hep-ex] (cit. on p. 89).

[107] M. Bordone, B. Capdevila, and P. Gambino, *Three loop calculations and inclusive Vcb*,
Phys. Lett. B **822** (2021) 136679, arXiv: 2107.00604 [hep-ph] (cit. on p. 93).

[108] F. Bernlochner et al., *First extraction of inclusive V_{cb} from q^2 moments*,
JHEP **10** (2022) 068, arXiv: 2205.10274 [hep-ph] (cit. on p. 93).

[109] G. D'Agostini, *On the use of the covariance matrix to fit correlated data*,
Nucl. Instrum. Meth. A **346** (1994) 306 (cit. on p. 141).

List of Figures

List of Tables